Understanding the Localization of States in Dense Plasmas via First Principles Quantum Electronic Structure Calculations



Thomas Daniel Gawne

Magdalen College
University of Oxford

Supervised by:
Prof. Sam M. Vinko and Prof. Justin S. Wark

Thesis Submitted for the Degree of
Doctor of Philosophy

Trinity Term 2023

©*British Crown Copyright 2023/AWE*

This document is of United Kingdom origin and contains proprietary information which is the property of the Secretary of State for Defence. It is furnished in confidence and may not be copied, used or disclosed in whole or in part without prior written consent of Defence Intellectual Property Rights DGDCDIPR-PL-Ministry of Defence, Abbey Wood, Bristol, BS34 8JH, England.

Understanding the Localization of States in Dense Plasmas via First Principles Quantum Electronic Structure Calculations

Thomas Daniel Gawne
Magdalen College, University of Oxford
Thesis Submitted for the Degree of Doctor of Philosophy
Trinity Term 2023

Abstract

Modelling is an important part of plasma research, providing a means to make predictions and interpret spectroscopic data. As exact calculations by solving the many-body Hamiltonian are computationally impossible for any realistic plasma system, a variety of models have been developed that simplify the physics behind different plasma processes. To make meaningful predictions, it is vital to be sure that the underlying approximations are appropriate and well-founded. This thesis focuses on the fundamental process of continuum lowering, which, until recently, has been thought to be adequately treated using simple analytical models known as ionization potential depression (IPD). However, a growing number of experiments show that widely-used IPD models do not make accurate predictions, leading to significant concerns about our ability to model high energy density (HED) systems. There has since been a large theoretical and computational effort to understand why these discrepancies arise, and if they can be resolved. Despite this, significant controversy and disagreement still surround IPD. In this thesis, I present first principles investigations into continuum lowering. A particular focus is made on the underlying assumption of IPD models: that electrons can be easily distinguished as purely bound to ions or purely free. To start, a new model is developed that allows for the evaluation of IPD from first principles by quantifying the spatial localization of Kohn-Sham states calculated using finite-temperature density functional theory (FT-DFT). Using this model, it is possible to investigate localization mechanisms in a variety of routine plasma processes, and to scrutinize the bound-or-free assumption of IPD models. Then, the first experimental observations of K_β emission from highly charged Mg ions at solid density are presented, which indicates that the $n = 3$ orbitals rebind to the Mg ions. This places new constraints on the strength of the IPD. Using the localization metric with FT-DFT calculations, it is found that during heating the $n = 3$ states smoothly relocalize around the Mg ions. It is also seen that widely-used analytical IPD models are unable to reproduce the relocalization behaviour, in part as a consequence of the bound-or-free model generally being an overly-simplistic representation of reality. Remaining discrepancies with a similar previous experiment are resolved by a re-interpretation of the data in light of the localization metric. Another investigation is presented into definitions of ionization in HED plasmas. Ionization is a problematic quantity in that it does not have a well-defined thermodynamic definition, yet it is a key parameter within plasma modelling. One therefore still aims to find a consistent and unambiguous definition for the ionization state. Within this context, FT-DFT calculations of the ionization state of CH plasmas is presented using two potential definitions: one based on counting the number of continuum electrons, and another based on the optical conductivity. Differences of up to 10% are observed between the two methods. However, including "Pauli forbidden" transitions in the conductivity reproduces the counting definition, suggesting such transitions are important to evaluate the ionization state. The work presented in this thesis has important implications about our ability to predictively model HED systems.

Acknowledgements

There are many people whom I would like to thank for helping me reach the end of my doctorate. Firstly, I must first thank my supervisors Professor Sam Vinko and Professor Justin Wark, to whom I am heavily indebted. Their knowledge, support, enthusiasm for my work, and the opportunities they have provided me have been invaluable during my research and certainly in my future. I am a better scientist for having researched under them. Secondly, my partner Anna Matthew for her unconditional love and support during my doctorate. Despite her non-physics background, she has diligently read any work I have presented to her and provide helpful feedback over the last few years, for which I am ever thankful. Likewise, my parents Simon and Julie and my siblings Dan and Frances have supported me throughout my growing-up and education, and now my doctorate. Sooty the cat has been loud and rude since adopting him two years ago, but he's very adorable and so has helped in his own special way.

There are many folks who have passed through the Simon Room during my time that deserve thanks for their support. Despite the quirks of the office space, it has been a good place to work thanks to the people there. I would like to especially mention Thomas Campbell, Alessandro Forte, Pontus Svensson, Patrick Heighway, Celine Crepisson, Hannah Poole, and Charlie Arrowsmith for being on hand to grab coffees and to listen to my ~~rants~~ thoughts on IPD models and ionization. I would also like to thank the members of the Vinko-Wark group as a whole for their useful feedback and discussions of my work. A special mention also goes to Olly Humphries for his help and advice early on in my doctorate; Patrick Hollebon for many useful discussions regarding DFT and IPD; and Tom Preston for introducing me to Hamburg and encouragement in my postdoctorate search.

Surprisingly, despite the events of the last few years, I did manage to have a social life. My thanks go to Harry, Kristian, Ryan, Callum, Adam, and Rosie for the fantastic D&D games. And thank you to Indrani and Tilly the dog for the many walks, talks, and cups of tea over the past year.

Finally, I need to address the elephant in the room: I would specifically not like to thank COVID-19 for locking us away during two-and-a-half years of my DPhil. It truly would not have been the same without it.

The author would like to thank the Atomic Weapons Establishment (AWE) plc. for their support via the Oxford Centre for High Energy Density Science (OxCHEDS).

Contents

List of Figures vi

List of Acronyms vii

Notation viii

1 Introduction 1
- 1.1 High Energy Density Matter . . . 1
- 1.2 Plasma Generation by Free Electron Lasers . . . 4
- 1.3 Density Functional Theory . . . 6
  - 1.3.1 Hohenberg-Kohn Theorems . . . 7
  - 1.3.2 Finite-temperature DFT . . . 10
  - 1.3.3 Kohn-Sham DFT . . . 11
  - 1.3.4 The Exchange-Correlation Potential . . . 16
  - 1.3.5 The Projector Augmented-wave Method . . . 17
  - 1.3.6 Hybrid Kohn-Sham Orbital-Free DFT . . . 19
- 1.4 Structure of Thesis . . . 24
- 1.5 Author Contributions . . . 26

2 Ionization Potential Depression 28
- 2.1 Continuum Lowering . . . 28
- 2.2 Deriving Ionization Potential Depression . . . 31
  - 2.2.1 Perturbation Approach . . . 32
  - 2.2.2 Thermodynamic Approach . . . 33
- 2.3 Traditional IPD Models . . . 37
  - 2.3.1 Weakly-Coupled Limit: Debye Screening . . . 37
  - 2.3.2 Strongly-Coupled Limit: Ion-Sphere Model . . . 41
  - 2.3.3 Ecker-Kröll Model . . . 43
  - 2.3.4 Stewart-Pyatt Model . . . 48
  - 2.3.5 Summary of Models . . . 52
- 2.4 Additional IPD-like Processes . . . 56
- 2.5 Experimental Measurements of IPD . . . 58
- 2.6 Theoretical Studies of Continuum Lowering . . . 63
- 2.7 Summary . . . 76

3 Theory of State Localization 81
- 3.1 Boundness and Localization . . . 82
- 3.2 Localization of Bloch States . . . 83
  - 3.2.1 Electron Localization Function . . . 84
  - 3.2.2 Wannier Functions . . . 85

3.2.3 Inverse Participation Ratio . . . 86
3.3 Localization from Dimensionality . . . 90
3.3.1 Dimensionality of Model Functions . . . 91
3.3.2 Effects of Function Overlap . . . 93
3.4 Dimensionality in Real Systems . . . 96
3.4.1 Localization in Simple Metals and Ionic Compounds . . . 98
3.4.2 Crystal Symmetry Effects on Localization . . . 101
3.4.3 Dimensionality of d-band Metals . . . 102
3.5 Summary . . . 104

4 Localization During Heating **106**
4.1 Experimental measurements . . . 107
4.2 DFT Simulations . . . 111
4.3 Results . . . 114
4.4 Ionization Potential Depression . . . 122
4.5 Summary . . . 130

5 Ionization in Hot Dense Systems **133**
5.1 Defining Ionization . . . 134
5.2 Counting the Conduction Electrons . . . 140
5.3 Results . . . 141
5.4 Discussion . . . 143

6 Conclusions and Future Work **146**
6.1 Summary of Thesis . . . 146
6.2 Future Work . . . 151
6.2.1 Dimensionality Analysis . . . 152
6.2.2 Future of IPD Models . . . 154
6.2.3 Defining Ionization . . . 156

Bibliography **158**

List of Figures

1.1 Temperature-density phase diagram of high energy density matter 2
1.2 Kohn-Sham DFT self-consistent field cycle 15

2.1 Schematic of K_α and K_β transitions 30
2.2 Schematic of various level shift effects 56
2.3 Schematic of line red-shifting by spectator electrons 61
2.4 Comparison of IPD energies by different models 77
2.5 Charge state distribution of Al at 100 eV 78

3.1 Localization of Gaussian functions 87
3.2 Different dimensionalities and their interpretations for toy functions 92
3.3 Localization of overlapping functions 95
3.4 Density of states and dimensionality of cold ground state Mg and MgF_2 . . 99
3.5 Crystal symmetry effects on localization 100
3.6 Dimensionality and DOS of Zn near the continuum edge 103
3.7 Dimensionality and DOS of Zn at 70 eV 103

4.1 Experimental spectra of double-core-hole K_α and K_β lines in Mg and MgF_2 108
4.2 Average charge state of metal ions versus temperature from DFT 113
4.3 Density of states of Mg, Al, and MgF_2 at different ionization states 115
4.4 Dimensionality and DOS of isochorically heated Mg 117
4.5 Dimensionality and DOS of isochorically heated Al 119
4.6 Dimensionality and DOS of isochorically heated MgF_2 121
4.7 Experimental emission intensity of the K_α lines of Mg 123
4.8 Mg and Al IPD energies from different schemes 127
4.9 Comparison of IPD energies for Mg and MgF_2 from DFT 129

5.1 Dimensionality and DOS of CH at different temperatures 135
5.2 A comparison of the CH ionization states from the continuum electron versus delocalized electrons only 137
5.3 Comparison of the mean ionization state of CH from the conductivity, counting the continuum electrons, and XRTS measurements. 141
5.4 Kubo-Greenwood conductivity of CH at different temperatures 144

List of Acronyms

BZ	Brillouin Zone
CL	Continuum Lowering
CR-AK	Collisional-Radiative Atomic Kinetics
DFT	Density Functional Theory
DH	Debye-Hückel
DOS	Density of States
EK	Ecker-Kröll
FT	Finite Temperature
GGA	Generalized Gradient Approximation
HDM	Hot Dense Matter
HED	High Energy Density
HEG	Homogeneous Electron Gas
HK	Hohenberg-Kohn
IPD	Ionization Potential Depression
IPR	Inverse Participation Ratio
IS	Ion-Sphere
KS	Kohn and Sham
LCLS	Linac Coherent Light Source
LDA	Local Density Approximation
LTE	Local Thermodynamic Equilibrium
MD	Molecular Dynamics
MHK	Mermin-Hohenberg-Kohn
MIS	Mean Ionization State
PAW	Projector Augmented-Wave
PPS	Plasma Polarization Shift
PWA	Plane Wave Approximation
OF	Orbital-Free
SP	Stewart-Pyatt
TF	Thomas-Fermi
WDM	Warm Dense Matter
XC	eXchange-Correlation
XFEL	X-ray Free Electron Laser
XRTS	X-Ray Thomson scattering

Notation

Quantity	Symbol	Value/Units
Average ionization state	$\langle z \rangle = \sum_i n_i z_i / \sum_i n_i$	–
Boltzmann constant	k_B	8.617×10^{-5} eV K^{-1}
Coupling parameter	Γ	–
Eigenenergy	ϵ	eV
Electron charge	e	1.602×10^{-28} C
Electron density	n_e	cm^{-3}
Electron mass	m_e	9.1094×10^{-28} g
Dimensionality	D	–
Free electron density	n_f	cm^{-3}
Ion density	n_i	cm^{-3}
Ionization state	z_i, Z_i	–
Particle number	N	–
Planck's constant	h ($\hbar = h/2\pi$)	1.239×10^{-4} eV cm c^{-1}
Mass density	ρ	g cm^{-3}
Speed of light	c	2.998×10^{10} cm s^{-1}
Temperature	T	eV
Vacuum permittivity	ϵ_0	55.263×10^4 e^2 eV^{-1} cm^{-1}
Wavefunction	ψ, Ψ	cm$^{-3/2}$

Chapter 1: Introduction

1.1 High Energy Density Matter

The work in this thesis predominantly concerns itself with high-energy density (HED) plasmas, namely warm dense matter (WDM) and hot dense matter (HDM). Matter in this regime have densities $\gtrsim 0.1$ g cm^{-3}, and temperatures $\sim 1-10$s eV in WDM and 100s eV in HDM (1 eV $\approx$ 11,600 K). These conditions, while they seem extreme, are prevalent throughout the universe in solar, Jovian, and white dwarf environments [1–4]. They are also regularly generated in the laboratory, including in direct- [5–7] and indirect-drive [8, 9] inertial confinement fusion (ICF) [10, 11], laser heating experiments [12], and free electron laser experiments [13]. There is therefore enormous interest in understanding and modelling HED systems, both out of fundamental physical interest and application.

In light of recent successes towards ICF ignition [14–16], plasma modelling is becoming increasingly critical [17]. This is, however, no small feat. The plasma conditions covered in an ICF implosion, for example, can span from ambient conditions (300 K, 1 bar, $\sim$ 1 g cm^{-3}) up to temperatures $\sim 10^5 - 10^6$ K, pressures $\sim 0.1-1$ Gbar, and 10s times solid density [18]. Numerous important plasma properties such as the equation of state, radiation transport, opacity, energy dissipation, the ion charge state distribution, electron and ion temperatures, particle densities, and more all depend on each other and external influences (e.g. laser light incident on the system). To highlight the challenges of modelling plasmas, this thesis predominantly focuses on just a single plasma process – continuum lowering – which will be introduced in the following chapter. Despite this, numerous techniques exist

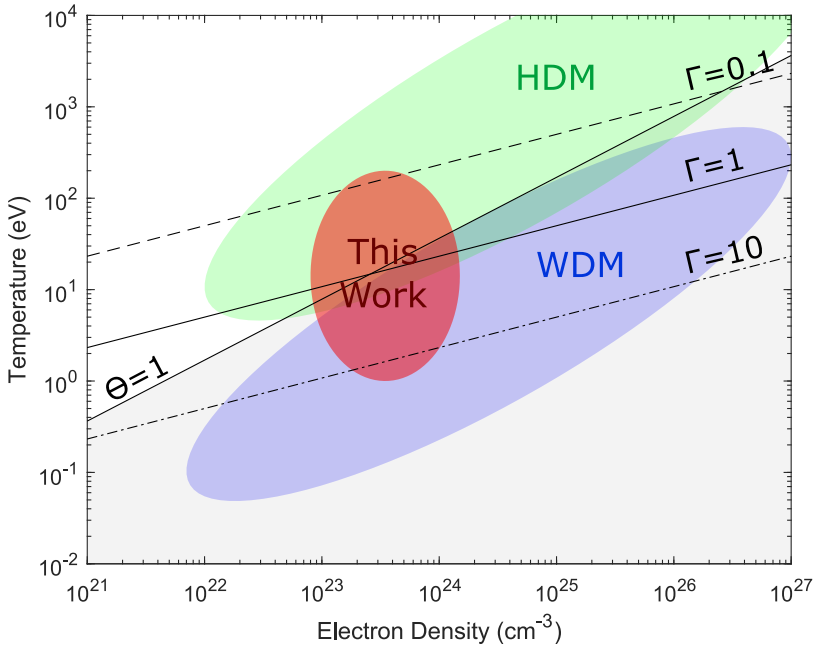


Figure 1.1: A temperature-density phase diagram for matter. Regions of WDM and HDM are indicated by the blue and green shaded regions, respectively. The red shaded area represents the conditions simulated in this thesis. Isolines of coupling parameters Γ_{ee} and the degeneracy parameter $\theta_e = 1$ are included. The grey shaded region represents $\theta_e < 1$, so it is the region where matter is degenerate. WDM and HDM values taken from [19].

to model plasmas and make predictions of experimental results, which continue to be developed and refined today.

Returning to the definitions of WDM and HDM, plasmas may be classed by a couple of dimensionless parameters. Generally, a plasma is treated as a system which contains free electrons with number density n_f at a temperature T_e; and ions at temperature T_i with charges $z_j e$ and number densities n_j. As a plasma is a quasi-neutral system, $n_f = \sum_i z_i n_i = \langle z \rangle n_i^{tot}$, where $\langle z \rangle$ is the mean charge state of the plasma. The first dimensionless parameter is the (Coulomb) coupling parameter, $\Gamma_{\alpha\beta}$, which is the ratio of the mean potential energy to the mean kinetic energy of the plasma; i.e. the mean Coulomb energy to thermal energy. The electron-electron coupling parameter is:

$$\Gamma_{ee} = \frac{e^2}{4\pi\epsilon_0 k_B T_e} \left(\frac{4\pi n_f}{3} \right)^{1/3}, \tag{1.1}$$

where k_B is the Boltzmann constant, ϵ_0 is the vacuum permittivity, and e is the elementary charge. Similarly, the ion-ion and electron-ion coupling parameters are:

$$\Gamma_{ii} = \langle z \rangle^{5/3} \frac{T_e}{T_i} \Gamma_{ee} \,; \qquad \Gamma_{ei} \sim \langle z \rangle \, \Gamma_{ee} \,. \tag{1.2}$$

Particles in a system are weakly-coupled if $\Gamma \ll 1$; that is, the thermal energy of the particles dominates over Coulomb interactions between them, and the particles are essentially randomly-distributed with just a minutiae of structure by the Coulomb interactions [20]. Strongly-coupled particles have $\Gamma \gtrsim 1$, so the Coulomb interactions dominate over the thermal energy, and close-pack structures may form if the coupling is sufficiently strong [21–23]. The degeneracy parameter θ_α, as the name implies, describes the degeneracy of the particles:

$$\theta_\alpha \equiv \frac{T_\alpha}{T_{F,\alpha}} \,, \tag{1.3}$$

where the Fermi temperature $T_{F,\alpha} = {k_B}^{-1} E_{F,\alpha}$ is related to the Fermi energy:

$$E_{F,\alpha} = \frac{\hbar^2}{2m_\alpha} \left(3\pi^2 n_\alpha\right)^{2/3} \,. \tag{1.4}$$

If $\theta_\alpha \leq 1$, then the particles in the system are degenerate and can no longer be treated with a classical approach. The distributions of the particles are therefore described by the Fermi-Dirac (electrons) and Bose-Einstein (ions) statistics; see Eq. (2.28). If $\theta_\alpha \gg 1$, then the particles are classical and can be described using Maxwell-Boltzmann statistics, Eq. (2.29), which can be much more convenient for calculating particle densities compared to the quantum distributions. Another useful parameter for describing plasma particles is the thermal de Broglie wavelength, Λ_α:

$$\Lambda_\alpha = \left(\frac{2\pi\hbar^2}{m_\alpha k_B T_\alpha}\right)^{1/2} \,. \tag{1.5}$$

A temperature-density phase diagram of high energy density matter, showing the various regimes of interest and plasma parameters, is plotted in Fig. 1.1.

This thesis is concerned with systems that have mid-to-strong coupling, and are

generally degenerate to some degree. In the simulations in Chapter 4, for example, the electrons have plasma parameters $\Gamma_{ee} \sim 0.1 - 10$ and $\theta_e \sim 0.1 - 10$. This is a challenging regime to model. As will be seen in Chapter 2, these combinations of coupling and degeneracy introduces considerable complexity as convenient approximations to simplify the particle distributions are no longer usable. How exactly one should bridge the gap between weakly-coupled non-degenerate systems to strongly-coupled degenerate systems is not trivial and is still being investigated.

1.2 Plasma Generation by Free Electron Lasers

It is worth briefly outlining how plasmas are created by, and interact with, x-ray free electron lasers (XFEL), and the various timescales involved in the interactions, as it is informative to the approximations made for the calculations presented in this thesis. A full explanation on the operating principles of an FEL is forgone here as it is not directly relevant to this work, but it is widely-described in the literature [24–26].

The XFEL pulses in experiments that will be examined in Chapter 4 have durations $\sim 10 - 100$ fs and peak intensities up to $\sim 10^{17}$ W cm^{-2}. At x-ray energies, photons strongly interact with the electrons bound to ions – typically K-shell ($1s$) electrons in the experiments considered here – to either photoionize the electron if the photon energy exceeds the binding energy of the electron, or excite the electron to another bound state if the photon energy matches the transition energy. If photoionized, the electron is initially non-thermal but, if it does not rebind to the ion, it thermalizes with the surrounding free electrons and increases the electron temperature. After the K-shell electron is ionized, the ion is in an excited state. For the materials of interest in this work, the most likely way the ion fills the K-shell hole is not by emitting a photon, but by Auger decay [27] – in Al, for example, radiative emission only accounts for 3.8% of recombination events from the L-shell ($n = 2$) [13]. The ejected Auger electron is likewise initially non-thermal, but may also thermalize and increase the electron temperature [13]. Generally, the heating by

non-thermal electrons is considered so fast that the non-thermal electrons are treated as instantaneously thermalizing with the surrounding free electrons [28–30]. A recent investigation has shown that for mid-Z elements such as Mg, non-thermal processes are only important for sub-10 fs pulses, or intensities exceeding 10^{17} W cm^{-2} [31]. Simulations show that the free electrons can be heated to in excess of 100 eV within just a few 10s fs [13].

Electron-ion collisional events predominantly drive the ions to higher ionization states, along with additional photoionization events [13, 32, 33]. Collisional events occur on sub-femtosecond timescales [32, 33]. The free electron density then reaches an approximately constant value after a few 10s fs. Radiative emission and Auger decay occur on the timescales of $\lesssim 1$ fs [27], meaning that the K-shell core hole is extremely short-lived. For the XFEL experiments considered in Chapter 4, the peak temperatures reached are not sufficient to thermally ionize the K-shell. Therefore, any K-shell emission can only occur in a time equal to the convolution of the XFEL pulse duration and the core-hole lifetime [34], which is essentially just the XFEL pulse duration. For the duration of the XFEL pulse, the ions remain relatively cold as the XFEL cannot directly heat the ions. Instead, electron-phonon interactions increase the lattice temperature. But, the timescales on which this occurs is on the order of picoseconds [35–37], so that the ion temperature does not change significantly during radiative emission, and the ions remain close to their crystal lattice positions.

These properties of XFELs interacting with solid density matter provide unique plasma conditions: the electrons can be driven to very high temperatures and high ionization states can be reached without substantial ion motion while the plasma fluoresces. The ion density can therefore be approximated as solid density, with the exact ion temperature generally unimportant to the electronic density of states [38] and the spectral results [13, 30, 39, 40]. They also present a useful testbed by creating plasmas at precisely known densities, which better constrains the possible plasma conditions by reducing the parameter space [41]. Furthermore, the XFEL acts as both pump and probe [13, 33] due to the tunability of the photon energy by

adjusting the FEL parameters [24].

1.3 Density Functional Theory

A proper theoretical description of the properties of plasmas requires a good and complete quantum mechanical description of the electrons and ions in the plasma. For a system containing N electrons and M ions, the many-body Hamiltonian that describes the system is:

$$\hat{H} = \hat{K}_e + \hat{K}_i + \hat{V}_{ee} + \hat{V}_{ei} + \hat{V}_{ii} + \hat{V}_{\text{add}} \ , \tag{1.6}$$

where $\hat{K}_e$ and $\hat{K}_i$ are the electron and ion kinetic energy, $\hat{V}_{ee}$ are the full electron-electron interactions, $\hat{V}_{ei}$ are the electron-ion interactions, $\hat{V}_{ii}$ are the ion-ion interactions, and $\hat{V}_{\text{add}}$ are any additional external interactions acting on the plasma. The interactions between the plasma particles are all Coulomb interactions. The challenge is to find the spectrum of many-body wavefunctions $|\Psi_j\rangle$ by solving the eigenvalue problem:

$$\hat{H}\,|\Psi_j\rangle = E_j\,|\Psi_j\rangle \ . \tag{1.7}$$

If one is able to solve this equation and find $|\Psi_j\rangle$, then all properties of the system can be calculated. However, it is well-known that it is computationally impossible to solve Eq. (1.7) for more than a few particles, let alone for a realistic system that is sampled in experiments, where the number of particles is of the order of 10^{23} and higher. An elegant solution to this problem was introduced in 1964 in a seminal work by Hohenberg and Kohn [42], in the form of density functional theory (DFT). When neglecting ion dynamics, DFT maps the $3N$-dimensional problem for solving the N-body system described by Eq. (1.6) to a functional minimisation problem involving just the electron density $n(\boldsymbol{r})$ of the system. DFT represents a formal proof and an advancement of the Thomas-Fermi (TF) and Thomas-Fermi-Dirac (TFD) models [43–46], which first introduced minimisation of functionals of the electron density as a way to solve the many-body problem. As a testament

to its success, DFT is now the most widely used method for electronic structure calculations, and an invaluable tool for predicting chemical properties [47]. Finite-temperature DFT is crucial for the theoretical calculations done in this work, so an overview of the Mermin-Hohnberg-Kohn theorems and the Kohn-Sham method are given below. Also introduced are computational methods relevant to DFT.

1.3.1 Hohenberg-Kohn Theorems

DFT is founded on the two Hohenberg-Kohn (HK) theorems [42]. First, Eq. (1.6) is re-written so that the electrons are interacting with each other and an external potential $v_{\text{ext}}(\boldsymbol{r}) = \langle \boldsymbol{r} | \, \hat{V}_{\text{ext}} \, | \boldsymbol{r} \rangle$:

$$\hat{H} = \hat{K}_e + \hat{V}_{ee} + \hat{V}_{\text{ext}} \ . \tag{1.8}$$

As the timescales of ion dynamics are typically significantly longer than those of electron dynamics, ion motion is ignored for simplicity, although it can be reintroduced in DFT molecular-dynamics using, for example, the Born-Oppenheimer approximation [47, 48]. The (normalized) many-body wavefunction solutions to the system are $\langle \boldsymbol{r}_1, \sigma_1, \ldots, \boldsymbol{r}_N, \sigma_N | \Psi_j \rangle = \Psi_j(\boldsymbol{r}_1, \sigma_1, \ldots, \boldsymbol{r}_N, \sigma_N)$, with $j = 0$ denoting the ground state solution, and $\boldsymbol{r}_i$ and σ_i are the positions and spins of the electrons. The different energy contributions to the Hamiltonian are functionals of the many-body wavefunction by the relationship $E = \langle \hat{H} \rangle \equiv \langle \Psi | \, \hat{H} \, | \Psi \rangle$. The electron density is defined using the density operator $\hat{n} = \sum_{i=1}^{N} \delta(\boldsymbol{r} - \boldsymbol{r}_i)$:

$$\begin{aligned} n_j(\boldsymbol{r}) &= \langle \Psi_j | \, \hat{n} \, | \Psi_j \rangle \\ &= N \sum_{\sigma_1} \cdots \sum_{\sigma_1} \int d\boldsymbol{r}_2 \cdots \int d\boldsymbol{r}_N |\Psi_j(\boldsymbol{r}, \sigma_1, \ldots, \boldsymbol{r}_N, \sigma_N)|^2 \, . \end{aligned} \tag{1.9}$$

HK Theorem I

The external potential $v_{\text{ext}}(\boldsymbol{r})$ is, to within a constant, uniquely determined by the ground state electron density $n_0(\boldsymbol{r})$. $n_0(\boldsymbol{r})$ therefore uniquely determines all ground state and excited state properties of the system.

Now consider a second system with a different external potential $\hat{V}'_{\text{ext}}$. The Hamiltonian of the new system is $\hat{H}' = \hat{K}_e + \hat{V}_{ee} + \hat{V}'_{\text{ext}}$. As the functional form of the kinetic energy and the electron-electron interaction energy are the same as the original system, it is the external potential that uniquely describes a system. Let $\left|\Psi_0^{(\prime)}\right\rangle$ be the ground state wavefunction for $\hat{H}^{(\prime)}$ with ground state energy $E^{(\prime)}$. Assume both $|\Psi_0\rangle$ and $|\Psi'_0\rangle$ have the same ground state electron density $n_0(\boldsymbol{r})$. Unless $v'_{\text{ext}}(\boldsymbol{r}) - v_{\text{ext}}(\boldsymbol{r}) = const.$, $|\Psi'_0\rangle \neq |\Psi_0\rangle$ as they are solutions to two different Hamiltonians. As the ground state has the minimum energy of the system:

$$E' = \langle\Psi'_0|\,\hat{H}'\,|\Psi'_0\rangle < \langle\Psi_0|\,\hat{H}'\,|\Psi_0\rangle = \langle\Psi_0|\,(\hat{H} + \hat{V}'_{\text{ext}} - \hat{V}_{\text{ext}})\,|\Psi_0\rangle \ . \tag{1.10}$$

This inequality leads to the inconsistency:

$$E' < E + \int [v'_{\text{ext}}(\boldsymbol{r}) - v_{\text{ext}}(\boldsymbol{r})] n_0(\boldsymbol{r})\ d\boldsymbol{r}\,, \tag{1.11}$$

$$E < E' - \int [v'_{\text{ext}}(\boldsymbol{r}) - v_{\text{ext}}(\boldsymbol{r})] n_0(\boldsymbol{r})\ d\boldsymbol{r}\,. \tag{1.12}$$

Therefore $v_{\text{ext}}(\boldsymbol{r})$ is, to within a constant, uniquely determined by the ground state density, $n_0(\boldsymbol{r})$. As the external potential uniquely determines the wavefunction via the Hamiltonian, all ground state properties and the Hamiltonian can be determined from $n_0(\boldsymbol{r})$. There is one further implication: as the Hamiltonian also describes all the excited states of the system, all ground and excited state properties may be derived from the ground state density alone.

HK Theorem II

The minimum of the total energy functional $E[n(\boldsymbol{r})]$ is the ground state energy E_0 if and only if the density $n(\boldsymbol{r})$ is the true ground state density $n_0(\boldsymbol{r})$. The ground state density $n_0(\boldsymbol{r})$ is uniquely determined by the minimisation of the total energy functional $E[n(\boldsymbol{r})]$.

First, it is again noted that the kinetic energy functional $K_e[n(\boldsymbol{r})]$ and the electron-electron interaction functional $V_{ee}[n(\boldsymbol{r})]$ take the same forms regardless of

the size of the system or the external potential, so we can define a universal energy functional $F[n(\boldsymbol{r})] = K_e[n(\boldsymbol{r})] + V_{ee}[n(\boldsymbol{r})]$. The total energy functional is then defined as:

$$E[n(\boldsymbol{r})] = F[n(\boldsymbol{r})] + V_{\text{ext}}[n(\boldsymbol{r})]\,, \tag{1.13}$$

where the external interaction functional is defined as:

$$V_{\text{ext}}[n(\boldsymbol{r})] = \int v_{\text{ext}}(\boldsymbol{r}) n(\boldsymbol{r})\; d\boldsymbol{r}\,, \tag{1.14}$$

The particle number functional is trivially:

$$N[n(\boldsymbol{r})] = \int n(\boldsymbol{r})\; d\boldsymbol{r} = N \tag{1.15}$$

For a N-particle system with Hamiltonian $\hat{H}$ with a ground state wavefunction $|\Psi_0\rangle$, density $n_0(\boldsymbol{r})$, and energy $E_0 \equiv E[n_0(\boldsymbol{r})]$. The variational principle states that for a trial wavefunction $|\Psi'\rangle \neq |\Psi_0\rangle$ from some external potential $v'_{\text{ext}}(\boldsymbol{r})$, which has an associated density $n'(\boldsymbol{r})$ that satisfies $N[n'] = N$:

$$\langle\Psi'|\,\hat{H}\,|\Psi'\rangle > \langle\Psi_0|\,\hat{H}\,|\Psi_0\rangle\;\;. \tag{1.16}$$

Therefore, using Eq. (1.13):

$$E[n'(\boldsymbol{r})] = F[n'(\boldsymbol{r})] + \int v_{\text{ext}}(\boldsymbol{r}) n'(\boldsymbol{r})\; d\boldsymbol{r} > F[n_0(\boldsymbol{r})] + \int v_{\text{ext}}(\boldsymbol{r}) n_0(\boldsymbol{r})\; d\boldsymbol{r} = E_0\;, \tag{1.17}$$

which proves the second theorem.

To summarise the two HK theorems: *all* properties of the system are determinable from just the ground state electron density. Assuming the form of the functionals are known, the problem of determining the properties of a system is then just a matter of finding the ground state density via minimisation of the total energy functional.

1.3.2 Finite-temperature DFT

The Hohenberg-Kohn theorems as shown above only apply for ground state systems at zero temperature, without spin, in the absence of external magnetic fields. Similar theorems have been established that extended the Hohenberg-Kohn theorems to these other cases (e.g. spin- [49] and current- [50, 51] density functional theory extends the theorems to systems with spin and magnetic fields, respectively).

Of relevance to this thesis is the finite-temperature case, for which the analogous theorems to the Hohenberg-Kohn theorems were proven to exist by Mermin [52]. Instead of the total energy functional, the key functional is the Mermin grand potential functional $\Omega[n(\boldsymbol{r})]$, which when minimised gives the grand potential Ω_0 of the grand canonical ensemble. It can be demonstrated that for fixed electron temperature $\beta^{-1} = k_B T_e$ and chemical potential μ, $\Omega[n(\boldsymbol{r})]$ consists of a universal functional $G[n(\boldsymbol{r})]$ and the external potential $V_{\text{ext}}[n(\boldsymbol{r})]$:

$$\Omega[n(\boldsymbol{r})] = G[n(\boldsymbol{r})] + V_{\text{ext}}[n(\boldsymbol{r})] = G[n(\boldsymbol{r})] + \int v_{\text{ext}}(\boldsymbol{r}) n(\boldsymbol{r}) \, d\boldsymbol{r} \ , \tag{1.18}$$

where the universal functional is:

$$G[n(\boldsymbol{r})] = K_e[n(\boldsymbol{r})] + V_{ee}[n(\boldsymbol{r})] + \mu N[n(\boldsymbol{r})] - \beta^{-1} S[n(\boldsymbol{r})] \ , \tag{1.19}$$

and $S[n(\boldsymbol{r})]$ is the entropy functional. In other words, the external potential still uniquely defines a system at fixed β^{-1} and μ. The density $n(\boldsymbol{r})$ is now defined as:

$$n(\boldsymbol{r}) = \text{Tr}[\rho_0 \Psi^\dagger \Psi] \ , \tag{1.20}$$

where ρ_0 is the grand canonical density:

$$\rho_0 = \frac{\exp(-\beta[H - \mu N])}{\text{Tr}[\exp(-\beta[H - \mu N])]} \ , \tag{1.21}$$

and H is the Hamiltonian from Eq. (1.6). The proof of the Mermin-Hohenberg-Kohn (MHK) theorems is similar to the HK theorems, except all of a system's properties

are now functionals of the equilibrium density instead of the ground state density, and the equilibrium density is found by the minimisation $\Omega[n(\boldsymbol{r})]$. For completeness:

MHK Thorem I: *For a system with fixed temperature and chemical potential, the external potential $v_{\text{ext}}(\boldsymbol{r})$ is, to within a constant, uniquely described by the equilibrium density $n_0(\boldsymbol{r})$. Therefore, $n_0(\boldsymbol{r})$ uniquely determines all properties of the system.*

MHK Thorem II: *The functional $\Omega[n(\boldsymbol{r})] = G[n(\boldsymbol{r})] + \int v_{\text{ext}}(\boldsymbol{r})n(\boldsymbol{r})\, d\boldsymbol{r}$ is minimum and equal to the grand potential Ω_0 if and only if the density $n(\boldsymbol{r}) = n_0(\boldsymbol{r})$.*

The MHK theorems outline the finite-temperature DFT (FT-DFT) method, which is to determine the equilibrium state density via minimisation of the Mermin grand potential functional, then use this density to determine the properties of the system. However, while the Mermin-Hohenberg-Kohn theorems provide the outline of a method to greatly simplify the many-body problem, the theorems do not provide a practical approach for actually using them. The elegance of the method conceals the real difficulty: determining the functional forms of energy functionals. While some, such as the external interaction and the electron number have known functional forms, others such as the exact form of the universal energy functional $F[n(\boldsymbol{r})]$ are not known. To be clear, theoretically exact forms should exist because of the theorems, but there is no procedure on how to find them. This has lead to a variety of approaches on how to approximate the functionals leading to a variety of DFT approaches, such as orbital-free methods [53, 54] and the Kohn-Sham scheme, with the latter being used extensively in this thesis.

1.3.3 Kohn-Sham DFT

Much like Hohenberg and Kohn's paper outlining DFT, Kohn and Sham's 1965 paper [55] was hugely influential on the application of DFT, by virtue of providing an efficient method for applying DFT to real systems. The Kohn-Sham (KS) method is widely used today in a variety of popular DFT codes, such as ABINIT [56, 57], Quantum Espresso [58, 59], and VASP [60, 61]. The current problem of the finite-temperature DFT (FT-DFT) scheme from the previous section is that there is no

known exact functional forms for many system properties, including the functionals $K_e[n(\boldsymbol{r})]$, $V_{ee}[n(\boldsymbol{r})]$, and $S[n(\boldsymbol{r})]$ which are necessary to determine the equilibrium density $n_0(\boldsymbol{r})$. Mapping functionals of the many-body wavefunction to functionals of the density is decidedly non-trivial, largely because of the interactions between the particles. However, if the problem of solving Eq. (1.7) can be decoupled into solving independent single-particle Schrödinger equations, the problem is simplified significantly:

$$\left[-\frac{\hbar^2}{2m_e}\nabla^2 + v_{\text{eff}}(\boldsymbol{r})\right]\psi_\alpha(\boldsymbol{r}) = \epsilon_\alpha\psi_\alpha(\boldsymbol{r}) \ . \tag{1.22}$$

In this equation, α is the set of quantum numbers that describes the state, and $v_{\text{eff}}(\boldsymbol{r}) \equiv v_{\text{ext}}(\boldsymbol{r}) + v_H(\boldsymbol{r}) + v_{\text{XC}}(\boldsymbol{r})$ (terms defined below) is the effective potential the single particle states interact with. The starting point of the Kohn-Sham (KS) method is to assume that the interacting N-electron system with wavefunction Ψ_j can be represented by non-interacting single-particle equations, with all the interactions of the true system represented by an effective potential $v_{\text{eff}}(\boldsymbol{r})$. The density of the single-particle system at finite-temperature is given by:

$$n(\boldsymbol{r}) = \sum_{\alpha=1}^{\infty} f(\epsilon_\alpha;\mu,\beta)|\psi_\alpha(\boldsymbol{r})|^2 \ , \tag{1.23}$$

where $f(\epsilon_\alpha;\mu,\beta)$ is the Fermi-Dirac occupation number of a KS state with eigenenergy ϵ_α in a system with chemical potential μ at temperature β^{-1}:

$$f(\epsilon_\alpha) \equiv f(\epsilon_\alpha;\mu,\beta) = \frac{1}{1+\exp(-\beta(\epsilon_\alpha-\mu))} \ , \tag{1.24}$$

Eqs. (1.22) and (1.23) are the Kohn-Sham equations. At this point, we make the Kohn-Sham ansatz: *The equilibrium density of the non-interacting system is equal to the equilibrium density of the fully-interacting system.* This ansatz is yet to be proven generally, though it has been proven in certain systems. For this thesis, it is postulated to be true, which is reasonable on account of the success of the method in application to many materials.

Next, the Mermin grand potential Eq. (1.18) can be re-written as:

$$\Omega[n(\boldsymbol{r})] = \int v_{\text{ext}}(\boldsymbol{r}) n(\boldsymbol{r})\, d\boldsymbol{r} + \frac{1}{2}\int\int \frac{n(\boldsymbol{r})n(\boldsymbol{r}')}{|\boldsymbol{r}'-\boldsymbol{r}|}\, d\boldsymbol{r}' d\boldsymbol{r} + \mu N[n(\boldsymbol{r})] + \tilde{G}[n(\boldsymbol{r})]\ , \quad (1.25)$$

where the first term is the external interaction functional $V_{\text{ext}}[n(\boldsymbol{r})]$, the second term is the Hartree interaction functional $V_H[n(\boldsymbol{r})]$ which accounts for Coulomb interactions between electrons, the third term contains the electron number functional $N[n(\boldsymbol{r})]$, and the last term is a universal functional for which we are trying to find a usable form:

$$\tilde{G}[n(\boldsymbol{r})] = K_e[n(\boldsymbol{r})] - \beta^{-1} S[n(\boldsymbol{r})] + V_{\text{XC}}[n(\boldsymbol{r})]\ . \quad (1.26)$$

The functional $V_{\text{XC}}[n(\boldsymbol{r})] \equiv V_{ee}[n(\boldsymbol{r})] - V_H[n(\boldsymbol{r})]$ is a potential term that contains remaining quantum effects – namely exchange and correlation (XC) – that are not accounted for by the Hartree term [42]. We will revisit this term in a moment. We first note that the KS approach now gives usable expressions for the kinetic energy and entropy functionals in the form of their single-particle equivalents:

$$K_1 = -\frac{1}{2}\sum_{\alpha=1}^{\infty} f(\epsilon_\alpha) \langle\psi_\alpha| \nabla^2 |\psi_\alpha\rangle\ , \quad (1.27)$$

$$S_1 = -\sum_{\alpha=1}^{\infty} \{f(\epsilon_\alpha)\ln f(\epsilon_\alpha) - [1-f(\epsilon_\alpha)]\ln[1-f(\epsilon_\alpha)]\}\ . \quad (1.28)$$

The single-particle Mermin grand potential is:

$$\begin{aligned}\Omega[n(\boldsymbol{r})] &= K_1 - \beta^{-1} S_1 + \mu N[n(\boldsymbol{r})] \\ &\quad + \int v_{\text{ext}}(\boldsymbol{r}) n(\boldsymbol{r})\, d\boldsymbol{r} + \frac{1}{2}\int\int \frac{n(\boldsymbol{r})n(\boldsymbol{r}')}{|\boldsymbol{r}'-\boldsymbol{r}|}\, d\boldsymbol{r}' d\boldsymbol{r} + V_{\text{XC}}[n(\boldsymbol{r})]\ .\end{aligned} \quad (1.29)$$

The single-particle Schrödinger equation is then:

$$\left[-\frac{1}{2}\nabla^2 + v_{\text{ext}}(\boldsymbol{r}) + \frac{1}{2}\int \frac{n(\boldsymbol{r}')}{|\boldsymbol{r}'-\boldsymbol{r}|}\, d\boldsymbol{r}' + v_{\text{XC}}(\boldsymbol{r})\right]\psi_\alpha(\boldsymbol{r}) = \epsilon_\alpha \psi_\alpha(\boldsymbol{r})\ , \quad (1.30)$$

where the exchange-correlation potential is the functional derivative of the XC func-

tional:

$$v_{\mathrm{XC}}(\boldsymbol{r}) = \frac{\delta V_{\mathrm{XC}}[n(\boldsymbol{r})]}{\delta n(\boldsymbol{r})} \tag{1.31}$$

In application, the Kohn-Sham method is solved in a self-consistent manner, as outline in Fig. 1.2. An initial guess is made of the single particle wavefunctions (usually random), which gives an initial guess of the total potential. Eq. (1.22) is then used to calculate the states ψ_α based on the density from the initial guess. A new density is calculated from these wavefunctions, and the process repeats until some conditions – typically the density, potential, wavefunctions, or total energy – have reached the desired level of convergence.

Lastly, one must bear in mind that the KS orbitals $\psi_\alpha(\boldsymbol{r})$ are *not* electronic wavefunctions. They are single particle wavefunctions which we have postulated are proxies for the real electronic systems via the electron density. The same is true of the eigenvalues ϵ_α which do not correspond to real eigenenergies, but are instead defined as [62]:

$$\epsilon_\alpha = \frac{\partial E_{tot}}{\partial n_\alpha} = \int d^3\boldsymbol{r} \frac{\delta E_{tot}[n(\boldsymbol{r})]}{\delta n(\boldsymbol{r})} \frac{\partial n(\boldsymbol{r})}{\partial n_\alpha} \,. \tag{1.32}$$

In essence, beyond the mathematical definition above, the KS eigenvalues do not have a physical meaning [63], except for the highest value which is equal to minus the first ionization energy [64]. Otherwise, it is not guaranteed that ϵ_α match the true eigenvalues. A well-known example of this manifests in the "band-gap problem", a phenomenon where the KS DFT band-gap is an underestimation of the true band-gap [65]. More generally, binding energies are typically underestimated by the KS system. Whether the KS orbitals can be meaningfully used as proxies to the real electronic wavefunctions is important, as later the KS orbitals will be used to derive information about the localization of electrons in real systems. Indeed, there is an interesting philosophical and physical debate over the meaning of the Kohn-Sham auxiliary system (see e.g. [63, 64, 66–71]), which goes well beyond the scope of this thesis. The practicalities of using the KS orbitals for this work will be discussed later in Chapter 3.

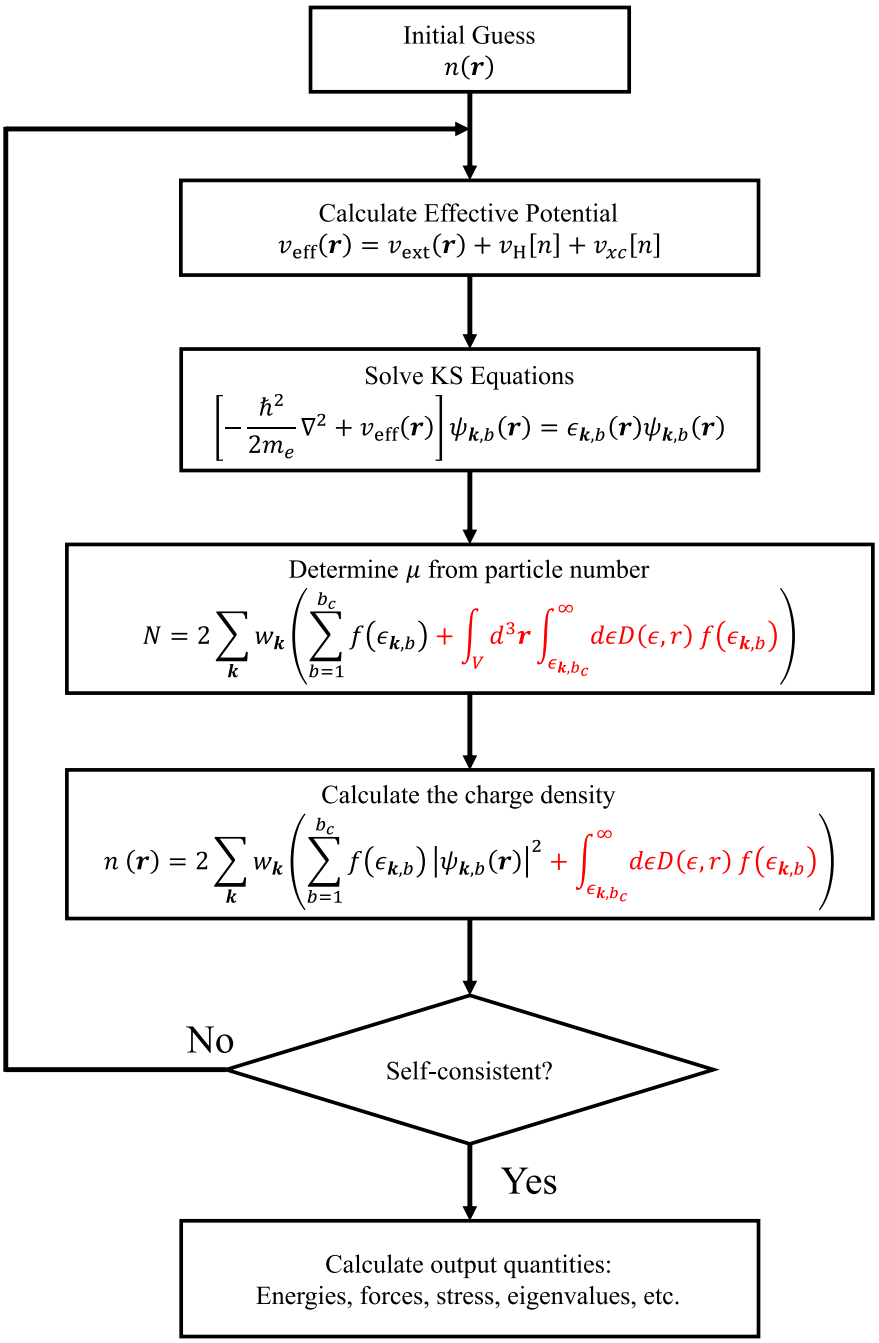


Figure 1.2: The self-consistent field (SCF) cycle for KS DFT. The red integrals are orbital-free terms used in Kohn-Sham orbital-free DFT (see Section 1.3.6). As the calculations are concerned with Bloch states, one performs averages over the Brillouin zone with k-point weights $w_{\boldsymbol{k}}$.

1.3.4 The Exchange-Correlation Potential

The final, and arguably most important, problem in the Kohn-Sham method is what form $V_{\mathrm{XC}}[n(\boldsymbol{r})]$ and $v_{\mathrm{XC}}(\boldsymbol{r})$ should take. Unfortunately, the exact form of the XC functional remains unknown, in spite of 60 years of research effort. Lacking any exact formulation, approximate forms are used instead. The decision matters because the results one obtains from a DFT calculation can heavily depend on the form of the XC potential used. This has lead to the development of a huge number of exchange-correlation functionals. These functionals vary from generalized forms that are designed to be applied a wide group of materials (with varying success), to those tailored to calculate properties for a specific material. For perspective, in April 2023 version 6.1.0 of the growing LibXC library [72] listed about 630 different XC potentials. Of course, the true prize would the discovery of the exact XC functional, should it exist. While this may be a long way away, recently machine learning has been applied to attempt to make improvements to existing functional forms [73, 74], with the hope being to search for new functional forms.

The most popular forms of the XC functional in use are those based on the free electron gas. If it is assumed that $n(\boldsymbol{r})$ varies slowly, then the exchange-correlation energy per unit density ϵ_{XC} can be approximated using the local density approximation (LDA):

$$V_{\mathrm{XC}}^{LDA}[n(\boldsymbol{r})] = \int n(\boldsymbol{r})\epsilon_{\mathrm{XC}}^{\mathrm{LDA}}(n(\boldsymbol{r}))\ d\boldsymbol{r}\ . \tag{1.33}$$

This is the simplest approximation that can be used, and it performs moderately well for many systems. The LDA approximation treats the local electron density as a homogeneous electron gas with density $n(\boldsymbol{r})$. A famous example of an LDA functional is Perdew and Wang's functional, LDA-PW [75]. In cases where there are significant spatial gradients of the density, the generalized-gradient approximation (GGA) is used instead: then, $\epsilon_{\mathrm{XC}} \approx \epsilon_{\mathrm{XC}}^{\mathrm{GGA}}(n(\boldsymbol{r}), \nabla n(\boldsymbol{r}))$. The most well-known of the GGA functionals is that of Perdew, Burke and Ernzerhof, GGA-PBE [76]. There are also higher order expansions that involve the kinetic energy density, such as meta-GGA functionals ($\epsilon_{\mathrm{XC}} \approx \epsilon_{\mathrm{XC}}^{\mathrm{mGGA}}(n(\boldsymbol{r}), \nabla n(\boldsymbol{r}), \nabla^2 n(\boldsymbol{r}))$). Spin-dependent equivalents

to LDA, GGA, and metaGGA also exist. Of course, this gradient approach assumes that ϵ_{XC} can be accurately treated using a series expansion of gradient terms, but this may not be true. As the Hartree-Fock method [77–79] provides an exact form for the exchange functional, so-called "hybrid" functionals that use exact exchange and approximated correlation functionals also see some use. Until recently, XC functionals have generally ignored any explicit temperature-dependence. While temperature is implicitly included through the density, quantum Monte Carlo (QMC) simulations have shown that there is also an explicit temperature-dependence that can significantly alter results for a region of temperatures and densities [80]. Various fittings to this QMC dataset have led to finite-temperature equivalents to LDA [81, 82], GGA [83], and hybrid functionals [84]; with finite-temperature meta-GGA functionals in development [85].

1.3.5 The Projector Augmented-wave Method

Despite the vast improvement in computational efficiency provided by the Kohn-Sham DFT method, it can still be computationally expensive to run calculations as described. Given that widely-used XC functionals such as LDA and GGA are based on the free electron gas, a natural basis on which to resolve the KS orbitals is a plane-wave decomposition. The difficulty is that strongly-localized states, such as those close to atomic nuclei, can oscillate rapidly near nuclei. An accurate plane-wave decomposition of these orbitals can therefore require an impractically large number of plane-waves which creates a substantial computational time and memory burden. This can be, to a degree, alleviated using the frozen-core approximation [86] by assuming a particular orbital does not change much from its atomic form, although this method cannot always be used for every given set of conditions. The Coulomb potential is also problematic as it is a singularity, so sampling close to the singularity requires a huge number of plane-waves. And, regardless, faster calculations that do not sacrifice accuracy are always desirable. Psuedopotential methods [87–89] resolve these issues, though at the cost of physical meaning. Fortunately, the projector augmented-wave (PAW) method [90] provides the computational benefits of the

pseudopotential approach, while the physicality of calculations can be retrieved.

The PAW method is essentially a mapping of the initial KS wavefunctions (so-called "all-electron" or AE wavefunctions) $|\psi\rangle$ to a "psuedized" (PS) wavefunctions $|\tilde{\psi}\rangle$ by means of a transformation $\mathcal{T}$:

$$|\psi\rangle = \mathcal{T}\,|\tilde{\psi}\rangle = \left(1 + \sum_R \mathcal{T}_R\right)\,|\tilde{\psi}\rangle\ , \tag{1.34}$$

where $\mathcal{T}_R$ are transformations applied within atom-centered augmentation regions Ω_R. Outside the augmentation region, the AE and PS wavefunctions are identical. Within Ω_R, the wavefunctions are decomposed into partial waves $|\overset{(\sim)}{\phi}_i\rangle$ with quantum numbers $i = \{n, l, m\}$:

$$\begin{aligned} |\psi\rangle &= \sum_i c_i\,|\phi_i\rangle \\ |\tilde{\psi}\rangle &= \sum_i c_i\,|\tilde{\phi}_i\rangle \end{aligned} \qquad \boldsymbol{r} \in \Omega_R\,. \tag{1.35}$$

Projector functions $\langle\tilde{p}_i|$ are defined to give the constants $c_i = \langle\tilde{p}_i|\tilde{\psi}\rangle$, and are found by the orthogonality condition $\langle\tilde{p}_i|\tilde{\phi}_j\rangle = \delta_{ij}$. The partial waves $|\tilde{\phi}_i\rangle$ must match $|\phi_i\rangle$ outside Ω_R. $|\phi_i\rangle$ can be found by solving the radial Schrödinger equation for the atom. The PAW transformation is therefore defined as:

$$\mathcal{T} = 1 + \sum_R \sum_i \left(\,|\phi_{i,R}\rangle - |\tilde{\phi}_{i,R}\rangle\right)\,\langle\tilde{p}_{i,R}|\ . \tag{1.36}$$

Operators in the PS system are related to the AE operators by $\tilde{A} = \mathcal{T}^\dagger A \mathcal{T}$. Aside from increased efficiency through smoothness, for local operators (such as position $|\boldsymbol{r}\rangle\,\langle\boldsymbol{r}|$) it can be shown there is additional freedom to add an arbitrary operator term $B - \sum_R \sum_i |\tilde{p}_{i,R}\rangle\,\langle\tilde{\phi}_{i,R}|\,B\,|\tilde{\phi}_{i,R}\rangle\,\langle\tilde{p}_{i,R}|$ to $\tilde{A}$. As a consequence, one can remove the Coulomb singularity in the psuedized space. As an additional benefit, particularly over the pseudopotential method [86], after the calculations have been performed in the PS space, one can simply transform all quantities back to the original AE space. The PAW method therefore provides a scheme where one could realistically perform

an all-electron (in the true sense) calculation; although, in practice, for additional computational efficiency the frozen-core method is still used where possible.

1.3.6 Hybrid Kohn-Sham Orbital-Free DFT

A practical limitation of the KS method is the computational cost at high temperatures. While at $T = 0$ K, KS DFT is exactly described by a finite number KS states, the finite-temperature case requires an infinite number of states to be calculated for an exact calculation. The reason is that the statistical occupation number of states is given by the Fermi-Dirac distribution Eq. (1.24), and at non-zero temperatures this distribution has finite values for arbitrarily high state energy ϵ. In practice, at low temperatures ($T \lesssim 10$ eV), $f(\epsilon) \approx 0$ at finite ϵ, and so the summations can be cut off after a finite number of states without affecting the results of a calculation. However, the number of states required in a calculation scales as $T^{3/2}$ [91]. As the temperature rises, states with energies far above the Fermi energy quickly have non-negligible occupation numbers. This presents two problems with high temperature KS DFT: first, a huge number of states need to be considered in order to perform a sufficiently accurate calculation; second, the high energy states require very high plane-wave cut-off energies in order to be able to accurately model them. Both of these facts make high-temperature DFT calculations extremely computationally-costly both in time and memory requirements. Previous experimental work at XFELs have reported peak electron temperatures approaching 200 eV [13, 30], a value some 20 times higher than the Fermi energy. Performing such calculations using traditional KS DFT is prohibitively expensive. In light of these challenges, an alternative method is sought.

One approach is orbital-free DFT (OF DFT) [53, 54]. As the name implies, orbital-free methods forgo calculating electronic orbitals and only deal with the density. These calculations are particularly efficient at high temperatures. However, they suffer from accuracy issues at low-temperatures [92], and spectral calculations such as opacity are not possible due to the lack of orbitals. Another common approach for high temperature calculations is the path integral Monte Carlo (PIMC)

method [93–95]. However, due to the fermion sign problem, PIMC calculations are typically restricted to non-degenerate systems ($\theta_e \gg 1$).

What is desired, particularly for this work, is a method that still allows for the calculations of states while maintaining a high-temperature computation scaling like that of OF DFT. Such an approach was recently derived by Zhang *et al.* [92] that extends KS DFT to arbitrarily high temperatures, in a hybrid Kohn-Sham orbital-free (KS-OF) DFT scheme. Key to the method is the realization that for a state with sufficiently high energy, typically with de Broglie wavelength smaller than the interparticle spacing, the states begin to behave increasingly as single plane-waves. For a Bloch state in a unit cell of volume V:

$$\psi_{s,\boldsymbol{k},b}(\boldsymbol{r}) = V^{-1/2} \exp\left[-i\left(\boldsymbol{G}+\boldsymbol{k}\right)\cdot\boldsymbol{r}\right] \tag{1.37}$$

where $s = -1/2, 1/2$ is the spin, $\boldsymbol{k}$ is the crystal momentum, b is the band number, $\boldsymbol{G}$ is the wavenumber, and $\boldsymbol{r}$ is the spatial co-ordinate within the unit cell. To simplify the solution, consider the total electron density as an example:

$$n(\boldsymbol{r}) = \sum_{\boldsymbol{k}} w_{\boldsymbol{k}} \sum_{s} \sum_{b=1}^{\infty} f(\epsilon_{s,\boldsymbol{k},b}) |\psi_{s,\boldsymbol{k},b}(\boldsymbol{r})|^2 \ , \tag{1.38}$$

where $w_{\boldsymbol{k}}$ is the k-point weighting ($\sum_{\boldsymbol{k}} w_{\boldsymbol{k}} = 1$) when averaging over the Brillouin zone. The calculation is then split into two regions by a cut-off energy ϵ_c: for $\epsilon_i \leq \epsilon_c$ the KS states are still calculated explicitly; above the cut-off energy, the wavefunctions are treated as a homogeneous electron gas with wavefunctions Eq. (1.37). Therefore, above ϵ_c the structure is approximately continuous across the Brillouin zone, and the summation can be converted to an integral for states above ϵ_c. The density, and other functionals, are then split into KS contributions and integral OF "corrections"; e.g. $n(\boldsymbol{r}) = n_{\mathrm{KS}}(\boldsymbol{r}) + n_{\mathrm{OF}}(\boldsymbol{r})$.

Most DFT codes have a user choose the number of bands in a calculation, not the maximum energy. In the original method [92], Zhang *et al.* suggest ϵ_c should be set to the average energy across the uppermost band. However, this leaves gaps in the band structure in some parts of the Brillouin zone, and double-counting the

contributions of multiple bands in other parts. A better choice is a k-dependent cut-off energy $\epsilon_{\boldsymbol{k},b_c}$ chosen along the uppermost band number b_c.

Zhang *et al.*'s suggestion was to use a plane-wave approximation (PWA) for the OF corrections. A slightly more generalized approach was recently suggested by Hollebon *et al.* [96] by treating the high-energy states as a locally homogeneous electron gas, so the OF corrections are TF-like. In this KS-TF DFT approach, the orbital-free contribution to $n(\boldsymbol{r})$ is:

$$n_{\mathrm{OF}}(\boldsymbol{r}) = \sum_{\boldsymbol{k}} w_{\boldsymbol{k}} \int_{\epsilon_{\boldsymbol{k},b_c}}^{\infty} d\epsilon f(\epsilon) D(\epsilon, \boldsymbol{r}) \,. \tag{1.39}$$

where $D(\epsilon, \boldsymbol{r})$ is the local density of states (LDOS):

$$D(\epsilon, \boldsymbol{r}) = \frac{2^{1/2} m_e^{3/2}}{\pi^2 \hbar^3} \sqrt{\epsilon - u(\boldsymbol{r})} \,, \tag{1.40}$$

which related to the total density of states by $D(\epsilon) = \int_V d^3\boldsymbol{r} D(\epsilon, \boldsymbol{r})$; and $u(\boldsymbol{r})$ is the potential experienced by the high-energy states. The KS-PWA approach is recovered if $u(\boldsymbol{r}) = u_0$, where u_0 is the mean of $u(\boldsymbol{r})$, which is the high-energy limit of the KS-TF approach. To calculate u_0, Zhang *et al.* used the mean difference between the KS states' eigenenergies and kinetic energies over the highest bands. However, this means a large number of excess bands need to be included in order to have a meaningful average potential experienced by the plane-waves. Blanchet *et al.* [97] showed that this is essentially just the spatial average over the local contribution to the total potential $v_L(\boldsymbol{r})$, so they propose just averaging over $v_L(\boldsymbol{r})$ and forgoing the band averaging. For the KS-TF model, it is proposed that $u(\boldsymbol{r}) = v_L(\boldsymbol{r})$ [96]. For all of these KS-OF approaches, it has been noted that the non-local potential may contribute if the cut-off energy is sufficiently low; however, for most applications, it seems not to matter.

To complete the method, the revised density $n(\boldsymbol{r}) = n_{\mathrm{KS}}(\boldsymbol{r}) + n_{\mathrm{OF}}(\boldsymbol{r})$ is then inserted into functionals of the density, and the KS-OF DFT method naturally fits in the SCF cycle, Fig. 1.2. Other functionals that are expressed in terms of KS

wavefunctions – such as the total eigenenergy E, pressure P, and entropy S – also have orbital free corrections:

$$E_{\mathrm{OF}} = \sum_{\boldsymbol{k}} w_{\boldsymbol{k}} \int_V d^3\boldsymbol{r} \int_{\epsilon_{\boldsymbol{k},b_c}}^{\infty} d\epsilon f(\epsilon) D(\epsilon, \boldsymbol{r}) \epsilon \,, \tag{1.41}$$

$$P_{\mathrm{OF}} = \frac{1}{3V} \sum_{\boldsymbol{k}} w_{\boldsymbol{k}} \int_V d^3\boldsymbol{r} \int_{\epsilon_{\boldsymbol{k},b_c}}^{\infty} d\epsilon f(\epsilon) D(\epsilon, \boldsymbol{r}) \left[\epsilon - u(\boldsymbol{r})\right] \,, \tag{1.42}$$

$$S_{\mathrm{OF}} = -k_B \sum_{\boldsymbol{k}} w_{\boldsymbol{k}} \int_V d^3\boldsymbol{r} \int_{\epsilon_{\boldsymbol{k},b_c}}^{\infty} d\epsilon f(\epsilon) D(\epsilon, \boldsymbol{r}) \left\{f(\epsilon) \ln f(\epsilon) + \left[1 - f(\epsilon)\right] \ln \left[1 - f(\epsilon)\right]\right\} \,. \tag{1.43}$$

These integral contributions are of minimal computational burden as they take the form of Fermi-Dirac integrals [98], which can be solved with extremely efficient algorithms [99–101]. Furthermore, the summations of k-space only need to be done in a relatively small energy interval, which can be rapidly completed. Once the maximum band energy of the entire KS system is reached, these integrals are k-independent and so only one integral needs to be solved.

The KS-PWA approach is useful as it places a very reasonable finite limit on the number of KS states that need to be calculated for a converged calculation. One does not even need to have exact plane-wave-like behaviour, with Blanchet *et al.* suggesting that even a 10% deviation from true plane-wave behaviour still results in reasonably accuracte calculations. The KS-TF approach drops the number of KS states that need to be calculated explicitly further, allowing for even more efficient calculations [96]. Additionally, by considering a spatially-dependent OF electron density rather than a completely homogeneous electron gas in the volume, the forces exerted by the high-energy electrons in molecular-dynamics calculations are properly accounted for. There may be higher-order approximations to the OF contributions which improve the accuracy of the KS-OF calculations further, although this still needs to be investigated [96].

Author Contribution to the KS-OF Method

The author has implemented the KS-PWA method, as described by Blanchet *et al.* in a local copy of the open-source DFT code ABINIT v8.10.3 [56, 57, 102]. Although the KS-PWA method is now natively implemented in ABINIT v9.6+, the author implemented the method from Zhang *et al.*'s paper before the release of ABINIT v9.0. During the original implementation, it was found that the self-consistent field (SCF) cycle converged extremely slowly (100+ iterations) when using the KS-PWA method, with convergence not always guaranteed; this issue was also observed by Blanchet *et al.* [103]. To further clarify, equivalent full KS DFT calculations would converge as normal, suggesting the issue was with the PWA part of the method. The reason is that the eigenvalues calculated by the Hamiltonian solver for the highest energy states can fluctuate substantially between SCF iterations. As per the ABINIT documentation, sometimes the last few bands need to be ignored when determining if the wavefunctions are converged. For usual applications, these fluctuations are not a problem as these bands should have low occupation numbers close to zero, so the influence on the system is negligible. But in KS-OF DFT, this is no longer true, and it causes the cut-off energy and u_0 to fluctuate. This results in fluctuations in both the density and the potential, ultimately making it difficult (or even impossible) for the SCF cycle to converge.

The fix the author has proposed [103], which has been accepted and released in ABINIT v9.10.3 [104], is to designate a number of the uppermost bands b_{buff} to act as a buffer in the Hamiltonian solver. The buffer bands have their occupation numbers forced to zero, so they do not contribute directly to the density or functionals. The band cut-off from which the OF contributions are calculated is then the total input bands b_{in} minus the buffer bands (i.e. $b_c = b_{\text{in}} - b_{\text{buff}}$). The number of buffer bands used is up to the user, with the caution that these buffer states still take space in memory, need to be solved, and offer no improvement after a certain number. However, too few buffer bands will do little to solve the SCF convergence issues. A buffer of 10% of the total band number was used in the calculations in Chapter 4.

However, for some calculations in Chapter 5, good convergence was achieved with just 5 buffer bands out of a total of thousands. The decision needs to be made on a case-by-case basis, but limited testing suggests that a buffer of 5-10% of the total number of bands is more than sufficient for a user wishing to run calculations immediately.

1.4 Structure of Thesis

This thesis is split into six chapters. This first two chapters provide an introduction to many of the basic concepts and tools relevant to this thesis. Chapter 1 provides an overview of high energy density matter and density functional theory, which is used throughout this thesis. A mention is also given to the relevant timescales of FEL-matter interactions to help the reader understand approximations made in later calculations.

As ionization potential depression (IPD) is central to this thesis, an extended introduction into the concepts of continuum lowering and IPD is provided in Chapter 2. This chapter takes the reader through derivations and a discussion of the analytical IPD models that have seen widespread use in plasma codes. This is followed by an overview of the experimental measurements of IPD, which demonstrates the inability of analytical IPD models to make accurate predictions in hot dense plasmas. Finally, an overview of recent theoretical developments in the area is presented to complete the context on which this thesis is built.

The remainder of the thesis reflect the author's contributions to the field. Chapter 3 introduces dimensionality as a parameter to describe the spatial localization of Kohn-Sham states. While this method was developed to interpret experimental results presented in Chapter 4 from first principles calculations, a self-contained chapter is deemed more useful for the reader. A description of existing methods to describe the localization of electrons is given, along with an explanation as to why they are not desirable for this work. This is followed by a derivation of the dimensionality parameter, with particular emphasis placed on distinguishing between the

spatial *extent* and spatial *localization* of single-particle wavefunctions. Insight into the dimensionality parameter is given by an analysis of simple model functions, followed by a demonstration of its ability to give meaningful localization information in real systems. This chapter is concluded by discussion of the dimensionality metric's ability to give insight into state localization mechanisms, as well as essentially acting as a first principles IPD model.

Chapter 4 begins by presenting experimental measurements of K_β emission in highly-ionized solid density Mg, which is contrary to the results of a similar previous experiment [40]. FT-DFT calculations are presented along with a dimensionality analysis in order to interpret these results. Included are a comparison of localization in Al and an ionic compound. IPD energies are then extracted from the FT-DFT calculations and compared with experimental data and the analytical IPD models. The remaining discrepancies between the results presented in this chapter and previously published data are addressed. The contents of Chapters 3 and 4 were written by the author into an extensive paper that has been published in the journal *Physical Review E*, and is available in Ref. [105].

Chapter 5 presents FT-DFT calculations of the mean ionization state (MIS) of hot dense CH plasmas. The MIS is often defined using a bound-or-free electron picture, so the concept is directly relevant to IPD. The chapter starts by discussing experiments that have used x-ray Thomson scattering (XRTS) to measure the MIS of hot dense plasmas. In these conditions, plasma modelling significantly underpredicts the MIS compared to that inferred directly from the XRTS spectra. However, it has been recently claimed that another definition of ionization based on the optical conductivity produces better agreement with the experimental data. FT-DFT calculations are presented that compare the MIS calculated by counting the number of continuum ("free") electrons and from the conductivity. Differences of up to 10% are observed between the two methods. However, including "Pauli forbidden" transitions in the conductivity reproduces the counting definition, suggesting such transitions are important to evaluate the ionization state. The contents of Chapter 5 were written by the author into a letter that, at the time of writing, has been

submitted to the journal *Physical Review E*. The preprint of the letter is available in Ref. [106].

The final chapter, Chapter 6, provides concluding remarks, and comments on potential directions this work and ionization potential depression could be taken.

1.5 Author Contributions

Like all theses, much of the work presented in here took years to develop, and so is inherently collaborative in nature. My supervisors Prof. Sam M. Vinko and Prof. Justin S. Wark have naturally been heavily involved my work. I have also regularly presented this work to the members of the Vinko-Wark research group, who have kindly provided me feedback; I will acknowledge particular substantive contributions below. The following should serve as a breakdown of the specific contributions made by the author and others to the research presented in this thesis:

The theoretical sections of Chapter 1 are purely introductory and contain no original work. Similarly, Chapter 2 is a review of ionization potential depression, and so none of the models or studies described in this chapter are original to the author. Section 1.3.6 outlines a contribution the author has made to the ABINIT code. The contribution solves a technical issue in the SCF convergence when the KS-PWA method is used, and it has been released in ABINIT v9.10.3 [104].

Although the author implemented the KS-PWA method into ABINIT v8.10 before the official implementation in v9.6, the author has decided to re-implement the method into v8.10 to match the official release, but with the fix described in Section 1.3.6. This is due to the technical and physical improvements over Zhang *et al.*'s description [92]. As such the final version of the KS-PWA method used for the FT-DFT calculations presented in this thesis is as described by Blanchet *et al.* [97]. The author wishes to acknowledge useful discussions with Dr Patrick Hollebon on how to implement the method into ABINIT.

The idea of using the changes in the inverse participation ratio of Kohn-Sham wavefunctions to study state localization, as presented in Chapter 3, was initially

explored by Dr Patrick Hollebon, but was fully developed by the author into a practical method by investigating how it can be applied in real systems. The analysis of model functions to understand the interpretations of the dimensionality parameter were performed by the author. All of the FT-DFT calculations presented in Chapter 3 were performed and analysed by the author.

The experimental data presented in Chapter 4 was not collected by the author, with the experiment occurring before the author's doctorate began. A large number of people were involved in this experiment, a list of whom may be taken from Ref. [105]. The Bragg spectroscopy analysis code used to analyse the data was developed in collaboration with Dr Oliver Humphries, Mr Alessandro Forte and Mr Thomas Campbell, and was later used for a number for experiments that the author has participated in. The final analysis of the Mg and MgF_2 spectra presented in this chapter was performed by the author. Other experimental spectroscopic data presented in this chapter was taken with permission from Ciricosta *et al.* [40]. All of the FT-DFT simulations presented in this chapter were performed and analysed by the author. The author acknowledges Dr Oliver Humphries for providing an initial analysis of the Mg and MgF_2 data, and advice into Bragg spectroscopy. The author also acknowledges Dr Sam Azadi for his suggestion of comparing the presented results with finite-temperature exchange correlation functionals. The author would like to especially thank Prof. Sam M. Vinko and Prof. Justin S. Wark for their vital insight and feedback in the development of the dimensionality analysis method, and on the final results presented in Chapters 3 and 4.

The FT-DFT calculations presented in Chapter 5 were performed and analysed by the author. The author acknowledges Prof. Sam M. Vinko for highlighting Kobayasi and Watabe's previous work in calculating the ionization from conductivity. The author also acknowledges Prof. Justin S. Wark for providing additional contextual information and data which, while not presented here, has been useful in guiding the analysis for this chapter. The author would also like to thank his supervisors and Mr Pontus Svensson for reading the manuscript for the chapter, and providing useful feedback on clarifying the arguments and derivations.

Chapter 2: Ionization Potential Depression

2.1 Continuum Lowering

Continuum lowering (CL) is a fundamental process in plasmas. When an atom is immersed in a plasma, electrostatic interactions between the atom and the plasma particles cause the continuum level of the atom to lower [107–110]. This reduces all atomic binding energies, and can result in ionization when the amount of CL exceeds the binding energy of an electron, a process known as "pressure-ionization". CL therefore has a direct impact on many important plasma processes, including the ionization and ion charge state distribution, the equation of state, the opacity, and transport properties. A good understanding of the physics behind the CL process is therefore vital to our ability to predictively model HED systems, including those relevant to inertial confinement fusion research [95] and to astrophysical plasmas [111].

Collisional-radiative atomic kinetics (CR-AK) models are widely used to understand the behaviour of HED plasmas, and constitute a key simulation framework needed to interpret the results of x-ray spectroscopy experiments. Because these models essentially deal with time-dependent ionization dynamics, they require clear definitions of ionization and, specifically, whether an electron is bound to some particular ion or not. Unbound electrons are considered free, and are treated as forming a homogeneous (and often classical) free-electron gas. In such simulations the process of CL is commonly accounted for via an ionization potential depression (IPD) model. The IPD is an energy that is subtracted from the electron binding energies in all ionic charge states: if an electron in isolated ion has an ionization energy $I_i^{(0)}$,

and in a plasma the ionization energy is I_i, the IPD is defined as:

$$\mathrm{IPD}_i = I_i^{(0)} - I_i \,. \tag{2.1}$$

As the name suggests, its effect is to decrease the amount of energy required to ionize an ion. Ionization potential depression is a crude representation of an otherwise complex quantum many-body problem, but it is chosen because of its computational convenience and simplicity. For relatively hot systems, where IPD energies are small compared with other energies in the system, this approach can be adequate to represent the main effect of increasing electron density on the energetics of the plasma. In contrast, IPD models tend to falter for dense systems at lower temperatures, particularly for conditions where the mean particle separation distance starts to become comparable to the plasma Debye length, such as in warm dense matter.

There are many simple IPD models in use today. In the low-temperature and high-density limit, the ion-sphere IPD model is often used, the energy of which is evaluated from the spatially uniform free-electron density inside a Wigner-Seitz sphere [107–109]. At the opposite end, at high-temperatures and low-densities, Debye-Hückel theory [20, 108] is thought to be applicable and the IPD is evaluated in terms of the Debye screening length. At intermediate conditions the Stewart-Pyatt model [109] is popular, yielding the ion-sphere and Debye-Hückel expressions at their respective limits. A modified version of the Ecker-Kröll model [110, 112] has enjoyed some renewed popularity recently due to experimental results from the Linac Coherent Light Source (LCLS) [113] FEL at SLAC, but it has only been applied successfully to relatively low-Z materials.

In recent years there has been a series of novel experiments attempting to measure the IPD in highly-ionized dense plasmas, and compare the experimental results with theoretical predictions. Much of this work relies on the physics of atomic $n = 1, 2, 3$ orbitals (spectroscopically called the K-, L- and M-shells), and the related K_α and K_β line emission. As this nomenclature will be often used, the various terms using a simple atomic physics picture are illustrated in Fig. (2.1). The overarching con-

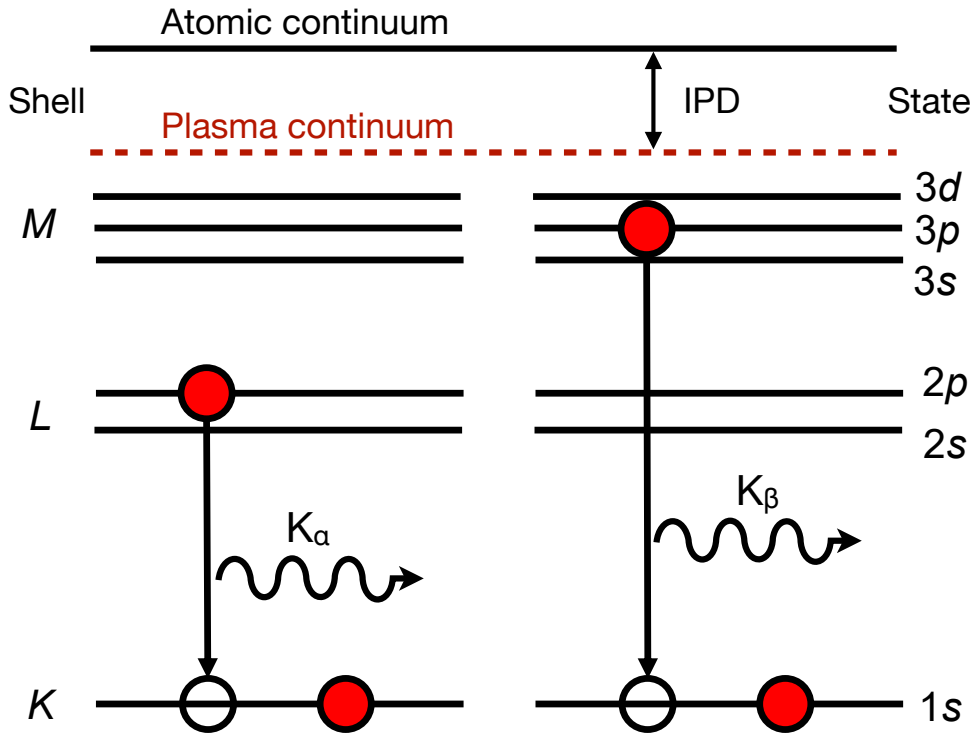


Figure 2.1: A schematic of K, L and M atomic shells, continuum level, IPD, and related K_α and K_β transitions, discussed in the text. An additional hole in the K-shell would give rise to a 'double-K hole' transition.

clusion of these experiments is that traditional models of IPD are poor descriptors of continuum lowering in hot dense plasmas, and that they have significant discrepancies with experimental measurements. This rich collection of experimentally observed discrepancies has spurred a flurry of theoretical investigations into how best to model, predict, and understand, the effect of IPD. Efforts have been made using ion-sphere models [114–121], Hartree-Fock-Slater calculations [122], models based on plasma theory [123, 124], classical molecular dynamic simulations [125], quantum statistical models [126–128], Monte Carlo methods [129], and density functional theory calculations with and without molecular dynamics [38, 130, 131]. Unfortunately, no consistent agreement has emerged between all these methods. However, the majority of them do predict, as does the experimental data, that the IPD should lie energetically somewhere between the predictions of the Stewart-Pyatt and Ecker-Kröll models.

This is our starting point. The work in this thesis seeks to resolve some of the existing discrepancies across the various theoretical modelling approaches, and

present a first principles understanding of continuum lowering based on the localization and delocalization of states near the continuum of a dense plasma. To start, it is important to understand how IPD models are constructed in order to identify and understand their deficiencies.

2.2 Deriving Ionization Potential Depression

The primary process that will be discussed in the context of deriving IPD models is the ionization of an electron from an ion, with the inverse process being three-body recombination. The process can be described by the balance equation:

$$i^z + s \rightleftharpoons i^{z+1} + e + s' \tag{2.2}$$

where i^z is an ion with ionization state z, e is a free electron, and s and s' are an additional particle, before and after the event, which is required for conservation laws. The additional particle might be a photon that is absorbed, emitted or scattered, or a collisional electron. The general procedure for deriving the IPD is to calculate the total electrostatic potential $\Phi(\boldsymbol{r})$ from the Poisson equation:

$$-\epsilon_0 \nabla^2 \Phi(\boldsymbol{r}) = -e n_e(\boldsymbol{r}) + \sum_{n=1}^{N_i^{tot}} e Z_n \delta^{(3)}(\boldsymbol{r} - \boldsymbol{R}_n)\,, \tag{2.3}$$

where Z_n are the nuclear charges in the plasma (treated as point-charges), and $n_e(\boldsymbol{r})$ is the total electron density; then, using the Schrödinger equation or Dirac equation, the potential and the electron densities are solved self-consistently. The IPD is given by the differences in the ionization energies with and without the plasma, which may be derived from the Schrödinger equation or Dirac equation. However, such an approach is time-consuming, and prohibitively so when used in time-evolved CR-AK modelling to predict plasma dynamics. Therefore, approximations are made to derive analytical IPD models. The first approximation made to this effort is to assume the electrons can be easily distinguished as either being purely bound to an ion or purely free, so that $n_e(\boldsymbol{r}) = n_b(\boldsymbol{r}) + n_f(\boldsymbol{r})$. All existing IPD models use this

fundamental assumption, which underpins the ability to derive analytical equations for IPD. Usually, the bound electrons are those that occupy atomic orbitals that are bound to ions, while the free electrons are the remaining electrons. As will be seen, the effect of the free electrons is often reduced to treating them as a homogeneous electron gas (HEG). Next, various approximations are made to simplify the physics of plasmas, which allows for the IPD to be calculated using an analytical equation. Finally, an approach using either perturbation theory or thermodynamics is used to quantify the IPD from the potential. The last step is outlined be low.

For clarity of notation in this chapter, subscripts of Greek letters $(\alpha, \beta, \gamma, \ldots)$ will refer to both ions and electrons, and subscripts of Latin letters $(a, b, c, \ldots)$ will refer to just ions. There are two common approaches for deriving IPD models that will be considered for now – perturbation arguments and thermodynamic arguments – although they derive similar results.

2.2.1 Perturbation Approach

In cases where the atomic orbitals are relatively small, bound electrons can be treated as point particles centered on the point-particle nucleus. One can then treat the bound electrons and nucleus as a single composite ion with charge state $z_i = Z_n - N_b$. For orbitals which are spatially large relative to the inter-particle spacing, this assumption is dubious. But, the appeal is the IPD can be found by evaluating the mean of the plasma potential at the ion center. Using perturbation theory, the IPD is then:

$$\text{IPD} = -e \cdot \lim_{r \to 0} \left(\Phi(r) - \frac{e(z_i + 1)}{4\pi\epsilon_0 r} \right) , \tag{2.4}$$

where $\Phi(r)$ is the plasma's total electrostatic field, and z_i is the charge state of the initial ion. Note that in this equation, the IPD depends on the final charge state of the ion, (z_i+1), not the initial charge state: this is imposed. This charge dependence can be derived naturally from thermodynamic arguments. It is intuitive, though, as otherwise neutral atoms would not experience any IPD with the natural consequence

being, for example, a large collection of Al atoms would not be pressure-ionized to form a metal.

2.2.2 Thermodynamic Approach

Alternatively, if the plasma is semi-classical ($n_\alpha {\Lambda_\alpha}^3 \sim \theta^{-3/2} \ll 1$), the problem can be approached using classical statistical mechanics. This derivation will be much more detailed through the inclusion of relevant relationships. In the most general case, a plasma is a system of N_f free electrons and N_A^z ions of species A with charge state z, contained in a volume V. By charge neutrality, the particle numbers are related by [132]:

$$N_f = \sum_{A=1}^{M} \sum_{z=-j}^{k} z N_A^z \,. \tag{2.5}$$

The total particle number $N = N_f + \sum_A \sum_z N_A^z$. If the system is in local thermal equilibrium (LTE) at a temperature $k_B T$, the partition function Z for this composite system is:

$$Z = \frac{1}{h^{3N} N_f! \prod_A \prod_z N_A^z!} \int \cdots \int \exp(-E/k_b T) \prod_{\gamma=1}^{N_f} d\omega_\gamma \prod_{A=1}^{M} \prod_{z=-j}^{k} d\omega_A^z \,, \tag{2.6}$$

where $d\omega_\alpha = d^3\boldsymbol{p}_\alpha d^3\boldsymbol{r}_\alpha$ is the phase space element for a particle α, and the total energy of the system is:

$$E = \sum_{\gamma=1}^{N_f} E(\boldsymbol{p}_\gamma, \boldsymbol{r}_\gamma) + \sum_{A=1}^{M} \sum_{z=-j}^{k} E(\boldsymbol{p}_A^z, \boldsymbol{r}_A^z) \,. \tag{2.7}$$

The Helmholtz free energy (per particle) of the system with internal energy U and entropy S is:

$$F \equiv U - TS = -k_B T \ln(Z) \,. \tag{2.8}$$

Assuming the particles are not charged so there are no interactions between them, the particle partition functions are $\varphi_\alpha(T) = \zeta_\alpha(T)\sigma_\alpha(T)$, where $\zeta_\alpha(T)$ is the translational partition function and $\sigma_\alpha(T)$ is the intrinsic partition function containing

internal degrees of freedom for the ions:

$$\sigma_A^z(T) = \frac{1}{h^l} \sum_{i=1}^{l} g_A^z(i) \exp(-\epsilon_A^z(i)/k_B T)\,, \tag{2.9}$$

where $\epsilon_A^z(i)$ are the energy of the internal state i in the ion (A, z), with degeneracy $g_A^z(i)$. $i = 1$ denotes the ground state of the ion. The internal degrees of freedom summed over in σ_A^z are all the bound state configurations for the ion (A, z). The partition function excluding interactions is therefore:

$$Z_0 = \frac{1}{N_f!} \left[\varphi_e\right]^{N_f} \prod_A \prod_z \frac{1}{N_A^z!} \left[\varphi_A^z\right]^{N_A^z}\,. \tag{2.10}$$

Using the equilibrium condition:

$$\frac{\partial F}{\partial N_A^z} = \frac{\partial F}{\partial N_A^{z+1}}\,, \tag{2.11}$$

the ionization balance of an LTE plasma is described by coupled Saha ionization equations [133]:

$$\frac{n_A^{z+1} n_f}{n_A^z} = \frac{2}{{\Lambda_e}^3} \frac{\sigma_A^{z+1}}{\sigma_A^z} \exp\!\left(-\beta \left[\epsilon_A^{z+1}(1) - \epsilon_A^z(1)\right]\right), \tag{2.12}$$

where the energies in the intrinsic partition functions have been zeroed against the ground state. $(I^{(0)})_A^z = \epsilon_A^{z+1}(1) - \epsilon_A^z(1)$ is identified as the ionization energy of the ion (A, z) in absence of any interactions.

Turning on the charges of the particles, the partition function is now $Z = Z_0 Z_{ch}$, where Z_0 is the non-interacting partition function, and:

$$Z_{ch} = \frac{1}{\prod_\alpha N_\alpha!} \int \cdots \int \exp\left(-W_{ch}/k_B T\right) \prod_{\alpha=1}^{N} (d\omega_\alpha) \tag{2.13}$$

where W_{ch} is the potential energy of the charged interactions, and the particle product notation has been simplified for clarity. The free energy associated with

the system is:

$$F = F_0 + F_{ch} = -k_B T \ln(Z_0) - k_B T \ln(Z_{ch}) \tag{2.14}$$

The interaction W_{ch} can be decomposed further into $W_{ch} = W_{self} + W_{el}$ [132]. W_{self} is the energy associated with turning on each charge in the system effectively in the absence of the other charges, and is assumed to be configuration-independent. W_{el} is the interaction between all the different charges. W_{el} can be decomposed into electrical moments, but it is only necessary to consider the first moment, Coulomb interactions. The charged-contribution to the free energy therefore becomes:

$$F_{ch} = W_{self} + F_{el} \tag{2.15}$$

$$= W_{self} - k_B T \ln\left(\frac{1}{\prod_\alpha N_\alpha!}\int\cdots\int \exp\left(-W_{el}/k_B T\right)\prod_{\alpha=1}^{N}(d\omega_\alpha)\right) + const \tag{2.16}$$

Using Eqs. (2.11), (2.14) and (2.15) one can then derive the Saha equation for an interacting system:

$$\frac{n_A^{z+1} n_f}{n_A^z} = \frac{2}{{\Lambda_e}^3}\frac{\sigma_A^{z+1}}{\sigma_A^z}\exp\left(-\beta\left[(I^{(0)})_A^z + \frac{\partial F_{el}}{\partial N_A^{z+1}} + \frac{\partial F_{el}}{\partial N_e} - \frac{\partial F_{el}}{\partial N_A^z}\right]\right). \tag{2.17}$$

The effect of continuum lowering appears in two ways. First, the derivatives of F_{el} may be interpreted as a changing the ionization energy of (A, z), and will be identified as the IPD:

$$\mathrm{IPD}_A^z = -\frac{\partial F_{el}}{\partial N_A^{z+1}} - \frac{\partial F_{el}}{\partial N_e} + \frac{\partial F_{el}}{\partial N_A^z}. \tag{2.18}$$

Second, the intrinsic partition functions σ_A^z may also be affected if the number of internal (bound) states is altered by the change in ionization energy. This second effect is usually negligible, except for high principal quantum number states, and so it is typically ignored.

Dealing with F_{el} using the partition functions explicitly is unwieldy. Fortunately, some simpler formulae can be used. First, returning to Eqs. (2.8) and (2.15), the

relationship between the entropy and free energy, $S = -\left(\partial F/\partial T\right)_{V,N}$, can be used to express the electrostatic free energy in terms of the electrostatic internal energy U_{el} and the temperature T:

$$F_{el} = -T \int^{T} dT'\, T'^{-2} U_{el}\,. \tag{2.19}$$

If the electrostatic potential of a particle in the plasma $\Phi_\alpha(\boldsymbol{r})$ interacts with the plasma's charge density $\rho(\boldsymbol{r})$, the electrostatic internal energy of the interaction is:

$$U_\alpha = \int_V d^3\boldsymbol{r}\rho(\boldsymbol{r})\Phi_\alpha(\boldsymbol{r})\,, \tag{2.20}$$

which gives a total electrostatic free energy per unit volume of:

$$F_{el} = -T \sum_\alpha n_\alpha \int^{T} dT'\, T'^{-2} U_\alpha\,. \tag{2.21}$$

This equation may be readily used in Eq. (2.18) to derive the IPD [134].

Another useful expression can be derived from Eq. (2.16) [132]. Often, one calculates the potential $\Phi(\boldsymbol{r})$ from the center some particular charge in the plasma α, where $\boldsymbol{r}$ is the positional coordinate that is centered on α. Differentiating Eq. (2.16) with respect to the charge of α gives:

$$\frac{\partial W_{self}}{e\partial z_\alpha} + \frac{\partial F_{el}}{e\partial z_\alpha} = \frac{\int\cdots\int \frac{\partial W_{ch}}{e\partial z_\alpha}\exp(-W_{ch}/k_BT)d\Omega}{\int\cdots\int \exp(-W_{ch}/k_BT)d\Omega} = \left\langle \frac{\partial W_{ch}}{e\partial z_\alpha} \right\rangle\,, \tag{2.22}$$

where the angular brackets refer to configurational averages. $\langle \partial W_{ch}/e\partial z_\alpha\rangle$ is the increase in charge energy, averaged over all configurations, per unit increase of the charge at α. This is also equal to the increase in energy per unit increase of the charge at the location occupied by α. In other words, the electrostatic potential at the point occupied by α:

$$\frac{\partial W_{self}}{e\partial z_\alpha} + \frac{\partial F_{el}}{e\partial z_\alpha} = \langle \Phi(0)\rangle_{-\alpha}\,. \tag{2.23}$$

$\langle\cdot\rangle_{-\alpha}$ refers to configurational averages excluding the particle α [1]. $\partial W_{self}/e\partial z_\alpha$ is the contribution of α to the electrostatic potential due to the charge of α. As it is a property of the particle α and independent of the other particles in the system, it can be removed from $\langle\Psi(0)\rangle_{-\alpha}$ to determine the mean potential at the position of particle α due to the surrounding plasma, $\overline{\Phi}_\alpha(z_\alpha)$:

$$\overline{\Phi}_\alpha(z_\alpha) \equiv \langle\Phi(0)\rangle_{-\alpha} - \frac{\partial W_{self}}{e\partial z_\alpha} = \frac{\partial F_{el}}{e\partial z_\alpha}\,. \tag{2.24}$$

With Eq. (2.24), the free energy can be derived from the mean potential by making the variable change $\partial z_\alpha = z_\alpha \partial x$:

$$F_{el}^{\alpha} = e z_\alpha \int_0^1 dx\, \overline{\Phi}_\alpha(z_\alpha x)\,, \tag{2.25}$$

and the total electrostatic free energy per unit volume is:

$$F_{el} = \sum_\alpha e z_\alpha n_\alpha \int_0^1 dx\, \overline{\Phi}_\alpha(z_\alpha x)\,. \tag{2.26}$$

This equation, just like Eq. (2.21), can be used in Eq. (2.18) to find the IPD energy.

2.3 Traditional IPD Models

2.3.1 Weakly-Coupled Limit: Debye Screening

In the weakly-coupled limit ($\Gamma \ll 1$), where classical plasma theory holds, the Debye-Hückel (DH) model [20] may be used to treat the plasma. To calculate the IPD, the total electrostatic potential $\Phi(\boldsymbol{r})$ at each of the charges γ needs to be found. But because $\Phi(\boldsymbol{r})$ should be independent of the co-ordinates of a specific particle, one can determine the plasma potential on γ using the configurational average $\Phi_\gamma(\boldsymbol{r}) \equiv \langle\Phi(\boldsymbol{r})\rangle_{-\gamma}$:

$$-\epsilon_0 \nabla^2 \Phi_\gamma(\boldsymbol{r}) = \sum_\alpha q_\alpha n_\alpha(\boldsymbol{r})\,, \tag{2.27}$$

[1] This is because α is a test particle at which the potential is being evaluated, therefore we are averaging over the different configurations around the particles α.

If it is assumed the plasma is in LTE at a temperature $\beta^{-1} = k_B T$, the free electrons are distributed by Fermi-Dirac statistics (+1) and the ions by Bose-Einstein statistics (−1):

$$n_\alpha(\boldsymbol{r}) = \frac{g_\alpha}{2\pi^2} \int_{p_0}^{\infty} dp\, p^2 \left\{ \exp\left(\beta \left[\frac{\hbar^2 p^2}{2m_\alpha} + q_\alpha \Phi_\gamma(\boldsymbol{r}) - \mu_\alpha \right] \right) \pm 1 \right\}^{-1} , \tag{2.28}$$

where g_α is the degeneracy ($g_f = 2$, $g_{ion} = 1$), p is the momentum, μ_α is the chemical potential of the particle species, and m_α is the particle mass. The condition $p \geq p_0 = \sqrt{2 m_e e \Phi(\boldsymbol{r})}$ ensures the free electrons have sufficient kinetic energy to overcome the electrostatic potential. For the ions, $p_0 = 0$. In the weakly-coupled limit, the exponential in the denominator is much greater than one and the distributions reduce to a Maxwell-Boltzmann distribution:

$$\begin{aligned} n_\alpha(\boldsymbol{r}) &= \frac{g_\alpha}{2\pi^2} \exp\left(\beta \left[\mu_\alpha - q_\alpha \Phi_\gamma(\boldsymbol{r})\right]\right) \int_{p_0}^{\infty} dp\, p^2 \exp\left(\frac{-\beta \hbar^2 p^2}{2m_\alpha} \right) && (2.29) \\ &= \frac{g_\alpha}{{\Lambda_\alpha}^3} \exp\left(\beta \left[\mu_\alpha - q_\alpha \Phi_\gamma(\boldsymbol{r})\right]\right) \times \\ &\qquad \left[1 - \operatorname{erf}\left(p_0 \sqrt{\frac{\hbar^2 \beta}{2m_\alpha}} \right) + \frac{p_0}{2} \sqrt{\frac{\hbar^2 \beta}{2m_\alpha}} \exp\left(-\frac{{p_0}^2 \hbar^2 \beta}{2m_\alpha} \right) \right] . && (2.30) \end{aligned}$$

where $\operatorname{erf}(x)$ is the error function [98]. In the limit $\beta \to 0$ (or, if $p_0 = 0$), the square bracket term equals one. As the particles are weakly interacting, the chemical potentials are the same as the ideal gas [135]:

$$\mu_\alpha^{ideal} = -k_B T_\alpha \ln\left(\frac{g_\alpha}{\langle n_\alpha \rangle} \left[\frac{m_\alpha k_B T_\alpha}{2\pi\hbar^2} \right]^{3/2} \right) \tag{2.31}$$

where $\langle n_\alpha \rangle$ is the mean particle density. With these approximations, the charge density of the particles becomes:

$$n_\alpha(\boldsymbol{r}) = \langle n_\alpha \rangle \exp\left(-\beta q_\alpha \Phi_\gamma(\boldsymbol{r}) \right) , \tag{2.32}$$

Inserting this particle density into Eq. (2.27) gives the Poisson-Boltzmann equation:

$$-\epsilon_0 \nabla^2 \Phi_\gamma(\boldsymbol{r}) = \sum_\alpha q_\alpha \langle n_\alpha \rangle \exp\left(-\beta q_\alpha \Phi_\gamma(\boldsymbol{r})\right). \tag{2.33}$$

In the weakly-coupled limit $\beta \ll q_\alpha \Phi_\gamma(\boldsymbol{r})$, a first-order Taylor expansion can be performed on the exponential term to derive a linearized Poisson-Boltzmann equation:

$$\begin{aligned} \nabla^2 \Phi_\gamma(\boldsymbol{r}) &= {\lambda_D}^{-2} \Phi_\gamma(\boldsymbol{r}) - \frac{1}{\epsilon_0} \sum_\alpha q_\alpha \langle n_\alpha \rangle \\ &= {\lambda_D}^{-2} \Phi_\gamma(\boldsymbol{r}), \end{aligned} \tag{2.34}$$

where in the last step, charge neutrality $\sum_\alpha q_\alpha \langle n_\alpha \rangle = 0$ has been invoked. The parameter λ_D is the Debye screening length, defined as:

$$\lambda_D = \left(\frac{\epsilon_0 k_B T}{\sum_\alpha {q_\alpha}^2 \langle n_\alpha \rangle} \right)^{1/2}, \tag{2.35}$$

The solution to Eq. (2.34), centered on one of the charges γ, is a screened Coulomb potential for that charge [20]:

$$\Phi_\gamma(\boldsymbol{r}) = \frac{z_\gamma e}{4\pi\epsilon_0 r} e^{-r/\lambda_D} \tag{2.36}$$

where $r = |\boldsymbol{r}|$, $z = z_i$ for an ion, and $z = -1$ a free electron.

To see the effect of the plasma on the ionization potentials of the test charge, the methods outlined in Section 2.1 can be used. From Eq. (2.36), the free energy can be calculated using Eqs. (2.20) and (2.21), or from Eq. (2.24) with:

$$\overline{\Phi}_\alpha(z_\alpha) = \lim_{r \to 0} \left(\frac{z_\alpha e}{4\pi\epsilon_0 r} \exp(-r/\lambda_D) - \frac{z_\alpha e}{4\pi\epsilon_0 r} \right) = -\frac{z_\alpha e}{4\pi\epsilon_0 \lambda_D}, \tag{2.37}$$

noting that with the variable change $e\partial z_\alpha \to e z_\alpha \partial x$, $\lambda_D \to \lambda_D / x$. In either case, the total electrostatic free energy is:

$$F_{el} = -\frac{e^3}{12\pi\epsilon_0} \left(\epsilon_0 k_B T\right)^{-1/2} \left(n_f + \sum_i n_i {z_i}^2 \right)^{3/2}, \tag{2.38}$$

which gives the IPD in the DH limit as:

$$\mathrm{IPD_{DH}} = {\lambda_D}^{-1}(z+1)\frac{e^2}{4\pi\epsilon_0}\,, \tag{2.39}$$

where z is the charge state of the initial ion. If the Debye screening was instead considered to be a perturbation effect by the mean potential around a point-particle ion, then using Eq. (2.4):

$$\mathrm{IPD_{DH}} = \lim_{r\to 0}\left(-\frac{ze^2}{4\pi\epsilon_0 r}\exp(-r/\lambda_D) + \frac{ze^2}{4\pi\epsilon_0 r}\right) = \frac{ze^2}{4\pi\epsilon_0\lambda_D}\,, \tag{2.40}$$

which is the same result as Eq. (2.39) if z is identified as the charge state of the final ion. The strength of the IPD from Debye screening is characterized by the Debye screening length. Written in an alternative form:

$$\mathrm{IPD_{DH}} \propto {n_f}^{1/2}\,\beta^{1/2}\,\left(z^*+1\right)^{1/2}(z+1)\,. \tag{2.41}$$

where $z^* = \langle z^2\rangle \,/\, \langle z\rangle$, and:

$$\langle z^n\rangle = \frac{\sum_i {z_i}^n n_i}{\sum_i n_i}\,, \tag{2.42}$$

The IPD energy in the weakly-coupled limit scales with the square roots of the free electron density and the inverse temperature, and linearly with the charge of the ion. It also depends on the *charge state distribution* of the ions, not just the mean ionization, as generally $z^* \neq \langle z\rangle$ except for highly ionized systems.

There are two further points to note about this derivation: First, it has been assumed the electrons and ions are in thermal equilibrium with one another, however it is often the case that the electrons and ions will have different temperatures. In this case, the plasma's Debye length is given by:

$$\lambda_D^{-2} = \epsilon_0^{-1} n_f e^2\left(\beta_e + z^*\beta_i\right)\,. \tag{2.43}$$

If the ions are cold, then by Eq. (2.28) only their average density $\langle n_i\rangle$ needs to be considered (see Section 2.3.2) so their contribution to the screening vanishes.

Second, the IPD energy in Eq. (2.39) is applied equally to all the binding energies of the ion z.

2.3.2 Strongly-Coupled Limit: Ion-Sphere Model

In the strongly-coupled limit ($\Gamma \geq 1$), the ion-sphere (IS) model is thought to be applicable. For an IS model, the plasma is treated as being composed of a set of spheres with radii R_i centered on each of the ions' positions. Each ion's sphere corresponds to the ion's share of the total plasma, in that each sphere contains enough electrons – both bound and free – so that the sphere is electrically neutral. Typically, outside the sphere is treated with fictitious uniform positive and negative charges so that the outside is quasi-neutral and uniform [108], and the electrostatic potential will be zero. Alternatively, one can view that there is no potential between spheres as the concept does not exist: the plasma only consists of the ion spheres [117].

Taking the bound electrons to be entirely localized on the ion centers, the Poisson equation centered on an ion is:

$$-\epsilon_0 \nabla^2 \Phi(r) = \begin{cases} -e n_f(\boldsymbol{r}) + z_i e \delta^{(3)}(\boldsymbol{r}) & \text{if } r < R_i, \\ 0 & \text{if } r \geq R_i, \end{cases} \tag{2.44}$$

where z_i is the ion's charge in the sphere, $n_f(\boldsymbol{r})$ is the free electron density in the sphere, and $\boldsymbol{r} = (r, \theta, \psi)$ is the spherical co-ordinate centered on the ion. By construction, as the sphere is charge neutral beyond the surface, the boundary condition $\Phi(r \geq R_i) = 0$ can be used. The potential inside the sphere is then:

$$\Phi(\boldsymbol{r}) = \frac{z_i e}{4\pi\epsilon_0 r} - \frac{z_i e}{4\pi\epsilon_0 R_i} + \frac{e}{4\pi\epsilon_0} \int_R^r dr' \left(\int_{V(r''=0)}^{V(r''=r')} d^3\boldsymbol{r}'' \, n_f(\boldsymbol{r}'') \right). \tag{2.45}$$

To simplify the free electron density, the low temperature limit ($T \to 0$) can be

considered. In this limit, the Fermi-Dirac distribution is a Heaviside step function:

$$\frac{1}{1+\exp(\beta[\epsilon(p)-\mu])} = \begin{cases} 1 & \text{if } \epsilon(p) < \mu, \\ 0 & \text{if } \epsilon(p) \geq \mu, \end{cases} \tag{2.46}$$

so the free electron density becomes:

$$n_f(\boldsymbol{r}) = \frac{2^{3/2}{m_f}^{3/2}}{3\pi^2}\left([\mu_f + e\Phi(\boldsymbol{r})]^{3/2} - [e\Phi(\boldsymbol{r})]^{3/2}\right) , \tag{2.47}$$

In the low temperature limit, the chemical potential is the Fermi energy with mean free electron density $\langle n_f \rangle$, and density may be expressed as:

$$n_f(\boldsymbol{r}) = \langle n_f \rangle \left(\left[1 + \frac{e\Phi(\boldsymbol{r})}{E_F}\right]^{3/2} - \left[\frac{e\Phi(\boldsymbol{r})}{E_F}\right]^{3/2} \right) . \tag{2.48}$$

Finally, in the high density limit, $E_F \gg e\Phi(\boldsymbol{r})$, and the free electron density is uniform $n_f(\boldsymbol{r}) = \langle n_f \rangle = n_f$. Therefore, at low temperatures and high densities – the strongly-coupled limit – the total potential inside an ion sphere is:

$$\Phi(r) = \frac{z_i e}{4\pi\epsilon_0 r} - \frac{1}{2}\frac{z_i e}{4\pi\epsilon_0 R_i}\left(3 - \frac{r^2}{{R_i}^2}\right) , \tag{2.49}$$

and the total charge density within an ion sphere is:

$$\rho(r) = z_i e\delta^{(3)}(r) - en_f \, . \tag{2.50}$$

The IPD can be found using Eq. (2.4):

$$\mathrm{IPD_{IS}} = \frac{3}{2}\frac{(z+1)}{R_{\mathrm{IS}}}\frac{e^2}{4\pi\epsilon_0} , \tag{2.51}$$

where z is the ion's initial charge state, and R_{IS} is the ion sphere radius of the final ion:

$${R_{\mathrm{IS}}}^3 = \frac{3(z+1)}{4\pi n_f} , \tag{2.52}$$

This is the general form of the IS IPD in the literature (see e.g. Refs. [107, 108, 136,

137]), although the constant 3/2 may be a different number of order unity depending on the approach taken.

There are numerous differences in the IPD calculated using the IS model and the DH model. Notably, the characteristic length scale of the IS IPD is not λ_D, but is instead R_{IS} due to the charge neutrality condition of the sphere. As a consequence, there are differences in the scaling relationships between the two models. Expressing the IS IPD as:

$$\mathrm{IPD}_{\mathrm{IS}} \propto {n_f}^{1/3}(z+1)^{2/3}\,, \tag{2.53}$$

it is clear the IS IPD scales more weakly with the free electron density and the ion charge state than the DH IPD in Eq. (2.41). Secondly, there is no explicit temperature-dependence of the IPD in the IS model, unlike the DH model which has both implicit and explicit temperature-dependence. Instead, the effect of temperature on the IS IPD appears from the mean ion charge state via n_f. Additionally, the IS model does not depend on the charge state distribution, just the mean charge state of the plasma. Like Debye screening, the IS IPD is applied equally to all binding energies of the ion. Finally, it should be clear that the dependence of the IS IPD on the final charge is being artificially imposed instead of being a natural result of the derivations.

2.3.3 Ecker-Kröll Model

Based on the two previous sections, the limits of the decrease in the ionization potential for an ion with initial charge state z_i is:

$$\mathrm{IPD} = \frac{e^2}{4\pi\epsilon_0} \cdot \begin{cases} {\lambda_D}^{-1}(z+1) & \text{if } \Gamma \ll 1, \\ \\ \dfrac{3}{2} R_{\mathrm{IS}}^{-1}(z+1) & \text{if } \Gamma \geq 1, \end{cases} \tag{2.54}$$

The question is then, in the intermediate region, when lacking approximations to simplify the Poisson equation and the quantum distributions, what form should the IPD take? This is a particularly pertinent issue as this regime covers a large

number plasmas produced in the laboratory and in nature. The historic approach for deriving in the IPD in the intermediate regime is to interpolate between the ion-sphere and Debye screening limits. One of the first attempts to achieve this was by Ecker and Kröll in 1963 [110]. However, the physical validity of the model is questionable due to a lack of charge conservation. An alternative approach by Stewart and Pyatt in 1966 [109] appears to have a better physical grounding and has therefore generally been preferred. Both models are now derived, starting with the Ecker-Kröll model, as they highlight the difficulty of deriving analytical IPD models in the mid-coupling limit. It will also transpire that both models provide bounds on the strength of IPD.

The Ecker-Kröll (EK) model is derived in the semi-classical limit $n_\alpha {\Lambda_\alpha}^3 \ll 1$. This implies the particle distributions can be described by the Maxwell-Boltzmann distribution Eq. (2.29). The derivation is similar to that of the Debye model, where the potential of a test particle in the plasma is calculated. The free energy is evaluated using Eq. (2.24), and the IPD is calculated using Eq. (2.18). Ecker and Kröll identify three characteristic radii around the point particles that describe the system:

1. $\boldsymbol{r_{lin}}$: The smallest radius for which:

$$\frac{|z_\alpha z_\beta| \, e^2}{4\pi\epsilon_0 r k_B T} \ll 1 \,, \tag{2.55}$$

   is applicable, so the Maxwell-Boltzmann distribution can be linearized.

2. $\boldsymbol{R_{\mathrm{EK}}}$: The distance that separates individual and collective regions. This is the smallest radius at which the particle ensemble can be treated as a continuous probability distribution. The exact distance is not defined, but $R_{\mathrm{EK}} \sim \mathcal{O}(r_0)$, where:

$$R_{\mathrm{EK}} \sim r_0 \equiv \left(\frac{3}{4\pi n} \right)^{1/3} , \tag{2.56}$$

   and $n = n_f + \sum_i n_i$ is the total particle density.

3. $\boldsymbol{r_c}$: The largest distance from the test particle at which the potential can be

approximated by the Coulomb potential.

Over the full range $r > R_{\mathrm{EK}}$, the Poisson-Boltzmann equation Eq. (2.33) holds. In the region $r > R_{\mathrm{EK}}$ and $r > r_{lin}$, the Poisson-Boltzmann equation can be linearized to Eq. (2.34). The simple solutions to the Poisson-Boltzmann equations are:

$$\Phi(r) = \frac{A}{r} \exp\left(-\frac{r}{\lambda_D}\right) \qquad \text{if } r \geq \max(r_{lin}, R_{\mathrm{EK}})\,, \tag{2.57}$$

$$\Phi(r) = \frac{z_\alpha e}{4\pi\epsilon_0 r} + B \qquad \text{if } 0 \leq r \leq r_c\,, \tag{2.58}$$

where A and B are constants to be found by boundary conditions. But in the intermediate region $r_c < r < \max(r_{lin}, R_{\mathrm{EK}})$, it is difficult to evaluate $\Phi(r)$. Therefore, the Ecker-Kröll model consider two cases. The cases are separated by the relationship of R_{EK} and r_{lin}. The critical density n_{crit} is defined when $R_{\mathrm{EK}} = r_{lin}$:

$$n_{crit} = \frac{3}{4\pi}\left(\frac{4\pi\epsilon_0 k_B T}{e^2 {Z_n}^2}\right)^3\,, \tag{2.59}$$

where Z_n is the nuclear charge of the ion.

Case I: $r_{lin} \ll R_{\mathrm{EK}}$ ($n \ll n_{crit}$). This condition means that when the distance is in the collective region, the system is also linear. It is also still the case that $0 \leq r \leq r_c$, the potential is still a Coulomb potential. Therefore, in the region $r_c \leq r \leq R_{\mathrm{EK}}$, the potential lies somewhere between:

$$\left|\frac{z_\alpha e}{4\pi\epsilon_0 r} + B\right| \geq \Phi(r) \geq \left|\frac{A}{r}\exp\left(-r/\lambda_D\right)\right|\,. \tag{2.60}$$

While the exact form of $\Phi(r)$ in this region is not known, Ecker and Kröll suggest it is of "negligible importance". So, instead, they propose to join the two known solutions by invoking the smoothness of $\Phi(r)$ and its derivatives at some boundary $r_c \lesssim \overline{r} \lesssim R_{\mathrm{EK}}$:

$$A = \frac{z_\alpha e}{4\pi\epsilon_0}\frac{1}{1+\overline{r}/\lambda_D}\,, \qquad B = \frac{-z_\alpha e}{4\pi\epsilon_0}\frac{1}{\lambda_D + \overline{r}}\,. \tag{2.61}$$

It also becomes clear that the mean potential $\overline{\Phi}_\alpha = B$. Finally, it is shown that a

specific choice of $\overline{r}$ is irrelevant in this case:

$$\overline{r}/\lambda_D \leq R_{\rm EK}/\lambda_D \sim \left(r_{lin}/r_{\rm EK}\right)^{1/2} \ll 1\,. \tag{2.62}$$

Therefore the mean potential around the test particle is:

$$\overline{\Phi}_\alpha = \lim_{r\to 0}\left(\Phi(r) - \frac{z_\alpha e}{4\pi\epsilon_0 r}\right) = -\frac{z_\alpha e}{4\pi\epsilon_0\lambda_D}\,. \tag{2.63}$$

This recovers the DH IPD, Eq. (2.39), for the weakly-coupled limit.

Case II: $r_{lin} \geq R_{\rm EK}$ ($n > n_{crit}$). In this limit, the Poisson-Boltzmann equation cannot be linearized across the entire region; but, $0 \leq r \leq r_c$ is still described by the Coulomb potential. It is now the region $r_c \leq r \leq r_{lin}$ in which a form for the potential needs to be derived. To achieve this, it is first noted that in the strongly-coupled regime, $r_c = \gamma r_0$ where $\gamma \lesssim 1$. To find $\Phi(r)$, the limits of the potential are considered based on screening arguments: because $n > n_{crit}$, the screening will be stronger than the linearized Poisson-Boltzmann solution ($\Phi(r) \leq \Phi_{\rm LPB}(r)$); and the extreme screening limit is trivially $\Phi(r) = 0$. Therefore, after enforcing the steadiness of the potential and its derivatives at $r = \gamma r_0$, the mean potential (i.e. the constant B) is described by the inequality:

$$-\frac{z_\alpha e}{4\pi\epsilon_0 r_0}\frac{1}{\gamma} \leq \overline{\Phi}_\alpha \leq -\frac{z_\alpha e}{4\pi\epsilon_0 r_0}\frac{1}{3^{-1/2}+\gamma}\,. \tag{2.64}$$

where the relation $\lambda_D^{cr} \sim 3^{-1/2} r_0$ has been used, and λ_D^{cr} is the Debye length at the critical density. This suggests that:

$$\overline{\Phi}_\alpha = -C\frac{z_\alpha e}{4\pi\epsilon_0 R_{\rm EK}}\,, \tag{2.65}$$

where

$$\left(3^{-1/2}+\gamma\right)^{-1} \leq C \leq \gamma^{-1}\,, \tag{2.66}$$

is an unknown constant. To reach a solution, Ecker and Kröll enforce that C must

smoothly connect Case I and II, and suggest that it could be:

$$C_{\mathrm{EK}} = \left.\frac{R_{\mathrm{EK}}}{\lambda_D}\right|_{n=n_{crit}} = \left(\frac{4\pi n_{crit}}{3}\right)^{-1/3} \left(\frac{e^2}{\epsilon_0 k_B T}\sum_\alpha {z_\alpha}^2 n_\alpha^{crit}\right)^{1/2} . \tag{2.67}$$

However, as they note, this choice is somewhat arbitrary as the potential between the two cases is poorly defined. But, it is known that C_{EK} will be a constant that is independent of the ion's initial and final charge states.

Finally, the Ecker-Kröll model gives IPD energy of:

$$\mathrm{IPD}_{\mathrm{EK}} = \frac{e^2(z+1)}{4\pi\epsilon_0 R_{\mathrm{EK}}} \cdot \begin{cases} R_{\mathrm{EK}}/\lambda_D & \text{if } n \ll n_{crit}, \\ C_{\mathrm{EK}} = (R_{\mathrm{EK}}/\lambda_D)|_{n=n_{crit}} & \text{if } n \geq n_{crit}\,. \end{cases} , \tag{2.68}$$

The limit expressed by C_{EK} is the EK-equivalent to the IS model but, because C_{EK} is independent of $(z+1)$, it is not a charge-conserving IS model [109], which has led to concerns about the physical applicability of the EK model to strongly-coupled systems. This fact cannot be ignored: for the plasmas of interest in this thesis, the particle densities are many orders of magnitude above their critical densities. Given that the EK model has been explicitly derived in the weakly-coupled semi-classical limit, and forced into the strongly-coupled regime, these issues are perhaps not surprising.

In recent years, it has been noted that setting $C_{\mathrm{EK}} = 1$ provides excellent agreement with some experimental results [34, 38–40] as a consequence of the IPD now being significantly larger. Though, there is no physical reason as to why this modified-Ecker-Kröll (mEK) model should perform as well as it does. Note that the mEK model removes any explicit temperature dependence of the IPD on temperature in the high density limit. The scaling of the mEK model in the strongly-coupled limit is:

$$\mathrm{IPD}_{\mathrm{mEK}} \propto (z+1)\left(n_f + \sum_i n_i\right)^{1/3} . \tag{2.69}$$

for an initial charge state z. The mEK IPD scales like a mixture of the DH and IS models. The mEK scaling with the ion charge state is the same as the DH

IPD, but scales with n_f in a similar way to the IS IPD with the exception that the ion densities now also feature explicitly. Additionally, like the IS model, there is no explicit temperature-dependence in the mEK model nor a dependence on the charge state distribution.

2.3.4 Stewart-Pyatt Model

The final traditional IPD model that will be derived in detail is the Stewart-Pyatt (SP) model [109]. This is by far the most popular IPD model, and has been widely implemented in plasma codes as the way to account for continuum lowering. The formulation is based on the finite-temperature TF model [43], with the IPD is evaluated at the ion center, per Eq. (2.4). Again, we wish to solve the Poisson equation for the system. In this model, the bound and free electrons are treated with Fermi-Dirac statistics, and the ions are treated with Maxwell-Boltzmann statistics:

$$n_e(r) = n_e(\infty)\frac{F(e\Phi(r)/k_BT - a)}{F(-a)}\,, \tag{2.70}$$

$$n_i(r) = n_i(\infty)\exp\left(-z_i\frac{e\Phi(r)}{k_BT}\right)\,, \tag{2.71}$$

where $-a = \mu/k_BT$ and $F(x) \equiv F_{1/2}(x)$ is the complete Fermi-Dirac integral:

$$F_j(x) = \frac{1}{\Gamma(j+1)}\int_0^\infty dt\frac{t^j}{1+\exp(t-x)}\,, \tag{2.72}$$

and $\Gamma(j+1)$ is the gamma function [98]. The limiting conditions are $\Phi(r\to\infty) = 0$, $\lim_{r\to 0} r\Phi(r) = z_i e/4\pi\epsilon_0$, and $n_e(\infty) = 2\Lambda_e^{-3}F(-a)$. It is assumed that $F(-a) \approx \exp(-a) \ll 1$, so that the free electrons are non-degenerate and the electron chemical potential is that of the ideal gas, Eq. (2.31). The charge neutrality condition is defined at the far distance, $\sum_i z_i n_i(\infty) = n_e(\infty)$.

Using the substitutions:

$$y = \frac{e\Phi}{k_BT} \qquad\qquad x = \frac{r}{\lambda_D}\,, \tag{2.73}$$

the Poisson equation can be re-written as:

$$\frac{1}{x}\frac{d^2}{dx^2}(xy) = \frac{1}{z^*+1}\left(\frac{F(y-a)}{F(-a)} - \frac{\langle z\exp(-zy)\rangle}{\langle z\rangle}\right), \tag{2.74}$$

where $z^* = \langle z^2\rangle / \langle z\rangle$, and $\langle f\rangle = \sum_i n_i f_i / \sum_i n_i$. If y is small – so $|e\Phi| \ll k_B T$ – then the second term on the right hand-side can be expanded and:

$$\frac{1}{x}\frac{d^2}{dx^2}(xy) = \frac{1}{z^*+1}\left(\frac{F(y-a)}{F(-a)} - \exp(-z^* y)\right). \tag{2.75}$$

This equation suggests that the Poisson equation can now be solved for a fictitious system with a single charge state z^*, instead of the full ionic distribution. The limits now are:

$$y(x\to\infty) = 0 \qquad \lim_{x\to 0} xy = \frac{ze^2}{4\pi\epsilon_0\lambda_D k_B T} \equiv K\,. \tag{2.76}$$

It is then assumed that because the bound electrons are also present on the isolated ion, their distribution does not directly influence the IPD. This makes it possible to find the perturbed screening potential, because a distribution can be assumed for the bound electrons, allowing for their influence on the surrounding free electron and ion distributions to be approximated by the TF model. Then, an approximate solution is found by considering the perturbed potential $\Phi_{scr}(r)$, given by the Poisson equation:

$$\frac{1}{x}\frac{d^2}{dx^2}(xv) = \frac{1}{z^*+1}\left(\frac{F(y-a,y)}{F(-a)} - \exp(-z^* y)\right). \tag{2.77}$$

where $v(x) = e\Phi_{scr}/k_B T$ and $F(y-a,y)$ is the incomplete Fermi-Dirac integral:

$$F(y-a,y) \equiv F_{1/2}(x,y) = \frac{2}{\sqrt{\pi}}\int_y^\infty dt \frac{t^{1/2}}{1+\exp(t-x)}\,. \tag{2.78}$$

The term $F(y-a,y)/F(-a)$ is the ratio of the free electron density to the total electron density in the TF model. An electron is considered free if it has kinetic energy greater than $e\Phi$, as given by the lower limit of the integral y. The limits on $v(x)$ are $-v(0) = J$ (see below) and $v(x\to\infty) = 0$. From Eq. (2.77), the perturbing

potential is:

$$v(x) = -J + \int_0^x S(t)t^2dt - \frac{1}{x}\int_0^x S(t)t^2dt\,, \tag{2.79}$$

$$= -\frac{1}{x}\int_0^\infty S(t)t^2dt + \frac{1}{x}\int_x^\infty S(t)t^2dt - \int_x^\infty S(t)tdt \tag{2.80}$$

where $S(x)$ is the right hand-side of Eq. (2.77), which contains the total potential $y(x)$, and $J = \int_0^\infty S(t)tdt$. The problem is then to find a form for $v(x)$, which will involve solving Eq. (2.74) to find $y(x)$. This is achieved using expansions of the Fermi-Dirac integrals for non-degenerate free electrons ($\exp(a) \gg 1$) – which explicitly limits the model to low densities – and the cases $y \ll a$ and $y \gg a$ [138]. Stewart and Pyatt then identify four characteristic length scales that define distinct regions of the potential y. With decreasing x and increasing y, they are:

Region I: Large x, and small $y \ll 1/z^*$. In this limit, the charge densities of the electrons and ions cancel, and only the electrons that are free need to be treated. The Poisson equation becomes:

$$\frac{1}{x}\frac{d^2}{dx^2}(xy) = y\,, \tag{2.81}$$

which is simply the DH limit. The potential is $y = C\exp(-x)/x$.

Region II: If there is a region $z^* \gg 1$, then there is a region where $1/z^* \ll y \ll 1$. In this region, the bound electron and ion densities are smaller than the free electron density. The free electron density can be approximated as a constant equal to the $n_e(\infty)$. The Poisson equation is therefore:

$$\frac{1}{x}\frac{d^2}{dx^2}(xy) = \frac{1}{z^*+1}\,, \tag{2.82}$$

and the potential is:

$$y = \frac{A}{x} + B + \frac{x^2}{6(z^*+1)}\,. \tag{2.83}$$

Region III: The region where $1 \ll y \ll a$. This region is close to an ion, and the number of bound electrons is greater than the number of free electrons. The

occupation numbers of the bound states is below capacity, and $n_e(r) > n_e(\infty)$. The local electron distribution can be approximated using Maxwell-Boltzmann statistics. The potential is found by solving the equation:

$$\frac{1}{x}\frac{d^2}{dx^2}(xy) = \frac{1}{z^* + 1}\exp(y)\,. \tag{2.84}$$

Region IV: This is the region of the ionic core, with $y \gg a$. The electrons are in fully occupied states, and the Poisson equation for the total potential becomes the finite-temperature TF equation:

$$\frac{1}{x}\frac{d^2}{dx^2}(xy) \propto \frac{1}{z^* + 1}(y - a)^{3/2}\,, \tag{2.85}$$

The procedure is therefore to evaluate the Poisson equation $y(x)$ by cascading through the different regions and connecting them. Then, $v(x)$ can be calculated using Eq. (2.80). To find an analytical form for the IPD, it is assumed that all the bound electrons are point particles centered on the ion nucleus, and the free electron density is uniform. Under this assumption, only Regions I and II need to be considered to calculate the IPD, which is given by Jk_BT/e. Interestingly, the IPD calculated using these approximations is similar to those found by numerically solving Eqs. (2.74) and (2.80). Using the boundary conditions Eq. (2.76) gives the constant $A = K$. In the limit of small x, $y(x) = K/x - J + \cdots$, therefore $B = -J$. Enforcing the continuity of $y(x)$ and its derivatives at some distance $\overline{x}$ between the regions gives the relationships:

$$Ce^{-\overline{x}} = K - J\overline{x} + \frac{\overline{x}^3}{6(z^* + 1)}\,, \quad Ce^{-\overline{x}} = J - \frac{\overline{x}^2}{2(z^* + 1)}\,, \quad Ce^{-\overline{x}} = \frac{\overline{x}}{(z^* + 1)}\,, \tag{2.86}$$

which together gives:

$$J = \frac{1}{2(z^* + 1)}\left\{\left[3K(z^* + 1) + 1\right]^{2/3} - 1\right\}\,. \tag{2.87}$$

Finally, it is imposed that the charge state z in K is the charge state of the final ion

so that the DH IPD is reproduced in the low-density limit. Note that unlike the EK model where the correct charge state dependence naturally arises, for the SP model it has to be imposed. The SP IPD for an ion with initial charge state z is:

$$\mathrm{IPD}_{\mathrm{SP}} = \frac{k_B T}{2(z^*+1)} \left\{ \left[\frac{3(z^*+1)(z+1)e^2}{4\pi\epsilon_0 \lambda_D k_B T} + 1 \right]^{2/3} - 1 \right\} . \tag{2.88}$$

The scaling relations of this IPD model with the temperature and density are much more complex than the other IPD models, but the charge state dependence is:

$$\mathrm{IPD}_{\mathrm{SP}} \sim (z+1)^{2/3} , \tag{2.89}$$

which is the same scaling as the IS model – and, in a sense, the SP model is a more complex IS model. This scaling with the ion charge is weaker than the scaling for the mEK model, and in general the SP model tends to give a lower estimate of the IPD than the mEK model.

Another useful way of expressing the Eq. (2.88) is by the ratio of the Debye length to the ion-sphere radius of the final ion, $\gamma = \lambda_D / R_{\mathrm{IS}}$:

$$\mathrm{IPD}_{\mathrm{SP}} = \frac{3}{2} \frac{(z+1)}{R_{\mathrm{IS}}} \frac{e^2}{4\pi\epsilon_0} \left\{ \left[1 + \gamma^3 \right]^{2/3} - \gamma^2 \right\} . \tag{2.90}$$

The similarities between the SP and IS models are much more obvious in this form. Additionally, the limits of the SP model can be more easily seen:

$$\mathrm{IPD}_{\mathrm{SP}} = \frac{e^2}{4\pi\epsilon_0} \cdot \begin{cases} \dfrac{3}{2} \dfrac{(z+1)}{R_{\mathrm{IS}}} & \text{if } R_{\mathrm{IS}} \gg \lambda_D \ (\gamma \ll 1), \\ \dfrac{(z+1)}{\lambda_D} & \text{if } R_{\mathrm{IS}} \ll \lambda_D \ (\gamma \gg 1). \end{cases} \tag{2.91}$$

These are the ion-sphere and Debye-Hückel limits, respectively.

2.3.5 Summary of Models

The IPD energy for an initial ion z using the different models are:

$$\text{Debye-Hückel:} \qquad \frac{(z+1)}{\lambda_D}\frac{e^2}{4\pi\epsilon_0}$$

$$\text{Ion-sphere:} \qquad \frac{3}{2}\frac{(z+1)}{R_{\mathrm{IS}}}\frac{e^2}{4\pi\epsilon_0}$$

$$\text{Ecker-Kröll:} \qquad \frac{(z+1)}{R_{\mathrm{EK}}}\frac{e^2}{4\pi\epsilon_0}\cdot\begin{cases} R_{\mathrm{EK}}/\lambda_D & (n \ll n_{crit}) \\ C_{\mathrm{EK}} = (R_{\mathrm{EK}}/\lambda_D)|_{n=n_{crit}} & (n \geq n_{crit}) \end{cases}$$

$$\text{Modified Ecker-Kröll:} \qquad \frac{(z+1)}{R_{\mathrm{EK}}}\frac{e^2}{4\pi\epsilon_0} \qquad (n \geq n_{crit})$$

$$\text{Stewart-Pyatt:} \qquad \frac{3}{2}\frac{(z+1)}{R_{\mathrm{IS}}}\frac{e^2}{4\pi\epsilon_0}\left\{\left[1+\left(\frac{\lambda_D}{R_{\mathrm{IS}}}\right)^3\right]^{2/3}-\left(\frac{\lambda_D}{R_{\mathrm{IS}}}\right)^2\right\}$$

with the characteristic length scales:

$$\text{Debye Length:} \qquad \lambda_D = \left[\frac{e^2}{4\pi\epsilon_0 k_B T}\left(n_f + \textstyle\sum_i {z_i}^2 n_i\right)\right]^{-1/2}$$

$$\text{Ion Sphere Radius:} \qquad R_{\mathrm{IS}} = \left(\frac{4\pi n_f}{3(z+1)}\right)^{-1/3}$$

$$\text{Ecker-Kröll Radius:} \qquad R_{\mathrm{EK}} = \left[\frac{4\pi}{3}\left(n_f + \textstyle\sum_i n_i\right)\right]^{-1/3}$$

The Debye-Hückel and ion-sphere models are generally considered the limiting cases for weakly-coupled and strongly-coupled systems. To briefly comment on whether these are good limits: the DH model is a good approximation of the IPD effect in very weakly-coupled systems, and arises naturally in general plasma models and quantum approaches. Meanwhile, the electrostatic internal energy of the IS model is very close to theoretical calculations of the minimum electrostatic energy of stable close-pack lattices such as face-centered cubic (fcc), body-centered cubic (bcc), and hexagonal close-packed (hcp) lattices [139, 140]. Therefore, the IS model appears to be a good approximation of strongly-coupled systems, even if the physicality of treating a plasma as only made of spheres is questionable. However, the IS model will eventually break down in the strongly-degenerate limit as it does not account

for degenerate quantum effects. The EK and SP models aim to interpolate between the DH and IS limits, when the Debye length and ion-sphere radius (the inter-particle separation) become comparable. However, as will become apparent in the Section 2.5, neither the EK or SP models are generally applicable.

In general terms, part of the problems with applying the EK and SP models is that they both treat the electrons and ions as semi-classical particles that obey Maxwell-Boltzmann statistics, but this is not generally true. The electrons in particular will in general be governed by Fermi-Dirac statistics, Eq. (2.28). The effect of the free electrons in the models is as if they are a fully-delocalized homogeneous electron gas (HEG). However, it should be expected that the free electrons have more complex distributions as evidenced by LDA and GGA treatments of electrons in first-principles calculations, and the presence of quasi-bound continuum resonances such as d-bands. Additionally, the bound electrons are treated as being localized entirely on the atomic centers, so that the nuclei and bound electrons can be treated as composite ion point-particles. So while the bound electrons are said to occupy atomic orbitals, in practice they are treated as being very strongly localized in space. In reality, atomic orbitals do have a finite size that will lead to the IPD depending on the specific shape and size of an orbital. For example, a simple first-order perturbation correction to the IS model with finite-size orbitals $|\psi^z_{nlm}\rangle$ might be:

$$\mathrm{IPD}^z \sim \frac{1}{2}\frac{z+1}{R_{\mathrm{IS}}}\frac{e^2}{4\pi\epsilon_0}\left(3 - \frac{1}{{R_{\mathrm{IS}}}^2}\left\langle\psi^{z+1}_{nlm}\right| r^2 \left|\psi^{z+1}_{nlm}\right\rangle\right) , \tag{2.92}$$

An evident way these finite-size effects manifests is in so-called "plasma polarization shift" [141], where transition lines are shifted in energy by an amount dependent on the principal quantum numbers (n, l, m) involved in the transitions. This indicates the binding energies of orbitals shift unevenly [142]. However, the benefit of these approximations is that a self-consistent calculation is no longer needed as the Poisson-Boltzmann equations can be solved analytically, so it becomes easier to express the IPD as analytical equations. The approximations of the electrons as bound-or-free – strongly localized or fully delocalized – will be investigated later in

this thesis.

There are specific issues with the two models. The EK model is actually only defined in two limits: the very low-density limit, where it is well-characterized by the DH model; and the high-density limit, where the model is only defined up to the inequality Eq. (2.66), and the functional form of γ is not known. To produce an analytical equation, C_{EK} was originally set to smoothly connect the low density and high density region at the critical density. But there is a large discontinuity between these two regions: the density jumps from $n \ll n_{crit}$ to $n \geq n_{crit}$. As Ecker and Kröll admit, this choice is arbitrary, and other choices which will give different IPD results could be made. Further, the EK model suggests the DH model should then be applied for all densities below n_{crit}, but this is unlikely to be true. Regardless, the plasmas of interest in this thesis have densities several orders of magnitude above the critical density. In this regime, the model generally fails to describe dense plasmas by overpredicting the IPD in some hot dense systems, such as in Hoarty 2013 [143].

In an attempt to find an analytical solution, the SP model makes the assumption that to approximate the IPD, the potential only needs to be resolved in weakly-coupled regions (Regions I and II). The benefit of this assumption is these are the two regions where analytical solutions to the potential exist, while Regions III and IV need to be solved numerically. As a consequence, the difficulty of solving the mid-coupling regime can be ignored. However, this explcitly disregards the details of electronic structure near the ion centers, which is exactly the region where the IPD is then evalutated. Also of note, the SP model is constructed based on the TF model [43–45], which is known to generally produce inaccurate results for many plasma systems. One can solve the Thomas-Fermi(-Dirac) equation and calculate the IPD effect (the so-called modified SP model), but it remains questionable how accurate the result will be to most systems.

Lastly, another notable deficiency of the models is that the exact electron configuration of the ion is ignored, with the IPD only depending on the overall charge state of the ion. Yet, given the influence of the configuration on energy levels and orbital wavefunctions, and the non-homogeneity of IPD effect on the atomic orbitals,

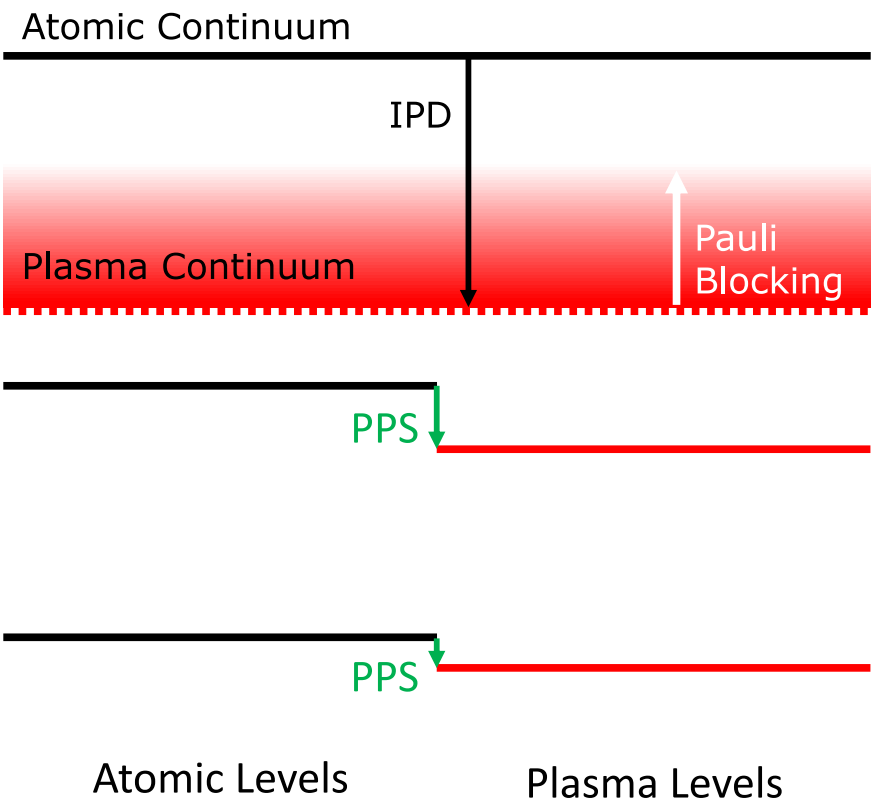


Figure 2.2: A schematic of various shifts that effect the ionization energy of a level. The shaded red above the plasma continuum represent the occupation of the continuum states. Pauli blocking raises the spectroscopic edge, but does not effect the ionization threshold so it is not included in the IPD effect. PPS provides an additional small IPD shift.

it should be expected to matter. For example, despite having the same number of bound electrons, the IPD of the valence electron for an ion with configuration $1s^2 2s^2 2p^1$ is likely to be different to the configuration $1s^2 2s^2 3p^1$ due to differences in screening by the bound electrons and the response of the neighbouring free electrons to the configurations. Granted, this difference may be small, but it could matter in discussing states that are on the verge of bound or free.

2.4 Additional IPD-like Processes

There are additional effects which also influence the ionization energies of bound electrons, however they are not all considered as part of the ionization potential depression effect. The two effects that will be discussed here – Pauli blocking and plasma polarization shift – are shown in Fig. 2.2. While this is to a degree semantics,

it is important to be clear what is being referred to when IPD is discussed. The primary question is what is the continuum lowered relative to? There are in fact two edges you could measure against: the first is the "spectroscopic edge", which refers to the total energy required to ionize an electron from an atom; the second is the "ionization threshold", which is the energy required to place an electron at the bottom of the continuum. Generally, these are not the same. For avoidance of doubt, in literature the IPD is generally measured from the ionization threshold, and this notion is followed throughout this thesis.

As the traditional IPD models are semi-classical, they do not account for degeneracy effects that do not have classical analogues. This includes Pauli blocking [144] which, due to electrons being fermions, only allows for electrons to be excited to vacant states. In the low temperature limit, this means it takes an additional amount of energy equal to the Fermi energy to excite an electron into the continuum. However, even at finite temperatures, the bottom of the continuum is still has a statistical occupation number so there is still an additional energy shift associated with Pauli blocking. The obvious effect is that it makes the effective continuum lowering smaller. Evidently, Pauli blocking influences the position of the spectroscopic edge, so it is typically excluded from IPD calculations [38, 145]. Nonetheless, it still makes an appearance in newer models to ensure the ionization threshold aligns with the bottom of the continuum [123].

Another effect is a shift in transition line energies due to the presence of the plasma particles, known as plasma polarization shift (PPS) [141]. PPS arises due to the surrounding plasma particles perturbing the wavefunctions of an ion's orbitals, with the perturbation increasing with the principal quantum number of an orbital [142]. Like IPD, PPS is controversial – the shifts that are measured are very small ($\lesssim 5$ eV), are difficult to distinguish from other effects such as Doppler shifts, and to make meaningful comments the plasma conditions need to be well-known. There are disagreements surrounding whether transition lines should be red-shifted, blue-shifted, or no shift at all. The author does not wish to wade into these debates (the controversy of IPD is more than enough), but will note that the majority of the recent

experimental measurements of PPS suggest that lines are red-shifted [142, 146–153]. The red-shift increases with plasma density, and depends on the orbital quantum numbers (n, l, m) involved in the transitions with higher principal quantum numbers n experiencing a larger PPS [142]. As a result, PPS slightly increases the binding energy (i.e. more negative) of outer orbitals relative to inner orbitals. In other words, the IPD should appear smaller for higher n states. PPS shifts the binding energies relative to the ionization threshold, and so it can be considered part of the IPD. PPS is typically ignored in IPD models (it is a reasonably small correction) although there attempts to include it in some newer analytical IPD models [118, 124]. While PPS is small, the author argues it should be accounted for in newer IPD models, as even the small shift can allow for states that would be scarcely free to remain bound. This allows for the state to be occupied by a bound electron which will have a cascading effect on the amount of IPD and other shifts in the lines due to the presence of spectator electrons; see Refs. [13, 39] and Fig. 2.3.

2.5 Experimental Measurements of IPD

Until recently, it has been difficult to directly measure continuum lowering in hot, dense plasma systems. This is because of the stringent requirements to make meaningful comments on the degree of continuum lowering:

- Well-defined plasma conditions where charge states, particle densities, and temperature are known.
- Atomic states and the continuum need to be distinguished. Due to Stark broadening of atomic states, the true bound-free edge can be obscured in a way similar to the Inglis-Teller effect [154].
- And the plasma must have an appreciable IPD that is beyond what is approximated by the Debye-Hückel model.

Attempts to measure IPD in dense plasma systems have therefore been relatively limited in the conclusions that can be drawn [155–158]. It is striking to see then that the Stewart-Pyatt model has seen widespread use to make predictions about

plasma properties and interpret spectroscopic results with little experimental evidence confirming the validity of the model, despite earlier concerns about its applicability [137, 159]. In recent years, a flurry of different experiments have been conducted that have given new insight into the nature of continuum lowering. Care is needed in the interpretation of the IPD measured from experiments. The IPD described by the EK and DH models is for quasistatic changes between two equilibrium plasma states. The IS and SP models treat IPD as the mean electrostatic energy at the ion center, with the plasma in equilibrium. However, the IPD directly inferred from spectroscopic measurements is subtly different in that photoionization is a non-equilibrium process. This point was raised by Ecker and Weizel in 1956 [160], and was reiterated by Ecker and Kröll in 1963 [110], and again by Crowley in 2014 [123]. None of the experiments examined here specifically account for this point, but given how IPD models are used to model photon absorption to make plasma and spectral predictions, a direct comparison between the IPD models and experiments is warranted.

An early experiment by Ciricosta 2012 [39] at LCLS measured the K-edge energy for the first few charge states in solid density Al plasmas containing cold ions and electrons heated up to 180 eV. With a FEL pulse duration of 80 fs, the ions remain at low temperature throughout the duration of the pulse and resulting K_α emission due to the ion temperature evolution being dominated by electron-phonon interactions, which have timescales of order several picoseconds [35–37]. This allowed for CL to be examined at precisely known densities. The time-resolved temperature, density, and ionization states of the system was determined using time-resolved CR-AK simulations using the SCFLY code [29] to model the plasma and predict spectroscopic results. The innovation here is that by using the high intensity and monochromatic properties of the LCLS XFEL pulses, it was possible to infer the IPD for individual charge states by the onset of K_α emission as the FEL photon energy was changed: in order for K_α emission to occur, a K-shell core-hole needs to be produced; as the temperatures reached are not hot enough to thermally ionize the K-shell, the only way for K_α emission to occur is by excitation of a $1s$ electron to a higher energy

orbital or photoionization by an FEL photon. The onset of K_α emission may therefore be able to identify bound atomic states and the continuum edge, if they are well separated. For charge states IV-VIII ($z = 3+$ to $7+$, with $3+$ being the lowest meaningful charge state of solid density Al), the K-edge had good agreement with the mEK model and poor overall agreement with the SP model. Further comparisons of the predicted and experimentally obtained spectral results showed the SP model could not reproduce the observed K_α spectrum, while the mEK model was better able to. Another key result from this experiment was the lack of observation of the M-shell recombining to the Al ions, which is in agreement with the predictions of the mEK model. In contrast, the SP model predicts M-shell recombination above the $7+$ charge state. This results in a slightly more subtle error in the SP model's spectral predictions: the K_α lines for charge states above $7+$ are red-shifted (lower photon energy) compared with the experimental energies. This occurs because the recombined M-shell allows for additional spectator electrons to be bound to the ions during K_α emission which lowers the relative binding energies of the L- and K-shells; this is shown diagrammatically in Fig. 2.3. The mEK model does not predict systematic red-shifting as the M-shell never rebinds. Ciricosta *et al.* do not place any physical significance on the mEK model's performance as the model is not physically well-justified, and instead they advocate for further development of IPD models.

Subsequent measurements by Ciricosta 2016 [40] extended this technique to measure the onset of K_α emission in Mg, Al, Si, and various compounds of these materials. The IPD was extracted up to the highest available ionization states, extending the range of conditions which models could be compared against. While the mEK model showed better consistency with the data, the overall IPD of the full suite of materials could not be reproduced with any single IPD model. The compounds were particularly poorly treated by IPD models. This may be viewed as a consequence of the IPD models only considering bulk plasma properties – a result of the models being derived at large distances from the charges – and failing to account for local plasma conditions around the ions. The data also suggests the mEK model

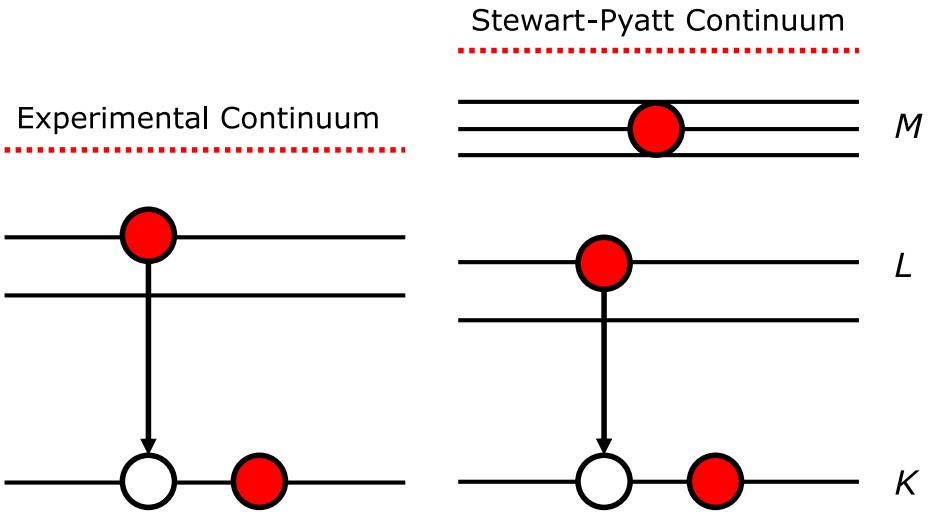


Figure 2.3: A schematic of the red-shifting of K_α emission compared with experiment due to the rebinding of the M-shell in the SP model, which allows for spectator electrons.

may underestimate the IPD at very high charge states. Importantly, the authors reported they were unable to detect any K_β emission from the highest charge states, concluding that the M-shell of the systems investigated was likely pressure-ionized due to high IPD. These results will be examined further in Chapter 4.

The IPD of high-lying charge states was, in parallel, explored in experiments [12, 143] conducted at the Orion laser facility [161], where Al plasmas were driven to much higher temperatures of 500-700 eV, and shock-compressed up to around 3 times solid density. In contrast to the LCLS experiments, K_β emission for very high charge states was observed and was used to diagnose the plasma conditions. These Ly_β and He_β lines were observed to vanish only at the highest densities achievable, a result attributed to the pressure-ionization of the $n = 3$ atomic shell. Simulations performed using FLYCHK [28] – the code SCFLY is based on – using the mEK and SP models were used to make predictions on the densities when these lines vanish. By comparing the densities at which the lines vanished with the experiment, it was clear the mEK model substantially overpredicted the IPD, while the SP model underpredicted it. This indicates that the true value of CL should lie somewhere between the two models.

Warm dense matter experiments conducted at higher densities and lower temperatures have produced complementary results to the experiments above. Measure-

ments [162] of shifts in the K_α and K_β lines in Fe impurities in Be liners at Sandia's Z machine showed poor agreement with both the mEK and SP models. The plasma temperature reached 10 eV, and the density reached 8 times solid density (electron density $n_e \simeq 2 \times 10^{24}$ cm^{-3}). In work at the OMEGA Laser Facility [5], Fletcher 2014 [163] compressed CH to around 7 times solid density and heated it to 10-20 eV temperatures. They find some agreement with the SP model, but in this regime the differences between mEK and SP models are negligible. In a similar experiment with CH capsules at the National Ignition Facility [9] using spherically convergent shocks, Kraus 2016 [164] reached higher temperatures of around 90 eV. From their fitting to XRTS data, they claim to have measured a mean ionization state of the C ions that is greater than the mEK, SP, and IS models predict. This suggests the IPD models all underpredict the experimental IPD. These results will be examined further in Chapter 5.

More recently, measurements by Kritcher 2020 [4] of the equation of state along the principal shock Hugoniot of a hydrocarbon (C_9H_{10}) showed an increase in the compressibility due to the partial ionization of the C core orbitals. Theoretical models that include electronic shell structure were better able to reproduce the measured EOS than those that lacked detailed structure, like the simple IPD models. An experiment by Hu 2022 [18] reported results from OMEGA where Cu-doped CH capsules were compressed and heated, with densities and temperatures reaching ∼2-10 times solid density and ∼10-50 eV in the in-flight stage, then reaching ∼10-25 times solid density and ∼200-500 eV in the stagnation stage. The time-integrated K_α emission of the Cu was compared against the mEK and SP models in different spectral models, and against the VERITAS code which uses a DFT-based model to predict a band structure on which the spectral results are formed. The mEK and SP models were not able to reproduce the K_α emission, whereas VERITAS performed well. These results highlight the importance of detailed electronic structure in quantifying the continuum lowering effect.

This is by no means an exhaustive list of experiments on which conclusions about continuum lowering and IPD can be drawn. As continuum lowering is intrinsic to

dense plasma systems, there are a huge number of experiments where results can give insights into the nature of IPD. However, this selection of experiments, which covers a wide range of different warm- and hot-dense plasma conditions, provides much insight into the nature of IPD. Isochoric heating of solid density mid-Z elements such as Mg, Al and Si [30, 39], which can reach high ionization states, suggest that the SP model underpredicts the IPD. The mEK model appears to agree well with data in sub-200 eV mid-Z plasmas [30, 39], but overpredicts the IPD at higher temperatures [12, 143]. Measurements of IPD in compounds suggest neither the mEK or SP model are equipped to handle them [30]. However, in laser-compression experiments involving lower Z elements such as C, the results seem to suggest that the mEK, SP, and the IS model all underpredict the IPD [164]. Such experiments also highlight the importance of detailed modelling of electronic shell structure in being able to accurately calculate continuum lowering [4, 18]. As a whole, the traditional IPD models are not always accurate for warm- and hot-dense plasmas, and the differing ways in which they are wrong gives insight into the true complexity of continuum lowering.

2.6 Theoretical Studies of Continuum Lowering

The significant discrepancies between the predictions of simple IPD models and experimental results have spurred a renewed effort of theoretical investigations into continuum lowering. Given the appeal of simple analytical IPD models, it is no surprise there have also been attempts to create new ones. The wide array of approaches have provided much insight into the nature of IPD, and are examined below.

First Principles Calculations

First-principles studies provide a useful insight into the nature of continuum lowering as the electronic structure is calculated directly, and so any effects that would be considered to contribute to continuum lowering are included self-consistently during

the calculation of the ground state. So while they may not provide simple models at the end, they do allow for controlled, systematic studies on the influences of different plasma properties. A number of different studies have been performed, with and without molecular dynamics.

Vinko 2014 [38] performed FT-DFT calculations to investigate continuum lowering in solid density Al in ionization and temperature conditions similar to those produced in FEL experiments such as Ciricosta 2012 [39]. 32 atom supercells were used with the ions evolved from their initial fcc crystal positions using molecular dynamics at ion temperatures of 300-1000 K, matching estimated ion temperatures for relevant sub-100 fs FEL pulses. For these ion temperatures, no significant differences in the continuum lowering was observed from an fcc lattice. The frozen core method was used to freeze K- and L-shell ionization states of the Al ions so the effects of ionization and temperature could be decoupled and investigated separately. First, it is observed that when the ionization states of the three neighbouring ions around a fixed-charge test ion are varied, the electronic DOS of the test ion changes considerably, indicating that the local charge state distribution is of importance to the continuum lowering of a particular ion. Then, the charge states of the test and neighbouring ions were fixed ($1\times Al^{6+}$, $3\times Al^{7+}$) and the electronic temperature was varied from 1 eV to 100 eV. As the system was heated, broad features were observed to break off from the continuum. One of these was identified as quasi-3s orbitals on the Al^{7+} ions that were difficult to assign as bound or free. On the one hand, peaks in the electronic DOS are typically associated with bound states; on the other hand, bound states are expected to be spatially localized, but energy broadening due to the Pauli exclusion principle indicates states have long range knowledge of the plasma. However, the authors also note this as evidence that orbitals can rebind in Al at very high temperatures, establishing a link to the experimental results of Hoarty 2013 [143]. There is also evidence of what will be identified in this thesis as a 3p orbital, but it bears even less resemblance to an atomic state and has an extremely large 10 eV width. Finally, the authors used the energy difference between two ground state calculations – one with a K-shell core-hole and one without – to

calculate the K-edge energy, and so the IPD, for the different charge states. With the extreme broadening of the $3p$ orbital, it was considered part of the continuum; as a consequence it appears the continuum edge does not change as the temperature varies, so the calculations were performed at electron temperatures of 1 eV and the ionization was varied using the frozen core method. Pauli blocking and electron thermalization were accounted for by subtracting the chemical potential from the internal energy difference of the calculations. The results found good agreement with the experimentally-inferred IPD for the Al charge states $z = 3+$ to $7+$, and concur the mEK model provides better agreement with the experiment than the SP and IS models in this charge state range.

Ciricosta 2016 [40] also report that the predictions using the method of Vinko 2014 [38] are in excellent agreement for all ionization states of the hot solid density Mg, Al, and Si plasmas produced in the experiment. The paper reports an interesting observation that the continuum edge was approximated very well by the K-M excitation energy of neutral atom calculations with the appropriate number of L-shell holes; i.e. $\mathrm{K}^2\mathrm{L}^x\mathrm{M}^{z-x-2} \rightarrow \mathrm{K}^1\mathrm{L}^x\mathrm{M}^{z-x-1}$, with the M-shell electrons placed in the lowest available orbitals. If one identifies that the M-shell is pressure-ionized, then the these unbound "M-shell" states are the lowest available states in the continuum, hence this neutral atom approach allows for a much quicker approximation of the K-edge energy, and thus the IPD.

Hu 2017 [130] investigated continuum lowering in strongly-coupled degenerate carbon plasmas using quantum molecular dynamics (QMD), with $T_e = T_i$ =15,625 K ($\sim$ 1.3 eV) and the ion density varying between 10-150 g cm^{-3} (the density of diamond is 3.5 g cm^{-3} [165]). At the extreme densities $\rho > 100$ g cm^{-3}, the C K-shell is observed to be massively broadened to widths of $\sim$ 100 eV. Meanwhile, the Fermi energy escapes high into the continuum, resulting in increasing the spectroscopic edge with increasing density. Once Pauli blocking is accounted for [145, 166], the QMD simulations agree reasonably well with the SP model, except for densities exceeding 100 g cm^{-3} where there are noticeable discrepancies.

Collisional-Radiative Atomic Kinetics Modelling

Collisional-radiative atomic kinetics models are used to understand the evolution of plasmas in laboratory plasmas; but, solving the collisional and radiative rate equations is computationally intense. Often, a number of simplifications are made to improve the efficiency of the calculations, the primary being super-configuration accounting (SCA) of the atomic energy levels [28, 29]. That is, the energy levels used are calculated only at the level of the principal quantum number by assuming they are degenerate in angular momentum. SCA benefits from a much improved computational efficiency as the occupations and coupling strengths of fewer energy levels need to be tracked and calculated. However, the transition energies will differ from their true values. Furthermore, as the level energies are dependent on the specific electronic configuration of the ion, a calculation involving detailed configuration accounting (DCA) will find the ionization thresholds are different from their SCA equivalents.

Iglesias 2014 [167] investigated the effect of less precise level accounting. For bound-bound transitions, Iglesias employed an even finer level of accounting than DCA with detailed configuration term accounting (DTA), which includes LS-coupling. DTA and DCA were compared for different spectral predictions. First, it is observed that DCA spectra were noticeably red-shifted relative to DTA spectra, suggesting that the lower accuracy level accounting results leads to artificial spectral features. Iglesias therefore argues that the red-shifts observed when using the SP model with SCA [39] could be errors due to SCA. It is further argued that the continuum edge and bound-bound transitions can be difficult to distinguish in DTA and DCA calculations for near-edge bound states as the photo-absorption cross-section suffers from configuration broadening due to overlapping levels. For example, the M-shell was bound in Al^{6+} using the SP model, but DCA calculations of the photo-absorption cross-section found a sharp rise in absorption lying below the Al^{6+} SP continuum edge and above the experimentally-inferred edge. Iglesias argues this suggests that the M-shell could be bound, and so the experiment might be described by the SP

model. However, it is difficult to be definitive. Iglesias therefore advocates for more detailed accounting of the levels than simple SCA when drawing conclusions about spectral interpretations.

Iglesias 2013 [115] investigated the effects of fluctuations in the free electron density within the SP and EK ion sphere limits. They argue their results show that the changes in the IPD due to fluctuations can be similar in scale to differences in the IPD between the non-fluctuating mEK and SP models. They therefore advocate for the inclusion of fluctuations in IPD modelling, although note that the degree of differences will depend on the fluctuation model chosen and if ion motion is included.

Ciricosta 2016 [30] pushed back on these conclusions, stating that emission modelling using the SP model disagrees over a number of peaks. Furthermore, using the SP model the K-M transition has a distinct signature to K-shell photoionization: if the M-shell is bound as the SP model says, it was neither observed directly as K_β emission or indirectly by resonantly pumping the transition.

Crowley's Model

A new analytical IPD model was derived by Crowley [123], based on a very general plasma model. The plasma has free electron density n_f, ions z_j with ion densities n_j, and electron and ion temperatures T_e and T_i. During ionization, a new free electron is created, but n_f and and T_e remain constant. The total ion density n_i^{tot} and T_i are also unaffected. The crux of Crowley's model is to identify that, depending on the process being described, there are actually multiple different types of ionization potential depression in the plasma that are related but distinct. *Thermodynamic IPD (TIPD)*, such as the DH and EK models, is the IPD that arises in the Saha equation, Eq. (2.17). *Static continuum lowering (SCL)* is the depression that results from the average electrostatic potential at the ion due to the surrounding plasma. The IS and SP models are examples of SCL. However, ionization is not a quasi-static process. When a single photon ionizes an electron from a single ion, the ionized electron is initially still strongly-localized at the ion; it takes time for the electron to drift far enough from the ion for the rest of the plasma to respond, with the electrons

and ions then responding on different timescales. The initial ionization process is therefore adiabatic, and when the electron drifts there is an energy transfer – the relaxation energy, $\Delta\chi$ – with the surrounding plasma to maintain constant n_f and T_e by expanding the plasma's volume by $\Delta V = 1/n_f$. Therefore, when calculating the IPD, the energy $I_{j,\alpha}$ to ionize an electron from the state α on the ion j in the adiabatic process and the relaxation energy both need to be accounted for. The total energy change in the plasma is therefore:

$$\Delta E_{j,\alpha} = I_{j,\alpha} + \Delta\chi\,. \tag{2.93}$$

The energy transferred to the plasma is also:

$$\Delta E_{j,\alpha} = I^{(0)}_{j,\alpha} + \Delta U_{j,\alpha} + K\,, \tag{2.94}$$

where $-\Delta U_{j,\alpha}$ is the SCL and K is the kinetic energy of the ionized electron. Defining $I_{j,\alpha} = I^{(0)}_{j,\alpha} - \text{SIPD} + \Delta_e$, and combining the two energy equations provides the *spectroscopic IPD (SIPD)*:

$$\text{SIPD} = -\Delta U_{j,\alpha} + \Delta\chi - K + \Delta_e\,, \tag{2.95}$$

where $\text{AIPD} = -\Delta U_{j,\alpha} + \Delta\chi - K$ is the IPD associated with adiabatic ionization and, $\Delta\chi$ includes Pauli blocking. Δ_e is an offset term that ensures the SIPD corresponds to the ionization threshold energy. The SIPD applies for all adiabatic ionization events, including collisional, and hence it is the IPD that should be used in atomic kinetics modelling. Note that because the plasma is assumed to be adiabatic, this model only applies if the photon-ion interaction rate is sufficiently low (~ 1 event) within the relaxation time.

To derive the SIPD, the delightfully-named "fried egg" plasma model [168] is used. This is a plasma model where space is divided into arbitrarily-shaped non-overlapping regions containing enough free electrons to neutralize the ion (the "egg"). Contained in this region is the "ion-core" spheres that only contain a single ion (the

"yolk"). The relevant ion radii in the model are the ion-core radius $r_j \equiv r_j^0 = X_j^0 R_j$ and the ion-sphere radius $R_j = (4\pi n_f/3z_j)^{-1/3}$, where X_j^0 is defined below. The plasma screening length λ is expressed in the TF approximation:

$$\frac{1}{\lambda^2} = \frac{1}{{\lambda_i}^2} + \frac{1}{{\lambda_e}^2} = \frac{1}{{\lambda_i}^2} + \frac{n_f e^2}{\epsilon_0 k_B T_e} \frac{F'_{1/2}(\eta_e)}{F_{1/2}(\eta_e)} \,. \tag{2.96}$$

$\eta_e = \mu_e/k_B T_e$, $F_l(x)$ is the Fermi-Dirac integral Eq. (2.72), and $F'_l(x) = F_{l-1}(x)$ is its derivative. Using the ion Debye screening length for λ_i is sufficient, so $\lambda_i = R_j(\Lambda_j^0)^{-1/3}$ (see below). The SCL associated with this model is:

$$\Delta U_{j,\alpha} \approx \Delta U_j = -\frac{k_B T_i}{2z^*} \left[\left(1 + \tilde{\Lambda}_j^0 \right)^{2/3} - 1 \right] \equiv -\frac{k_B T_i}{2z^*} h(\tilde{\Lambda}_j^0) \,. \tag{2.97}$$

where in the first step it is approximated that the potential energy is independent of the specific orbital; and the various parameters are:

$$\tilde{\Lambda}_j^\nu = \xi_j^\nu \Lambda_j^\nu; \qquad \Lambda_j^\nu = \frac{z_j + \nu}{\langle z \rangle} \Lambda_0^0; \qquad \Lambda_0^0 = (3\Gamma)^{3/2}; \qquad \Gamma = \frac{z^* \langle z \rangle e^2}{4\pi\epsilon_0 R_{WS} k_B T_i};$$
$$R_{WS} = \left(\frac{3}{4\pi n_i} \right)^{1/3}; \qquad \xi_j^\nu = \alpha \left\{ 1 + \left[\alpha^2 \left(\frac{10}{9} C_j \right)^{3/2} - 1 \right] (X_j^\nu)^3 \right\};$$
$$\alpha = \frac{\lambda_i}{\lambda}; \qquad (X_j^\nu)^3 + 3\alpha(\Lambda_j^\nu)^{-1/3}(X_j^\nu)^2 + 3(\Lambda_j^\nu)^{-2/3}(X_j^\nu) - 1 = 0$$

where C_j is the force constant for the plasma's structure[2], and X_j^ν is the positive real root for the cubic polynomial, which is:

$$X_j^\nu = (\Lambda_j^\nu)^{-1/3} \left(2^{-1/3} f(\alpha, \Lambda_j^\nu) - 2^{1/3}(1-\alpha^2) f(\alpha, \Lambda_j^\nu)^{-1} - \alpha \right) ,$$
$$f(\alpha, \Lambda) = \left[\Lambda + 3\alpha - 2\alpha^3 + \left(\Lambda^2 + (6\alpha - 4\alpha^3)\Lambda + (4 - 3\alpha^3) \right)^{1/2} \right]^{1/3} .$$

There are clear similarities between Eq. (2.97) and the SP model, and the SP model is reproduced in the limit $\alpha = 1$. Next, the total electrostatic energy is expressed as:

$$U = -\frac{k_B T_i}{2z^*} \sum_{j=1}^{N_i^{tot}} z_j g(\Lambda_j^0) \,. \tag{2.98}$$

[2] $C_j = 9/10$ (IS/fluid), 0.99025 (fcc/hcp), 1.01875 (bcc), 1.09189 (sc).

Using $\Delta U_j \sim \partial U/\partial z_j$:

$$g(\tilde{\Lambda}_j^0) = \frac{1}{\tilde{\Lambda}_j^0}\left\{\frac{3}{5}\left[\left(1+\tilde{\Lambda}_j^0\right)^{5/3}-1\right]-\tilde{\Lambda}_j^0\right\}. \tag{2.99}$$

It is also approximated that the general result for $\Delta\chi$ is similar to the limit $\alpha \approx 1$, so that $\Delta\chi = \Delta\chi_i + \Delta\chi_e$, with:

$$\Delta\chi_i = \frac{k_B T_i}{4N_i^{tot}\langle Z\rangle z^*}\sum_{j=1}^{N_i^{tot}} z_j\left(h(\tilde{\Lambda}_j^0)-g(\tilde{\Lambda}_j^0)\right), \tag{2.100}$$

$$\Delta\chi_e = K - \frac{3}{2}k_B T_B, \tag{2.101}$$

$$T_B \equiv T_e\frac{F_{1/2}(\eta_e)}{F_{-1/2}(\eta_e)}. \tag{2.102}$$

In the degenerate limit, $\Delta\chi_e - K = -k_B T_F = -E_F$, so Pauli blocking is accounted for. In the non-degenerate limit, $\Delta\chi_e - K = -3/2 k_B T_e$, which is the mean kinetic energy of the free electrons, and so it is the energy required to thermalize the ionized electron. The adjustment term Δ_e therefore takes the form:

$$\Delta_e = \frac{3}{2}k_B T_B - k_B T_e w(\eta_e), \tag{2.103}$$

where $w(\eta_e)$ is a function that accounts for all degeneracy-related effects in the SIPD. This function has the properties that it is monotonic, positive definite, and has the limits:

$$w(\eta) \sim \begin{cases} \eta - 2 & \text{if } \eta \gg 2, \\ 0 & \text{if } \eta < 2. \end{cases}$$

where the Fermi surface has been taken to have an effective width of $2T_e$ and centered on μ_e. There are a number of possible choices, but they must vanish quickly enough in the non-degenerate limit. Crowley proposes:

$$w(\eta) = (\eta - 2)H(\eta - 2), \tag{2.104}$$

where $H(x)$ is the Heaviside step function, as a good-enough form for $w(\eta)$. Finally,

using a slight improvement in the approximation of the SCL:

$$\text{SCL} = U_{z+1} - U_z \approx \left(\frac{\partial U}{\partial z_j}\right)_{n_f}\Bigg|_{z_j=z+1/2} = \Delta U_{z+1/2} \tag{2.105}$$

the SIPD is given by the equation:

$$\text{SIPD} = \frac{k_B T_i}{2z^*}\left[h(\tilde{\Lambda}_j^{1/2}) + \frac{1}{2N_i^{tot}\left\langle z\right\rangle}\sum_{j=1}^{N_i^{tot}} z_j\left\{h(\tilde{\Lambda}_j^0) - g(\tilde{\Lambda}_j^0)\right\}\right] - k_B T_e w(\eta_e)\,. \tag{2.106}$$

The SIPD depends on the charge state distribution of the plasma. If this is not know exactly, Crowely suggests the following provides a good approximation of the SIPD:

$$\text{IPD}_{\text{Spec}} = k_B T_i\left[\frac{1}{2z^*}h(\tilde{\Lambda}_j^{1/2}) + \frac{1}{4\left\langle z\right\rangle}\left\{h(\tilde{\Lambda}_0^0) - g(\tilde{\Lambda}_0^0)\right\}\right] - k_B T_e w(\eta_e)\,. \tag{2.107}$$

In the weakly-coupled limit, the SIPD reduces to the DH model. If the free electron density is uniform ($\alpha = 1$), this model becomes the SP model and in the strongly-coupled limit, the SIPD reduces to the IS model.

In the conditions of the Ciricosta 2012 and Hoarty 2013 experiments, the SIPD lies between the SP and mEK models. For the Ciricosta 2012 experiment, the SIPD is closer to the mEK model as the data seems to indicate (see Chapter 4), while for the Hoarty 2013 experiment the SIPD lies closer to the SP model, in agreement with the data.

Quantum Statistical Mechanics

The thermodynamic IPD models in this chapter are constructed from classical statistical mechanics. As plasmas are fundamentally quantum systems, a natural extension is a quantum statistical mechanical (QSM) treatments of plasmas. In Refs. [126, 127], it is shown the IPD can be evaluated from the single-particle self-energies $\Sigma_\alpha(\epsilon, \boldsymbol{p})$ of the ions and free electrons using the Green's function technique. One can then consider a broader concept of a generalized IPD (GIPD) that depends

on the particle self-energies:

$$\mathrm{GIPD}(\epsilon, \boldsymbol{p}) = \Sigma_z(\epsilon, \boldsymbol{p}) - \left[\Sigma_{z+1}(\epsilon, \boldsymbol{p}) + \Sigma_e(\epsilon, \boldsymbol{p}) + \Sigma_{bf}(\epsilon, \boldsymbol{p})\right] , \tag{2.108}$$

where Σ_{bf} is the bound-free self-energy associated with ionization. The standard $\mathrm{IPD} = \mathrm{Re}\left[\mathrm{GIPD}(\epsilon, 0)\right]$, and broadening effects are the imaginary component. Electrons are still distinguished as bound or free in this method. The $\Sigma_\alpha(\epsilon, \boldsymbol{p})$'s are evaluated as a series expansion using Feynman diagrams [169]. In Refs. [127, 128], the self-energies are expanded to second-order terms to include Fock shifts, Pauli blocking, and correlation shifts. The QSM model finds that the self-energies can be split into "statistical contributions" which contain purely quantum effects with no classical analogue (e.g. Fock shifts, Pauli blocking), and "dynamical interaction contributions" which includes correlation. In the weakly-coupled limit, the dynamical contributions reduce to the DH model and the statistical contributions become negligible. The advantage of the model is that, in principle, the IPD can be treated to any level of accuracy by including as many Feynman diagrams as desired, which may be useful in determining what effects are necessary to accurately describe CL in a given system. In practice, including higher order terms become increasingly difficult. To produce something resembling a numerical model, a large number of assumptions, with varying degrees of acceptability, needs to be made [127]. The resulting model shows that the IPD depends on the ion-ion and electron-electron dynamic structure factors (DSF). However, the DSF will generally need to be found by molecular dynamics or Monte Carlo simulations, which are restrictively expensive for an inline IPD model, and such simulations can calculate the IPD directly.

In Ref. [127], the QSM method was used, with approximate forms of the DSF, to numerically calculated the IPD for Mg, Al, and Si for the conditions in conditions Ciricosta 2016 [40]. The QSM model generelly agreed with Ciricosta *et al.*'s interpretation of the data, but predicts an even larger IPD than the data for the highest charge states of Al.

Hartree-Fock Theory

Son 2014 investigated IPD using a two-step finite-temperature Hartree-Fock-Slater (HFS) model [122]. The HFS model is based on the Hartree-Fock model [77–79, 170], but simplified by treating the electrons as moving in a weighted-mean potential [171]. The proposed two-step calculation is to: (1) perform an average-atom calculation with a muffin-tin potential to calculate the electron configuration; then (2) use the configuration to calculate the microcanonical ensemble that is then used in the HFS calculation. Results from the two-step HFS calculation were compared against Ciricosta 2012 and Hoarty 2013. The model estimated the Al He_β and Ly_β lines vanished at density and temperature conditions that are consistent with Hoarty 2013. For the first few charge states of Al, the HFS model lies within the error bars of the IPD inferred in Ciricosta 2012, but falls out of range for $z \geq 7+$. As a whole, the IPD extracted by the two-step HFS model lies between the SP and mEK models.

Rosmej presented [124] a semi-analytical IPD study based on Hartree-Fock theory called the "atom-in-solid plasma" (ASP) model. The ASP model is based on performing Hartree-Fock calculations for a given number of $2s$ and $2p$ holes, and correcting for Pauli blocking with analytical formulae that reproduce the Fermi energy in the limit of zero temperature. The ASP model agreed well with the experimental results of Ciricosta 2016 when thermal effects are accounted for in the Pauli blocking.

Ion-Sphere Models

A very popular method for the creation of dense plasma IPD models has been to develop more complex IS models [115–121], with some of the approximations removed. The models benefit from spherical symmetry and relatively simple boundary conditions on which to solve the Schödinger or Dirac equation, depending on whether relativistic effects are important. By construction, these models are restricted to cases where the ion spheres do not overlap and so presume the ions are frozen in a

crystal structure. For the evaluation of the IPD in plasmas created in femtosecond FEL experiments, this is sufficient. Many of the models are based on either treating the bound and free electron densities within the ion sphere more exactly, using more complex screening potentials, or both.

Li 2019 [117] treated the bound electron density using a multi-configuration Dirac-Fock (MCDF) approach, and then re-parameterized a new potential that tries to capture the free and bound electron distributions. The result is a class of so-called "b-potentials". The IPD from this model was approximated using the K-edge energy and assuming a point-particle-like electron:

$$\mathrm{IPD}_{\mathrm{b-pot}} = \frac{e^2}{4\pi\epsilon_0}\frac{z}{R_{\mathrm{IS}}}\left[1+\frac{1}{x-1}\right], \tag{2.109}$$

where x is:

$$x = 3 - \frac{b}{\pi}\sqrt{\frac{e^2}{4\pi\epsilon_0}\frac{z}{R_{\mathrm{IS}}k_B T_e}}\,. \tag{2.110}$$

The parameter b in x characterizes the self-consistent electron distribution inside the ion-sphere. A value of $b \approx 4$ is supposed to represent solid-density matter, while $b \approx 2$ represents a Maxwellian electron distribution. $b = 0$ is for a uniform electron distribution that recovers the IS limit. Except, it should be noted the charge state dependence is for the initial ion (z) not the final ion ($z+1$). This model is evidently not generally-applicable as there is are conditions $T_e \propto {n_f}^{1/3}(z+1)^{2/3}b$ at which the IPD will diverge to infinity. This is actually quite restrictive as the model predicts non-sensible IPD energies for plasmas accessible by FEL experiments. The IPD shift for $b = 1, 2$, and 4 with fixed $T_e = 100$ eV and $n_f = 5 \times 10^{23}$ cm^{-3} was compared against experimental K-edges from Ciricosta 2016 [40]. For $z = 3$ and 4, a value of $b = 1$ (the "b1-potential") produced the best agreement, but for $z = 5-7$ the b4-potential had better agreement. However, the available charge states and the free electron density depend on temperature as the charge state distribution changes with heating. Using the mean charge state at the temperatures quoted in Ciricosta 2016 reveals the b-potentials has poor overall performance, particularly at low temperatures and charge states, as shown in Fig. 2.4.

More recently, the b-potential model developed further to include finite-size orbital effects [118] to account for (n, l)-dependent shifts. As the MCDF structure is now explicitly considered, this IPD will be referred to as the "MCDF-b-potential". The model appears to have good agreement with experimental line shifts when $b = 4$ and the z-dependence is still for the initial charge state. The analytical form of the IPD is quite complex, however for a $1s$ orbital the IPD is:

$$\mathrm{IPS}_{\mathrm{MCDF-b}} = \frac{z}{4\pi\epsilon_0 R_{\mathrm{IS}}}\left[1 + \frac{1}{x-1} - \frac{1}{2}\frac{1}{x-1}\frac{{a_B}^{x-1}}{{R_{\mathrm{IS}}}^{x-1}}\frac{\Gamma(2+x)}{(2z_{\mathrm{eff}})^{x-1}}\right], \tag{2.111}$$

where a_B is the Bohr radius, z_{eff} is the effective nuclear charge experienced by the electron, $\Gamma(x)$ is the gamma function [98]. Again, note the charge state dependence on the initial ion and the presence of singularities.

In the same work as the ASP model, Rosmej also presented an optical electron finite-temperature ion-sphere (OEFTIS) model [124]. The model is based on an analytical potential description (including exchange) [172] in a finite-temperature ion-sphere [173]. The IPD shift seen by the optical (ionizing) electron is dependent on the effective charge z_{eff} seen by the electron, as well as being (n, l)-dependent. The set of formulae for the IPD are:

$$\mathrm{IPD}_{\mathrm{OEFTIS}} = \frac{e^2}{4\pi\epsilon_0}\frac{(z+1)}{R_{\mathrm{IS}}}\frac{F(\langle r\rangle, \langle r^2\rangle)}{F(R_0, {R_0}^2)}, \tag{2.112}$$

$$F(x,y) = \frac{{R_0}^2}{2} - \frac{y}{6} + \left(\frac{2\mathrm{Ry}(z+1)}{k_B T_e}\right)^{1/2}\left[\frac{4{R_0}^{3/2}}{3\pi^{1/2}} - \frac{8}{15\pi^{1/2}}\left(\frac{4x}{\pi^{1/2}} + \frac{y}{10}\right)\right], \tag{2.113}$$

where:

$$\langle r\rangle = \frac{1}{2z_{\mathrm{eff}}}[3n^2 - l(l+1)], \qquad \langle r^2\rangle = \frac{n^2}{2z_{\mathrm{eff}}}[5n^2 + 1 - 3l(l+1)],$$
$$z_{\mathrm{eff}} = n\sqrt{|E_0|/\mathrm{Ry}}, \qquad R_0 = R_{\mathrm{IS}}/a_B, \qquad \mathrm{Ry} = \frac{e^2}{8\pi\epsilon_0 a_B} \approx 13.606\mathrm{eV}$$

a_B is the Bohr radius, and E_0 is the ionization potential for the optical electron in an isolated Coulomb potential with effective charge z_{eff}. Rosmej estimates the

temperature and density range of validity for the model as $k_B T_e > 3E_F$ and $n_e \ll 2 \times 10^{24} z^3 \langle z \rangle / n^6$ cm^{-3}. As this model directly includes (n, l)-dependence, PPS is accounted for within the model. There is no ion temperature dependence, but the ion density does appear in R_0. As for performance, the predicted line shifts for He- and H-like Al agree well with experimental data [142, 146, 147, 152]. Additionally, there is good agreement with the observation, and lack thereof, of the He_β and Ly_β lines seen in Hoarty 2013. The model predicts lower IPD for Mg than inferred by Ciricosta *et al.* [40], so Rosmej suggests a reparameterization of R_0 to fit the data. However, based on the results presented in Chapter 4, the reparameterization seems unnecessary.

Zeng *et al.* [119, 120] developed a self-consistent IS model to investigate IPD in Fe plasmas at a wide variety of conditions. Fe plasmas are poorly described by both the mEK and SP models, with the indication being the SP model underpredicts and the mEK model over predicts it. They also compared their results with the b4-potential [117]. The results show there is no consistent scaling between the traditional IPD models, the b4-potential, or Zeng *et al.*'s model. While the b4-potential and Zeng *et al.*'s model are typically closer with each other than with the other models, there are still substantial differences in the IPD values and scaling, sometimes up to ~ 100 eV.

2.7 Summary

Continuum lowering is a fundamental, but complex, plasma process which has a significant impact on plasma properties. As a result, attempts have been made to use simple analytical models of ionization potential depression to model CL. These analytical models are compelling as they simplify the physical interpretation of continuum lowering and are easy to implement in plasma codes. In the weakly-coupled limit, when Debye-Hückel theory [20] is applicable, the IPD is described by Debye screening. In the strongly-coupled limit, the ion-sphere model [107–109] is thought to apply. Attempts to interpolate between these two limits with simple analytical

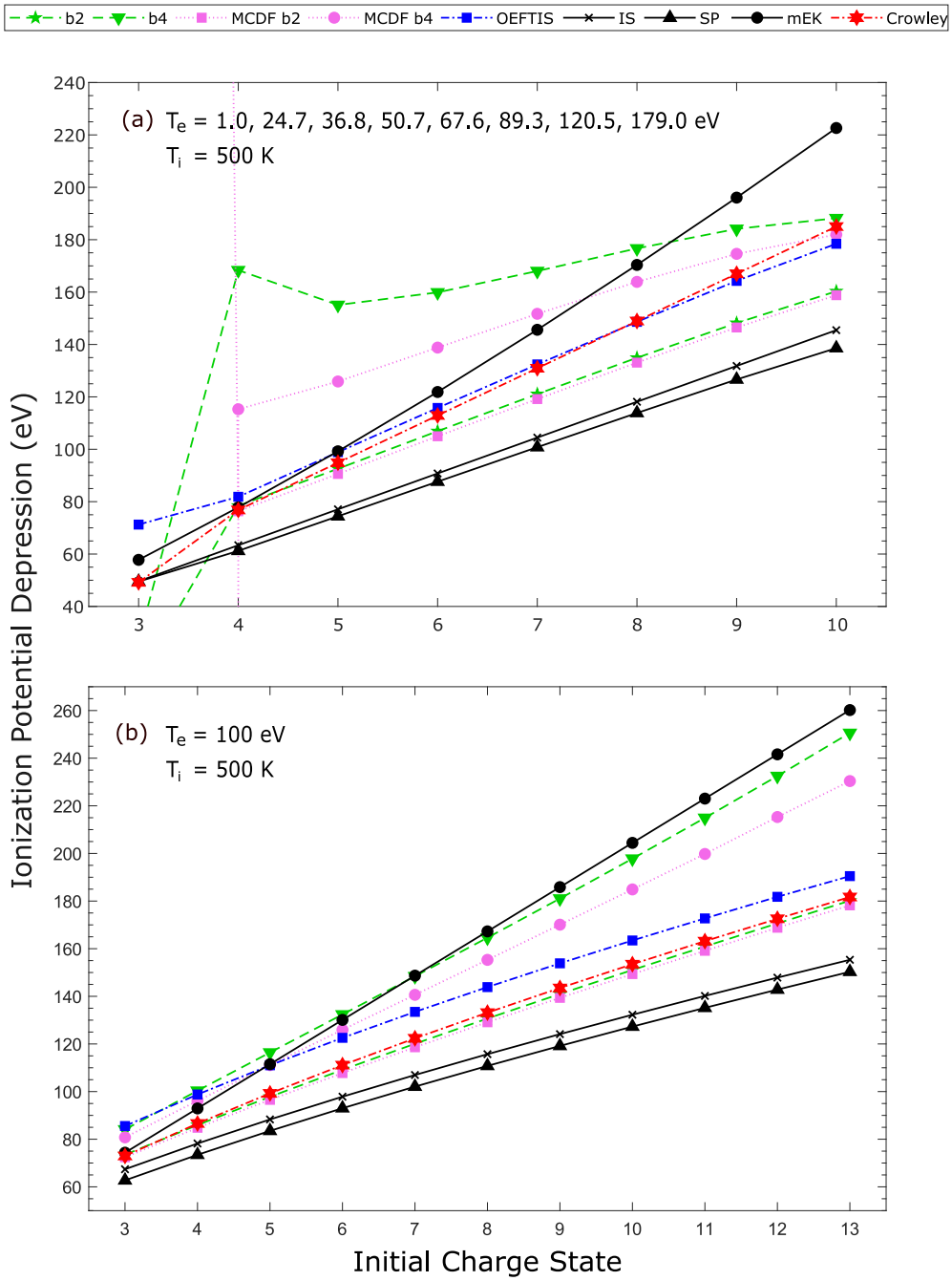


Figure 2.4: A comparison of the IPD for Al predicted by different models: b-potentials (Eq. (2.109)), MCDF-b-potentials (Eq. (2.111)), optical electron finite-temperature ion-sphere (Eq. (2.112)), ion-sphere (Eq. (2.51)), Stewart-Pyatt (Eq. (2.88)), modified Ecker-Kröll (Eq. (2.69)), and Crowley's model (Eq. (2.107)). (a) The electron temperature is varied from from 1 eV to 179 eV, and the IPD is calculated assuming the plasma only contain a single charge state equal to the mean (see Fig. 4.2). The ion temperature is fixed at 500 K. (b) The electron and ion temperature are fixed (100 eV and 500 K), and an approximate charge state distribution is used (see Fig. 2.5). The OEFTIS and MCDF models are calculated for a $1s$ electron.

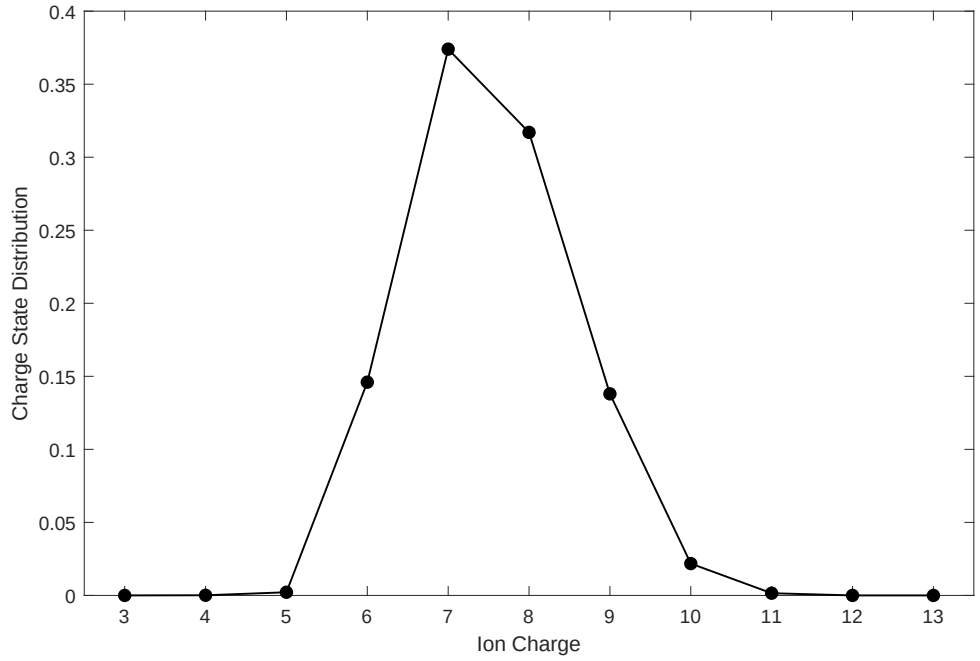


Figure 2.5: The charge state distribution used to calculate the IPD energies in Fig. 2.4 (b), calculated using the FLYCHK code for solid density Al at 100 eV, which utilises the Stewart-Pyatt model. Note that the actual distributions for each model would be different due to the differences in the IPD.

models, such as the Ecker-Kröll [110] and Stewart-Pyatt [109] have, until recently, been difficult to test against experiments. However, a growing number of experiments are showing that these simple IPD models are generally not applicable in mid-to-strongly coupled plasmas. This has spurred a number of theoretical investigations into continuum lowering, as well as attempts to create new analytical IPD models via a number of different approaches.

Fig. 2.4 plots the predictions of the potential depression in different Al plasmas for a number of these new IPD models, alongside the predictions from the mEK, SP, and IS models. Unfortunately, there is no general agreement between the models on the degree of IPD or the scaling with different bulk plasma properties. The b-potential (Eq. (2.109)) and MCDF-b (Eq. (2.111)) models show particularly unphysical behaviour in Fig. 2.4 (a) due to the fractional term. Meanwhile the OEFTIS and Crowley models disagree in the scaling of the IPD, but they both predict the IPD for mid-to-highly charged Al should lie somewhere between the SP and mEK models.

For mid-Z elements such as Mg and Al, the experiments of Ciricosta 2012, Ciricosta 2016 [40], and Hoarty 2013 [143] all suggest the SP model underpredicts the IPD. The mEK model appears to perform well at sub-200 eV temperatures, but falters for temperatures exceeding 500 eV. Some theoretical studies suggest the IPD may lie somewhere between the mEK and SP models [38, 120, 122], while others agree with Ciricosta 2016 that the IPD is better predicted by the mEK model across a wide range of ionization states [38, 125–127]. Part of the support for the mEK model has been the lack of K_β emission or pumping in Mg, Al, and Si that should be seen if the M-shell has not been pressure-ionized [30, 115, 167]. In any case, there is no good physical reason for the mEK model to be considered a good IPD model [39]. For dense degenerate plasmas, such as the C plasmas produced in Kraus 2016 [164], the mEK and SP models appear to underestimate the IPD shift, which might be explained by their semi-classical derivations lacking quantum mechanical effects [127, 128].

Other experimental evidence of transition line shifts, known as PPS [108], indicate that changes in the ionization potentials by the plasma environment are dependent on the orbital quantum numbers. There have been some attempts to incorporate such effects into new IPD models, with authors reporting consistency between their models and experimental measurements of PPS [118, 124]. First principles calculations also indicate that local plasma conditions have a dramatic impact on the electronic structure of an ion [38], which indicates that the IPD should likewise incorporate the effects of local, not just global, conditions. Likewise, fluctuations in local densities may have a significant impact on the degree of IPD [167] and whether states can partially rebind [123].

Finally, an important assumption of IPD models is that the electrons can be easily distinguished as purely bound to ions or purely free. More specifically, the bound electrons occupy atomic-like orbitals around ions, which are then often approximated as being entirely localized on the point-like ion center. The free electrons are treated as a homogeneous electron gas, with local structural effects averaged out. Such an approach has been preferable due to its conceptual and computational simplicity,

and for allowing for the construction of analytical IPD models. However, this is a great simplification of reality. It is within this context that this thesis is presented. In the remaining chapters, continuum lowering will be studied using first principles calculations. The aim is to understand how the bound-or-free assumption of IPD models falters in hot dense plasmas, and what effect this has on the predictions IPD models make.

Chapter 3: Theory of State Localization

Atomic kinetics simulations and IPD models require a clear definition of ionization, and so they use a binary picture of boundness. Electronic states are either purely bound or purely free, but this is not a complete picture of reality, especially in the hot dense plasma regime. This is particularly pertinent for IPD models that treat the bound electrons as point-particles, which implies they are extremely strongly localized in space. By averaging out the influence of the free electrons to their global mean density, their effect is as if they are a fully-delocalized homogeneous electron gas. However, the binary picture is convenient, in that it is an efficient scheme for predicting the evolution and spectral behaviour of plasmas. Recently, it has been suggested that the ionization of a system – which is a measure of how many electrons are bound to an ion – can be related to physical properties of plasmas such as conductivity [131] and pressure [174], which suggests a tangible connection between first-principles calculations and the binary picture. However, as these methods deal with bulk properties, they do not concern themselves with which states are bound or free, which is central to predicting spectra and opacity in atomic kinetics schemes.

In this chapter, I will establish a method to quantify the "boundness" of a state based on one of its physical properties: the spatial localization of the wavefunction. To demonstrate and help intuit the model, examples based on simple model functions are explained. The model is then applied to physical systems where the boundness is thought to be known to understand how it might be applied to understand IPD models and investigate localization mechanisms during routine plasma processes.

3.1 Boundness and Localization

Defining rigorously the boundness of a state is a non-trivial problem. However, the following is expected: a purely free state should be spatially-extended throughout a plasma, whereas one bound to an ion should be localized to some specific ion. The boundness of a state may therefore be associated to its spatial localization. Indeed, it will be demonstrated that, if properly constructed, the spatial localization provides a meaningful definition of boundness in a wide range of systems. Taking such an approach allows one to study localization mechanisms during a variety of processes, such as heating or compression, and provides a means to scrutinize the bound-or-free basis of IPD models.

In order to quantify the localization of a state, the state itself must first be calculated at some level of theory. Here, finite-temperature DFT [42, 52] is chosen to calculate the wavefunctions of the valence states, $\psi_i(\boldsymbol{r})$, through the Kohn-Sham (KS) equations [55]. This approach is convenient for two reasons. Firstly, DFT makes no prior assumption on the boundness of individual Kohn-Sham states, and both valence and core states are treated on equal footing. Secondly, because this method calculates the electronic structure directly, any effect that would be considered to contribute to continuum lowering in the plasma system is already included self-consistently in the calculation of the ground state wavefunction. In taking this approach, two assumptions are made. The first is that the Kohn-Sham wavefunctions are a good proxy for the electrons under investigation, and the second is that the choice for exchange-correlation (XC) functional in v_{eff} is sufficiently accurate to account for the many-body physics of the dense plasmas. The second assumption is well-founded as the XC functionals used here produce accurate results in a wide range of materials, including those examined in this work. The applicability of the KS wavefunctions warrants some consideration – after all, the KS states are not real electronic states. For atomic states, it transpires that the KS wavefunctions look nearly identical to single particle wavefunctions derived using the Hartree-Fock single-Slater determinant method for both a ground state atom and an excited state

atom [175]. Therefore, the KS states are representative of wavefunctions in the atomic limit. For free electrons, an equivalent conclusion can be drawn from the observation that the KS equations reproduce metallic band structures. There is therefore reassurance that the KS auxiliary system provides meaningful information about the localization of the real electronic states.

3.2 Localization of Bloch States

The DFT calculations in this work were performed in both single primitive unit cells of crystals and in larger disordered supercells of the chosen materials. In both cases, the electrons are treated with finite temperature, and the ions are fixed in the crystal lattice. The difference is in the latter case, the ion positions are shifted from their perfect crystal lattice positions. For clarity, unit cells are the smallest repeating cell that can be infinitely repeated to describe a system – even though supercells are used to describe a disordered system, in practice they are still infinitely repeating units of the system with a crystal symmetry that is pushed out to larger distances. Therefore, for both primitive cells and supercells, the KS states can be described by Bloch wavefunctions, $\psi_{b,\boldsymbol{k}}(\boldsymbol{r})$:

$$\psi_{b,\boldsymbol{k}}(\boldsymbol{r}) = u_{b,\boldsymbol{k}}(\boldsymbol{r})e^{i\boldsymbol{k}\cdot\boldsymbol{r}}, \tag{3.1}$$

where $\boldsymbol{r}$ is the position vector, b is the band index, $\boldsymbol{k}$ is the crystal momentum, and $u_{b,\boldsymbol{k}}(\boldsymbol{r})$ is a periodic function that has periodicity of the crystal lattice. Bloch states are spatially extended: in a unit cell an arbitrary distance from the home unit cell, they have non-zero amplitude. Instead, localization is considered for the periodic function $u_{b,\boldsymbol{k}}(\boldsymbol{r})$ in a single unit cell. Spatially localized states – such as an atomic orbital or bond – are described by a $u_{b,\boldsymbol{k}}(\boldsymbol{r})$ that is localized within a region of the unit cell. Extended states have significant overlap with functions in other unit cells. Conceptually, this is similar to Kohn's theory of localization for insulating states [176], except here it is considered on a state-by-state basis rather than for the all-electron wavefunction. A Kohn-localized wavefunction $|\psi\rangle$ that is

periodic in a lattice is one that can be decomposed into a sum of wavefunctions $|\psi_{\boldsymbol{M}}\rangle$ that are exponentially localized within disconnected regions $\boldsymbol{M}$, such as unit cells:

$$|\psi\rangle = \sum_{\boldsymbol{M}} |\psi_{\boldsymbol{M}}\rangle \,. \tag{3.2}$$

For localization, the overlap of $|\psi_{\boldsymbol{M}}\rangle$ and $|\psi_{\boldsymbol{M'}}\rangle$ is exponentially vanishing for different regions $\boldsymbol{M'} \neq \boldsymbol{M}$. Localization can therefore be considered within each unit cell rather than across the whole lattice.

Multiple schemes exist to describe the localization of Bloch states within the home unit cell. Typically, they involve measuring the size of a state either by quantifying its spread or by using a physical process, the strength of which depends on the degree of spatial localization. Two common schemes are the electron localization function (ELF) and Wannier functions.

3.2.1 Electron Localization Function

The ELF [177, 178] is a function in real space that quantifies regions in which electrons are localized by measuring Pauli repulsion in the space of the unit cell. It measures of the probability of finding an electron with spin σ in the neighbourhood of another electron with the same spin. While originally designed for interacting systems [177], it has been extended to single-particle wavefunctions, like the Kohn-Sham systems [178]. The ELF for a single-particle system is defined as:

$$\mathrm{ELF}(\mathbf{r}) = \frac{1}{1 + (\tau_{\mathrm{P}}(\mathbf{r})/\tau_{\mathrm{P,h}}(\mathbf{r}))}, \tag{3.3}$$

where $\tau_P(\boldsymbol{r})$ is the Pauli kinetic energy:

$$\tau_P(\boldsymbol{r}) = \tau(\boldsymbol{r}) - \frac{1}{8}\frac{|\nabla n(\boldsymbol{r})|^2}{n(\boldsymbol{r})}. \tag{3.4}$$

$\tau(\boldsymbol{r})$ is the kinetic energy density, and $n(\boldsymbol{r})$ is the electron density. $\tau_{P,h}$ is the Pauli kinetic energy for the homogeneous electron gas with local density $n(\boldsymbol{r})$. The ELF is advantageous as it takes values $0 \leq \mathrm{ELF} \leq 1$, which have simple interpretations.

If the ELF = 0, then the kinetic energy is large and an electron in the region of $\boldsymbol{r}$ is delocalized; if the ELF $\rightarrow 1$, then an electron is strongly localized at that point. By construction, values of ELF = 1/2 correspond to the homogeneous electron gas. The ELF has proved particularly useful for identifying bonding features. However, as the localization is determined by the total density of the system, it is not possible to calculate localization for individual states.

3.2.2 Wannier Functions

The approach of Wannier functions (WF) [179] is to use unitary transformations to convert the extended Bloch states into functions that are localized. The transformation averages individual bands and manifolds over the Brillouin zone (BZ), and the resulting functions are localized within single unit cells. A band manifold here refers to groups of connected bands that are separated from other bands and manifolds across the BZ. A basis of these functions is formed by shifting a WF from the home unit cell into another cell. The general form of a Wannier transformation is [180]:

$$|\boldsymbol{R}, n\rangle = \frac{V}{(2\pi)^3} \int_{\mathrm{BZ}} d\mathbf{k} e^{i\boldsymbol{k}\cdot\boldsymbol{R}} \sum_{m=1}^{J} U_{mn}^{(\boldsymbol{k})} |\psi_{m,\boldsymbol{k}}\rangle \,, \tag{3.5}$$

where $|\boldsymbol{R}, n\rangle$ is the Wannier function with band-like index n which has been shifted by lattice parameter $\boldsymbol{R}$ from the home unit cell, and $|\psi_{m,\boldsymbol{k}}\rangle$ are the Bloch states. The matrix $U_{mn}^{(\boldsymbol{k})}$ is a unitary transformation that is periodic in the BZ which mixes the bands in a manifold. Wannier functions have proved particularly popular for quantum chemistry applications, where the shapes of these localized functions can elucidate the nature of bonds, although they also have wider applications. For localization information, a parameter needs to be chosen to represent the size of the WF, such as the quadratic spread or inverse participation ratio. The localization of a WF may then be measured by its spatial extent; or, in the context of a processes, it can be understood by changes in size of the WFs, with growing WFs during a process indicating the states are delocalizing [181]. It is important to note, however, that the Wannier transformation and the resulting WFs are strongly non-unique. This

is because matrix U represents a gauge-invariance in the mixing of band manifold. While one is free to choose a particular transformation – and there is a general preference for "maximally-localized" WFs [180] – the interpretations drawn from a Wannier function, including its localization, can be very different depending on the choice of transformation, and no choice can be said to be better than another [181]. While the freedom to choose the transformation scheme may be desirable for some applications, here it is not. Instead, a localization parameter that is not dependent on a chosen gauge is preferable.

3.2.3 Inverse Participation Ratio

The approaches described above have limitations that are undesirable for studying the localization of KS states. Fortunately, an alternative approach can be found by computing inverse participation ratios (IPR) [182, 183] and the effective dimensionality of the Kohn-Sham states directly. First, though, it is important to understand how the spatial *localization* is related to the spatial *extent* of a state. Kohn's interpretation of localization says that well-localized states do not significantly cross the walls of the unit cell. This is a compelling picture. Note that this does not preclude localized wavefunctions that are spatially large in the unit cell; the only condition is that the overlap of two functions in neighbouring unit cells is exponentially vanishing. An important implication is that the spatial spread of a wavefunction does not provide a complete picture of localization. It therefore seems prudent to compare the spatial extent of wavefunctions that are extended or localized to see what information can be extracted about their localization.

To start, a measure of the spatial extent of the wavefunction is required. A simple way to do this is with the inverse participation ratio (IPR) [182, 183]. For non-interacting states such as KS states, the IPR is a measurement of extent by quantifying the portion of a space (real space, momentum space, number of atoms in a crystal, etc.) for which a wavefunction is significantly non-zero. For a wavefunction

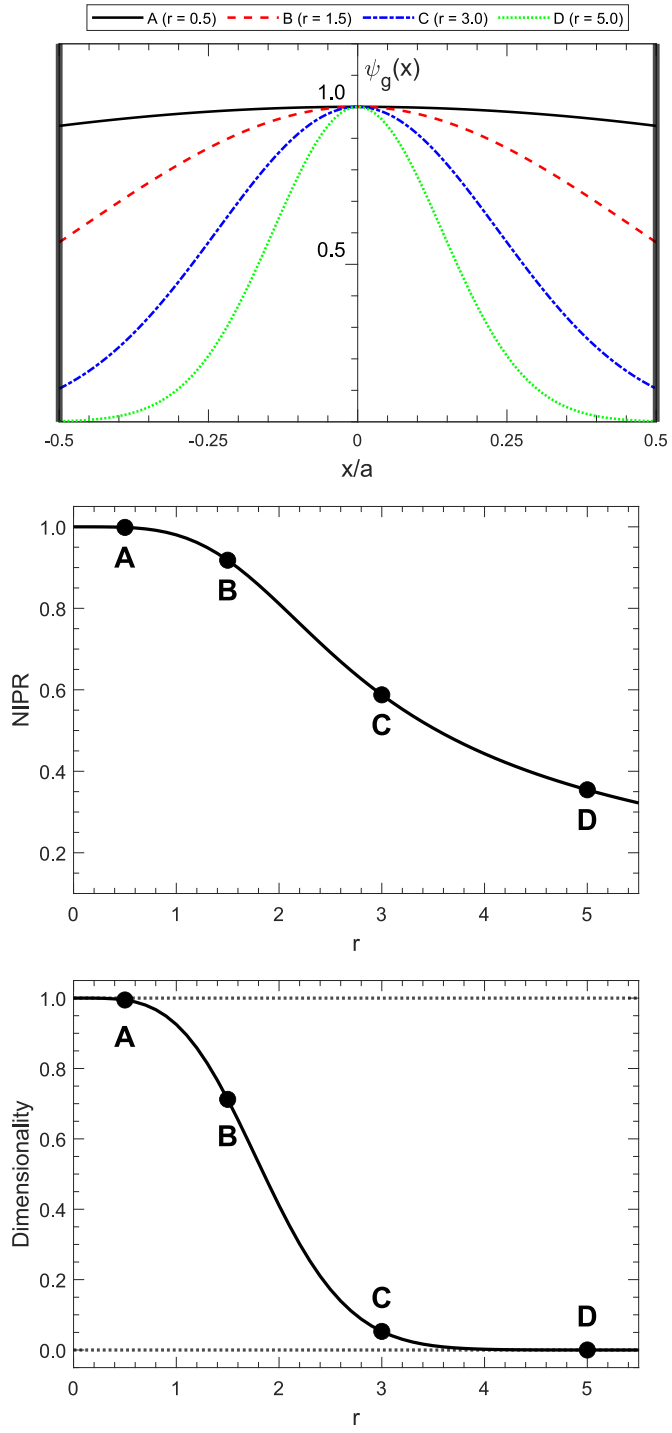


Figure 3.1: Plots of $\psi_g(x)$ (Eq. (3.9)), and its NIPR (Eq. (3.11)) and dimensionality (Eq. (3.15)) for different ratios of the lattice parameter to function size, $r = a/\sigma$. At $r = 0.5$, the wavefunction fills much of the box, significantly crossing the walls of the unit cell. The dimensionality therefore has a value equal to the number of dimensions of the system ($D = 1$). As r increases, the function is increasingly localized within the cell, corresponding to a decrease in dimensionality. At $r > 4.0$, $D = 0$ and the functions are well-localized.

$\psi_\alpha(\boldsymbol{r})$ in a unit cell of volume V, the IPR is given by:

$$\mathrm{IPR}[\psi_\alpha(\boldsymbol{r})] = \frac{\left(\int_V |\psi_\alpha(\boldsymbol{r})|^2 \, d\mathbf{r}\right)^2}{\left(\int_V |\psi_\alpha(\boldsymbol{r})|^4 \, d\mathbf{r}\right)}. \tag{3.6}$$

The IPR is a bounded quantity, taking values between $0 \leq \mathrm{IPR} \leq V$. In usual applications of the IPR, it describes the localization of a state, with the limits having simple interpretations: delocalized states, such as single plane waves ($\psi = V^{-1/2} e^{i\boldsymbol{G}\cdot\boldsymbol{r}}$), have IPR $= V$. Well-localized states, such as a delta-function, have IPR $\to 0$. In other words, localized states occupy a small volume of the cell while delocalized states fill most of it. This follows the same spatial extent interpretations of localization from the previous section. However, the size of the wavefunction does not give a complete picture of its localization. To illustrate this, consider two different model functions in an isolated one-dimensional cell with lattice parameter a.

First, consider a box function:

$$\psi_{\mathrm{box}}(x) = \begin{cases} 0 & \text{if } |x| > \gamma/2, \\ A/2 & \text{if } |x| = \gamma/2, \\ A & \text{if } |x| < \gamma/2, \end{cases} \tag{3.7}$$

where the normalization constant $A = \gamma^{-1/2}$, and γ is the width of the box ($\gamma > 0$). For $\gamma < a$, $\psi_{\mathrm{box}}(x)$ is contained entirely within the cell and it does not cross the walls. By Kohn's definition of localization, a repeating set of these functions in different unit cells would form a localized Bloch function. The IPR of this function is:

$$\mathrm{IPR}[\psi_{\mathrm{box}}(x)] = \gamma, \tag{3.8}$$

which is just the width of the box function. The function is localized and has a finite size that could occupy a large portion of the unit cell. Importantly, its IPR is independent of the lattice parameter.

Next, consider the Gaussian function:

$$\psi_g(x) = Ae^{-x^2/\sigma^2}, \tag{3.9}$$

where σ is the width of the function ($\sigma > 0$) and A is the normalization constant

$$A^{-2} = \sigma\sqrt{\frac{\pi}{2}}\,\mathrm{erf}\left(\frac{a}{\sqrt{2}\sigma}\right), \tag{3.10}$$

with $\mathrm{erf}(x)$ the error function [98]. In the limit that $\sigma \to 0$, $\psi_g(x)$ becomes a delta function, $\delta(x)$. This function is plotted in Fig. 3.1 for various ratios of $r = a/\sigma$. For this function, the IPR is:

$$\mathrm{IPR}[\psi_g(\boldsymbol{x})] = \sigma\sqrt{\pi}\frac{\mathrm{erf}(r/\sqrt{2})^2}{\mathrm{erf}(r)}. \tag{3.11}$$

The IPR is dependent on the volume of the cell, but the dependence is non-trivial, and is not a binary picture of bound or free. The normalized IPR, NIPR = IPR/a, is plotted in Fig. 3.1. There are two extremes for the IPR of this function. The first is where $r \gg 1$ (i.e. $\sigma \ll a$, a well-localized function). In this case, $\mathrm{erf}(r) \to 1$, and the IPR = $\sigma\sqrt{\pi}$. Again the IPR can take a finite value, but is independent of the size of the cell. In the case of a delta-function ($\sigma \to 0$), the IPR is zero, as expected. The other case is when $r \ll 1$. This function is completely delocalized as it significantly crosses the walls of the unit cell. A Taylor expansion of the error function gives $\mathrm{erf}(r) = \frac{2}{\sqrt{\pi}}\left(r - \mathcal{O}(r^3)\right)$, which leads to an IPR = a. The IPR of the completely delocalized state is directly proportional to the volume.

In general, well-localized states, which may be considered to be bound, have IPR values which are independent of the cell volume. Completely delocalized states have IPR $\propto V$. The localization of a state can therefore be measured from its volume dependence.

3.3 Localization from Dimensionality

To overcome the general complexity of the IPR's volume-dependence, consider instead the response of the IPR when the unit cell is expanded by a small amount. In real space, a D-dimensional unit cell is drawn by its set of D lattice vectors, which are given by primitive lattice vectors, $\boldsymbol{p}_i = \sum_{j=1}^{D} p_{i,j}\hat{\boldsymbol{x}}_j$, and the set of lattice parameters, a_i. The set of lattice vectors are $\boldsymbol{R}_i = a_i\boldsymbol{p}_i$. The lattice vectors can be expressed in a matrix $(\boldsymbol{R}_i)_j$ which can be used to determine the volume of the unit cell:

$$V = \det[(\boldsymbol{R}_i)_j] = \det[a_i p_{i,j}]. \tag{3.12}$$

Expanding the lattice parameters of the unit cell by a small amount $a_i \to a_i + \delta a_i$, the volume increases to $V' = \det[a_i(1 + \delta a_i/a_i)p_{i,j}]$. If all the lattice parameters change by the same proportion $\delta a_i/a_i = \delta a/a = \epsilon$ then the expanded volume can be expressed as:

$$\begin{aligned} V' &= \det[a_i(1+\epsilon)p_{i,j}] \\ &= (1+\epsilon)^D \det[a_i p_{i,j}] \\ &= (1+\epsilon)^D V. \end{aligned} \tag{3.13}$$

Now consider a fully delocalized state, which has IPR $\propto V$. The IPR of the delocalized state in the expanded cell is IPR$' = (1+\epsilon)^D$IPR. If $\epsilon \ll 1$, then IPR$' \approx (1 + D\epsilon)$IPR. The number of dimensions of the system, D, of the fully delocalized state is then given by:

$$D = \frac{a}{\delta a}\frac{\text{IPR}' - \text{IPR}}{\text{IPR}} = \frac{a}{\text{IPR}}\frac{d(\text{IPR})}{da}, \tag{3.14}$$

As will be shown below, Eq. (3.14) can be used to measure the localization of a state. It is termed 'dimensionality' as it gives the effective number of dimensions in which a function is delocalized. To help intuit the dimensionality, different dimensionalities and their interpretations, along with simple toy functions, are plotted in Fig. 3.2.

For the three-dimensional unit cells used here, a fully delocalized state, such as a plane wave, will recover $D = 3$, indicating it is delocalized in all directions. By comparison, a delta-function has $D = 0$, a reflection of the fact that a delta-function is a zero-dimensional object, and it does not respond to the increasing volume of the system. An exact, logarithmic definition for D is clearly also a possibility. However, the definition given in Eq. (3.14) is preferred as it also allows for a simpler interpretation: a measurement of the rate at which a state *changes size* as the unit cell expands, with the unit cell having D equal to the number of dimensions in the system. This interpretation will be conceptually clearer when the dimensionality is applied to more complex systems where $D < 0$ and $D > 3$ may occur.

The dimensionality has simple interpretations: if $D > 1$, the states are classed as delocalized, with $D = 3$ indicating complete delocalization. If D is small the states are localized, with $D = 0$ indicating perfect localization. For a three-dimensional case, $D < 1$ is typically a good indicator of localization as the function is not delocalized in any single dimension. Additionally, states with $D < 0$ may occur, indicating 'shrinking' as the unit cell expands, as well as states with $D > 3$ indicating expansions faster than the unit cell expands.

3.3.1 Dimensionality of Model Functions

Before discussing its application to real systems, it will be informative to apply the dimensionality to the model wavefunctions of Eqs. (3.7) and (3.9), in a one-dimensional unit cell of size a. For the box function, $\psi_{\text{box}}(x)$, the IPR $= \gamma$, which is the width of the box. Importantly, the IPR is independent of the volume of the cell. The dimensionality of this function is therefore $D = 0$. This reflects the fact that expanding the box does not change the IPR of the function, and so the state is localized.

The dimensionality of $\psi_g(x)$ is a smooth function that, like the IPR, depends on the relative sizes of the unit cell to the function, r:

$$D = \frac{2r}{\sqrt{\pi}} e^{-r^2} \left[\sqrt{2} e^{-r^2/2} \operatorname{erf}\left(\frac{r}{\sqrt{2}} \right)^{-1} - \operatorname{erf}(r)^{-1} \right]. \tag{3.15}$$

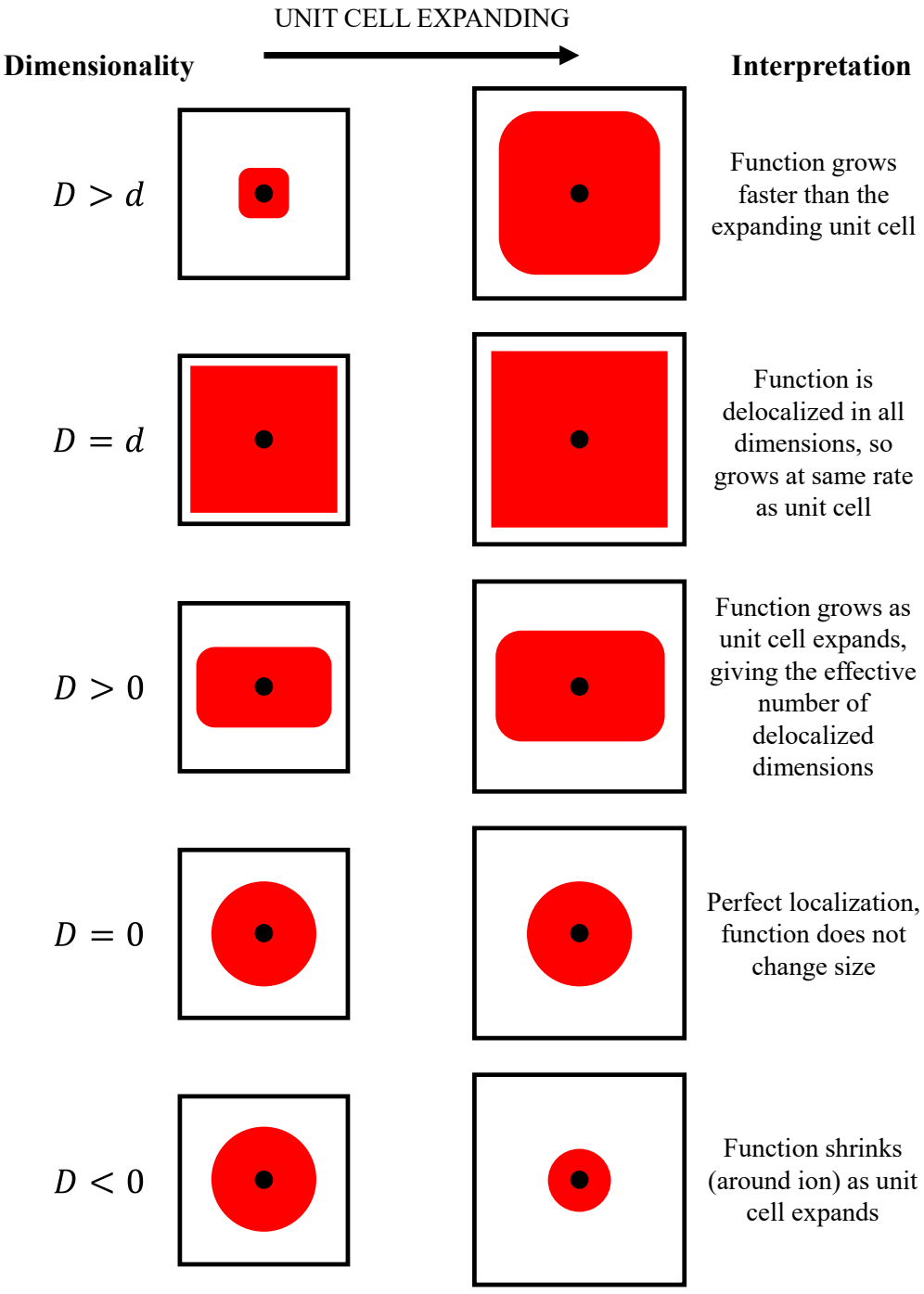


Figure 3.2: A schematic of different dimensionalities and their interpretations. The black squares outline simple unit cells ($d = 2$ here), which expand from left to right. The black circle at the center of each of the unit cells represents an ion nucleus. The red shapes represent electron wavefunctions, which change size as the unit cell expands in ways corresponding to the different dimensionalities. The dimensionality represents the effective number of dimensions in which a function is delocalized, which is measured by how much the function change in size as the unit cell expands.

Like the IPR, the dependence on r is non-trivial, but for the purpose of determining localization all that is important is single values of the dimensionality for a given a and σ. Eq. (3.15) is plotted in Fig. 3.1, along with the functions for various r for comparison. In the case of a localized $\psi_g(x)$ with $r \gg 1$, the IPR $\propto \sigma$. Again, the volume-independence of the IPR for a localized function leads to $D = 0$. But, when $r \ll 1$ and the state is delocalized, IPR $= a$. The dimensionality of this state is then $D = 1$, recovering the number of dimensions of the system for a fully delocalized state.

To show how the dimensionality reveals the number of delocalized dimensions, the dimensionality is calculated for the function $\Psi(x, y) = \psi_{\text{box}}(x)\psi_g(y)$ in a two-dimensional unit cell of size $a \times b$. The width of $\psi_{\text{box}}(x)$ is γ, and for $\psi_g(y)$ it is σ. Trivially, the x-direction will always be localized, while the localization of the y-direction will depend on σ. In this simple case where the directions are decoupled from each other, $\text{IPR}[\Psi(x, y)] = \text{IPR}[\psi_{\text{box}}(x)] \times \text{IPR}[\psi_g(y)]$. Therefore the total IPR of the function is:

$$\text{IPR}[\Psi(x, y)] = \sqrt{\pi}\gamma\sigma \frac{\text{erf}(b/\sqrt{2}\sigma)^2}{\text{erf}(b/\sigma)}. \tag{3.16}$$

The IPR only depends on the lattice parameters through $\psi_g(y)$. The dimensionality of this function is therefore the same as Eq. (3.15). In the localized limit of $\sigma \ll b$, the dimensionality is $D = 0$ as $\Psi(x, y)$ is localized in all directions. It also reflects that $\Psi(x, y)$ does not change size when the unit cell expands. In the delocalized limit of $\sigma > b$, the dimensionality is $D = 1$, indicating that the state is only delocalized in the y-direction. Equivalently, it can be said that $\Psi(x, y)$ is expanding at half the rate of the unit cell. For completeness, if the box function is replaced with a delocalized function, then $D \to 2$.

3.3.2 Effects of Function Overlap

So far, the model functions considered have been single functions in isolated unit cells, such that there is no overlap of functions between different unit cells or within unit cells. But, except for very well-localized states, there will often be overlapping

wavefunctions. The effects of function overlap, and the additional dimensionalities it allows for, are examined now.

Consider the case of two functions in an isolated cell of size a, which has a total wavefunction:

$$\Psi(x) = \psi_g(x - a/4) + \psi_g(x + a/4), \tag{3.17}$$

where $\psi_g(x)$ is the Gaussian from Eq. (3.9). This situation is equivalent to two atoms in an isolated unit cell with a single orbital. Some examples are plotted in the top figure of Fig. 3.3 for different ratios $r = a/\sigma$, where σ is the width of $\psi_g(x)$. The IPR and dimensionality have an exact solution, but the functional forms are significantly more complex than those of Eqs. (3.11) and (3.15), so they are omitted here. The NIPR and dimensionality of this function are also plotted in Fig. 3.3. Two interesting features appear in the dimensionality plot: first, the dimensionality is negative for $r \geq 4.8$, indicating a "shrinking" effect for the wavefunction. Second, the dimensionality goes above the number of dimensions in the system ($D > 1$) for $2.4 < r < 3.2$, indicating the function is expanding faster than the unit cell.

The reason for this more complex localization behaviour can be understood in the overlap behaviour of the functions. For $r = 1.0$, when D still indicates the function is delocalized, $\Psi(x)$ has a slight curvature that significantly crosses the walls of the cell, with a similar shape to that of Fig. 3.1 function A. At $r = 10.0$, when $D = 0$ and the function is well-localized, the two peaks are well-distinguished and have little overlap. When $r = 6.0$, the peaks are distinguished, but there is still a noticeable overlap between the functions. However, increasing a reduces this overlap, which results in an effective shrinking of the IPR, hence the dimensionality is negative. Such dimensionalities represent a region of states relocalizing. When $D > 1$, such as at $r = 2.8$, the function's behaviour is more complex. Initially, before $D > 1$, the function is curved much like for $r = 1.0$; as r increases so does the curvature and the dimensionality decreases. However, at about $r = 2.4$, the central part of the function flattens. This flat region grows until about $r = 3.2$, at which point the two peaks begin to separate out. The flat region of the function is

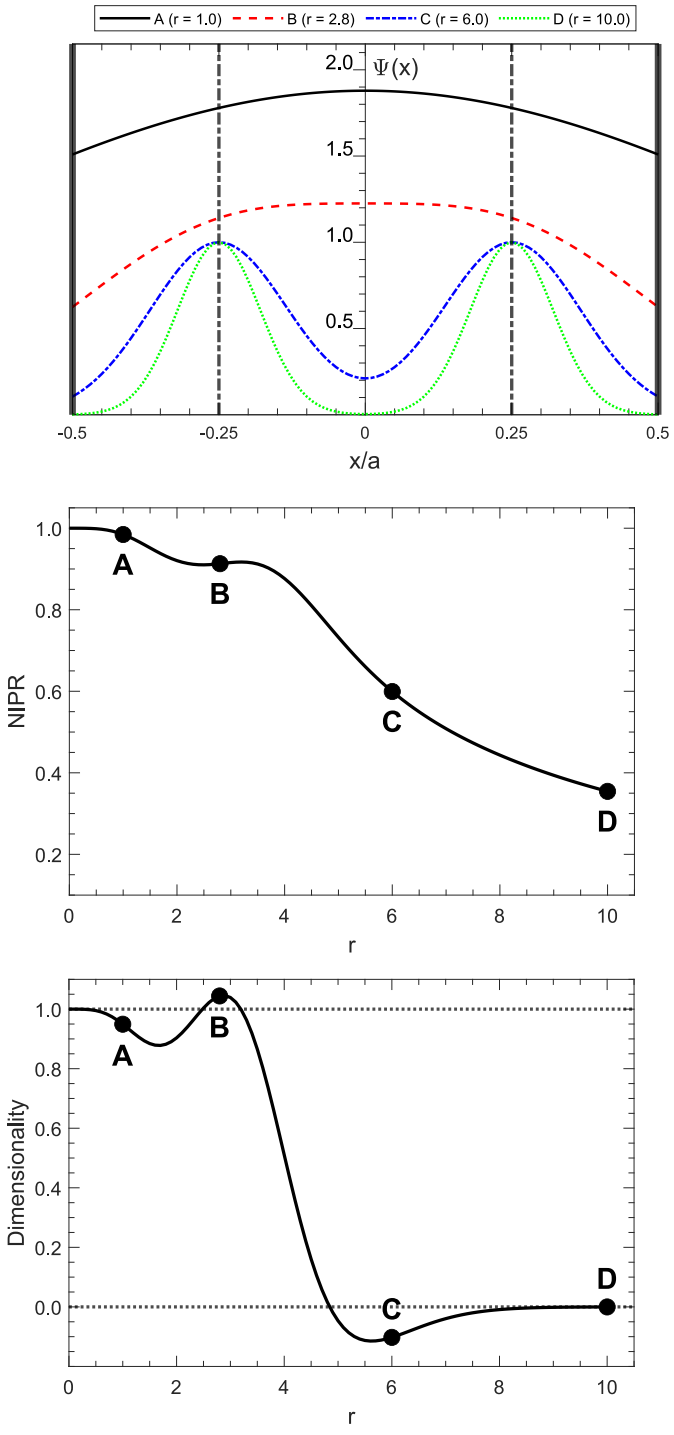


Figure 3.3: Plots of $\Psi(x)$ (Eq. (3.17)), and its NIPR and dimensionality for different ratios of the lattice parameter to function size, $r = a/\sigma$. σ is the width of $\psi_g(x)$. The centers of the two orbitals are indicated by the vertical black dashed lines. Two interesting features stand out: at $r \geq 4.8$, $D < 0$; and $D > 1$ for $2.4 < r < 3.2$, during which the NIPR briefly increases.

a delocalized region of the function. This results in the IPR growing with a causing the dimensionality to increase after $r > 2.0$. For a region $2.4 < r < 3.2$, the growth is faster than the rate of expansion of the unit cell, hence $D > 1$. Once the center of the peaks separates enough that the peaks begin to become distinguished, the IPR begins to decrease as a increases, and the function begins to relocalize.

3.4 Dimensionality in Real Systems

The behaviour of real systems is significantly more complex than the simple functions examined thus far. Not only do the wavefunctions take much more complex functional forms than the model cases, one must also contend with the fact that changing the lattice parameter also changes the solutions to the KS equations. Increasing the lattice parameter will change the potential the electrons interact with, as well as changing the density of the system. Therefore, changing the lattice parameter will affect the solutions to the KS equations and the minimisation of the Mermin grand potential [52]. However, if the expansion is sufficiently small then differences will be minimal, and the average dimensionality should predominantly capture the response to expanding the unit cell. In this work, $\delta a/a = 0.1 - 1.0\%$ was found to be sufficient to ensure this holds. Smaller values of $\delta a/a$ run into issues of computational accuracy where the two calculations produce too similar wavefunctions to see any difference.

$D > 3$ tends to occur just above the continuum edge, which typically marks boundary between localized and delocalized states. Such behaviour indicates that there are delocalized states which are sensitive to the specific conditions of the system. Such a conclusion is supported by the model functions, where certain conditions are required to be met for the overlaps to cause growth in the IPR. In testing with systems that had known localizations, $D < 0$ was seen to occur with states that were expected to be localized. This behaviour suggests the localized states are shrinking around ionic cores as the unit cell expands, and therefore have some awareness of the changing conditions as the cell expands.

When the dimensionality is calculated for the individual KS wavefunctions, there is large variation due to taking the numerical derivative of KS states and the changing conditions in the unit cell. However, the average of the dimensionality was found capture the localization information, so it is the averaged dimensionality that is considered. A few averaging schemes were considered, such as a fixed moving window and a DOS-like average. The results from both methods are the same when the window size is appropriate and the DOS is sufficiently smooth. A DOS-average is generally favourable though as it is reflective of the smearing required to create the DOS:

$$\mathrm{DOS}(\epsilon) = \sum_{\boldsymbol{k}} w_{\boldsymbol{k}} \sum_{b} \delta(\epsilon - \epsilon_{\boldsymbol{k},b}) \tag{3.18}$$

$$D(\epsilon) = \frac{\sum_{\boldsymbol{k}} w_{\boldsymbol{k}} \sum_{b} D_{\boldsymbol{k},b} \delta(\epsilon - \epsilon_{\boldsymbol{k},b})}{\sum_{\boldsymbol{k}} w_{\boldsymbol{k}} \sum_{b} \delta(\epsilon - \epsilon_{\boldsymbol{k},b})} \tag{3.19}$$

where $D(\epsilon)$ is the averaged dimensionality at an energy ϵ, $w_{\boldsymbol{k}}$ are the k-point weights, $D_{\boldsymbol{k},b}$ and $\epsilon_{\boldsymbol{k},b}$ are the dimensionality and eigenenergy of the state $(\boldsymbol{k}, b)$, and $\delta(\epsilon - \epsilon_{\boldsymbol{k},b})$ is the Dirac delta-function, which is represented using a finite-width Gaussian function as the eigenenergies cannot be sampled with an infinite number of points:

$$\delta(\epsilon - \epsilon_{\boldsymbol{k},b}) = \frac{1}{\sigma\sqrt{2\pi}} \exp\left[-\left(\frac{\epsilon - \epsilon_{\boldsymbol{k},b}}{\sigma} \right)^2 \right] \tag{3.20}$$

Testing has shown that if the DOS is not well-sampled, there will be unrealistic spikes in the dimensionality, in which case the moving window average is preferable.

As the dimensionality analysis will still be sensitive to changes in the wavefunctions that are due to changes in the crystal structure, there will be "unphysical" dimensionalities,that do not capture the localization as described above, but will spuriously affect the average. To deal with this, the dimensionality outside of some range is excluded from the averaging. In testing, it has been found that including states in the range of $D \in [-4, 7]$ works to reproduce the correct behaviour of states with known localizations, while also keeping the vast majority of states in the av-

eraging. Changing the range to, for example, $[-3, 6]$ and $[-5, 8]$, gives information on the sensitivity of the dimensionality to the particular averaging range. If the dimensionality substantially changes within the range, this typically suggests the average is not valid in describing the states.

3.4.1 Localization in Simple Metals and Ionic Compounds

To validate dimensionality as a localization parameter, it is now applied to ground state calculations of a simple metal (Mg) and an ionic compound (MgF_2). The orbitals of isolated atoms are completely localized around the core. However, this behaviour changes at higher densities when an atom can feel the presence of many other neighbouring atoms. In the case of metallic Mg, the $3s$ electrons delocalize to form the conduction band, a continuum that keeps the Mg atoms together. In MgF_2, the $3s$ electrons from the Mg ions relocalize around the F sites to fill the F L-shell. In both cases, the K- and L-shell states of the Mg and F ions are localized. In terms of the dimensionality parameter, the well-localized $2s$ and $2p$ orbitals should have $D < 1$. The simple metal will also have a delocalized continuum, with the continuum having $D = 3$ when it has the form of the free electron DOS. The dimensionality, along with the DOS, is plotted in Fig. 3.4 for the two systems.

In both cases, the L-shells have $D < 1$, indicating these states are localized, as expected. In Mg, the continuum has $D \simeq 3$, showing the dimensionality can identify both localized and delocalized states. Additional KS states can be included in the calculation without affecting the results when their occupation number is zero. The unoccupied continuum states of MgF_2 are included in Fig. 3.4; they are also delocalized. In both Mg and MgF_2, when the eigenenergy of the states is > 75 eV the dimensionality of the states is very close to a value of 3, indicating the single plane wave behaviour of the high energy KS states. The dimensionality can concisely identify the localization and delocalization of states for both a simple metal and an ionic compound.

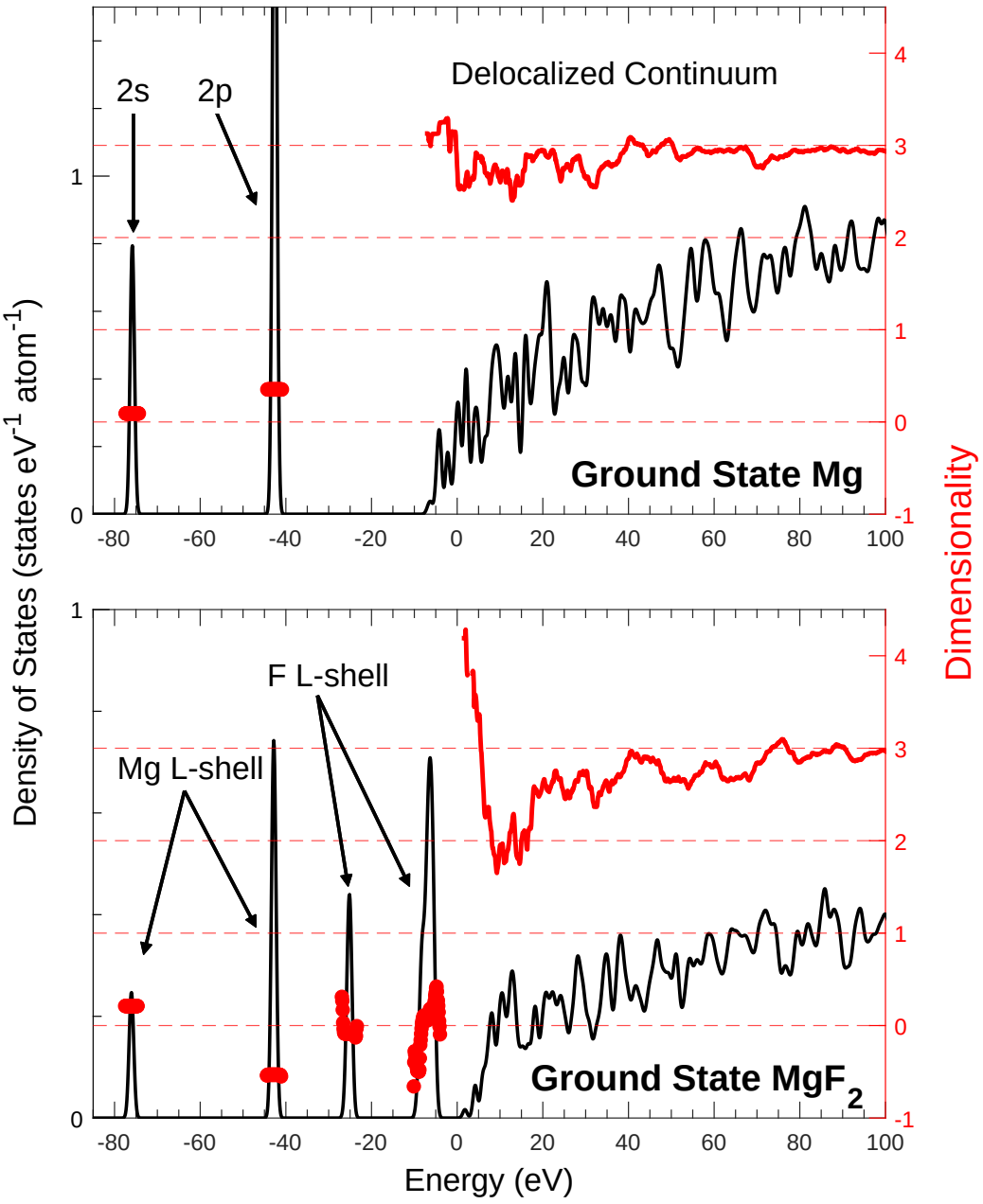


Figure 3.4: The dimensionality (red) and DOS (black) of (a) Mg and (b) MgF_2 in the ground state. The energy axis is shifted so the Fermi energy is the zero energy. The localized L-shells of the ions have $D < 1$, while the continuum has $D \gtrsim 2$ and $D = 3$ at high energies. This demonstrates the dimensionality correctly predicts localization of states in a simple metal and an ionic compound.

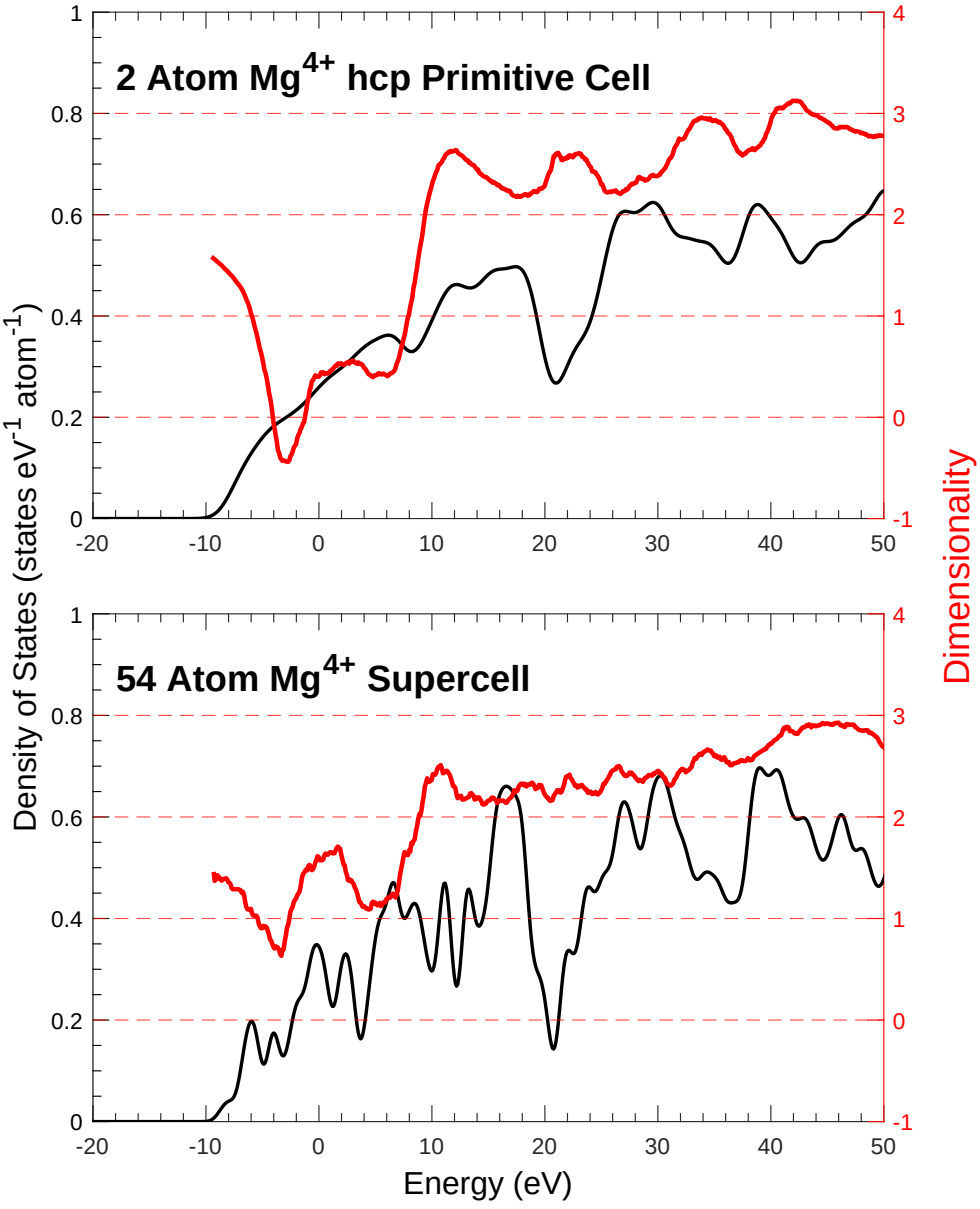


Figure 3.5: The dimensionality (red) and DOS (black) for Mg^{4+} in a 2 atom hcp primitive cell and a 54 atom supercell, comparing the effects of crystal symmetry on spatial localization. Crystal symmetry results in an apparent localization effect.

3.4.2 Crystal Symmetry Effects on Localization

The derivation of the dimensionality parameter was considered generally for any Bloch state. Therefore, the dimensionality theoretically can be applied to any type of repeating unit cell used in a calculation, including primitive unit cells and supercells. However, there is an interesting localization effect that arises when considering cells with high crystal symmetry, such as the perfect symmetry of primitive cells. In these cases, the perfect crystal symmetry can result in an enhancement in apparent localization, leading to states that appear to be localized where other metrics – such as the shape of the DOS – would otherwise suggest. For example, the top figure in Fig. 3.5 plots the dimensionality and DOS for Mg^{4+} ions in the hexagonal close-pack (hcp) primitive cell of Mg. The DOS at the bottom of the continuum shows a square-root dependence on the energy, which is typically associated with free electrons and would therefore indicate delocalization. However, the dimensionality of these states over a broad region has $D \lesssim 1$, suggesting the states are instead localized. Breaking the perfect crystal symmetry – such as by considering a supercell with the ions shifted from their perfect lattice positions – results in noticeably different localization behaviour. The bottom figure in Fig. 3.5 the dimensionality is plotted for a 54 atom supercell of Mg^{4+}. In this figure, the dimensionality and DOS is averaged over a number of different ion positions from a molecular dynamics (MD) simulation with an ion temperature of 300 K. As well as being more realistic to experimental measurements, sampling different ion positions allows for only sampling the gamma point in the BZ, which greatly reduces crystal symmetry effects on localization. The atom numbers involved are still relatively small, resulting in a DOS that is much less smooth than the primitive cell case. However, the general features of the DOS between the primitive cell and supercell calculations are the same. The localization behaviour at the bottom of the continuum has changed dramatically, tending towards delocalized states with dimensionalities $D \gtrsim 1$, as expected. There is a small dip in the dimensionality around $\epsilon = -5$ eV with $D < 1$, which may indicate the supercell used is too small to entirely remove crystal symmetry effects,

or under-sampling as evidenced by the comparatively less smooth DOS. However, as it is surrounded by delocalized states, it would suggest this region is actually still delocalized.

Supercells still have crystal symmetry as they are still repeated infinitely via the periodic boundary conditions of the simulation. However, the crystal symmetry is much weaker as it is pushed out to greater distances due to the larger lattice parameters and the random positions of the ions. One would expect then that even larger supercells would further dampen crystal symmetry effects on localization. However, as the calculations performed in this work still require a substantial number of bands, computational memory constrains the number of atoms that can be simulated.

3.4.3 Dimensionality of *d*-band Metals

d-band metals and compounds are an interesting class of materials as the *d*-band contains localized electrons, which can lead to incorrect predictions by DFT for strongly correlated systems [184, 185]. This is because the XC functionals used in DFT are typically based on the locally homogeneous electron gas, so electrons are treated at some level as if they were delocalized. Such XC functionals can therefore be too inaccurate for the strongly-localized electrons. A corrective approach may therefore be required, such as using a Hubbard-like potential (DFT+U) [184] and an additional exchange parameter (DFT+U+J) [185, 186]. As the special behaviour of strongly-correlated materials is of broad interest, the author has often been asked what the dimensionality says about the *d*-band in these materials.

Solid density Zn at different temperatures is now examined as an example of a *d*-band metal, but note that similar behaviours were seen in Fe. Calculations were performed with supercells containing 16 atoms, with the ion positions determined by evolving the ions at 300 K. The smaller atom number used here compared with the simulations above is due to the greater distances traversed by the heavier Zn ions, which provides a sufficient degree of symmetry breaking. The dimensionality and DOS from these calculations are plotted in Fig. 3.6, focusing on the region near the continuum edge. Note that in this figure – and in all figures in this thesis

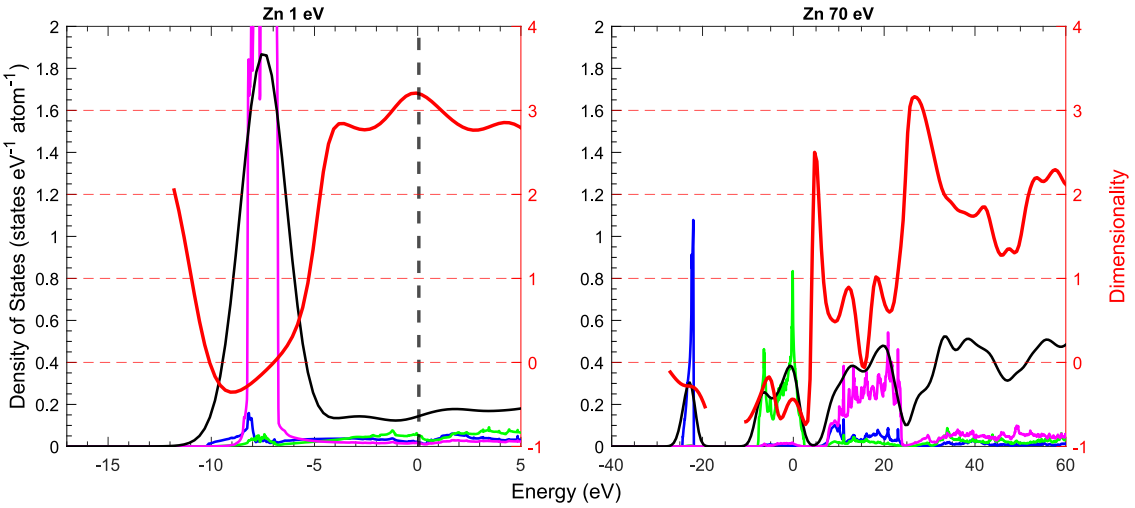


Figure 3.6: The dimensionality (red) and DOS (black) for Zn at $T_e = 1$ eV and 70 eV. The projected DOS ($l = 0$ in blue, $l = 1$ in green, and $l = 2$ in magenta) for primitive cell calculations are plotted to identify features in the DOS. The vertical dashed line indicates the chemical potential of the system – for $T_e = 70$ eV, the chemical potential is extremely negative and not visible on this scale (see Fig. 3.7).

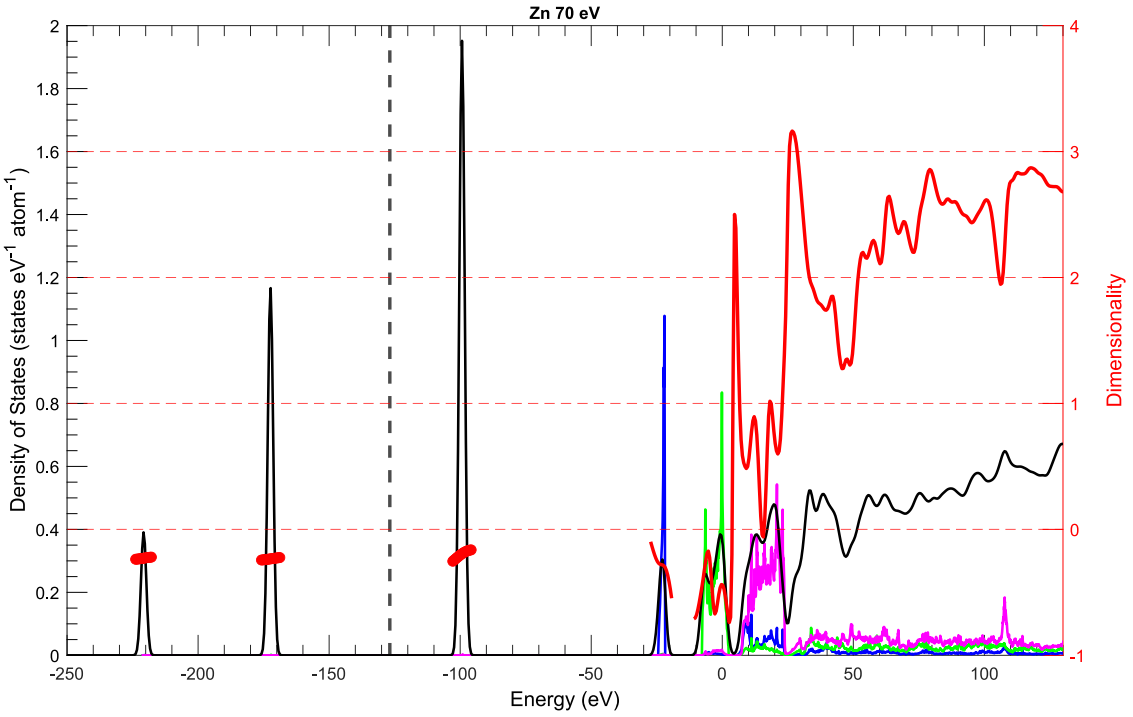


Figure 3.7: The dimensionality (red) and DOS (black) for Zn at $T_e = 70$ eV, with the energy range adjusted to show all the valence states. The projected DOS ($l = 0$ in blue, $l = 1$ in green, and $l = 2$ in magenta) for primitive cell calculations are plotted to identify features in the DOS. The PDOS of the $3s$, $3p$, and $3d$ – the three lowest energy peaks – are not visible on this scale to due to being extremely narrow features. The vertical dashed line indicates the chemical potential of the system.

that show the DOS – the energy axis has been shifted by the Fermi energy of the cold system. Also plotted are the projected DOS (PDOS), calculated via the tetrahedron method [187], for equivalent primitive cell calculations to identify the angular momentum components of features in the DOS. The large spike (called a "resonance") near bottom of the continuum of the $T_e = 1$ eV calculation corresponds to the localized $3d$-band. The dimensionality across this resonance is much lower than the fully-delocalized continuum at higher energies. The resonance reaches a value of $D = 0$ which indicates the band is strongly localized. Below the resonance, the dimensionality increases again to $D = 2$. The PDOS identifies this delocalized part of the DOS as corresponding to the $l = 0$ band. As the system is heated, states peel off from the continuum and relocalize. The $3d$ states fully relocalizes into an atomic orbital at $T_e \sim 10$ eV, and is visible as the third peak in Fig. 3.7. Returning to Fig. 3.6, at $T_e = 70$ eV the $4s$ and $4p$ orbitals are localized and peeling off from the continuum. Note that the $4p$ orbital is energetically broad, but identified as localized nonetheless. There is a localized $4d$-band at the bottom of the continuum, which is represented by states with $D < 1$. The continuum states above the d-band are not as delocalized as for $T_e = 1$ eV, which coincides with the DOS showing more structure, but at higher energies the states still have $D = 3$.

3.5 Summary

A scheme for quantifying the spatial localization of valence electronic states has been presented. While the spatial *localization* is determined from the spatial *extent*, these two quantities are distinct on the basis that spatially-large states can still have the localization properties of spatially-smaller states, which are more typically understood as localized. Localization can be quantified by the response of the spatial extent of a state to changes in the size of the unit cell. When spatial extent is quantified using IPR, the response is equal to the dimensionality of the states – the effective number of dimensions in which a state is delocalized. In this scheme, localized states of different spatial extents are identified as having the same dimen-

sionality, independent of their size. For example, in the $T_e = 70$ eV calculation of Zn shown in Fig. 3.7, it can be observed that the dimensionality of the atomic $n = 3$ orbitals, as well as the energetically-broader $4s$ and $4p$ features, all have $D \approx 0$. This is likewise true of the Mg and F $2s$ and $2p$ orbitals in Fig. 3.4. These are all localized orbitals that have very different spatial extents and shapes, yet their dimensionalities are the same. This property of the dimensionality is ideal for these purposes of comparing against IPD models in which atomic states are classed as "bound" regardless of their size. The dimensionality is be able to correctly identify the spatial localization of states with known localization in simple metals and an ionic compound. It can also identify the localized d-band electrons in Zn. The dimensionality therefore provides a useful metric for quantifying the spatial localization of states in wide range of materials, and will therefore prove useful in the remaining chapters for understanding state localization mechanisms in routine plasma processes such as isochoric heating. As states can be identified as localized or delocalized, direct comparisons with the bound-or-free approximation of IPD models is possible.

Chapter 4: Localization During Heating

With a theoretical framework established to describe the localization of valence electronic states, localization mechanisms can now be investigated in a common laboratory plasma process: isochoric heating. As outlined in Chapter 1, sub-picosecond XFEL pulses can rapidly heat the electrons in solid density matter to temperatures exceeding 100 eV [30], while the ions do not experience significant heating. Due to the short core-hole lifetimes involved, all the spectral emission occurs essentially within the duration of the XFEL pulse. As such, the density of the system is known, and the electron temperature and density evolution can be determined from simulations [13, 30]. The unique interactions of XFEL pulses with solid density matter enabled Ciricosta 2016 [40] to measure the IPD of various mid-Z materials. In order to determine the location of the bound-free edge of the different ionization states, Ciricosta 2016 used the onset of K_α emission: the peak temperatures reached were not hot enough to thermally excite electrons from the K-shells, so K_α emission can only occur if a K-shell electron is either excited to another bound state or photoionized into the continuum. As the availablility of the different charge states depends on the temeprature, the K_α spectrum contains information on the plasma conditions at the time of emission [13]. It is therefore possible to directly extract the IPD from the onset of K_α emission at the different charge states and compare to the predictions of the traditional IPD models. Conclusions on the location of the continuum edge in the Ciricosta 2016 analysis were, in part, drawn from the lack of direct observation of K_β emission. This was attributed to the pressure-ionization of the M-shell, but the possibility that the K_β emission was extremely weak could not be discounted. These observations that are now revisited. In this chapter, I

will first introduce results from an experiment at the LCLS which has successfully measured K_β emission from isochorically heated Mg. The experimental set up is similar to Ciricosta 2016, but with the spectral region now focused on the possible K_β transition energies. Extremely weak but detectable K_β line emission is observed for the highest charge states of Mg, which places new constraints on the strength of IPD. To place these results on firmer theoretical footing, a dimensionality analysis is performed using FT-DFT simulations at the experimental conditions to understand how states relocalize during isochoric heating. IPD energies are then extracted from these FT-DFT calculations and compared against the predictions of analytical models and the Ciricosta 2016 data. Finally, remaining discrepancies between this work and Ciricosta 2016 are addressed.

4.1 Experimental measurements

Isochoric heating experiments at XFELs have shown that it is possible to heat solid-density systems to temperatures approaching 200 eV on femtosecond scales [32–34], and probe their excitation thresholds using x-ray emission spectroscopy [13, 30, 188]. This method was successfully applied to the study of ionization thresholds in Al, Mg and other systems, from which the behaviour of the IPD could be studied as a function of ionic charge state [39, 40]. Interestingly, while copious amounts of K_α emission is promptly observed from both single-core-hole (one vacancy in the $1s$ orbital) and double-core-hole states (two vacancies in the $1s$ orbital), these experiments found no radiative recombination from the M-shell in excited ions in the form of K_β emission. Such emission is routinely observed in laser-plasma experiments, and is expected if the M-shell is bound and populated in low-Z simple metals like Al and Mg.

To investigate the presence of a bound M-shell, an experiment was performed at the SXR endstation of the LCLS XFEL, operating in SASE mode. Thin foil samples of Mg and MgF_2 were irradiated with intense x-rays at a range of photon energies between 1570-1670 eV. The samples used where 1 μm thick Mg foils deposited on

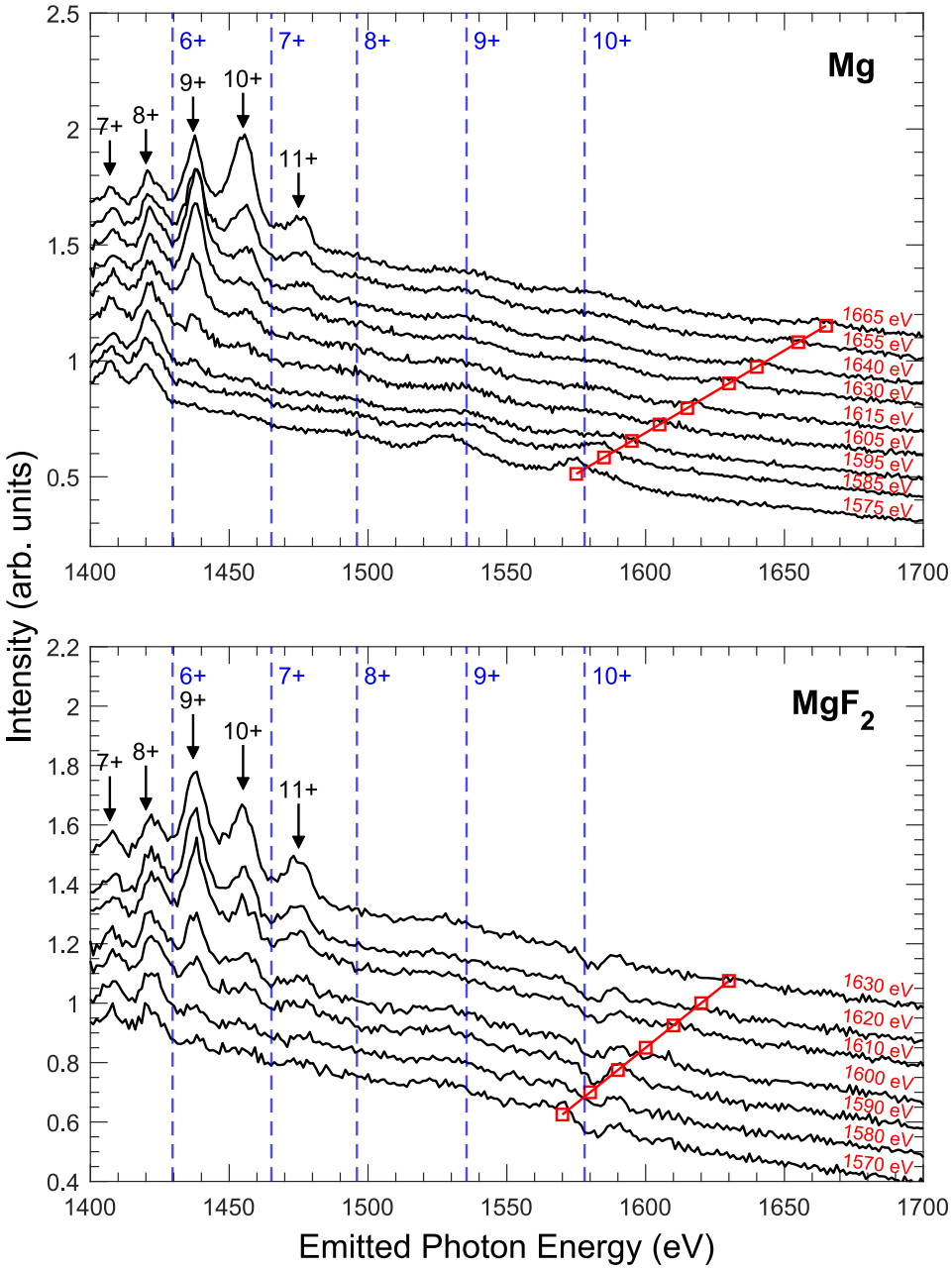


Figure 4.1: Spectra of Mg and MgF_2 for different incoming FEL photon energies. The intensity of the spectra has been normalized and displaced vertically for clarity. The incident photon energies are labelled in red above the respective spectra, and are also indicated by the red open squares. The black arrows indicate the double-K hole K_α lines. The energy of the atomic K_β transitions calculated using AAEXCITE [189–191] are indicated by the blue dashed lines. The labels refer to the charge state of the transition line. For the Mg spectra, there are broad peaks corresponding to the K_β transition lines for 8+, 9+, and 10+ Mg ions.

a 10 μm Parylene N substrate, and coated with 30 nm Si_3N_4 to prevent sample deterioration and oxidation. The MgF_2 samples were similar, but without the Si_3N_4 coating. The emission spectrum was collected using a flat Beryl $(10\bar{1}0)$ natural crystal coupled to a charge-coupled device detector, and integrated over 50 shots, providing a resolution better than 0.4 eV within a spectral window between 1400–1700 eV. Pulses of x-rays operating with a nominal duration of 60 fs, a spectral bandwidth of 0.4 % FWHM, and an energy of 1 mJ were focused on target to spot sizes on the order of 10 μm^2 by means of a Kirkpatrick-Baez mirror [192], yielding peak intensities reaching 10^{17} W cm^{-2}. The focus was optimized *in situ* so as to maximize the double-core-hole emission from the Mg sample. These parameters, and the experimental setup, are broadly similar to previous isochoric heating experiments at the LCLS, and further details can be found in Ref. [40]. As was observed in previous work, such plasmas created on femtosecond timescales rapidly reach partial local thermodynamic equilibrium, and the observed emission spectrum is a good indicator of the plasma environment, containing hot thermal electrons and cold ions still in their lattice structure [30]. It was recently reported that for mid-Z metals such as Mg, non-thermal electrons remain unimportant in determining the short-time plasma kinetics and electron dynamics unless intensities exceed 10^{17} W cm^{-2}, or for x-ray pulse durations below 10 fs [31].

The x-ray photon energies were chosen to allow resonant pumping of the Mg^{10+} K_β (He_β) transition ($1s^2 \rightarrow 1s^1 3p^1$) at the lowest energies, and to ensure the systems were driven above all single-core-hole K-edges at the highest energy. Copious amounts of Mg^{10+} K_α (He_α) emission was observed, indicating that high intensities were reached in the experimental setup, and demonstrating the successful creation of a substantial number of highly charged ions. This is consistent with previous measurements on Mg from Ciricosta 2016. However, unlike in previous work, the spectral window is focused beyond the K_α emission from double core holes that terminate with the Mg^{11+} K_α (Ly_α) peak at around 1475 eV. The measured emission from Mg and from MgF_2 is plotted in Fig. 4.1. The red line in the figures indicates the resonance condition, where the photon energy of incident x-rays equals

the emitted photon energy. On resonance, a small but noticeable quasi-elastic scattering peak is seen for the Mg sample, but not for MgF_2. The spectra are normalized and offset vertically for clarity.

At the lower emitted photon energy range, the spectra show a rich forest of double-core-hole K_α emission peaks indicated with black arrows. These correspond to spectral emission from bound-bound transitions of the group $K^0\ L^x \rightarrow K^1\ L^{x-1}$. The charge state is indicated using the number of holes in the K and L shells, but ignoring higher lying shells to simplify the notation. This means that 2+ is the lowest meaningful charge state of Mg that can be produced as the $3s$ electrons delocalize into the continuum. The 10+ transition is thus a combination of the $1s^0 2p^2 \rightarrow 1s^1 2p^1$ and $1s^0 2s^1 2p^1 \rightarrow 1s^1 2s^1 2p^0$ transitions in a Mg ion with a He-like core, together with any possible satellite lines containing spectator electrons in the M-shell. At energies above the Ly_α line, two broad peaks are observed in the Mg spectra associated with single-core-hole K_β emission ($K^1\ L^x\ M^y \rightarrow K^2\ L^x\ M^{y-1}$, $y = 1$ for no spectators) for the Mg^{9+} and Mg^{10+} charge states. In the Mg spectra for incoming photon energies of 1575-1605 eV, there is another broad peak corresponding to the Mg^{8+} K_β emission, though it appears to vanish at higher incoming photon energies. The energies of these peaks are similar to the equivalent atomic K_β transitions, calculated via the AAEXCITE code [189–191] using Hartree-Fock atomic wavefunctions, which are indicated by the blue-dashed lines. As with the double-core-hole K_α transitions, the charge state is indicated using the number of holes in the K- and L-shells in the lower state. The K_β transition lines will therefore consist of different configurations L-shell configurations – such as $1s^1 2p^1 3p^1 \rightarrow 1s^2 2p^1$ and $1s^1 2s^1 3p^1 \rightarrow 1s^2 2s^1$ for the 9+ transition – together with satellite lines containing M-shell spectator electrons. For clarity, only the lowest energy atomic K_β transitions with no spectator electrons are indicated in Fig. (4.1).

There is a dip in the spectrum for MgF_2 just above the He_β energy – this is an artefact due to the x-ray crystal used in the spectrometer. A similar feature is seen for the Mg data (not shown here) with the same crystal, but was no longer present in the data once the crystal was changed. While new spectroscopy measurements for

Mg were able to be taken, the same was not possible for MgF_2 due to experimental time constraints. This defect in the spectra makes establishing the presence of He_β emission challenging in MgF_2, and in general the presence of K_β emission is difficult to determine unambiguously for this material. However, at least three K_β emission lines can clearly be observed in Mg.

The K_β emission is seen to be extremely weak, even when compared with the intensity of the Ly_α line, and is far weaker than the K_α emission from the same sample. This may explain why previous experiments such as Ciricosta 2016 failed to observe any emission in this region, even when attempting to resonantly pump the lines with high intensity x-rays. The presence of K_β emission is important in the context of IPD because it indicates a relocalization of the M-shell has taken place, and thus allows theoretical predictions to be compared directly with experiment. For example, in the context of simple models used in time-dependent atomic kinetics modelling, the SP IPD model predicts the M-shell to be localized for most charge states, while according to the mEK model the M-shell is always pressure-ionized. While it is well-documented via the shape of the K_α emission spectrum that the SP model underestimates the IPD in x-ray driven solid-density systems [13, 30, 39], these observations of K_β emission in Mg indicate that the mEK model is no longer accurate for high charge states. This suggests a need to review the interpretation of experimental results from Ciricosta 2016, but also motivates a more detailed examination of the process of M-shell relocalization in solid-density plasmas from a theoretical standpoint.

4.2 DFT Simulations

The wavefunctions needed for the dimensionality study are obtained via finite-temperature Kohn-Sham DFT simulations using a locally-modified version of the plane wave code ABINIT v8.10.3 [56, 57, 102]. Modifications include the hybrid scheme detailed in Chapter 1, a module to calculate the IPR of the AE KS wavefunctions, and a finite-temperature local density approximation (LDA) exchange-

correlation (XC) functional [82] for testing if explicit finite-temperature effects on exchange-correlation are important.

To avoid spurious effects due to perfect symmetries in primitive cells, the systems are modelled with supercells: 32 atom ($2 \times 2 \times 2$) Al; 54 atom ($3 \times 3 \times 3$) Mg; and 48 atom ($2 \times 2 \times 2$) MgF_2. These sizes are kept relatively small to keep the calculations computationally manageable. The ions were evolved in a molecular dynamics simulation using ABINIT's isokinetic driver, with an ion temperature of 300 K in all cases, and an electron temperature $T_e = 1$ eV for Mg and Al, and $T_e = 300$ K for MgF_2; the specific electron temperatures are largely unimportant to the ion motion. The ions were allowed to evolve for a large number of time steps after reaching equilibrium to provide a selection of different ion positions. The ion positions therefore represent realistic deviations from the perfect crystal lattice that would be seen in experimental conditions. Static ground state calculations for a number of different ion positions with the desired electron temperature were then performed, and the dimensionality of the KS states averaged over the different ion positions.

For efficiency the ion cores are modelled in the PAW pseudopotential scheme [90], with the $1s$ orbital frozen in the core. The potentials were all generated for a ground-state configuration at $T = 0$ K using the *Atompaw* code [193]. For the temperatures considered in this work the thermal depopulation of the $1s$ orbital is negligible, justifying this frozen core approximation. In general, PAW potentials generated at zero temperature can be applied in finite-temperature calculations provided the frozen populations are set appropriately [175, 194].

The XC functional plays a minor role in this work as the DOS, which is the main interest, shows little dependence on the choice of XC model. For this, the GGA-PBE functional [76] is known to perform well across multiple systems, including those investigated here. Nevertheless, a comparison of the DOS and the dimensionality was performed for Mg and MgF_2 between the zero-temperature GGA-PBE and LDA-PW [75] functionals, and the finite-temperature LDA functional GDSMFB [82], at a few high temperature conditions. The GDSMFB eigenvalues were slightly shifted

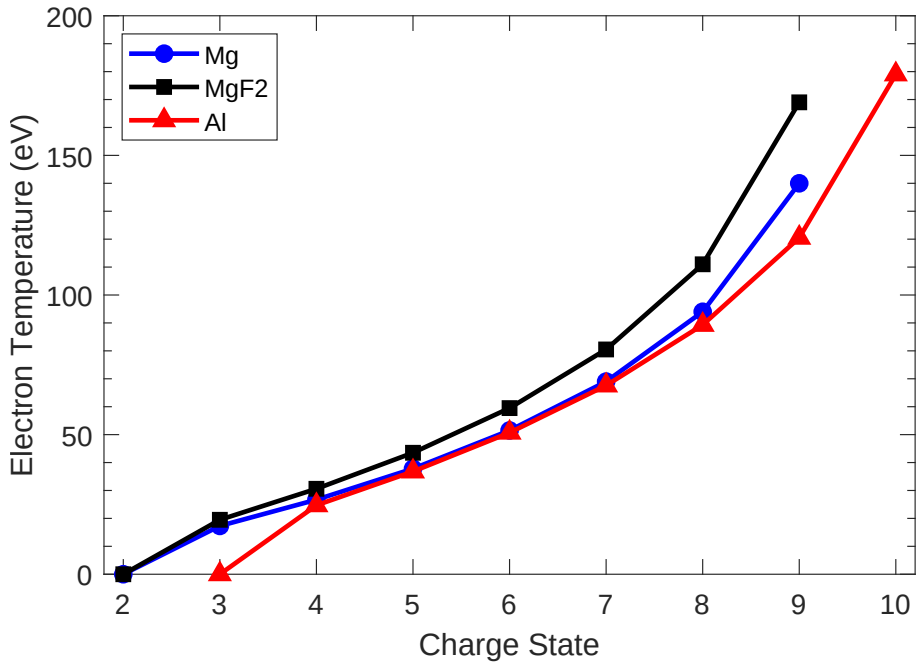


Figure 4.2: The temperatures required to produce each average charge state of the metal ion in Mg, MgF_2, and Al. Note the ionization of 2 and 3 for Mg and Al in the $T \to 0$ limit, consistent with a metallic ground state containing the full M-shell in the delocalized conduction band.

compared with results from GGA-PBE and LDA-PW, however the chemical potential was also shifted by a similar amount. The ionizations, shape of the DOS, and the dimensionalities were the same in all cases.

These calculations are performed over a range of temperatures consistent with those reached in isochoric heating experiments, as determined by time-dependent atomic kinetics simulations. This enables a simple comparison with the experimental data, while at the same time allowing us to study how the dimensionality of the valence states changes as the temperature is increased. The temperatures for the three materials were chosen to thermally ionize integer numbers of electrons from the L-shells of the metal ions. The temperatures required to produce each average charge state of the metal ion in the DFT calculations are shown in Fig. 4.2. With the KS-PWA scheme, the static supercell calculations could be performed with just 2200 bands for Al and MgF_2, and 4400 bands for Mg, which gives good convergence of the calculations, and a DOS sampled up to sufficiently high energies for this study. The energy of the highest states is also well within the regime of the hybrid

scheme [97].

As supercell calculations were performed, the DOS and dimensionality are averaged over a number of different ion positions until they are converged: 18 positions for Al and MgF_2, and 14 for Mg. While the definitions of IPR and dimensionality do not explicitly consider the ion centers, the form of a wavefunction – and so its eigenvalue for the DOS – does depend on local density conditions, and experimentally it is an average over different local conditions that are measured. Only the gamma point is sampled in the Brillouin zone (BZ) as the size of the BZ is greatly reduced by the disorder and large lattice parameters of the supercells. Furthermore, sampling just the gamma point excludes symmetry effects. A plane wave cut-off energy of 25 Ha for sampling the PAW pseudo-wavefunctions, and 50 Ha for sampling the real wavefunctions, was found to be sufficient for converging for the dimensionality parameter and the eigenvalues.

4.3 Results

As the Al, Mg and MgF_2 systems are isochorically heated by the FEL, their L-shell electrons start to thermally ionize, and are stripped from the core of the ion, reducing the overall nuclear screening. As a rule of thumb, the valence states are able to re-localize around individual ions when the strength of the ionized core overcomes the IPD. The localization of states is now studied as the temperature is increased and the L-shells of F, Mg and Al are increasingly ionized. For convenience, only integer L-shell ionizations, and thus integer charge states, will be discussed. Fig. 4.2 shows how this translates to temperature for each system. Note that as it is actually the mean ionization state that is calculated using DFT, in reality the ionization is continuous with temperature.

Fig. 4.3 shows the DOS of the supercell calculations of Mg, Al, and MgF_2 as the systems are heated. In all cases, three peaks peel off from the continuum DOS; these are the $3s$, $3p$, and $3d$ orbitals of the metal ions in the materials, as determined from the orbital projected DOS. The $3p$ and $3d$ orbitals appear to have merged together at

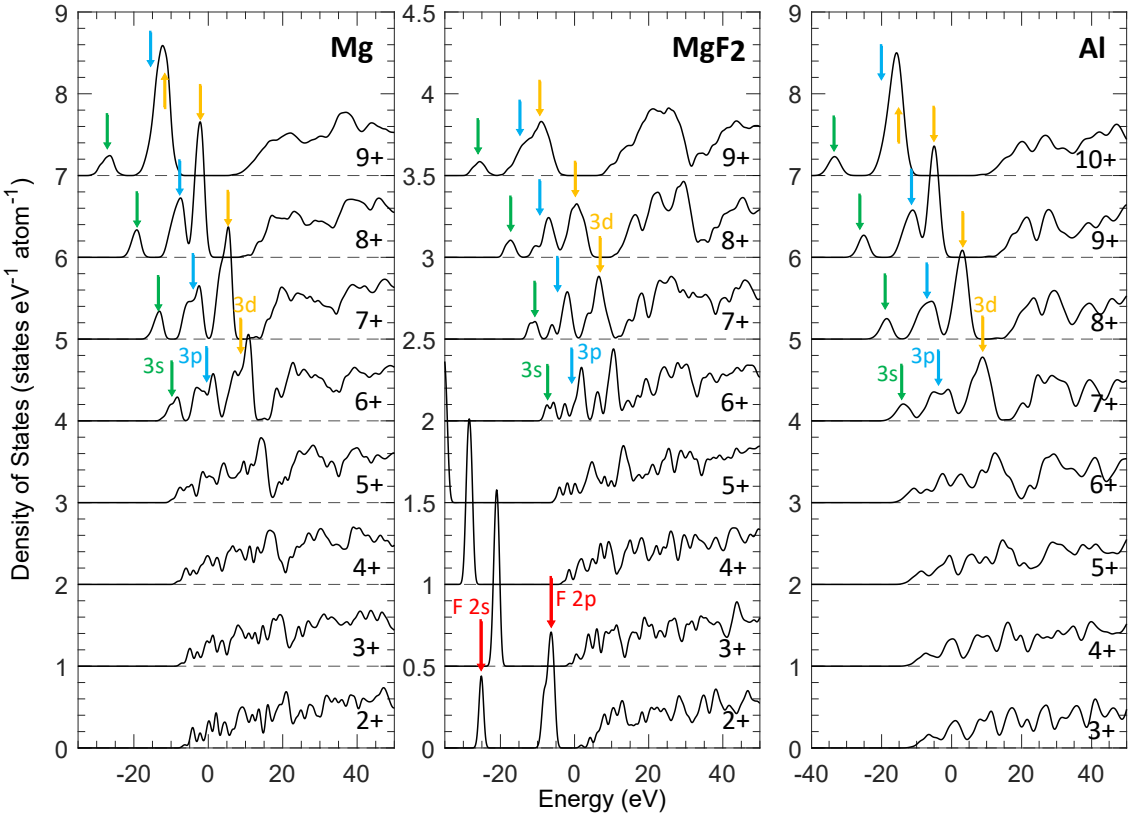


Figure 4.3: The DOS for Mg, Al and MgF_2 as the systems are isochorically heated. The DOS are displaced vertically for clarity, and the energy has been shifted by the Fermi energies of the materials. The charges indicate the charge state of the metal ions in the materials. The three arrows show the location of the $3s$ (green), $3p$ (blue), and $3d$ (orange) orbitals for the metal ions. The presence of these three peaks indicates that the $n = 3$ states have started localizing around the metal ions in each material, but does not show the localization mechanism or how well localized these orbitals are.

the highest charge states as a consequence of their eigenvalues getting close together. The order of the orbital recombination is interesting: the $3d$ orbitals recombine without the $4s$ orbital being present on the ion. It might be expected that the $4s$ orbital would recombine first given that, for an atom, it is typically filled before the $3d$ orbital. The $3d$ orbital has also been seen to recombine before the $4s$ orbital in FT-DFT calculations of Na [175]. There is therefore a consistent behaviour for the third period metals in which the $3d$ orbital recombines to the metal ions without the $4s$ orbital being present on the ions. However, this behaviour appears to be more universal, at least as far as FT-DFT is concerned, given that this same order is also observed in calculations of the transition metal Zn as seen in Fig. 3.7. An investigation into the reasons behind this behaviour is beyond the scope of the present thesis, and so the author will only postulate that the reason for this order of recombination is that it is the energetically preferred order. Nonetheless, this behaviour may be worth exploring in detail in another work.

In metallic Mg, the three peaks form at a charge state of 6+. Similarly, in Al the peaks are visible for a charge state of 7+. As Mg and Al are both metals and neighbours in the periodic table, it is not surprising they require the same number of L-shell holes for the M-shell to recombine to the metal ions. In MgF_2, the M-shell states also begin to form in the DOS when the Mg ions are at the 6+ charge state – though only the $3s$ and $3p$ orbitals are clearly forming, and the peaks that will form the $3d$ orbital remain largely merged with the rest of the continuum. The M-shell states are fully formed when the Mg ions have a 7+ charge state. In all cases, the occupation number of the M-shell orbitals is small, with around or less than one electron shared between all three orbitals on each ion. Intuitively, peaks forming in the DOS suggest that states are localized to some extent, and the dimensionality parameter allows us to examine this in more detail. In particular, it can be used to identify how the M-shell states relocalize to the Mg ions.

The dimensionality and DOS for Mg with charge states 2+ to 7+ is illustrated in Fig. 4.4. For Mg^{3+}, the dimensionality is already visibly lower in comparison with Mg^{2+}, which indicates relocalization is beginning. For Mg^{4+}, the states near

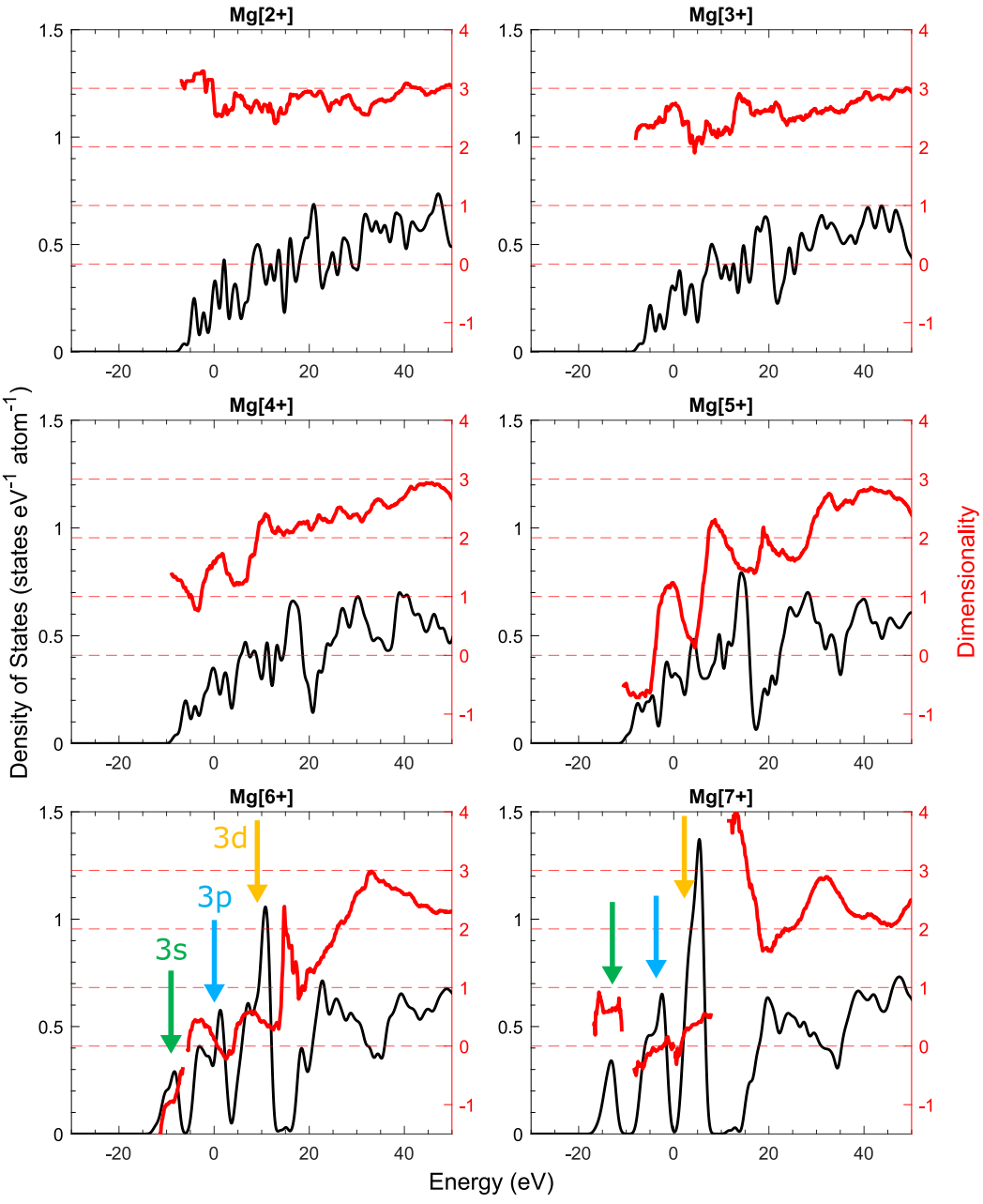


Figure 4.4: The dimensionality (red) and DOS (black) for Mg during isochoric heating. The three peaks that develop correspond to the M-shell. The dimensionality shows the state relocalization occurs while the M-shell recombines to the Mg sites.

the continuum edge are clearly in the process of relocalizing around the Mg ions, with the dimensionality of the bottom of the continuum being $D < 2$. At higher energies, the continuum still has $D = 3$. In Mg^{5+}, the bottom of the continuum at energies $\epsilon < -2.9$ eV has $D < 0$, indicating there are states that have relocalized. In an equivalent primitive cell calculation, this region corresponded to a localized quasi-3s orbital, with the majority angular momentum contribution from $l = 0$, and additional contributions from other angular momentum channels. Between ϵ = -2.9 and 5.7 eV, $D \lesssim 1$, indicating there are localized states – the primitive cell calculation reveals this to be a quasi-3p orbital. The quasi-orbitals are not distinguishable in the supercell calculations as the quasi-orbitals are broad, and their eigenvalues strongly depend on the ion positions. Therefore, due to sampling over many shifted ions, the quasi-orbitals blur together and are indistinguishable from the continuum in the DOS of the supercell calculation. In Mg^{6+}, the $n = 3$ orbitals have fully relocalized, and the three peaks have $D < 1$. In the IPD picture, the highly-ionized core has overcome the IPD and the M-shell has recombined to the Mg ions. At higher energies, there is still a delocalized continuum with $D \approx 3$.

The relocalization of the Al M-shell is plotted in Fig. 4.5. Due to an undersampling of the eigenenergies, Al^{3+} and Al^{4+} have been averaged with a broader 2 eV Gaussian to remove spurious effects. The relocalization behaviour is very similar to Mg, and requires the same number of L-shell electrons to be ionized in order for the M-shell states to relocalize. There is a sharp jump in the dimensionality at $\epsilon \approx 15$ eV in Al^{7+}, indicating a strong sensitivity of the continuum states on the lattice parameter immediately as the M-shell relocalizes.

The relocalization process in MgF_2 was also examined. The density of Mg ions in MgF_2 is lower (3.1×10^{22} cm^{-3}) than in Mg (4.3×10^{22} cm^{-3}). For IPD models, a lower ion density results in a lower IPD energy. There is an additional complexity in that initially, there are no free electrons in MgF_2 as it is an ionic compound. However, the F ions are easier to ionize than the Mg ions. So while initially there is a lower free electron density in MgF_2, as Mg and MgF_2 are thermally ionized the free electron density in MgF_2 will be higher than in Mg at high temperatures. The F

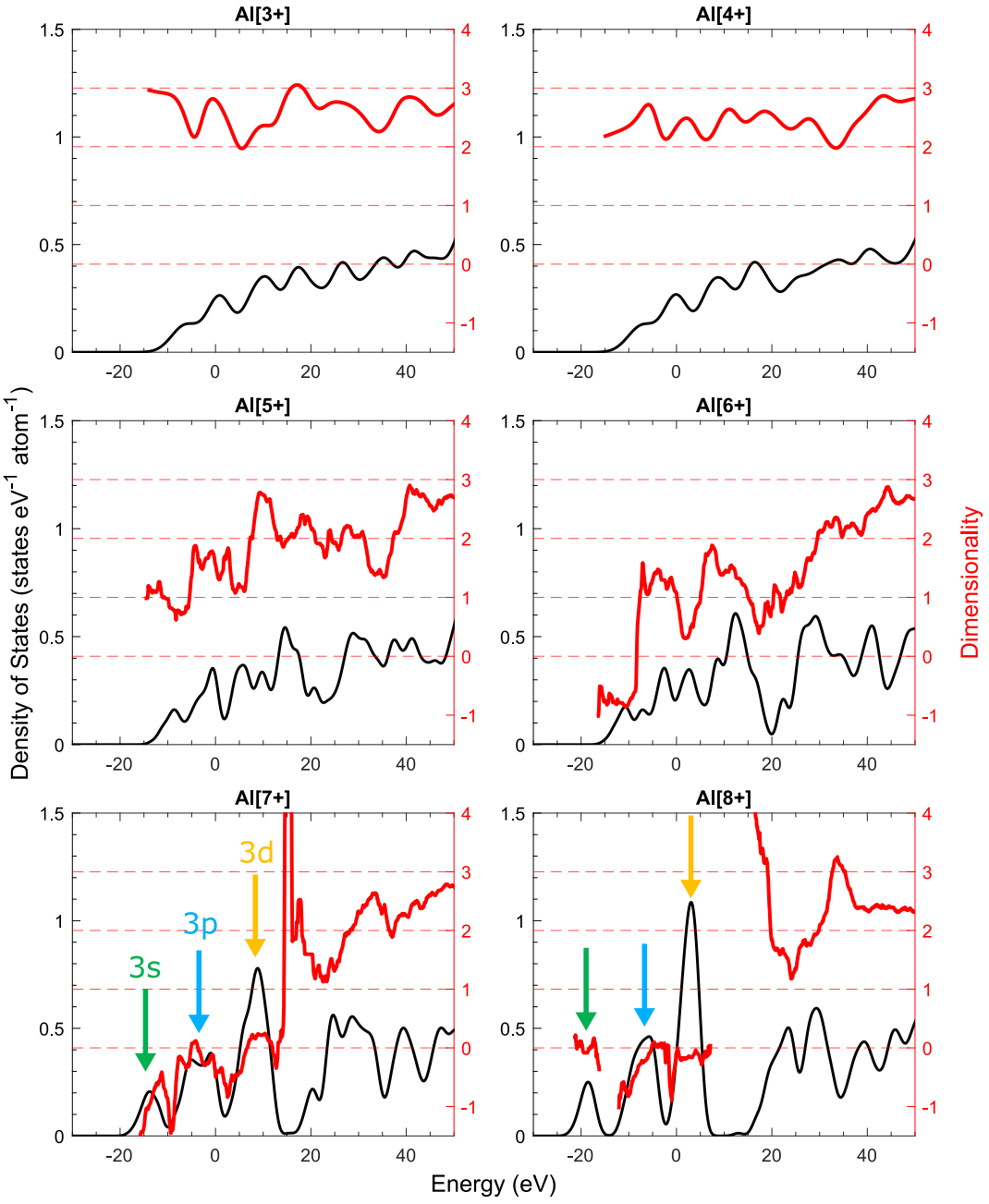


Figure 4.5: The dimensionality (red) and DOS (black) for Al during isochoric heating. The three peaks that develop correspond to the M-shell. The dimensionality shows the state relocalization occurs while the M-shell recombines to the Al sites.

ions therefore act as donors to increase the electron density. Despite the competing IPD effects from the electron and ion densities, IPD models predict that the IPD energy is greater in MgF_2 than in Mg. In general, it was found that IPD models are poor at predicting CL in compounds [40]. MgF_2 is therefore used to compare the differences in relocalization between a simple metal and an ionic compound, and the effects of additional electron density from donor ions on the relocalization process of thermal ionization. The relocalization of the Mg M-shell is plotted in Fig. 4.6. It is still a smooth process, and broad M-shell states relocalize around the Mg ions, however there are notable differences compared with Mg. First, the charge state of the Mg ions required to fully relocalize the M-shell is higher in MgF_2 than in Mg; 7+ versus 6+, respectively. Additionally, the M-shell states do not relocalize together at the same charge state. Instead, the $3s$ and $3p$ orbital have relocalized in $Mg^{6+}F_2$, but the $3d$ relocalizes at $Mg^{7+}F_2$. The difference in the relocalization behaviour of the M-shell compared with Mg is attributed to differences in the electron density around the Mg ions in the two materials. Immediately after the continuum level, there is a feature from $\epsilon = 15$ eV to 38 eV where the dimensionality is approximately constant with $1 \lesssim D < 2$. This feature is sensitive to the positions of the ions, and consists of contributions from both the Mg and F ions and many different angular momenta. Nonetheless, on average, it appears to be delocalized like the rest of the continuum. At higher energies, $D \approx 3$ as expected.

There are some similar behaviours seen in a all three materials. Firstly, the dimensionality indicates that states relocalize at the bottom of the continuum before there are any clear orbital features. Calculations using primitive cells of the materials indicates that these correspond to quasi-M-shell orbitals. However, as the widths and eigenvalues of the orbitals are strongly dependent on the structure of the system, due to the different electron densities surrounding the ions in different positions, these orbitals merge and blur together. This would indicate that despite the presence of localized states, they would be indistinguishable from the continuum. When the metal M-shell states do become distinct, they are significantly broader than the isoenergetic metal ion L-shell states. For example, the full width of the $3p$ orbital

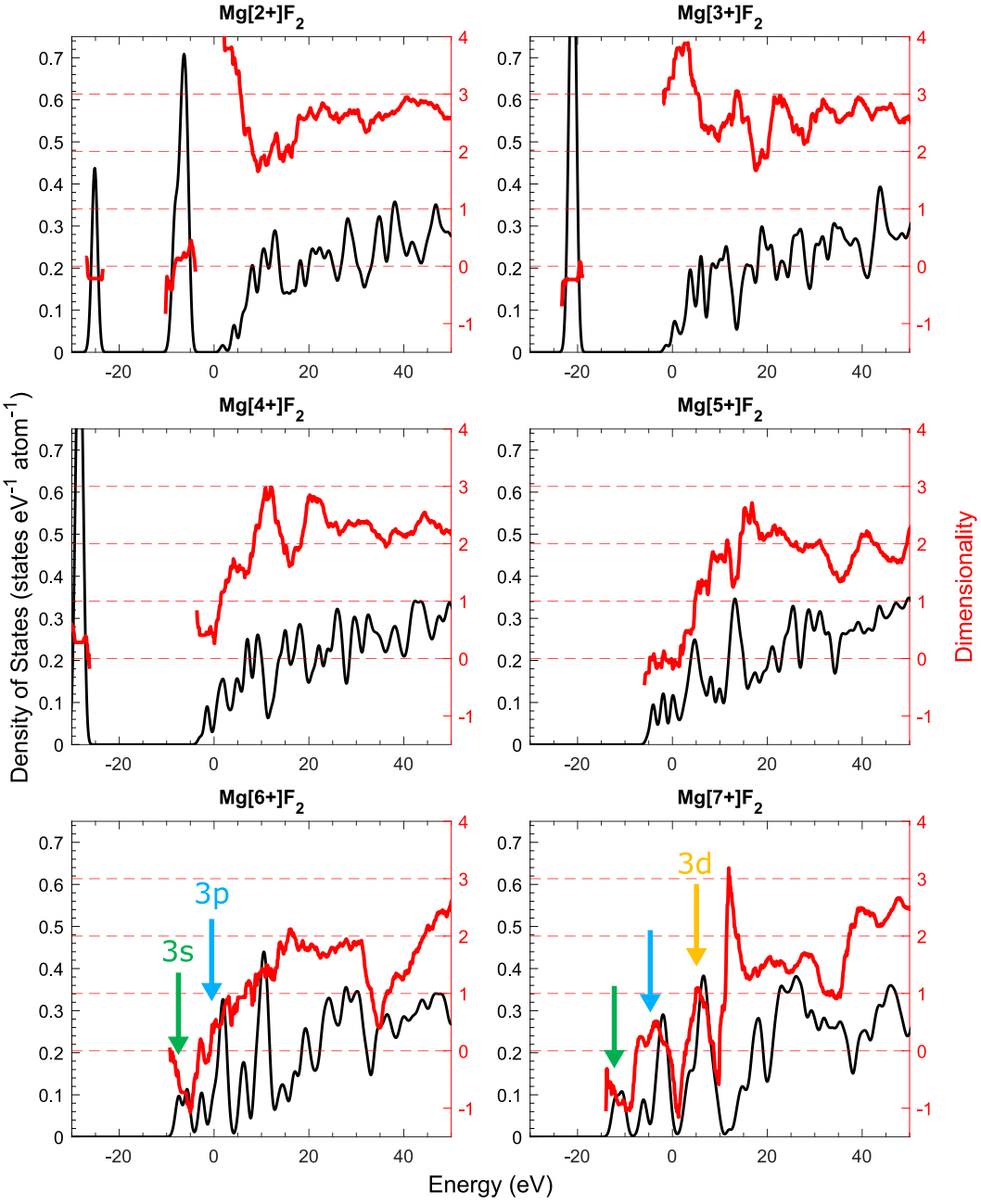


Figure 4.6: The dimensionality (red) and DOS (black) for MgF_2 during isochoric heating. The three peaks that develop correspond to the M-shell of the Mg ions. The three peaks do not relocalize at the same time. An additional broad, structurally-sensitive feature is also present just above the continuum edge for charge states $Mg^{7+}F_2$ and above.

for Mg^{6+} and Mg^{7+} is ~ 10 eV. Despite the relative broadness of the M-shell states, they are fully relocalized as they recombine to the ions. The large width of the $3p$ orbitals is in agreement with the observation of the very broad K_β transitions seen in Fig. (4.1). While the K_β transitions are broader than the $3p$ orbitals, FT-DFT only considers a mean static system, so it neglects other contributions such as configurational broadening. Numerous broad, overlapping features contribute to the overall large width of the K_β transitions.

The continuum states have $D > 1$, showing that there is still a delocalized continuum. There is a sharp increase in the dimensionality at the bottom of the continuum once the M-shell states have relocalized. A similar feature is seen in MgF_2 in Fig. 3.4, where states immediately above the Fermi level (the zero energy in the plot) also show large dimensionalities ($D \approx 4$) that reduce to $2 \lesssim D \lesssim 3$ as the energy of the states increases. These states at the bottom of the continuum are delocalized, but are not a free-electron gas. The high dimensionality would suggest they are sensitive to the structural conditions of the system, with the states rapidly delocalizing as the unit cell is expanded. At higher energies the dimensionality settles to $D = 3$ as expected.

4.4 Ionization Potential Depression

In the experiment presented in Ciricosta 2016, the XFEL was used to irradiate Mg foils over a range of x-ray photon energies, selectively ionizing the K-shell in increasingly high ion charge states. Only when the driving photon energy exceeds an ionization threshold, or matches an excitation energy, can a $1s$ core hole be created. These core-hole ions radiatively recombine predominantly via the K_α emission channel, providing a spectral signature of the charge states excited during the irradiation process. As there are eight electrons in an L-shell, eight K_α lines can be observed. The experimental emission intensity of these eight lines is plotted against the driving FEL photon energy in Fig. 4.7, reproduced from Ciricosta 2016. Clear edges are observed for the K_α lines, indicating a threshold energy required to excite a $1s$ electron

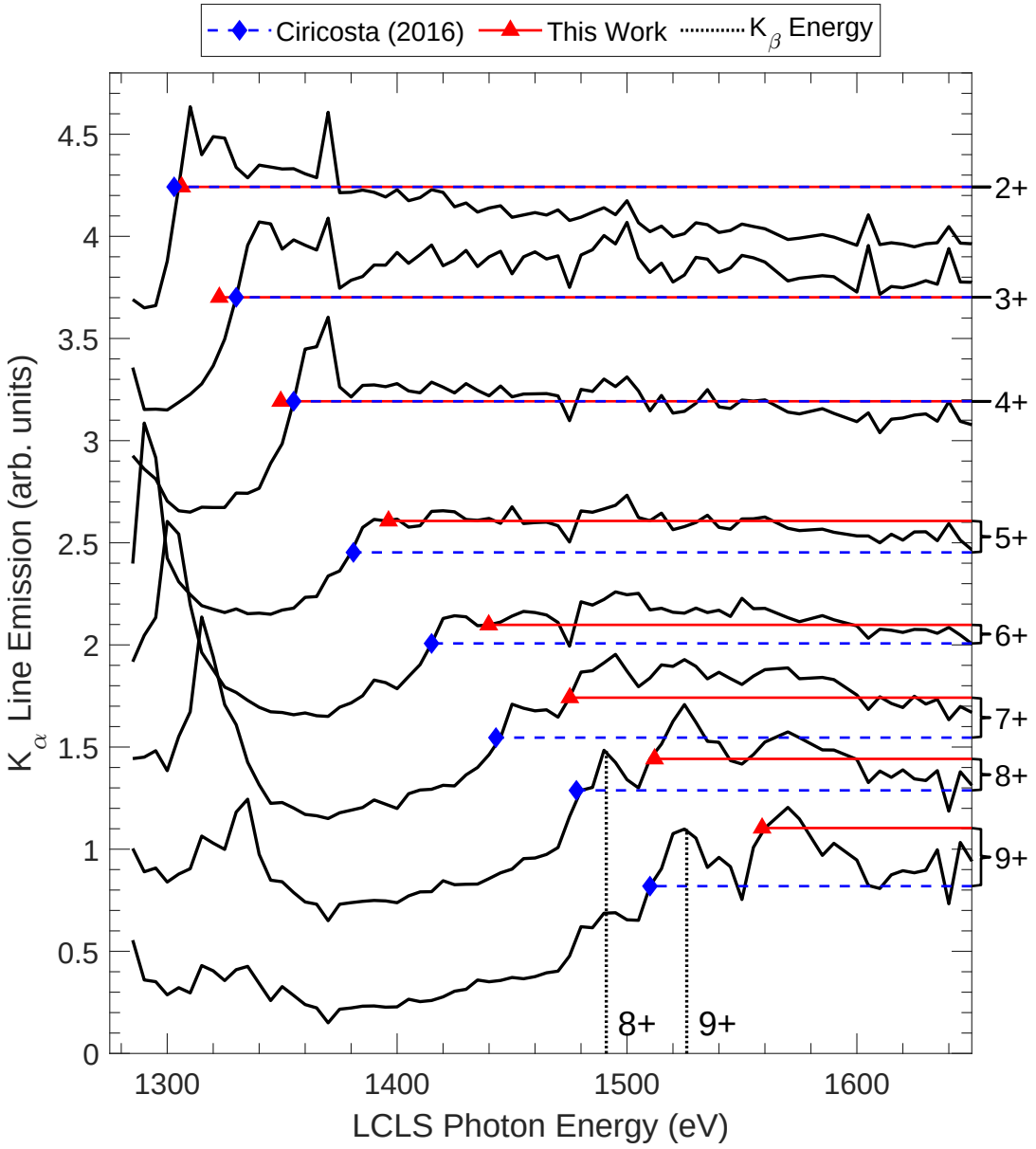


Figure 4.7: Lineouts for the emission intensity of the K_α lines of Mg at different charge states, reproduced from Ciricosta 2016. The horizontal blue lines indicates the K-edge energies inferred in Ciricosta 2016. There is a ±5 eV uncertainty due to the resolution of the measured FEL photon energy. The black-dashed lines indicate the measured Mg K_β lines from the peaks in Fig. 4.1. The horizontal red lines indicate the K-edge energies extracted using FT-DFT. For the 2+ to 4+ charge states, the Ciricosta 2016 edges overlap with the FT-DFT edges.

from the K-shell. In the absence of a bound M-shell, these thresholds represent the K-edges of the dense Mg system, and these are marked on the figure with blue lines. The difference in the measured ionization threshold in the solid-density system and the ionization energy of isolated Mg atoms gives an experimentally measured IPD energy.

The IPD energy from these DFT simulations is now extracted, taking into account the dimensionality metric described in the previous section, and compared with the Ciricosta 2016 experimental data shown in Fig. 4.7. Vinko 2014 [38] detailed two methods for extracting K-edge energies from DFT calculations. One is to take directly the energy difference between two DFT calculations, one with and one without a K-shell hole, while accounting for the additional energy required to thermalize the ionized electron. The second is to take the difference between the energy of the $1s$ orbital and the continuum edge. Both methods produce similar results, but for the work here the second method is chosen as it is more convenient when treating hot systems where the thermal energy in the valence electrons is considerable. It also makes it easier directly to include the dimensionality measure in the edge evaluation.

The continuum edge energy E_c is calculated in the extended system using a plane wave DFT calculation, as this allows appropriate modelling of the extended distribution of free electrons. In IPD models, the continuum edge is the boundary between an electron being bound or free. Following this definition, E_c is placed at the separation between localized and delocalized states. As previously noted, this separation can lie in a continuous region of the supercell DOS. The DFT calculations therefore suggest some localized states cannot be easily be distinguished from the delocalized continuum. The energy of the $1s$ orbital cannot be extracted directly from the same calculation as a pseudopotential is needed to represent the tightly bound $1s$ states in the plane wave DFT approach. Instead, the $1s$ energy can be found relative to the $2p$ state by computing the K_α energy E_{K_α} for the charge state of interest using the atomic DFT code *Atompaw* from which the frozen-core pseudopotential was constructed. This energy can then be subtracted from the $2p$

orbital energy E_{2p} found in the plane wave DFT calculation to yield the binding energy of the $1s$ state. The K-edge energy E_{K} is therefore computed as $E_{\mathrm{K}} = E_c - (E_{2p} - E_{\mathrm{K}_\alpha})$. The results of this calculation for the eight Mg K_α lines are plotted in Fig. 4.7 in red. For the first three charge states, the K-edge predictions from FT-DFT match the thresholds observed in the data, but start to differ for the highest five states. This is because the DFT simulations predict a relocalization of the M-shell for Mg ions with more than four holes in the L-shell. This M-shell relocalization process is depicted in Fig. 4.4 across the relocalization region for charge states between 4+ and 7+. It should be noted that if one takes E_c for Mg^{5+} as the bottom of the continuous region of the DOS, the DFT simulations agree well with the observed data. This further highlights the difficulty in distinguishing the delocalized continuum from close lying localized states, as well as demonstrating that the continuum generally has a more complex localization behaviour beyond the free-electron gas. Strictly speaking, once the M-shell has relocalized the charge state of the ion can no longer be identified using only the number of electrons in the K- and L- shells as there may be bound M-shell spectator electrons. However, this Ne-core based nomenclature is retained to keep a consistent notation, and also note that the high temperatures and low binding energies of the M-shell mean that this will not substantially alter the energetics of the system.

The observation of M-shell states in highly charged ions in the DFT simulations allows us to identify the $1s \rightarrow 3p$ excitation transitions in the experimental data of Fig. 4.7, marked in black. These structures in x-ray absorption (and subsequent K_α emission) are produced by an excitation into an M-shell state, rather than an ionization event into the continuum. While these excitation peaks are prominent for states 8+ and 9+, the process is far less obvious for states 6+ and 7+, neither of which display particularly notable features. The 5+ state also presents no notable feature. In contrast, some prominent peaks do not require reevaluation of the position of the K-edge. For example, the peak at 1525 eV observed in state 8+ can be understood as a combination of a) the ionization of the 8+ ion; and b) a resonant K_β excitation in the 9+ ion, followed by a collisional recombination event in the

L-shell before the K-shell is filled via radiative K_α emission in a now lower charge state 8+. Such ultrafast L-shell collisional dynamics within the duration of the $1s$ core hole lifetime has been studied previously for both ionization [32] and resonant K_α excitation [33], but not for resonant K_β excitation as seen here. Nevertheless, it is unsurprising that a similar process should occur for resonant K_β excitation once the M-shell relocalizes.

The IPD can be extracted from the DFT calculations by taking the difference of the E_K energy and the energy required to ionize the $1s$ orbital in an isolated ion with the same charge state. These energies are plotted in Fig. 4.8, alongside the experimental measurements of Ciricosta 2016 and the predictions from the analytical SP and mEK models, as well as the more recent Crowley [123] and OEFTIS [124] models. As expected, there is agreement between the results of this work and the IPD values found by Ciricosta 2016 for the first three charge states, but beyond that the predictions diverge due to the emergence of relocalizing states and a rebinding M-shell. The IPD values agree with the mEK model only for the first few charge states, with the mEK model overestimating the IPD at high ionization. There is no systematic agreement with the predictions of the SP model which generally underestimates the IPD. Overall, an IPD energy between the mEK and SP models at high charge states is qualitatively consistent with the results of other previous experiments [39, 40, 143, 162] in similar plasma conditions. There is also broad agreement between the results in this work and other theoretical studies [120, 122, 123, 125], but it is worth mentioning that the underlying assumptions are quite different between models, and few explicitly treat the rebinding of M-shell states in the continuum. Quite promisingly, the Crowely and OEFTIS models agree reasonably well with the FT-DFT results at the low and high ionization states. There are notable disagreements for the mid-charge states when the M-shell has just recombined in DFT which, again, is a process not treated in these IPD models. Still, it seems these more advanced treatments of IPD may point in the right directions to take in developing new analytical models.

Given the proximity of Al and Mg on the periodic table it is unsurprising to

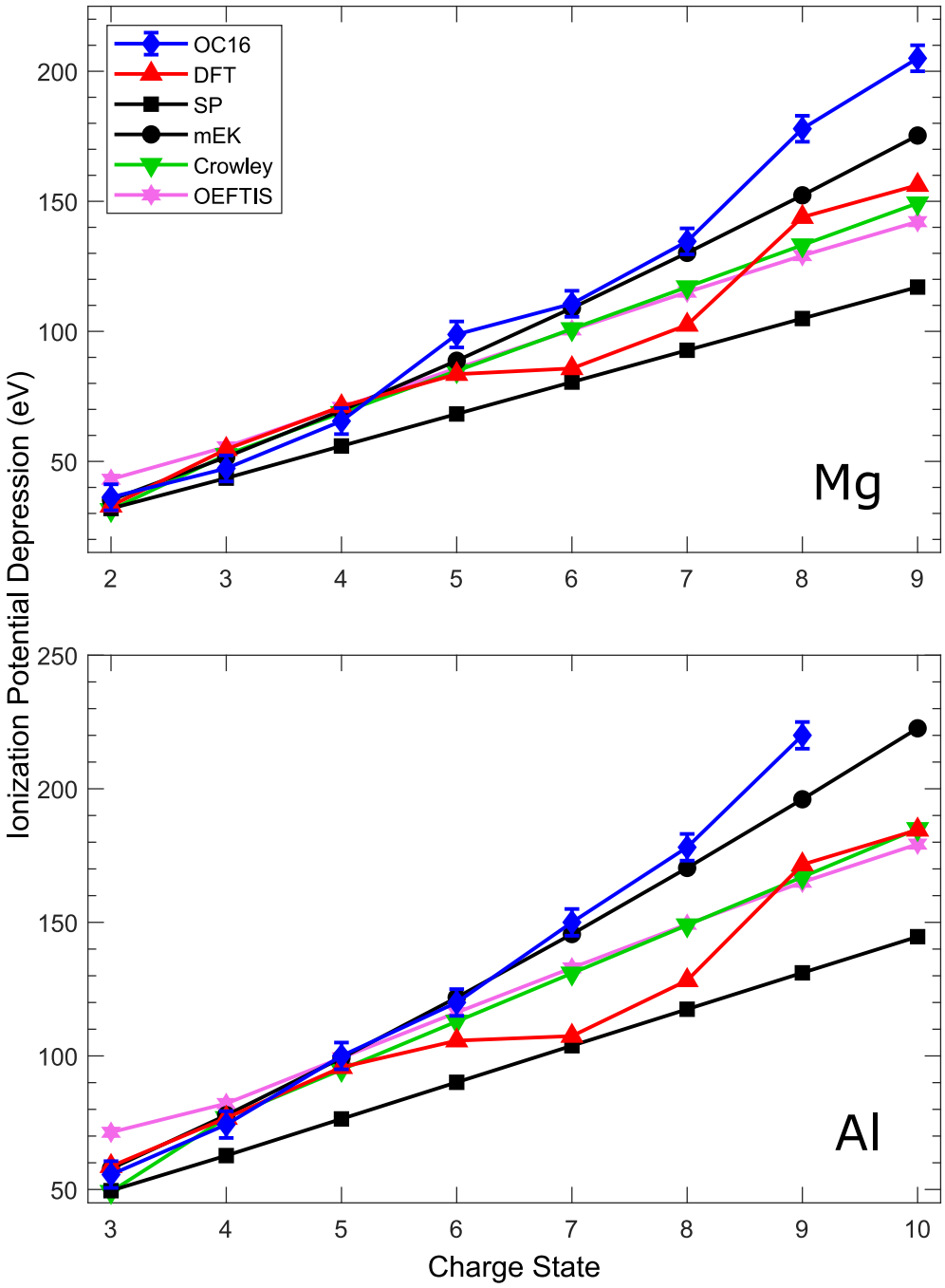


Figure 4.8: IPD levels for different charge states of Mg and Al, inferred from the DFT calculations in this work (red triangles), the experimental data published in Ciricosta 2016 (OC16, blue diamonds), and various IPD models: mEK (black circles), SP (black squares), Crowley [123] (green triangles), and OEFTIS [124] (pink stars).

note a similar trend in the predicted level of IPD in Al. As in Mg, Al also shows the M-shell relocalizing at higher charge states, leading to a more complicated IPD trend as a function of charge state. Again, the IPD values follow the mEK model well until the M-shell rebinds, after which the IPDs lie between the predictions of the SP and mEK models. Previous experimental work investigating the IPD in Al was only able to extract the IPD for the first 5 charge states [39]. The present calculations agree with these results for all but the highest charge states. The difficulty in extracting experimental IPD values for the highest charge states in Al is consistent with the predicted complex IPD behaviour from the DFT calculations, which cannot be reproduced by simple IPD models. This severely hinders our ability to model experiments using time-dependent atomic kinetics simulations, on which much of the experimental IPD work is based.

It is also worth comparing these IPD predictions with previous DFT-based results of Vinko 2014 [38], which generally showed good agreement with the predictions of the mEK model. The method described here is similar to Vinko 2014 in many ways, but differs in how the continuum is identified. Vinko 2014 assumed that the K-edge energy (and thus the IPD) could be found by comparing two DFT simulations for various charge states with and without a K-shell core hole. The system was always assumed to be charge-neutral, and any electron removed from the K- and L-shells was placed in the continuum and equilibrated. The energy difference calculated in this way therefore always assumed that the valence states are part of the continuum, and the K-edge is effectively defined as the lowest possible energy that allows for the excitation of a $1s$ electron. This method can successfully predict all the excitation thresholds, but is only a reliable way to find the K-edge if no states fully rebind in the continuum. The assumption of free valence electrons was based on the observation of relatively broad M-shell features in the DOS, which are normally indicative of unbound states. However, as has been seen in the IPR and dimensionality analysis here, the behaviour of the valence band is complex and the shape of the DOS alone is not always a reliable indicator of whether a state is bound or free. While the distinction between an excitation threshold and a K-edge is not critical for

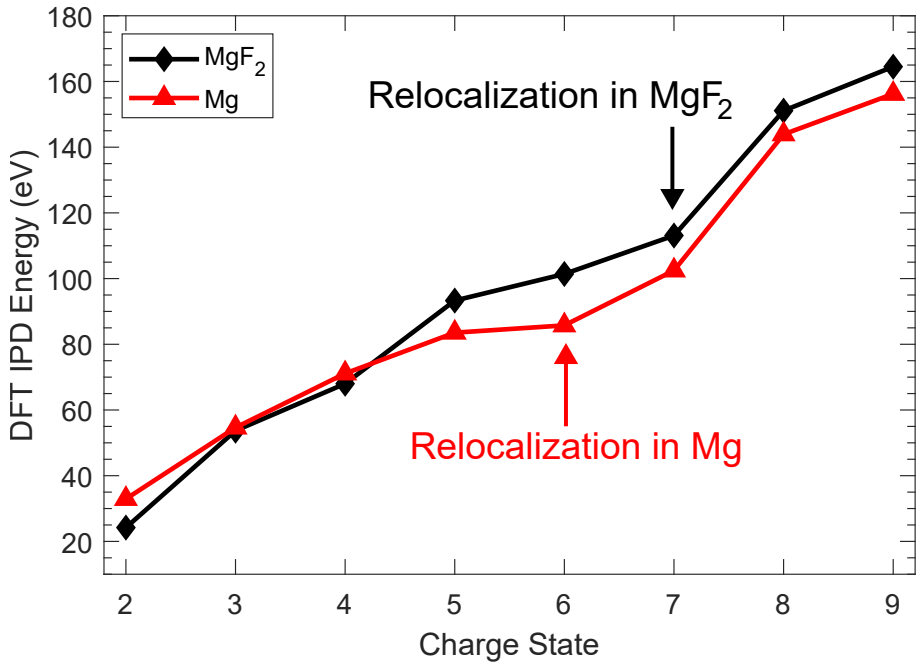


Figure 4.9: Comparison of IPD energies for Mg (red triangles) and MgF_2 (black diamonds) for different charge states of the Mg ions, inferred from the DFT calculations in this work. The arrows indicate when the M-shell fully relocalizes around the Mg ions in each material.

some plasma properties (e.g. the energetics), it does matter in the context of x-ray spectroscopy and IPD. For such investigations the more detailed analysis presented here is required.

In the case of compounds, Ciricosta 2016 observed for Al and its compounds that differences in the IPD energies were relatively minimal. Additionally, the mEK model vastly overpredicted the IPD for Al compounds. While the materials are different to this work, the overarching differences in the IPD between the metal and compounds can still be examined here by comparing the IPD energies extracted from the present DFT calculations of Mg and MgF_2. These are shown in Fig. 4.9, with the arrows indicating when the M-shell fully relocalizes around the Mg ions in each material. For the initial Mg charge state 2+, the IPD is noticeably lower in MgF_2 than in Mg, with a difference of -8.7 eV. Aside from the different ion densities, this may be attributed to the Mg $3s$ electrons being delocalized in metallic Mg, whereas they are localized on the F $2p$ orbitals in MgF_2. For the charge states 3+ and 4+, Mg has slightly higher IPD energies than MgF_2, but the difference is relatively minimal. For charge states 3+ and above, as the Mg L-shell is thermally ionized,

so too is the F L-shell, which eventually is seen to result in noticeably different localization behaviour. For charge states of 5+ and above, the IPD in MgF_2 is larger than in Mg, which may be attributed to differences in the delocalized electron densities arising from the highly-ionized F ions. The difference in IPD energies is largest, at 15.6 eV, when the M-shell relocalizes in Mg^{6+}, but it shrinks again after the full relocalization of the M-shell in $Mg^{7+}F_2$. The weaker relocalization of states, which begins at a charge state of 5+ in both materials, is reflected in the greater depression of the ionization potential in MgF_2.

4.5 Summary

The first experimental observation of K_β emission in highly ionized solid density Mg plasmas driven by an intense XFEL has been presented. These results indicate that the M-shell rebinds in highly charged Mg ions. This result is consistent with some popular IPD models, but contradicts several others. While the IPD and the need to distinguish between bound and free states in a dense plasma is an artificial construct from a physics standpoint, it is essential to many plasma physics simulations, including collisional-radiative modelling. As such, finding a robust method to determine the IPD in dense plasmas without the need for empirical parameters remains of considerable practical interest.

To interpret the experimental results and place the modelling of the IPD on a firm footing, the spatial localization of Kohn-Sham states calculated using FT-DFT was investigated using the dimensionality metric described in Chapter 3. Using this metric, valence states can be reliably evaluated as bound or free. This dimensionality has been applied to x-ray isochorically heated Al, Mg and MgF_2. It was found that the $n = 3$ states relocalize at high ionization in all three systems. The relocalization process is seen to be weaker in MgF_2 than in Mg owing to the change in environment around the Mg ions due to the presence of additional delocalized electrons from the F ions. While this approach builds on the previous DFT work of Vinko 2014 [38], it highlights the importance of the dimensionality metric in distinguishing between

excitation and ionization thresholds. While essential to compute a well-defined IPD energy, the concept of boundness of a state is not trivial to define for a dense plasma within the general framework of Kohn-Sham DFT.

In comparing the presented predictions with simple analytical IPD models, agreement with the mEK model applied only for the first four lower charges states in all three systems. For higher charge states, considerable complexity is observed in the relocalization of M-shell states, a process which cannot in general be reproduced by simple analytical models. In particular, for these higher ionisation states the mEK model overestimates the IPD, while the SP model systematically underestimates it. Based on this observation the interpretation of recent experimental results from Ciricosta *et al.* [40] has been revisited, and it has been shown how observed spectral features in the measured intensity of K_α emission as a function of x-ray photon energy can be attributed to the resonant pumping of the K_β transition for the higher ionisation states. Some newer IPD models [123, 124], despite not capturing the full IPD behaviour, agree better with these new results than the SP and mEK models.

Thus, as an overarching conclusion, it is found that the original experimental work performed at LCLS that identified the mEK model as providing a better description of the IPD than the SP model in Al [39] is justified, given that particular work provided IPD values for charge states only up to 7+. However, the current observation of rebinding of the M-shell for higher ionisation states is also consistent with the work of Hoarty *et al.* [143]. These findings further illustrate the inherent difficulties in attempting to use simplified models of the IPD in atomic kinetics calculations. Returning the statement by the authors of Ref. [39]:

> The reasons underlying the success of the mEK over the SP model are far from clear: both the SP and the mEK models are simple, semi-classical models, ultimately both unlikely to capture fully the complex physics of atomic systems embedded within dense plasma environments over wide ranges of plasma conditions and charge states.

While the DFT-based model presented here provides new insight into the mechanisms of continuum lowering, at present the model remains too computationally

cumbersome to be implemented in-line in atomic kinetics suites or in plasma opacity codes over multiple charge and atomic states. For this use, simpler analytical models are still required. Nevertheless, this approach, alongside the comparison with available experimental data, can provide a valuable framework to evaluate models for use across a wide range of plasma temperatures, densities and ionizations.

Chapter 5: Ionization in Hot Dense Systems

As has been previously described in this thesis, dense plasmas are complex, inherently quantum state of matter, covering a wide variety of different temperatures and densities. Given the extraordinarily large number of electrons and ions in realistic plasmas, it is impossible to directly solve the many-body quantum equations. Instead, simpler models that only deal with the relevant physics required to make a set of predictions are used. Of course, it is important to be sure that plasma models are able to make good predictions.

Within plasma modelling, there are a number of parameters that are used to describe a plasma and make predictions about experimental observables; often the temperature T, density ρ, and the ionization state of the ions Z. However, unlike the first two parameters, ionization does not have a well-defined thermodynamic definition [108]. This is not a trivial issue. The ionization state is an input parameter to many equations, so the choice of definition will have a cascading effect on the evolution of a plasma. It is also important to understand how the choice of definition used in plasma modelling relates to experimental observations. The ionization state is often defined in the bound-or-free picture: the number of electrons free from an ion is its ionization state (i.e. $Z = 0$ for a neutral atom). This definition is then fed directly into equations governing the physical properties of the plasma, such as an IPD model to treat the continuum lowering. As has already been discussed in detail in this thesis, a substantial body of research has emerged indicating a lack of consensus between widely-employed IPD models and experimental observations in dense plasma systems [39, 40, 143, 164, 195].

One such experiment at the NIF [164] found that the mean ionization state

(MIS) of hot dense CH plasmas inferred from x-ray Thomson scattering (XRTS) measurements was substantially higher than predicted by plasma modelling. The discrepancy was attributed to problems with the IPD models used in evaluating the ionization as simply increasing the MIS seemed to reproduce the XRTS data. However, more recent experimental measurements in hot dense Be [195] found that XRTS spectra could not be reproduced by artificially increasing the MIS, suggesting the reason for the discrepancies between these experiments and plasma models is more complex.

The primary interest of this chapter is in exploring whether the definition of ionization based on the concept of bound and free electrons is a suitable definition of ionization, and whether it is this quantity that is accessed in spectroscopy experiments involving high energy density systems. Within this context, I present FT-DFT calculations of the ionization state of carbon in CH plasmas are presented using two potential definitions: one based on counting the number of continuum electrons, and another based on the optical conductivity. Differences of up to 10% are observed between the two methods. However, including "Pauli forbidden" transitions in the conductivity reproduces the counting definition, suggesting such transitions are important to evaluate the ionization state.

5.1 Defining Ionization

For the present work, the equivalent definition of the bound-or-free MIS in a first-principles DFT calculation is to count the number of electrons in the continuum (c) bands N_{cond}:

$$\langle Z \rangle_{\text{count}} = \frac{1}{N_i} \sum_{\boldsymbol{k}} w_{\boldsymbol{k}} \sum_{n \in c} f(\epsilon_{\boldsymbol{k},n}) = \frac{N_{\text{cond}}}{N_i} \,, \tag{5.1}$$

where N_i is the number of ions, $\epsilon_{\boldsymbol{k},n}$ is the eigenenergy of the Bloch state $|\psi_{\boldsymbol{k},n}\rangle$, n is the band number, $\boldsymbol{k}$ is the crystal momentum, $w_{\boldsymbol{k}}$ is the k-point weight, and $f(\epsilon_{\boldsymbol{k},n})$ is the Fermi-Dirac occupation number of the state and includes the state's degeneracy. In light of the localization work in previous chapters, it is worth examining further whether simply integrating the whole continuum is appropriate, particularly

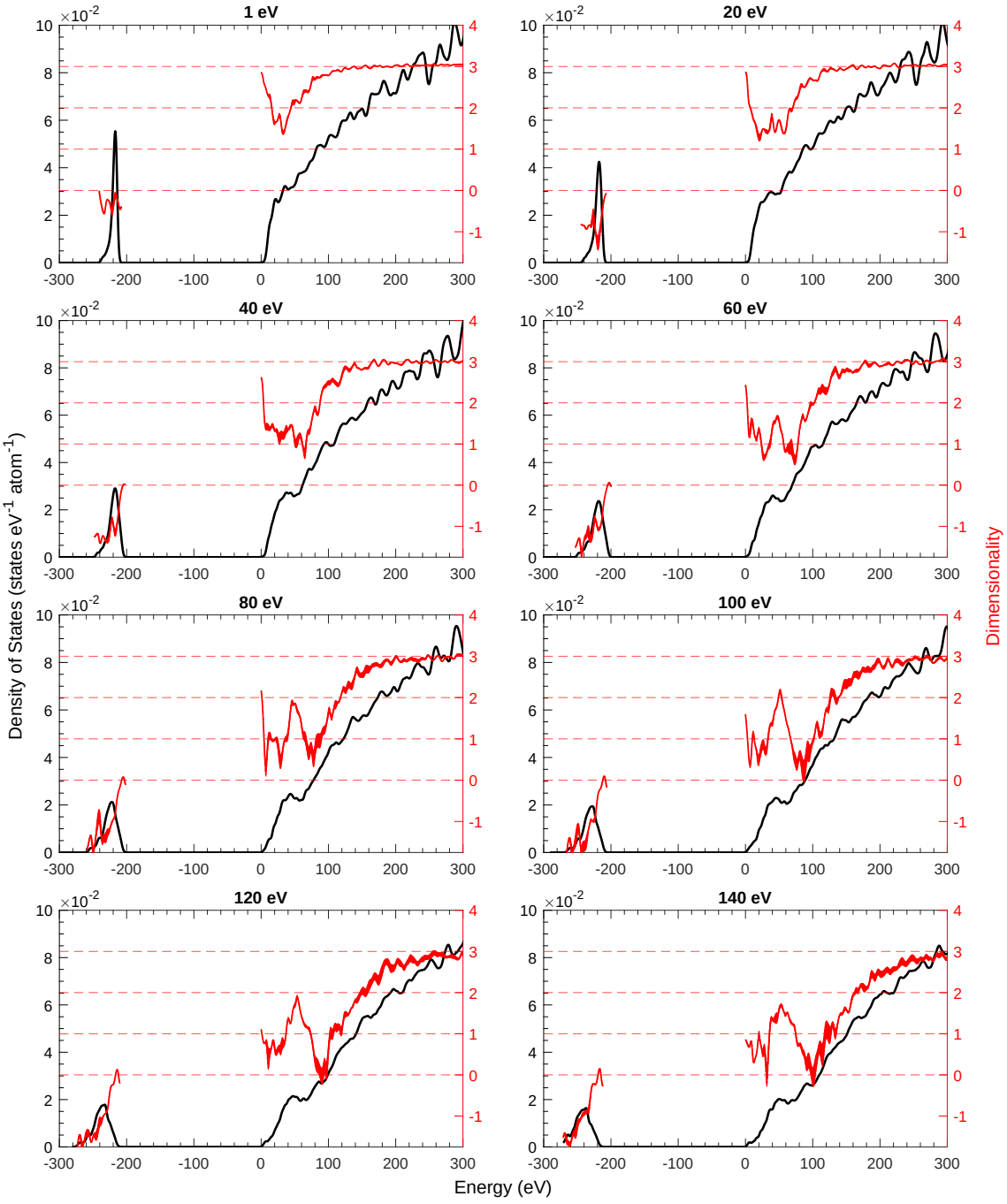


Figure 5.1: The density of states (black) and dimensionality (red) for 6.74 g cm^{-3} CH at different electron temperatures. The thickness of the dimensionality curve represents the stability of the averaging. As the system heats, states at the bottom of the continuum begin to relocalize. For $T_e \geq 40$ eV, the bottom of the continuum has a complex localization behaviour, which corresponds to a feature that develops in the DOS.

whether any states relocalize in the continuum and if they should be excluded. A dimensionality analysis of dense CH plasmas at numerous electron temperatures is plotted in Fig. 5.1 (details of the FT-DFT calculations can be found later in this chapter). The energy axis has been shifted so that the bottom of the continuous region is the zero energy. The two main features in the DOS are the continuous region above the zero-energy, and a broad peak below -200 eV that corresponds to the carbon K-shells. At $T_e = 1$ eV, the K-shell states are well-localized, while the continuum is delocalized. Immediately above the continuum edge, there are some states that show increased localization, however they still have $D > 1$. At higher energies above 100 eV, the states have $D = 3$ as expected. As the system is heated, states at the bottom of the continuum relocalize. At temperatures ≥ 40 eV, there are broad regions in the continuum where the states have $D \lesssim 1$, but there is also a peak in these localized regions where the states have $1 < D < 2$. This localization behaviour is much more complex than the simple bound-or-free picture, and the prevalence of states with $D \sim 1$ makes it difficult to assign some states as localized or delocalized. The MIS calculated using Eq. (5.1) using the whole continuum (blue) and only delocalized states ($D > 1$, black) is plotted in Fig. 5.2. The error bars in the delocalized MIS represents the uncertainty in the number of delocalized electrons due to states with $D \sim 1$. The blue curve behaves as would be expected – heating the system ionizes electrons from the K-shell to the continuum, so the MIS increases. However, as states relocalize during heating and they retain substantial occupation numbers, the MIS calculated from the delocalized states decreases with heating. The MIS from only the delocalized states would not be in agreement with experimental data [164, 195]. It has also been previously seen that only including the free electron-like DOS in calculating the MIS tends to make poor predictions versus experiments [196]. So while these localized continuum states demonstrate a more complex localization behaviour than the simple bound-or-free model, they should still be counted towards the MIS. For these CH systems, the MIS is therefore defined using the full continuum.

Recently, attempts have been made to define ionization based on other physical

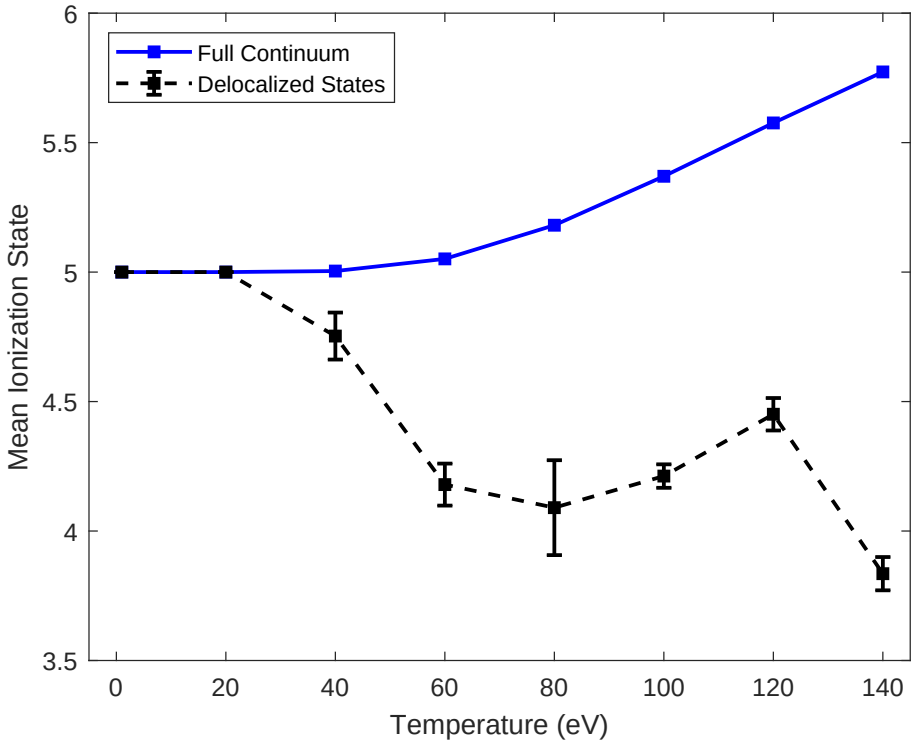


Figure 5.2: A comparison of the MIS from counting all the continuum electrons (blue) versus only counting the delocalized states (black). The error bars on the black curve represent the uncertainty in the number of delocalized electrons due to states with $D \sim 1$.

properties of systems [131, 174]. One such definition proposed in Bethkenhagen 2020 [131] is based on the real component of the frequency-dependent optical conductivity $\sigma(\omega)$ calculated using the Kubo-Greenwood (KG) formula [197, 198]:

$$\sigma(\omega) = \frac{\pi\hbar e^2}{m_e V} \sum_{\boldsymbol{k}} w_{\boldsymbol{k}} \sum_{n,m} \left[f(\epsilon_{\boldsymbol{k},m}) - f(\epsilon_{\boldsymbol{k},n}) \right] g^{\boldsymbol{k}}_{nm} \delta\left(\epsilon_{\boldsymbol{k},n} - \epsilon_{\boldsymbol{k},m} - \hbar\omega\right) , \tag{5.2}$$

where V is the volume of the system, and $g^{\boldsymbol{k}}_{nm}$ are the dipole transition matrix elements:

$$g^{\boldsymbol{k}}_{nm} = \frac{\hbar^2}{3m_e} \frac{\left| \langle \psi_{\boldsymbol{k},m} | \nabla | \psi_{\boldsymbol{k},n} \rangle \right|^2}{\epsilon_{\boldsymbol{k},n} - \epsilon_{\boldsymbol{k},m}} , \tag{5.3}$$

where, for Bloch states $|\psi_{\boldsymbol{k},n}\rangle = e^{i\boldsymbol{k}\cdot\boldsymbol{r}} |u_{\boldsymbol{k},n}\rangle$, it can be shown that [199, 200]:

$$\frac{\hbar^2}{i m_e} \langle \psi_{\boldsymbol{k},m} | \nabla | \psi_{\boldsymbol{k},n} \rangle = \delta_{m,n} \nabla_{\boldsymbol{k}} \epsilon_{\boldsymbol{k},m} + \left(\epsilon_{\boldsymbol{k},n} - \epsilon_{\boldsymbol{k},m}\right) \langle u_{\boldsymbol{k},m} | \nabla_{\boldsymbol{k}} u_{\boldsymbol{k},n} \rangle . \tag{5.4}$$

The Thomas-Reiche-Kuhn (TRK) sum rule [201–203] states that, for a complete basis set, the sum of the dipole matrix elements is unity. In momentum form, this

is:

$$2 \sum_{\substack{n \\ \epsilon_{\boldsymbol{k},n} \neq \epsilon_{\boldsymbol{k},m}}} g^{\boldsymbol{k}}_{nm} = 2 \sum_{n} g^{\boldsymbol{k}}_{nm} \tau(\epsilon_{\boldsymbol{k},n} - \epsilon_{\boldsymbol{k},m}) = 1 \,, \tag{5.5}$$

where $\tau(\epsilon_{\boldsymbol{k},n} - \epsilon_{\boldsymbol{k},m}) = 1 - \delta(\epsilon_{\boldsymbol{k},n} - \epsilon_{\boldsymbol{k},m})$ ensures the $\epsilon_{\boldsymbol{k},n} = \epsilon_{\boldsymbol{k},m}$ terms are excluded. The number of electrons in the system N_e can therefore be recovered by including a sum over the occupation numbers:

$$\begin{aligned} N_e &= \sum_{\boldsymbol{k}} w_{\boldsymbol{k}} \sum_{m} f(\epsilon_{\boldsymbol{k},m}) \\ &= 2 \sum_{\boldsymbol{k}} w_{\boldsymbol{k}} \sum_{m} f(\epsilon_{\boldsymbol{k},m}) \sum_{n} g^{\boldsymbol{k}}_{nm} \tau(\epsilon_{\boldsymbol{k},n} - \epsilon_{\boldsymbol{k},m}) \\ &= \sum_{\boldsymbol{k}} w_{\boldsymbol{k}} \sum_{n,m} \left[f(\epsilon_{\boldsymbol{k},n}) - f(\epsilon_{\boldsymbol{k},m}) \right] g^{\boldsymbol{k}}_{mn} \tau(\epsilon_{\boldsymbol{k},n} - \epsilon_{\boldsymbol{k},m}) \,, \end{aligned} \tag{5.6}$$

where the relationship $g^{\boldsymbol{k}}_{nm} = -g^{\boldsymbol{k}}_{mn}$ for $n \neq m$ and index swapping are used to derive the last line. A similar-looking sum can be constructed by integrating the KG conductivity over all frequencies:

$$\begin{aligned} S &= \frac{2 m_e V}{\pi e^2} \int_0^\infty \sigma(\omega) d\omega \\ &= \sum_{\boldsymbol{k}} w_{\boldsymbol{k}} \sum_{n,m} \left[f(\epsilon_{\boldsymbol{k},m}) - f(\epsilon_{\boldsymbol{k},n}) \right] g^{\boldsymbol{k}}_{nm} \,, \end{aligned} \tag{5.7}$$

where the delta function in Eq. (5.2) is used to derive the second line. It has therefore been proposed in Bethkenhagen 2020 that by splitting the states into conduction (c) and valence (v) states, so that $\sigma = \sigma^{c \to c} + \sigma^{v \to c} + \sigma^{v \to v}$, the MIS can be found by only considering the $c \to c$ transitions:

$$\langle Z \rangle_{\mathrm{TRK}} = \frac{2 m_e V}{\pi e^2 N_i} \int_0^\infty \sigma^{c \to c}(\omega) d\omega = \frac{N_{\mathrm{eff}}}{N_i} \,, \tag{5.8}$$

where N_{eff} is the number of conduction electrons calculated in this scheme. For the present work, the continuum and conduction electrons are synonymous. However, care is needed: the sums in S include the $\epsilon_{\boldsymbol{k},n} = \epsilon_{\boldsymbol{k},m}$ terms, whereas the TRK sum rule excludes them. When $n = m$, Eq. (5.4) shows that $\langle \psi_{\boldsymbol{k},n} | \nabla | \psi_{\boldsymbol{k},n} \rangle$ is not always zero, but is proportional to the curvature of the band at $\boldsymbol{k}$. Meanwhile, in

the limit of zero energy difference, the difference in the eigenenergies in $g^{\boldsymbol{k}}_{nn}$ and the occupation numbers in Eq. (5.2) resolve to the gradient of the Fermi-Dirac distribution at $\epsilon_{\boldsymbol{k},n}$, so the $n = m$ terms are finite and not necessarily zero [204]. Therefore, if the $g^{\boldsymbol{k}}_{nn}$ terms are included, $S \geq N_e$ [204]. In practice, converging the sums N_e and S requires a huge number of bands, even at moderate temperatures, so it can appear that $S < N_e$. If the $n = m$ terms are included, the number of electrons extracted from $\sigma^{c\to c}$ (which includes $g^{\boldsymbol{k}}_{nn}$ terms) may appear larger than it should when compared with the equivalent TRK sum.

The conductivity-based definition in Eq. (5.8) has recently been applied to predict the MIS found via XRTS measurements of hot dense Be plasmas generated in implosions at the NIF [195]. The conductivity measure was found to agree well with the XRTS-inferred MIS at the highest temperatures and densities produced ($T = 150$ eV, $\rho \geq 30$ g cm^{-3}), while the counting measure using the SP model under-predicts the MIS. However, at lower temperatures and densities ($T = 100$ eV, $\rho \sim 10$ g cm^{-3}) the counting measure agrees well with the experimental data, while the conductivity definition appears to over-predict the MIS. Furthermore, at mass densities $\rho \lesssim 10$ g cm^{-3}, differences in the predictions between the counting and conductivity definitions grow further as the temperature decreases, even in conditions where the counting definition is expected to be applicable [195].

Calculating the effective ionization state of a system using the $c\to c$ conductivity has been explored previously in condensed matter physics. Notably, when applied to experimental measurements of the conductivity in alkali metals in the early 70's, it was found that $N_{\text{eff}} > 1$ [205], causing consternation since this implies that the ionization state exceeds the number of electrons in the conduction band, N_{cond}. Kobayasi and Watabe [206] showed how this problem could be resolved by completing the TRK sum by including Pauli forbidden transitions in the calculation of the ionization state. An equivalent term does not appear to have been included in the ionization calculations of Refs. [131, 195]. In the following section, Kobayasi and Watabe's arguments are extended to finite temperatures, following which the size of this term is quantified using first principles calculations.

5.2 Counting the Conduction Electrons

To calculate the effective number of conduction electrons, the TRK sum over states is split into a sum over conduction states ($n \in c$) and valence states ($n \in v$):

$$\begin{aligned} N_e &= \sum_{\boldsymbol{k}} w_{\boldsymbol{k}} \sum_{n,m} \left[f(\epsilon_{\boldsymbol{k},n}) - f(\epsilon_{\boldsymbol{k},m}) \right] g^{\boldsymbol{k}}_{mn} \tau(\epsilon_{\boldsymbol{k},n} - \epsilon_{\boldsymbol{k},m}) \\ &= \sum_{\boldsymbol{k}} w_{\boldsymbol{k}} \left(\sum_{n\in c} + \sum_{n\in v} \right) \left(\sum_{m\in c} + \sum_{m\in v} \right) g^{\boldsymbol{k}}_{mn} \left[f(\epsilon_{\boldsymbol{k},n}) - f(\epsilon_{\boldsymbol{k},m}) \right] \tau(\epsilon_{\boldsymbol{k},n} - \epsilon_{\boldsymbol{k},m}) \,, \end{aligned} \tag{5.9}$$

It is proposed that only the $c \to c$ transitions need to be used to calculate the number of conduction electrons [131, 206]:

$$\begin{aligned} N_{\text{eff}} &= \sum_{\boldsymbol{k}} w_{\boldsymbol{k}} \sum_{n\in c} \sum_{m\in c} \left[f(\epsilon_{\boldsymbol{k},n}) - f(\epsilon_{\boldsymbol{k},m}) \right] g^{\boldsymbol{k}}_{mn} \tau(\epsilon_{\boldsymbol{k},n} - \epsilon_{\boldsymbol{k},m}) \\ &= 2 \sum_{\boldsymbol{k}} w_{\boldsymbol{k}} \sum_{n\in c} f(\epsilon_{\boldsymbol{k},n}) \sum_{m\in c} g^{\boldsymbol{k}}_{mn} \tau(\epsilon_{\boldsymbol{k},n} - \epsilon_{\boldsymbol{k},m}) \,. \end{aligned} \tag{5.10}$$

However, Eq. (5.10) does not include a complete sum rule [206]. To do so, the valence states need to be included again using:

$$\begin{aligned} N_{\text{eff}} &= 2 \sum_{\boldsymbol{k}} w_{\boldsymbol{k}} \sum_{n\in c} f(\epsilon_{\boldsymbol{k},n}) \left(\sum_{m} - \sum_{m\in v} \right) g^{\boldsymbol{k}}_{mn} \tau(\epsilon_{\boldsymbol{k},n} - \epsilon_{\boldsymbol{k},m}) \\ &= \sum_{\boldsymbol{k}} w_{\boldsymbol{k}} \sum_{n\in c} f(\epsilon_{\boldsymbol{k},n}) - 2 \sum_{\boldsymbol{k}} w_{\boldsymbol{k}} \sum_{n\in c} f(\epsilon_{\boldsymbol{k},n}) \sum_{m\in v} g^{\boldsymbol{k}}_{mn} \tau(\epsilon_{\boldsymbol{k},n} - \epsilon_{\boldsymbol{k},m}) \\ &\equiv N_{\text{cond}} - \Delta N_{\text{eff}} \,. \end{aligned} \tag{5.11}$$

The ΔN_{eff} term relates the number of ionized electrons from the conduction definition to the counting definition. $\Delta N_{\text{eff}} < 0$, so it represents an increase in the number of conduction electrons from the optical conductivity as compared with just counting them. In the cold limit, this term only includes transitions between the valence states (which are fully occupied) and the occupied conduction states. In other words, this term only includes forbidden transitions due to Pauli blocking [206]. In the finite-temperature limit, this term does not quite represent transitions between Pauli blocked states as there is no statistical weighting accounting for the

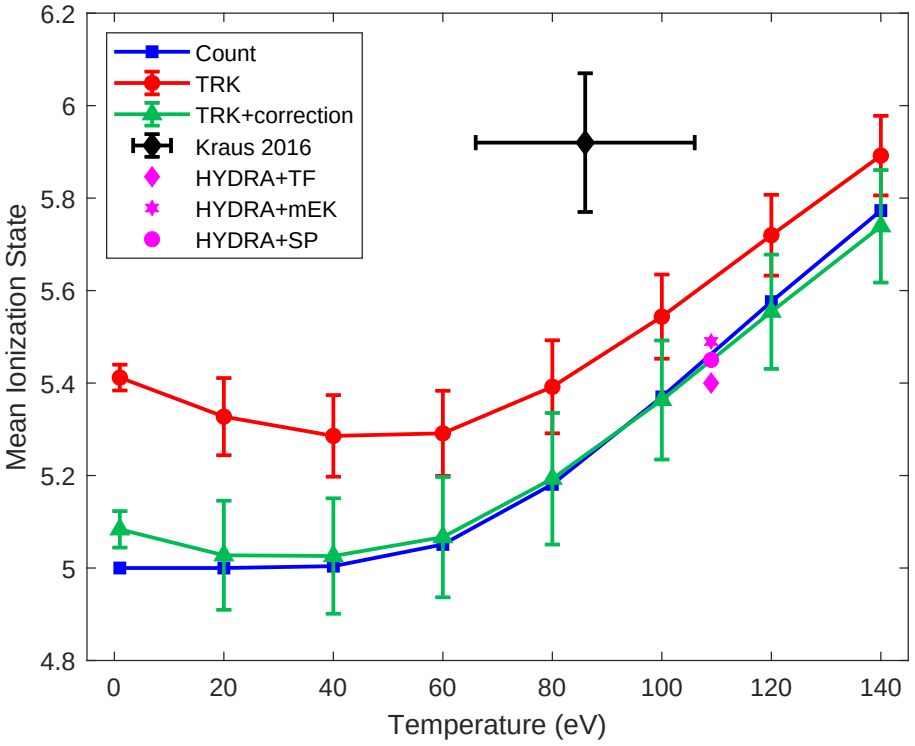


Figure 5.3: Mean ionization state of CH (N/N_{CH}) calculated using different methods. The red circles are the MIS using $N = N_{\mathrm{eff}}$ as suggested in Bethkenhagen 2020. The green triangles are from using $N = N_{\mathrm{eff}} + \Delta N_{\mathrm{eff}}$. The blue squares are the MIS using the counting definition, $N = N_{\mathrm{cond}}$. Also included is the MIS reported in Kraus 2016 [164]: the black point is the temperature-ionization conditions inferred from XRTS measurements, while the magenta points are the MIS calculated from their simulations using different IPD models.

thermal de-occupation of the valence states at high temperatures. This derivation reveals the link between the conductivity-based definition of ionization proposed in Bethkenhagen 2020 and the simple electron counting method.

5.3 Results

The degree to which the $c \to c$ conductivity over-predicts the ionization state is now examined via FT-DFT simulations of CH plasmas at different temperatures, performed using the ABINIT v8.10.3 package [56, 57, 102]. The simulations used supercells containing 32 atoms ($C_{16}H_{16}$), with the lattice parameters chosen to give a mass density of 6.74 g cm^{-3}. The electron temperature was varied from 1-140 eV. The density and temperatures were chosen to match the experimental conditions of Kraus 2016 [164], allowing the present ionization calculations to be compared against

experimental results. In order to have a well-converged TRK sum rule the vast majority of occupied bands need to be calculated explicitly. For each calculation, the number of bands used ensured the sum rule was at least 97% complete (4500-7000 bands). To ensure there are no high-level symmetries in the system, the ions were randomly placed in the cell. Though this effects the specific shapes of the density of states and the conductivity, the MIS was found to be largely independent of the exact ion positions. The *Atompaw* code [193] was used to generate projector augmented-wave (PAW) [90] potentials for the C and H atoms. All of the electrons are calculated explicitly, and the potentials were generated for atoms at zero-temperature. A PAW core radius of 0.5 Bohr is used for both atoms. For the ion positions that were sampled, there was no overlap of the cores. The PBE form of the generalized gradient approximation [76] was used for the exchange-correlation functional.

The mean ionization state of CH versus the electron temperature using the different definitions is plotted in Fig. 5.3. To avoid over-counting the electrons when integrating the conductivity, the TRK definitions were calculated using the sums over states, as in Eqs. (5.10) and (5.11). The error bars on the TRK calculations represent the uncertainty in the MIS due to the sum rule being incomplete. The red circles are the MIS calculated using N_{eff}, and the blue squares are the counting definition, Eq. (5.1). Across the entire temperature range, the $c \to c$ conductivity definition predicts a higher MIS than the counting definition, up to 10% at the lowest temperatures. This appears to be in agreement with previous observations [195, 205, 206]. Additionally, the red curve has an interesting behaviour whereby the MIS increases as the temperature decreases below 40 eV. This is in contrast to the blue curve which monotonically increases with temperature, and is approximately constant at $\langle Z \rangle_{\text{count}} = 5.0$ below 40 eV. When the correction term ΔN_{eff} is included (green triangles), the MIS from the conductivity reproduces the counting definition. There is a small deviation still at 1 eV, though this is likely due to the sum rule still being incomplete. The reproduction of the counting MIS should not be surprising as the ΔN_{eff} term directly connects N_{eff} to N_{cond}. These results suggest that the $c \to c$ conductivity-based definition, as proposed in Bethkenhagen

2020, does not provide the correct ionization state as it does not use a complete sum rule. The correction term ΔN_{eff} can be substantial, even at relatively high temperatures.

The present results can be compared to experimental measurements of the CH ionization state from Kraus 2016 (black point in Fig. 5.3). Their hydrodynamic simulations suggested a mean mass density of 6.74 g cm^{-3}, at which their XRTS spectrum could be fit with a mean temperature of 86±20 eV and a MIS of 5.92±0.15. This ionization state is substantially larger than is predicted by the FT-DFT calculations using the counting definition. Indeed, the MIS from the present FT-DFT calculations using the counting definition is in very close agreement with the MIS calculated from IPD models by Kraus 2016 (magenta points). The MIS calculated from N_{eff} is closer to the experimental data, though it is is still lower across the inferred temperature range. Once the correction ΔN_{eff} is applied, the conductivity-derived ionization is further from the experimental data. In Döppner 2023 [195], the MIS from N_{eff} appears to agree well with the XRTS spectrum of Be at very high densities and temperatures. This apparent improvement in the conductivity definition over the electron counting definition in these extreme conditions is precisely because N_{eff} overestimates the number of continuum electrons as compared with N_{count}. At lower temperatures, it becomes apparent that N_{eff} overestimates the MIS. Including a term involving transitions between valence and occupied conduction states – transitions which at low temperatures are Pauli forbidden [206] – allows for the conductivity to reproduce the number of electrons in the continuum. These results suggest these "Pauli forbidden" transitions are important to evaluating the MIS from the conductivity at finite temperatures.

5.4 Discussion

Of course, there remains the question of what are the additional electrons that XRTS measurements seem to suggest there should be compared with the counting definition. Döppner 2023 showed that simply increasing the MIS would still not reproduce

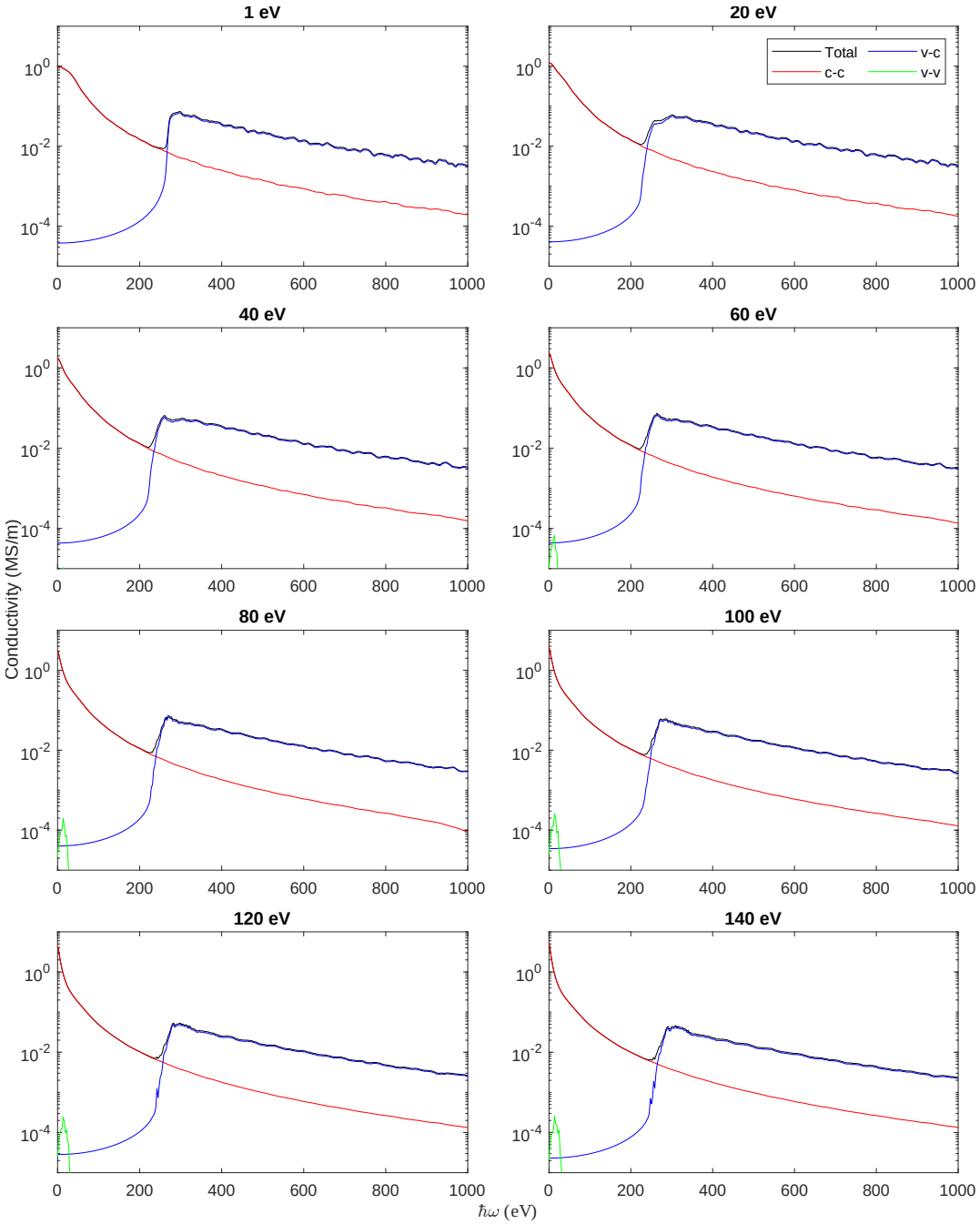


Figure 5.4: The optical conductivity (black), Eq. (5.2), for CH at different electron temperatures. Also plotted is the breakdown of the $v-v$ (green), $v-c$ (blue), and $c-c$ (red) contributions.

their XRTS data as the elastic feature would need to be larger than was measured. Instead, they found that the discrepancies in the XRTS spectrum can be explained by the delocalization of the K-shell wavefunctions, caused by the continuum electron density screening the atomic nuclei. As the screening electron density increases with temperature and compression, so does the delocalization, resulting in greater deviations of the XRTS spectrum from modelling. Using a simple self-consistent screening model, Döppner 2023 were able reproduce their XRTS spectra. In IPD models, the bound electrons are considered to be strongly localized around atomic sites, hence they cannot account for their gradual delocalization. A similar effect seems to be present in this work. The dimensionality of the K-shells in Fig. 5.1 at high temperatures becomes very negative ($D \leq -1$), suggesting the states are shrinking around the carbon ions as the unit cell expands. This would appear to be in agreement with the states becoming more localized as the screening electron density decreases with the expanding unit cell, and thus delocalizing upon compression.

Among other effects, the delocalization of the K-shell wavefunctions results in them overlapping, allowing their electrons to move between atomic sites. This may appear as an apparent increase in the MIS as there are more mobile electrons than just those in the continuum. For completeness, it is noted that electrons moving within the K-shell states would be represented by the $v \to v$ transitions in the optical conductivity, which are not included in N_{eff}. Fig. 5.4 plots the different contributions to the optical conductivity at different temperatures. Above $T_e = 40$ eV, there is a small but non-zero contribution to the conductivity from the $v \to v$ transitions. So while these contributions are not large enough to meaningfully increase the MIS directly, they still indicate the K-shell electrons are mobile at high temperatures. More detailed accounting for the effect of atomic electrons may therefore explain the higher ionization seen in XRTS experiments compared to counting the continuum electrons.

Chapter 6: Conclusions and Future Work

6.1 Summary of Thesis

In this thesis I have presented investigations of state localization mechanisms in hot dense plasma systems, which have provided insight into the fundamental plasma process of continuum lowering (CL) [108]. When electrons are assumed to be either purely bound to an ion or purely free, simple analytical models of ionization potential depression (IPD) [107, 109, 110] have been used to treat CL in many plasma calculations. However, the bound-or-free treatment of electrons is a crude approximation of the full electron behaviour. As explained in detail in Chapter 2, there is a large and growing body of experimental measurements that demonstrate that widely-used IPD models do not provide accurate predictions of plasma properties. One should bear in mind that the computational and conceptual convenience of IPD models is highly desirable, so there has been a large theoretical effort that has attempted to understand and resolve the discrepancies of IPD models. While there has yet to be a satisfactory resolution, the theoretical effort has elucidated much on the nature of continuum lowering. Experimental measurements have placed constraints on the strength of IPD in many plasma systems, and provide invaluable benchmarks for theoretical efforts. To that end, the evidence suggests that the popular Stewart-Pyatt (SP) model [109] under-predicts IPD, while a modified form of the Ecker-Kröll (mEK) model [110, 112] generally over-predicts it. These two models generally appear to give limits on the strength of IPD. This is the starting point for the subsequent studies in this thesis, in which the validity of the bound-or-free treatment of electrons is scrutinized.

Much of the present investigations into IPD is based on quantifying the "boundness" of valence electronic states. A method for doing so is established in Chapter 3. First, it is identified that the spatial localization of the states may quantify boundness because free electrons are spatially delocalized across the entire plasma, while bound electrons are strongly localized around ions and are often treated as point-particles on the ion centres. Finite-temperature Kohn-Sham DFT [42, 52, 55] is used to calculate the wavefunctions as all states, regardless of boundness, are treated equally, and any effects that would be considered to contribute to CL appear self-consistently. It is argued that the spatial *extent* and spatial *localization* are two related but different concepts. It is then established the spatial localization of the states can be determined from the response of the spatial extent of the wavefunction to changes in the size of the unit cell. If the spatial extent is measured using the inverse participation ratio (IPR) [182, 183], the localization metric is the effective number of dimensions in which a state is delocalized. Validation in a simple metal and an ionic compound shows that this dimensionality parameter can provide meaningful localization information. The dimensionality also identifies the localized continuum electron in *d*-band metals [184, 185]. For well-localized states, the value of the dimensionality is the same ($D = 0$) regardless of the shape or size of the orbital; likewise, delocalized states high into the continuum have $D = 3$. The dimensionality therefore poses two useful properties: (1) it is possible to investigate the localization mechanisms of states in routine plasma processes by identifying when states can be considered localized and delocalized, in contrast to the spatial extent where it is ambiguous if spatially large states can be considered localized; and (2) it is essentially a first-principles-equivalent to an IPD model, and so allows direct comparison of the predictions of IPD models to first principles calculations.

Following the establishment of a theoretical framework to study IPD from first principles calculations, it is put into practice in Chapter 4 to investigate CL in highly-ionized solid density plasmas, where existing IPD models are known to falter. First, experimental evidence of K_β emission from highly-charged Mg ions are presented. This in contrast to a similar previous experiment in Ciricosta 2016 [40] which did

not directly observe such emission. This places a new upper-limit on the IPD, as in order for this emission to occur the $3p$ orbital must rebind to the Mg ions. A lower limit is still provided by the SP model which is known to under-predict the IPD [39, 143]. FT-DFT calculations of isochorically heated Mg, Al, and MgF_2 are then presented. It is seen for all three materials that at mid-charge states of the metal ions, three broad peaks peel off from the continuum in the DOS. These peaks are the metal ion M-shell orbitals. This in and of itself is not new – similar peaks were observed in FT-DFT calculations of Al in Vinko 2014 [38]. However, in the Vinko 2014 study it was not possible to determine if such energetically-broad features could be considered as bound or free states [38, 167]: on the one hand, peaks in the DOS are typically associated with localized features, but the energy broadening due to the Pauli exclusion principle [144] shows the states are spatially-extended as they have long-range knowledge of the plasma. The dimensionality analysis reveals that these broad peaks are in fact localized. For an IPD model, these M-shell states may therefore be associated with bound orbitals. The FT-DFT calculations thus supports the experimental observation of the K_β emission. The extremely weak intensity of the emission is in part explained by the energetic broadness of the states, which spreads the total intensity over a larger energy range, and the very low occupation numbers of the M-shell states.

Following these results, IPD energies are extracted from the DFT calculations. As IPD models essentially consider the continuum edge to separate bound and free states, the equivalent edge from the DFT calculations was chosen by the localized-to-delocalized point. At low charge states, the FT-DFT calculations agree well with the EK model, which is also in agreement with similar previous studies [38–40]. At high charge states, the IPD lies somewhere between the mEK and SP models, a behaviour which has been seen in experiment [143], theoretical studies [122], and newer IPD models [123, 124]. At mid-charge states, the IPD suddenly lowers due to the relocalization of the M-shell states – this behaviour cannot be reproduced by existing IPD models.

The remaining discrepancies between this work and Ciricosta 2016 are addressed

by a reinterpretation of the Ciricosta 2016 data. In comparison to the K_α emission data from Ciricosta 2016 (see Fig. 4.7), peak-like features in the K_α emission intensity for Mg^{8+} and Mg^{9+} are now re-interpreted as evidence of pumping of the K_β transition. This re-interpretation is supported by these peaks having the same energies as the direct K_β emission measurements, and the FT-DFT calculations demonstrating localized M-shell states for these charge states. There are features in the K_α data for Mg^{6+} and Mg^{7+} which are not obviously peaks, but do have energies similar to the relevant K_β transitions. They therefore suggest the continuum edge may be higher than originally inferred at these charge states. For the Mg^{5+} charge state, there is no clear feature between the Ciricosta 2016 edge and the localized-delocalized edge from DFT. If the edge energy in DFT is chosen to be the continuum edge instead of the localized-delocalized edge, the Ciricosta 2016 and the DFT IPD K-edge energies are closer in energy. This demonstrates that it is generally difficult to unambiguously distinguish the true continuum edge from close-lying bound states. This will inevitably pose challenges in the development and testing of new IPD models.

Chapter 5 deals with the concept of ionization. Ionization is a problematic quantity in that it does not have a well-defined thermodynamic definition, unlike temperature and density, yet it is a key parameter within plasma modelling. As it is an input parameter to many equations, the choice of definition of ionization has a cascading effect on the evolution of a plasma during modelling. Often the ionization state is determined from the number of continuum electrons freed from ions, but it is not clear if such a bound-or-free definition is always appropriate, or whether this quantity is what is accessed in spectroscopic measurements. Indeed, recent experimental measurements of the mean ionization state (MIS) of hot dense CH (Kraus 2016) [164] and Be (Döppner 2023) [195] produced in implosions at the NIF suggest that the MIS predicted by this bound-or-free definition is significantly lower than inferred from x-ray Thomson scattering (XRTS) spectra. In Döppner 2023, a recently proposed definition of ionization – based on the TRK [201–203] sum of the conduction-conduction ($c \to c$) conductivity [131, 197, 198] – seemed to

agree well with the experimental data at the highest densities and temperatures achieved. However, at lower densities and temperatures, when simpler IPD modelling was able to reproduce the experimental data, the conductivity-based definition appeared to over-predict the MIS. It has previously been seen in condensed matter physics that the $c \to c$ conductivity-based definitions over-counts the number of conduction electrons [206]. However, Kobayasi and Watabe [206] showed that a correctional term involving Pauli-forbidden transitions needs to be included to ensure the conduction electrons are properly accounted for. In this chapter, Kobayasi and Watabe's argument have been extended to finite-temperatures, resulting in similar "Pauli forbidden" transitions, showing that the conductivity-based definition will over-count the number of electrons. The degree to which it does is investigated in hot dense CH plasmas, with the conditions chosen to match those inferred from Kraus 2016 [164] so the calculations could be compared against experimental data. First, it is remarked that the equivalent definition of bound-or-free ionization in the presented first principles calculations is to count the number of electrons in the continuum. It is then shown that using the $c \to c$ conductivity to define ionization, as proposed in Bethkenhagen 2020 [131], produces a significantly higher MIS than the counting definition. It is particularly apparent at low temperatures that the conductivity definition over-counts the number of electrons. However, including the "Pauli forbidden" transitions recovers the counting definition. Given that these corrective terms are substantial, even at high temperatures, it is argued that they are important to correctly calculating the MIS from the conductivity.

These results are then compared to the XRTS-inferred MIS from Kraus 2016. It is found that the counting definition still predicts a substantially lower MIS than was inferred from the experiment. The $c \to c$ conductivity-based definition is closer to the experimental MIS, but is still lower across the inferred temperature range. It is also noted that in Döppner 2023, the $c \to c$ conductivity-based definition agreed well with XRTS-inferred MIS at very high temperatures and densities, where the plasma modelling otherwise under-predicts the MIS. This apparent improvement in the predictions by the $c \to c$ conductivity-based definition is therefore ascribed

to the conductivity-based definition over-counting the number of electrons in the continuum. This does raise the question of what are the additional electrons that XRTS measurements seem to suggest there should be compared with the counting definition. Döppner 2023 identify that their XRTS spectra is reproduced when the Be K-shell is allowed to delocalize due to screening by the continuum electron density. The final MIS inferred from the XRTS spectra is still higher than predicted by IPD modelling. As IPD models consider electrons to be strongly localized around atomic sites, they are not able to treat the gradual delocalization of bound electrons. Among other effects, the delocalization of the K-shell also results in them overlapping. As a result, the K-shell electrons are able to move between atomic sites. These additional mobile electrons would appear as an increase in the MIS. If the K-shell electrons are mobile, they would be represented by $v \rightarrow v$ transitions in the conductivity, which has not been accounted for in any of the definitions of MIS used. For the present work, the contribution of these transitions are extremely small but non-zero at electrons temperatures exceeding 40 eV. So, while the $v \rightarrow v$ transitions cannot meaningfully change the MIS directly from their conductivity, they do suggest that there are mobile bound electrons. It is therefore speculated that a more detailed treatment of bound electrons may explain the increased ionization.

6.2 Future Work

To consider the future outlook of IPD models, it is worth returning to why they are compelling. The treatment of electrons as being purely bound to ions or purely free, while evidently an overly-simplistic picture of reality, allows for analytical continuum lowering models to be constructed that are conceptually simple to understand, and computationally convenient. After all, full spatial and time-evolved collisional-radiative atomic kinetics calculations are still extremely time consuming to model for the complete spectral emission of a plasma during laser and FEL interactions. To finish this thesis, I will briefly discuss and speculate on the future directions of the presented topics.

6.2.1 Dimensionality Analysis

The dimensionality analysis provides a means to investigate how states localize and delocalize during common plasma processes, in a relatively simple manner. It also provides a means to physically justify which states can be considered as bound or free, if such an approximation is being made. However, the method is currently too cumbersome and slow to use directly in-line atomic kinetic codes, though it is noteworthy that there are recent attempts to use DFT-like models to inform about levels that would be involved in transition processes [18]. Where the dimensionality parameter may be most useful for IPD modelling is as a benchmark of which states to expect to be bound or free. Experimental measurements of IPD are invaluable, but there are only a few datasets and firm conclusions on the IPD are difficult to extract. As FT-DFT simulations provide a way to generate large datasets that can provide information on continuum lowering, having a means to connect first principles calculations of IPD via the dimensionality to the models themselves is extremely useful in benchmarking.

The dimensionality analysis method still requires improvements. There are two main difficulties with the dimensionality that further development needs to address. The first is that the dimensionality requires a second calculation to be performed with an expanded unit cell. Expanding the unit cell changes the crystal structure, and so the solution to the KS wavefunctions. The dimensionality parameter inevitably captures this change. For a sufficiently small change in the lattice parameters, the averaged dimensionality describes the spatial localization behaviour, but the dimensionality for individual Kohn-Sham states can be very difficult to interpret. The change in lattice parameter also cannot be too small as otherwise the KS wavefunctions may not change meaningfully enough, and there are risks with the stability of the numerical derivative. As a consequence, for systems that are particularly sensitive to changes in the size of the unit cell, the dimensionality parameter may not be usable. Secondly, while the dimensionality comes from the solutions to the KS equations, it is otherwise agnostic to the ion centers as they

do not feature explicitly in Eq. (3.14). This makes it hard to associate a particularly dimensionality behaviour to a particular ion. Some other metrics, such as the projected DOS, can aid in identifying dimensionalities with features. But, if there are a lot of energetically-overlapping states and there are many different ions, understanding how the dimensionality corresponds to a particular state and ion is challenging. However, one can at least envision developing the method to account for the contributions from within PAW cores.

There is also a reasonably high computational cost associated with calculating the IPR with my present implementation in ABINIT v8, beyond the normal DFT cost. Currently, the IPR is calculated using the AE wavefunctions instead of the computationally-efficient PAW PS wavefunctions. As the IPR is calculated using $|\psi(\boldsymbol{r})|^4$, a very fine grid is needed to be able to accurately resolve the large oscillations in the quartic of the AE wavefunction. Limited testing performed early in the development of the method seemed to indicated that just calculating the IPR of the PS wavefunctions without also accounting for onsite contributions did not give useful localization information. This is perhaps because evaluating the PS wavefunctions directly in real space instead of the pseudo space is too far removed from meaningful orbitals. Still, an efficient implementation of the IPR calculation may be possible with careful use of PAW operators to evaluate the AE IPR from the PS wavefunctions. For the implementation of a parallelized IPR module using the PS wavefunctions in the ABINIT v8 code, there were challenges that I did not have time to resolve during my doctorate. But, they are certainly achievable, and will provide benefits of faster and less memory-intensive dimensionality calculations.

Further development of the dimensionality method may be able to address its short-comings. Nonetheless, the work in this thesis has demonstrated that the analysis of the spatial localization of states provides a useful tool comparing first principles calculations and IPD models. Given the importance of IPD to plasma calculations, there will certainly be more advanced models developed in the coming years. Spatial localization analysis will therefore continue to play a role in the development and analysis of these new models.

6.2.2 Future of IPD Models

In recent years there have been more advanced analytical IPD models beyond the SP and mEK models. Two particularly promising examples are the Crowley model [123] and the OEFTIS model [124]. Both of these models appear to agree much better with the first principles IPD calculations presented in Chapter 4, and agree qualitatively with some experimental measurements [30, 39, 143] and other theoretical studies [38, 120, 122].

The Crowley model is conceptually and mathematically quite complex. In essence, it identifies different continuum lowering effects in a plasma depending on the timescale of a given process. The IPD from an event such as photoionization or a collision are too fast for the plasma to be transitioning between thermal equilibrium states. Additionally, the underlying plasma model [168] used to derive the analytical IPD model is very general. The IS, SP, and DH models are all naturally derived in appropriate limits. Electron degeneracy effects are also accounted for as part of the construction. The more detailed theory underpinning the Crowley model may explain why it performs quite well when compared against the results of Chapter 4. The OEFTIS model is notable as it attempts to include (n, l)-dependence in the IPD. This allows for effects such as PPS to be accounted for, and the model appears to perform quite well in this regard [124]. However, the OEFTIS is still fundamentally an ion-sphere model and the screening effects of thermal ions are not accounted for. Indeed, Rosmej identifies a temperature and density range in which the model is expected to be applicable. Nevertheless, the OEFTIS model may be useful for FEL experiments in which the ion motion is negligible during emission, as seen in Fig. 4.8. Crowley's model can also include (n, l)-dependence via the term $\Delta U_{j,\alpha}$ in Eq. (2.95). When evaluating the $\Delta U_{j,\alpha}$, it is approximated that the specifics of the state α are negligible, so $\Delta U_{j,\alpha} \approx \Delta U_j$. However, as has been argued in this thesis, PPS is still an important effect in bound-or-free treatments of electrons as it can allow for an electron to remain bound where it would otherwise be (scarcely) free.

Another aspect that is missing from even the more advanced IPD models are sudden changes in the continuum level directly due to states rebinding. In Figs. 4.3 and 4.8, this appears as a rapid decrease in the IPD as the continuum level suddenly increases when the M-shell rebinds – the position of the continuum level and the rebinding of states are directly linked. For IPD models, the link between the continuum level and rebinding is weaker, with the continuum level being more akin to a sliding scale that adjusts against the set of possible bound energy levels. Even then, the IPD only changes when the rebound states become occupied due to collisional or radiative events, as this changes the charge states and free electron density. This is not nearly as strong a link as a broad region of the continuum breaking off into quasi-atomic states. How this might be modelled via IPD is unlikely to be trivial.

The dimensionality analysis highlights there is a particular need to treat the continuum (free) electrons beyond the simple free electron gas. This is likely to be very challenging. One potential avenue for understanding appropriate approximations of the continuum electrons is to return to the Kohn-Sham orbital-free method described in Chapter 1. The orbital-free approximations that were described in this section may be further generalized to higher order corrections [96]. One could then perform KS-OF calculations in which the non-continuum states are calculated with the KS equations, while the entire continuum is treated with an orbital-free approximation except for one KS band used to track the continuum edge energy. Equally, by initializing the calculation with the number of KS states equal to the number of atomic orbitals, while treating the remaining states as orbital-free, the effect of orbital-free approximations on the localization and delocalization of states during plasma processes can also be investigated. Systematic studies may therefore be performed to determine what level of orbital-free approximation beyond the HEG (i.e. the KS-PWA method) is acceptable. This would allow a more focused development of IPD models.

Newer IPD models are promising. They capture more of the physics behind continuum lowering, and are tending to produce more accurate predictions. And, at the very least, they are informative about which of the physics of continuum

lowering needs to be included. The methods laid out in this thesis demonstrate that first principles studies can provide useful insight into the physics of continuum lowering, as well as providing an important tool for benchmarking new models. First principles calculations may also be used to identify appropriate approximations to focus the development of new IPD models. Yet, further developments in analytical models are likely to be challenging. It may have to be accepted that a general analytical IPD model, applicable to all plasmas, may not be possible, and that the direction we take is finding models that are specific to certain plasmas. Nonetheless, the continued development of more advanced IPD models highlights that there may yet be a path to analytical IPD models that provide sufficiently accurate results in a wide class of plasmas.

6.2.3 Defining Ionization

Useful definitions of ionization are a necessity for making good predictions from plasma models. Much like for IPD, a definition of ionization based on bound-or-free electrons is conceptually and computationally simple. However, as with IPD, this is too simple a picture of reality to be a good representation of ionization in all cases. For x-ray scattering at least, Döppner 2023 has shown that it is also necessary to account for the gradual delocalization of the bound electron wavefunctions at very high temperatures and densities. This again reflects the limitations of a purely bound-or-free treatment of electrons in plasma modelling: bound electrons are considered to always be strongly localized on atomic nuclei, so current models cannot account for the gradual delocalization due to screening effects. It should also be expected that the gradual delocalization of bound electrons will also affect spectral properties by changing the transition line shapes and energies, as well as the available transitions.

Evidently, how best to account for the effect of the delocalizing bound electrons in ionization calculations should be investigated. Döppner 2023 suggests a simple Debye-like model provides sufficient modification to the Be K-shell for modelling their XRTS spectra. It should be noted that Debye theory is not applicable in

strongly-coupled degenerate systems, and that the screening model is based on hydrogenic wavefunctions, so it is unlikely that such an approach is generally suitable. Nonetheless, it appears to be sufficient for their analysis. The delocalization of the Be K-shell is primarily required to explain the reduced intensity of the elastic scattering feature compared with the Compton feature. However, the XRTS-inferred MIS is still higher than extracted from the IPD modelling. This might be explained by the K-shell electrons becoming mobile as a result of their delocalization, causing the MIS experienced by the scattering photons to be higher than from just the continuum electrons. In other words, the MIS in scattering would be a measure of the effective number of mobile electrons, not just those in the continuum. 'Effective' here refers to the fact that electrons that are quasi-localized would be less mobile than a completely delocalized electron, so their contribution to the MIS may be reduced. How to account for these effects should be examined further.

It should also be considered whether ionization is universally defined. There is an implicit assumption that the ionization state accessed in, for example, x-ray scattering is also the ionization accessed in an emission event, or experienced by particles moving in a plasma. Indeed, the fact that ionization is not a well-defined quantity means that different definitions of ionization may describe different properties of the plasma – such as the number of continuum electron versus the number mobile electrons – and that whether a particular definition can be considered good depends on the process being investigated. There is some evidence that suggests this is the case, such as in Sterne 2007 [196]. There, it was found that depending on the physical property under investigation, the ionization can be better described by the number of continuum electrons, or by the number of electrons beyond the Wigner-Seitz surface. Neither definition appears to be perfect, though this may also be in part due to limitations of the modelling. Equally, this may point to different measurements accessing the same underlying quantity in different ways, resulting in the measured ionizaition states appearing to be different. Nonetheless, it is evident that careful consideration of what is being described by ionization will be important in developing useful definitions for plasma modelling.

Bibliography

[1] Tristan Guillot. Interiors of giant planets inside and outside the solar system. *science*, 286(5437):72–77, 1999.

[2] N Nettelmann, R Redmer, and D Blaschke. Warm dense matter in giant planets and exoplanets. *Physics of Particles and Nuclei*, 39:1122–1127, 2008.

[3] James E Bailey, Taisuke Nagayama, Guillaume Pascal Loisel, Gregory Alan Rochau, C Blancard, James Colgan, Ph Cosse, G Faussurier, CJ Fontes, F Gilleron, et al. A higher-than-predicted measurement of iron opacity at solar interior temperatures. *Nature*, 517(7532):56–59, 2015.

[4] Andrea L Kritcher, Damian C Swift, Tilo Döppner, Benjamin Bachmann, Lorin X Benedict, Gilbert W Collins, Jonathan L DuBois, Fred Elsner, Gilles Fontaine, Jim A Gaffney, et al. A measurement of the equation of state of carbon envelopes of white dwarfs. *Nature*, 584(7819):51–54, 2020.

[5] J M Soures, S J Loucks, R L McCrory, C P Verdon, A Babushkin, R E Bahr, T R Boehly, R Boni, D K Bradley, D L Brown, et al. The role of the laboratory for laser energetics in the national ignition facility project. *Fusion Technology*, 30(3P2A):492–496, 1996.

[6] RL McCrory, DD Meyerhofer, R Betti, RS Craxton, JA Delettrez, DH Edgell, V Yu Glebov, VN Goncharov, DR Harding, DW Jacobs-Perkins, et al. Progress in direct-drive inertial confinement fusion. *Physics of Plasmas*, 15(5):055503, 2008.

[7] R Betti, K Anderson, TR Boehly, TJB Collins, RS Craxton, JA Delettrez,

DH Edgell, R Epstein, V Yu Glebov, VN Goncharov, et al. Progress in hydrodynamics theory and experiments for direct-drive and fast ignition inertial confinement fusion. *Plasma physics and controlled fusion*, 48(12B):B153, 2006.

[8] John Lindl. Development of the indirect-drive approach to inertial confinement fusion and the target physics basis for ignition and gain. *Physics of plasmas*, 2(11):3933–4024, 1995.

[9] E I Moses, R N Boyd, B A Remington, C J Keane, and R Al-Ayat. The National Ignition Facility: Ushering in a new age for high energy density science. *Physics of Plasmas*, 16(4):041006, 2009.

[10] John Nuckolls, Lowell Wood, Albert Thiessen, and George Zimmerman. Laser compression of matter to super-high densities: Thermonuclear (CTR) applications. *Nature*, 239(5368):139–142, 1972.

[11] Stefano Atzeni and Jürgen Meyer-ter Vehn. *The physics of inertial fusion: beam plasma interaction, hydrodynamics, hot dense matter*, volume 125. Oxford University Press, 2004.

[12] D J Hoarty, P Allan, S F James, C R D Brown, L M R Hobbs, M P Hill, J W O Harris, J Morton, M G Brookes, R Shepherd, et al. The first data from the Orion laser; measurements of the spectrum of hot, dense aluminium. *High Energy Density Physics*, 9(4):661–671, 2013.

[13] S M Vinko, O Ciricosta, B I Cho, K Engelhorn, H.-K. Chung, C R D Brown, T Burian, J Chalupskỳ, R W Falcone, C Graves, et al. Creation and diagnosis of a solid-density plasma with an X-ray free-electron laser. *Nature*, 482(7383): 59–62, 2012.

[14] H Abu-Shawareb, R Acree, P Adams, J Adams, B Addis, R Aden, P Adrian, BB Afeyan, M Aggleton, L Aghaian, et al. Lawson criterion for ignition exceeded in an inertial fusion experiment. *Phys. Rev. Lett.*, 129(7):075001, 2022.

[15] AB Zylstra, AL Kritcher, OA Hurricane, DA Callahan, JE Ralph, DT Casey, A Pak, OL Landen, B Bachmann, KL Baker, et al. Experimental achievement and signatures of ignition at the National Ignition Facility. *Phys. Rev. E*, 106 (2):025202, 2022.

[16] Breanna Bishop. National Ignition Facility achieves fusion ignition. *Lawrence Livermore National Laboratory, December*, 14, 2022.

[17] AL Kritcher, AB Zylstra, DA Callahan, OA Hurricane, CR Weber, DS Clark, CV Young, JE Ralph, DT Casey, A Pak, et al. Design of an inertial fusion experiment exceeding the Lawson criterion for ignition. *Phys. Rev. E*, 106(2): 025201, 2022.

[18] SX Hu, David T Bishel, David A Chin, Philip M Nilson, Valentin V Karasiev, Igor E Golovkin, Ming Gu, Stephanie B Hansen, Deyan I Mihaylov, Nathaniel R Shaffer, et al. Probing atomic physics at ultrahigh pressure using laser-driven implosions. *Nature Communications*, 13(1):6780, 2022.

[19] Byoung Ick Cho. X-ray Spectroscopies of High Energy Density Matter Created with X-ray Free Electron Lasers. *Applied Sciences*, 9(22):4812, 2019.

[20] P Debye and E Hückel. Zur theorie der elektrolyte. *Phys. Z*, 24:185–206, 1923.

[21] Elliott H Lieb and Heide Narnhofer. The thermodynamic limit for jellium. *Journal of statistical physics*, 12(4):291–310, 1975.

[22] Marc Baus and Jean-Pierre Hansen. Statistical mechanics of simple Coulomb systems. *Physics Reports*, 59(1):1–94, 1980.

[23] Eugene Wigner. On the interaction of electrons in metals. *Physical Review*, 46(11):1002, 1934.

[24] Evgenij L Saldin, Evgeny A Schneidmiller, and Mikhail V Yurkov. The physics of free electron lasers. An introduction. *Physics reports*, 260(4-5):187–327, 1995.

[25] Zhirong Huang and Kwang-Je Kim. Review of x-ray free-electron laser theory. *Physical Review Special Topics-Accelerators and Beams*, 10(3):034801, 2007.

[26] Peter Schmüser, Martin Dohlus, Jörg Rossbach, and Christopher Behrens. Free-electron lasers in the ultraviolet and X-ray regime. *Springer Tracts in Modern Physics*, 258, 2014.

[27] Manfred Otto Krause and JH Oliver. Natural widths of atomic K and L levels, K α X-ray lines and several KLL Auger lines. *Journal of Physical and Chemical Reference Data*, 8(2):329–338, 1979.

[28] H.-K. Chung, M. H. Chen, W. L. Morgan, Y. Ralchenko, and R. W. Lee. FLYCHK: Generalized population kinetics and spectral model for rapid spectroscopic analysis for all elements. *High Energy Density Physics*, 1(1):3–12, 2005. doi: https://doi.org/10.1016/j.hedp.2005.07.001.

[29] H.-K. Chung, M. H. Chen, and R. W. Lee. Extension of atomic configuration sets of the Non-LTE model in the application to the Kα diagnostics of hot dense matter. *High Energy Density Physics*, 3(1):57–64, 2007. doi: https://doi.org/10.1016/j.hedp.2007.02.001. Radiative Properties of Hot Dense Matter.

[30] O Ciricosta, S M Vinko, H.-K. Chung, C Jackson, R W Lee, T R Preston, D S Rackstraw, and J S Wark. Detailed model for hot-dense aluminum plasmas generated by an x-ray free electron laser. *Physics of Plasmas*, 23(2):022707, 2016.

[31] Shenyuan Ren, Yuanfeng Shi, Quincy Y van den Berg, Muhammad F Kasim, Hyun-Kyung Chung, Elisa V Fernandez-Tello, Pedro Velarde, Justin S Wark, and Sam M Vinko. Non-thermal evolution of dense plasmas driven by intense x-ray fields. *Communications Physics*, 6(1):99, 2023.

[32] S. M. Vinko, O. Ciricosta, T. R. Preston, D. S. Rackstraw, C. R. D. Brown, T. Burian, J. Chalupskỳ, Byeoung Ick Cho, H.-K. Chung, K. Engelhorn, et al. Investigation of femtosecond collisional ionization rates in a solid-density aluminium plasma. *Nature communications*, 6(1):1–7, 2015.

[33] Q. Y. van den Berg, E V Fernandez-Tello, T Burian, J Chalupský, H.-K. Chung, O Ciricosta, G L Dakovski, V Hájková, P Hollebon, L Juha, J Krzywinski, R. W. Lee, M. P. Minitti, Preston T. R., de laVarga A G, V Vozda, U Zastrau, J S Wark, P Velarde, and S M Vinko. Clocking femtosecond collisional dynamics via resonant x-ray spectroscopy. *Phys. Rev. Lett.*, 120(5): 055002, 2018.

[34] T R Preston, S M Vinko, O Ciricosta, P Hollebon, H.-K. Chung, G L Dakovski, J Krzywinski, M Minitti, T Burian, J Chalupskỳ, et al. Measurements of the k-shell opacity of a solid-density magnesium plasma heated by an x-ray free-electron laser. *Phys. Rev. Lett.*, 119(8):085001, 2017.

[35] A. Ng, P. Celliers, G. Xu, and A. Forsman. Electron-ion equilibration in a strongly coupled plasma. *Phys. Rev. E*, 52:4299–4310, 1995. doi: 10.1103/PhysRevE.52.4299.

[36] Matthieu Nicoul, Uladzimir Shymanovich, Alexander Tarasevitch, Dietrich von der Linde, and Klaus Sokolowski-Tinten. Picosecond acoustic response of a laser-heated gold-film studied with time-resolved x-ray diffraction. *Applied Physics Letters*, 98(19):191902, 2011. doi: 10.1063/1.3584864.

[37] T. G. White, P. Mabey, D. O. Gericke, N. J. Hartley, H. W. Doyle, D. McGonegle, D. S. Rackstraw, A. Higginbotham, and G. Gregori. Electron-phonon equilibration in laser-heated gold films. *Phys. Rev. B*, 90:014305, 2014. doi: 10.1103/PhysRevB.90.014305.

[38] S M Vinko, O Ciricosta, and J S Wark. Density functional theory calculations of continuum lowering in strongly coupled plasmas. *Nature Communications*, 5(1):3533, 2014.

[39] O. Ciricosta, S. M. Vinko, H.-K. Chung, B.-I. Cho, C. R. D. Brown, T. Burian, J. Chalupský, K. Engelhorn, R. W. Falcone, C. Graves, V. Hájková, A. Higginbotham, L. Juha, J. Krzywinski, H. J. Lee, M. Messerschmidt, C. D. Murphy, Y. Ping, D. S. Rackstraw, A. Scherz, W. Schlotter, S. Toleikis, J. J. Turner,

L. Vysin, T. Wang, B. Wu, U. Zastrau, D. Zhu, R. W. Lee, P. Heimann, B. Nagler, and J. S. Wark. Direct Measurements of the Ionization Potential Depression in a Dense Plasma. *Phys. Rev. Lett.*, 109:065002, 2012. doi: 10.1103/PhysRevLett.109.065002.

[40] O Ciricosta, S M Vinko, B Barbrel, D S Rackstraw, T R Preston, T Burian, J Chalupský, B I Cho, H-K Chung, G L Dakovski, K Engelhorn, V Hájková, P Heimann, M Holmes, L Juha, J Krzywinski, R W Lee, S Toleikis, J J Turner, U Zastrau, and J S Wark. Measurements of continuum lowering in solid-density plasmas created from elements and compounds. *Nature Communications*, 7 (1):11713, 2016.

[41] Kasim, M. F. and Galligan, T. P. and Topp-Mugglestone, J. and Gregori, G. and Vinko, S. M. Inverse problem instabilities in large-scale modeling of matter in extreme conditions. *Physics of Plasmas*, 26(11):112706, 2019. doi: 10.1063/1.5125979.

[42] P. Hohenberg and W. Kohn. Inhomogeneous Electron Gas. *Phys. Rev.*, 136: B864–B871, 1964. doi: 10.1103/PhysRev.136.B864.

[43] Llewellyn H Thomas. The calculation of atomic fields. In *Mathematical proceedings of the Cambridge philosophical society*, volume 23, pages 542–548. Cambridge University Press, 1927.

[44] Enrico Fermi. Un metodo statistico per la determinazione di alcune priorieta dell'atome. *Rend. Accad. Naz. Lincei*, 6(602-607):32, 1927.

[45] Enrico Fermi. Eine statistische Methode zur Bestimmung einiger Eigenschaften des Atoms und ihre Anwendung auf die Theorie des periodischen Systems der Elemente. *Zeitschrift für Physik*, 48(1-2):73–79, 1928.

[46] Paul AM Dirac. Note on exchange phenomena in the Thomas atom. In *Mathematical proceedings of the Cambridge philosophical society*, volume 26, pages 376–385. Cambridge University Press, 1930.

[47] Richard M Martin. *Electronic structure: basic theory and practical methods*. Cambridge university press, 2020.

[48] Max Born and W Heisenberg. Zur quantentheorie der molekeln. *Original Scientific Papers Wissenschaftliche Originalarbeiten*, pages 216–246, 1985.

[49] Ulf Von Barth and Lars Hedin. A local exchange-correlation potential for the spin polarized case. i. *Journal of Physics C: Solid State Physics*, 5(13):1629, 1972.

[50] G Vignale and Mark Rasolt. Current-and spin-density-functional theory for inhomogeneous electronic systems in strong magnetic fields. *Phys. Rev. B*, 37 (18):10685, 1988.

[51] G Vignale and Mark Rasolt. Density-functional theory in strong magnetic fields. *Phys. Rev. Lett.*, 59(20):2360, 1987.

[52] N. David Mermin. Thermal Properties of the Inhomogeneous Electron Gas. *Phys. Rev.*, 137:A1441–A1443, 1965. doi: 10.1103/PhysRev.137.A1441.

[53] M Pearson, Enrico Smargiassi, and PA Madden. Ab initio molecular dynamics with an orbital-free density functional. *Journal of Physics: Condensed Matter*, 5(19):3221, 1993.

[54] Flavien Lambert, Jean Clérouin, and Gilles Zérah. Very-high-temperature molecular dynamics. *Phys. Rev. E*, 73(1):016403, 2006.

[55] W. Kohn and L. J. Sham. Self-Consistent Equations Including Exchange and Correlation Effects. *Phys. Rev.*, 140:A1133–A1138, 1965. doi: 10.1103/PhysRev.140.A1133.

[56] Xavier Gonze, François Jollet, F Abreu Araujo, Donat Adams, Bernard Amadon, Thomas Applencourt, Christophe Audouze, J-M Beuken, Jordan Bieder, A Bokhanchuk, et al. Recent developments in the ABINIT software package. *Comput. Phys. Commun.*, 205:106–131, 2016. doi: 10.1016/j.cpc.2016.04.003.

[57] François Bottin, Stéphane Leroux, Andrew Knyazev, and Gilles Zérah. Large-scale ab initio calculations based on three levels of parallelization. *Computational Materials Science*, 42(2):329–336, 2008. doi: 10.1016/j.commatsci.2007.07.019.

[58] Paolo Giannozzi, Stefano Baroni, Nicola Bonini, Matteo Calandra, Roberto Car, Carlo Cavazzoni, Davide Ceresoli, Guido L Chiarotti, Matteo Cococcioni, Ismaila Dabo, et al. QUANTUM ESPRESSO: a modular and open-source software project for quantum simulations of materials. *Journal of physics: Condensed matter*, 21(39):395502, 2009.

[59] Paolo Giannozzi, Oliviero Andreussi, Thomas Brumme, Oana Bunau, M Buongiorno Nardelli, Matteo Calandra, Roberto Car, Carlo Cavazzoni, Davide Ceresoli, Matteo Cococcioni, et al. Advanced capabilities for materials modelling with Quantum ESPRESSO. *Journal of physics: Condensed matter*, 29 (46):465901, 2017.

[60] Georg Kresse and Jürgen Hafner. Ab initio molecular dynamics for liquid metals. *Phys. Rev. B*, 47(1):558, 1993.

[61] Georg Kresse and Jürgen Furthmüller. Efficient iterative schemes for ab initio total-energy calculations using a plane-wave basis set. *Phys. Rev. B*, 54(16): 11169, 1996.

[62] James F Janak. Proof that $\partial e/\partial n_i = \varepsilon$ in density-functional theory. *Phys. Rev. B*, 18(12):7165, 1978.

[63] John P Perdew and Michael R Norman. Electron removal energies in Kohn-Sham density-functional theory. *Phys. Rev. B*, 26(10):5445, 1982.

[64] Mel Levy, John P Perdew, and Viraht Sahni. Exact differential equation for the density and ionization energy of a many-particle system. *Phys. Rev. A*, 30 (5):2745, 1984.

[65] John P Perdew, Weitao Yang, Kieron Burke, Zenghui Yang, Eberhard KU Gross, Matthias Scheffler, Gustavo E Scuseria, Thomas M Henderson, Igor Ying Zhang, Adrienn Ruzsinszky, et al. Understanding band gaps of solids in generalized Kohn–Sham theory. *Proceedings of the national academy of sciences*, 114(11):2801–2806, 2017.

[66] SB Trickey. Comment on" Electron removal energies in Kohn-Sham density-functional theory". *Phys. Rev. B*, 30(6):3523, 1984.

[67] John P Perdew and Michael R Norman. Reply to "Comment on Electron removal energies in Kohn-Sham density-functional theory". *Phys. Rev. B*, 30 (6):3525, 1984.

[68] John P Perdew and Mel Levy. Physical content of the exact Kohn-Sham orbital energies: band gaps and derivative discontinuities. *Phys. Rev. Lett.*, 51(20): 1884, 1983.

[69] John P Perdew. What do the Kohn-Sham orbital energies mean? How do atoms dissociate? *Density Functional Methods in Physics*, pages 265–308, 1985.

[70] Ralf Stowasser and Roald Hoffmann. What do the Kohn- Sham orbitals and eigenvalues mean? *Journal of the american chemical society*, 121(14):3414–3420, 1999.

[71] Oleg Gritsenko and Evert Jan Baerends. The analog of Koopmans' theorem for virtual Kohn–Sham orbital energies. *Canadian Journal of Chemistry*, 87 (10):1383–1391, 2009.

[72] Susi Lehtola, Conrad Steigemann, Micael JT Oliveira, and Miguel AL Marques. Recent developments in libxc—A comprehensive library of functionals for density functional theory. *SoftwareX*, 7:1–5, 2018.

[73] Muhammad F Kasim and Sam M Vinko. Learning the exchange-correlation

functional from nature with fully differentiable density functional theory. *Phys. Rev. Lett.*, 127(12):126403, 2021.

[74] Muhammad F Kasim, Susi Lehtola, and Sam M Vinko. DQC: A Python program package for differentiable quantum chemistry. *The Journal of chemical physics*, 156(8):084801, 2022.

[75] John P Perdew and Yue Wang. Accurate and simple analytic representation of the electron-gas correlation energy. *Phys. Rev. B*, 45(23):13244, 1992.

[76] John P. Perdew, Kieron Burke, and Matthias Ernzerhof. Generalized Gradient Approximation Made Simple. *Phys. Rev. Lett.*, 77:3865–3868, 1996. doi: 10.1103/PhysRevLett.77.3865.

[77] Douglas R Hartree. The wave mechanics of an atom with a non-Coulomb central field. Part I. Theory and methods. In *Mathematical Proceedings of the Cambridge Philosophical Society*, volume 24, pages 89–110. Cambridge University Press, 1928.

[78] Vladimir Fock. Näherungsmethode zur Lösung des quantenmechanischen Mehrkörperproblems. *Zeitschrift für Physik*, 61:126–148, 1930.

[79] Douglas Rayner Hartree and William Hartree. Self-consistent field, with exchange, for beryllium. *Proceedings of the Royal Society of London. Series A-Mathematical and Physical Sciences*, 150(869):9–33, 1935.

[80] Ethan W Brown, Bryan K Clark, Jonathan L DuBois, and David M Ceperley. Path-integral Monte Carlo simulation of the warm dense homogeneous electron gas. *Phys. Rev. Lett.*, 110(14):146405, 2013.

[81] Valentin V Karasiev, Travis Sjostrom, James Dufty, and SB Trickey. Accurate homogeneous electron gas exchange-correlation free energy for local spin-density calculations. *Phys. Rev. Lett.*, 112(7):076403, 2014.

[82] Simon Groth, Tobias Dornheim, Travis Sjostrom, Fionn D Malone, W M C Foulkes, and Michael Bonitz. Ab initio exchange-correlation free energy of the

uniform electron gas at warm dense matter conditions. *Phys. Rev. Lett.*, 119 (13):135001, 2017.

[83] Valentin V Karasiev, James W Dufty, and SB Trickey. Nonempirical semilocal free-energy density functional for matter under extreme conditions. *Phys. Rev. Lett.*, 120(7):076401, 2018.

[84] DI Mihaylov, VV Karasiev, and SX Hu. Thermal hybrid exchange-correlation density functional for improving the description of warm dense matter. *Phys. Rev. B*, 101(24):245141, 2020.

[85] Valentin V Karasiev, DI Mihaylov, and SX Hu. Meta-GGA exchange-correlation free energy density functional to increase the accuracy of warm dense matter simulations. *Phys. Rev. B*, 105(8):L081109, 2022.

[86] Peter Schwerdtfeger. The pseudopotential approximation in electronic structure theory. *ChemPhysChem*, 12(17):3143–3155, 2011.

[87] D R Hamann, M Schlüter, and C Chiang. Norm-conserving pseudopotentials. *Physical Review Letters*, 43(20):1494, 1979.

[88] Andrew M Rappe, Karin M Rabe, Efthimios Kaxiras, and J D Joannopoulos. Optimized pseudopotentials. *Physical Review B*, 41(2):1227, 1990.

[89] David Vanderbilt. Soft self-consistent pseudopotentials in a generalized eigenvalue formalism. *Physical review B*, 41(11):7892, 1990.

[90] P. E. Blöchl. Projector augmented-wave method. *Phys. Rev. B*, 50:17953–17979, 1994. doi: 10.1103/PhysRevB.50.17953.

[91] Augustin Blanchet, Marc Torrent, and Jean Clerouin. Requirements for very high temperature Kohn–Sham DFT simulations and how to bypass them. *Physics of Plasmas*, 27(12):122706, 2020.

[92] Shen Zhang, Hongwei Wang, Wei Kang, Ping Zhang, and X. T. He. Extended application of Kohn-Sham first-principles molecular dynamics method with

plane wave approximation at high energy—From cold materials to hot dense plasmas. *Physics of Plasmas*, 23(4):042707, 2016. doi: 10.1063/1.4947212.

[93] David M Ceperley. Path integrals in the theory of condensed helium. *Reviews of Modern Physics*, 67(2):279, 1995.

[94] B Militzer. Path integral Monte Carlo and density functional molecular dynamics simulations of hot, dense helium. *Phys. Rev. B*, 79(15):155105, 2009.

[95] S X Hu, B Militzer, V N Goncharov, and S Skupsky. First-principles equation-of-state table of deuterium for inertial confinement fusion applications. *Phys. Rev. B*, 84(22):224109, 2011.

[96] P Hollebon and Travis Sjostrom. Hybrid Kohn-Sham+ Thomas-Fermi scheme for high-temperature density functional theory. *Phys. Rev. B*, 105(23):235114, 2022.

[97] A. Blanchet, J. Clérouin, M. Torrent, and F. Soubiran. Extended first-principles molecular dynamics model for high temperature simulations in the Abinit code: Application to warm dense aluminum. *Computer Physics Communications*, 271:108215, 2022. doi: https://doi.org/10.1016/j.cpc.2021.108215.

[98] Larry C Andrews. *Special functions of mathematics for engineers [electronic resource]*. SPIE monograph ; PM49. SPIE, Bellingham, Wash. (1000 20th St. Bellingham WA 98225-6705 USA), 2nd ed. edition, 1998. ISBN 9780819478467 (electronic).

[99] Michele Goano. Algorithm 745: Computation of the complete and incomplete Fermi-Dirac integral. *ACM Transactions on Mathematical Software (TOMS)*, 21(3):221–232, 1995.

[100] Michele Goano. Remark on Algorithm 745. *ACM Transactions on Mathematical Software (TOMS)*, 23(2):295–295, 1997.

[101] Valentin V Karasiev, Debajit Chakraborty, and Samuel B Trickey. Improved analytical representation of combinations of Fermi–Dirac integrals for finite-temperature density functional calculations. *Computer Physics Communications*, 192:114–123, 2015.

[102] Marc Torrent, François Jollet, François Bottin, Gilles Zérah, and Xavier Gonze. Implementation of the projector augmented-wave method in the ABINIT code: Application to the study of iron under pressure. *Computational Materials Science*, 42(2):337–351, 2008. doi: 10.1016/j.commatsci.2007.07.020.

[103] ABINIT Forums. EXTFPMD SCF Convergence Suggestion, 2022. `https://discourse.abinit.org/t/extfpmd-scf-convergence-suggestion/3162` [Last Accessed: 15.04.2023].

[104] ABINIT v9.10 Release Notes. B. Most Notable Achievements, B.9, 2023. `https://docs.abinit.org/about/release-notes/#b-most-noticeable-achievements` [Last Accessed: 29.09.2023].

[105] Thomas Gawne, Thomas Campbell, Alessandro Forte, Patrick Hollebon, Gabriel Perez-Callejo, Oliver S. Humphries, Oliver Karnbach, Muhammad F. Kasim, Thomas R. Preston, Hae Ja Lee, Alan Miscampbell, Quincy Y. van den Berg, Bob Nagler, Shenyuan Ren, Ryan B. Royle, Justin S. Wark, and Sam M. Vinko. Investigating mechanisms of state localization in highly ionized dense plasmas. *Physical Review E*, 108:035210, 2023. doi: 10.1103/PhysRevE.108.035210.

[106] Thomas Gawne, Sam M Vinko, and Justin S Wark. Quantifying ionization in hot dense plasmas. *arXiv preprint arXiv:2309.09612*, 2023.

[107] G. B. Zimmerman and R. M. More. Pressure ionization in laser-fusion target simulation. *Journal of Quantitative Spectroscopy and Radiative Transfer*, 23 (5):517–522, 1980. doi: https://doi.org/10.1016/0022-4073(80)90055-2.

[108] Hans R. Griem. *Principles of Plasma Spectroscopy*. Cambridge Mono-

graphs on Plasma Physics. Cambridge University Press, 1997. doi: 10.1017/CBO9780511524578.002.

[109] John C Stewart and Kedar D Pyatt Jr. Lowering of ionization potentials in plasmas. *The Astrophysical Journal*, 144:1203, 1966.

[110] G Ecker and W Kröll. Lowering of the ionization energy for a plasma in thermodynamic equilibrium. *The Physics of Fluids*, 6(1):62–69, 1963.

[111] C A Iglesias and F J Rogers. Opacities for the solar radiative interior. *The Astrophysical Journal*, 371:408–417, 1991.

[112] Thomas R Preston, Sam M Vinko, Orlando Ciricosta, Hyun-Kyung Chung, Richard W Lee, and Justin S Wark. The effects of ionization potential depression on the spectra emitted by hot dense aluminium plasmas. *High Energy Density Physics*, 9(2):258–263, 2013.

[113] W. F. Schlotter, J. J. Turner, M. Rowen, P. Heimann, M. Holmes, O. Krupin, M. Messerschmidt, S. Moeller, J. Krzywinski, R. Soufli, M. Fernández-Perea, N. Kelez, S. Lee, R. Coffee, G. Hays, M. Beye, N. Gerken, F. Sorgenfrei, S. Hau-Riege, L. Juha, J. Chalupsky, V. Hajkova, A. P. Mancuso, A. Singer, O. Yefanov, I. A. Vartanyants, G. Cadenazzi, B. Abbey, K. A. Nugent, H. Sinn, J. Lüning, S. Schaffert, S. Eisebitt, W.-S. Lee, A. Scherz, A. R. Nilsson, and W. Wurth. The soft x-ray instrument for materials studies at the linac coherent light source x-ray free-electron laser. *Review of Scientific Instruments*, 83(4): 043107, 2012. doi: 10.1063/1.3698294.

[114] Stephanie B Hansen, J Colgan, A Ya Faenov, J Abdallah Jr, SA Pikuz Jr, I Yu Skobelev, E Wagenaars, N Booth, O Culfa, RJ Dance, et al. Detailed analysis of hollow ions spectra from dense matter pumped by X-ray emission of relativistic laser plasma. *Physics of Plasmas*, 21(3):031213, 2014.

[115] Carlos A Iglesias and Philip A Sterne. Fluctuations and the ionization potential in dense plasmas. *High Energy Density Physics*, 9(1):103–107, 2013.

[116] Gérald Faussurier and Christophe Blancard. Density effects on electronic configurations in dense plasmas. *Phys. Rev. E*, 97(2):023206, 2018.

[117] Xiaojian Li, FB Rosmej, VS Lisitsa, and VA Astapenko. An analytical plasma screening potential based on the self-consistent-field ion-sphere model. *Physics of Plasmas*, 26(3):033301, 2019.

[118] X Li and FB Rosmej. Analytical approach to level delocalization and line shifts in finite temperature dense plasmas. *Physics Letters A*, 384(25):126478, 2020.

[119] Jiaolong Zeng, Yongjun Li, Yong Hou, Cheng Gao, and Jianmin Yuan. Ionization potential depression and ionization balance in dense carbon plasma under solar and stellar interior conditions. *Astronomy & Astrophysics*, 644: A92, 2020.

[120] Jiaolong Zeng, Chen Ye, Yongjun Li, and Jianmin Yuan. Ionization potential depression in dense iron plasmas near solid density. *Results in Physics*, page 105836, 2022.

[121] Jackson Richard White, W Johns, Christopher John Fontes, Nathanael Matthew Gill, Nathaniel Ray Shaffer, and Charles Edward Starrett. Charge state distributions in dense plasmas. *Physics of Plasmas*, 29 (4):043301, 2022.

[122] Sang-Kil Son, Robert Thiele, Zoltan Jurek, Beata Ziaja, Robin Santra, et al. Quantum-mechanical calculation of ionization-potential lowering in dense plasmas. *Phys. Rev. X*, 4(3):031004, 2014.

[123] B. J. B. Crowley. Continuum lowering–a new perspective. *High Energy Density Physics*, 13:84–102, 2014.

[124] F. B. Rosmej. Ionization potential depression in an atomic-solid-plasma picture. *Journal of Physics B: Atomic, Molecular and Optical Physics*, 51(9): 09LT01, 2018.

[125] Annette Calisti, Sandrine Ferri, and Bernard Talin. Ionization potential depression for non equilibrated aluminum plasmas. *Journal of Physics B: Atomic, Molecular and Optical Physics*, 48(22):224003, 2015.

[126] Chengliang Lin, Gerd Röpke, Wolf-Dietrich Kraeft, and Heidi Reinholz. Ionization-potential depression and dynamical structure factor in dense plasmas. *Phys. Rev. E*, 96(1):013202, 2017.

[127] Chengliang Lin. Quantum statistical approach for ionization potential depression in multi-component dense plasmas. *Physics of Plasmas*, 26(12):122707, 2019.

[128] Gerd Röpke, David Blaschke, Tilo Döppner, Chengliang Lin, Wolf-Dietrich Kraeft, Ronald Redmer, and Heidi Reinholz. Ionization potential depression and Pauli blocking in degenerate plasmas at extreme densities. *Phys. Rev. E*, 99(3):033201, 2019.

[129] M Stransky. Monte Carlo simulations of ionization potential depression in dense plasmas. *Physics of Plasmas*, 23(1):012708, 2016.

[130] S. X. Hu. Continuum lowering and Fermi-surface rising in strongly coupled and degenerate plasmas. *Phys. Rev. Lett.*, 119(6):065001, 2017.

[131] Mandy Bethkenhagen, Bastian B L Witte, Maximilian Schörner, Gerd Röpke, Tilo Döppner, Dominik Kraus, Siegfried H Glenzer, Philip A Sterne, and Ronald Redmer. Carbon ionization at gigabar pressures: An ab initio perspective on astrophysical high-density plasmas. *Phys. Rev. Research*, 2(2): 023260, 2020.

[132] R. H Fowler and E. A Guggenheim. *Statistical Thermodynamics : a version of statistical mechanics for students of physics and chemistry.* University Press, Cambridge, Eng., 1939.

[133] Meghnad Saha. LIII. Ionization in the solar chromosphere. *The London,*

Edinburgh, and Dublin Philosophical Magazine and Journal of Science, 40 (238):472–488, 1920.

[134] Hans R Griem. High-density corrections in plasma spectroscopy. *Physical Review*, 128(3):997, 1962.

[135] G Cook and R H Dickerson. Understanding the chemical potential. *American Journal of Physics*, 63(8):737–742, 1995.

[136] B H Armstrong, J Sokoloff, R W Nicholls, D H Holland, and R E Meyerott. Radiative properties of high temperature air. *Journal of Quantitative Spectroscopy and Radiative Transfer*, 1(2):143–162, 1961.

[137] Richard M More. Atoms in dense plasmas. *Atoms in Unusual Situations*, pages 155–215, 1986.

[138] Geoffrey Keller and Mary Fenwick. Tabulation of the Incomplete Fermi-Dirac Functions. *The Astrophysical Journal*, 117:437, 1953.

[139] Rosemary A Coldwell-Horsfall and Alexei A Maradudin. Zero-Point Energy of an Electron Lattice. *Journal of Mathematical Physics*, 1(5):395–404, 1960.

[140] Leslie L Foldy. Electrostatic stability of Wigner and Wigner-Dyson lattices. *Phys. Rev. B*, 17(12):4889, 1978.

[141] Hans R Griem. *Plasma spectroscopy.* McGraw-Hill, New York ; London, 1964.

[142] O Renner, D Salzmann, P Sondhauss, A Djaoui, E Krouskỳ, and E Förster. Experimental evidence for plasma shifts in Lyman series of aluminum. *Journal of Physics B: Atomic, Molecular and Optical Physics*, 31(6):1379, 1998.

[143] D. J. Hoarty, P. Allan, S. F. James, C. R. D. Brown, L. M. R. Hobbs, M. P. Hill, J. W. O. Harris, J. Morton, M. G. Brookes, R. Shepherd, J. Dunn, H. Chen, E. Von Marley, P. Beiersdorfer, H. K. Chung, R. W. Lee, G. Brown, and J. Emig. Observations of the Effect of Ionization-Potential Depression in Hot Dense Plasma. *Phys. Rev. Lett.*, 110:265003, 2013. doi: 10.1103/PhysRevLett.110.265003.

[144] W Pauli Jr. Über gasentartung und paramagnetismus. *Zeitschrift für Physik A Hadrons and nuclei*, 41(2-3):81–102, 1927.

[145] Carlos A Iglesias and Philip A Sterne. Comment on "continuum lowering and fermi-surface rising in strongly coupled and degenerate plasmas". *Phys. Rev. Lett.*, 120(11):119501, 2018.

[146] O Renner, P Sondhauss, D Salzmann, A Djaoui, M Koenig, and E Förster. Measurement of the polarization shifts in hot and dense aluminum plasma. *Journal of Quantitative Spectroscopy and Radiative Transfer*, 58(4-6):851–857, 1997.

[147] A Saemann, K Eidmann, I E Golovkin, R C Mancini, E Andersson, E Förster, and K Witte. Isochoric heating of solid aluminum by ultrashort laser pulses focused on a tamped target. *Phys. Rev. Lett.*, 82(24):4843, 1999.

[148] N C Woolsey, C A Back, R W Lee, Annette Calisti, C Mossé, R Stamm, B Talin, A Asfaw, and L S Klein. Experimental results on line shifts from dense plasmas. *Journal of Quantitative Spectroscopy and Radiative Transfer*, 65(1-3):573–578, 2000.

[149] Klaus Eidmann, Ulrich Andiel, Francesca Pisani, P Hakel, R C Mancini, G C Junkel-Vives, J Abdallah, and Klaus Witte. K-shell spectra from hot dense aluminum layers buried in carbon and heated by ultrashort laser pulses. *Journal of Quantitative Spectroscopy and Radiative Transfer*, 81(1-4):133–146, 2003.

[150] O Renner, P Adámek, P Angelo, E Dalimier, E Förster, E Krousky, F B Rosmej, and R Schott. Spectral line decomposition and frequency shifts in Al Heα group emission from laser-produced plasma. *Journal of Quantitative Spectroscopy and Radiative Transfer*, 99(1-3):523–536, 2006.

[151] F Y Khattak, O A M B Percie du Sert, F B Rosmej, and D Riley. Evidence of plasma polarization shift of Ti He-α resonance line in high density laser produced plasmas. *Journal of Physics: Conference Series*, 397(1):012020, 2012.

[152] CR Stillman, PM Nilson, ST Ivancic, IE Golovkin, C Mileham, IA Begishev, and DH Froula. Picosecond time-resolved measurements of dense plasma line shifts. *Phys. Rev. E*, 95(6):063204, 2017.

[153] Franciszek Sobczuk, Krzysztof Dzierżęga, and Evgeny Stambulchik. Plasma Stark effect of He ii Paschen-α: Resolution of the disagreement between experiment and theory. *Phys. Rev. E*, 106(2):L023202, 2022.

[154] Do R Inglis and E Teller. Ionic Depression of Series Limits in One-Electron Spectra. *The Astrophysical Journal*, 90:439, 1939.

[155] DK Bradley, J Kilkenny, SJ Rose, and JD Hares. Time-resolved continuum-edge-shift measurements in laser-shocked solids. *Phys. Rev. Lett.*, 59(26):2995, 1987.

[156] David Riley, O Willi, SJ Rose, and T Afshar-Rad. Blue shift of the K absorption edge in laser-shocked solids. *Europhysics Letters*, 10(2):135, 1989.

[157] M Nantel, G Ma, S Gu, CY Cote, J Itatani, and Donald Umstadter. Pressure ionization and line merging in strongly coupled plasmas produced by 100-fs laser pulses. *Phys. Rev. Lett.*, 80(20):4442, 1998.

[158] A Lévy, F Dorchies, A Benuzzi-Mounaix, A Ravasio, F Festa, V Recoules, O Peyrusse, N Amadou, E Brambrink, T Hall, et al. X-ray diagnosis of the pressure induced mott nonmetal-metal transition. *Phys. Rev. Lett.*, 108(5): 055002, 2012.

[159] R M More. Atomic physics in inertial confinement fusion. *Lawrence Livermore Labratory Report*, 1981.

[160] G Ecker and W Weizel. Zustandssumme und effektive Ionisierungsspannung eines Atoms im Inneren des Plasmas. *Annalen der Physik*, 452(2-3):126–140, 1956.

[161] Nick W Hopps, Thomas H Bett, Nicolas Cann, Colin N Danson, Stuart J Duffield, David A Egan, Stephen P Elsmere, Mark T Girling, Ewan J Harvey,

David I Hillier, et al. Overview of project Orion. In *High Power Lasers for Fusion Research*, volume 7916, pages 84–93. SPIE, 2011.

[162] S B Hansen, E C Harding, P F Knapp, M R Gomez, T Nagayama, and J E Bailey. Changes in the electronic structure of highly compressed iron revealed by x-ray fluorescence lines and absorption edges. *High Energy Density Physics*, 24:39–43, 2017.

[163] L B Fletcher, A L Kritcher, A Pak, T Ma, T Döppner, C Fortmann, L Divol, O S Jones, O L Landen, H A Scott, et al. Observations of continuum depression in warm dense matter with x-ray Thomson scattering. *Phys. Rev. Lett.*, 112 (14):145004, 2014.

[164] D Kraus, D A Chapman, A L Kritcher, R A Baggott, B Bachmann, G W Collins, S H Glenzer, J A Hawreliak, D H Kalantar, O L Landen, T Ma, S Le Pape, J Nilsen, D C Swift, P Neumayer, R W Falcone, D O Gericke, and T Doppner. X-ray scattering measurements on imploding CH spheres at the National Ignition Facility. *Phys. Rev. E*, 94(1):011202(R), 2016.

[165] Ralph W. G Wyckoff. *Crystal Structures*. Interscience Publishers, New York, 1948.

[166] S. X. Hu. Hu Replies: "continuum lowering and fermi-surface rising in strongly coupled and degenerate plasmas". *Phys. Rev. Lett.*, 120:119502, 2018. doi: 10.1103/PhysRevLett.120.119502.

[167] Carlos A. Iglesias. A plea for a reexamination of ionization potential depression measurements. *High Energy Density Physics*, 12:5–11, 2014.

[168] BJB Crowley. Average-atom quantum-statistical cell model for hot plasma in local thermodynamic equilibrium over a wide range of densities. *Phys. Rev. A*, 41(4):2179, 1990.

[169] Wolf-Dietrich Kraeft, Dietrich Kremp, Werner Ebeling, and Gerd Röpke. *Quantum statistics of charged particle systems*. Springer, 1986.

[170] John C Slater. Note on Hartree's method. *Physical Review*, 35(2):210, 1930.

[171] John C Slater. A simplification of the Hartree-Fock method. *Physical review*, 81(3):385, 1951.

[172] F Rosmej, K Bennadji, and VS Lisitsa. Effect of dense plasmas on exchange-energy shifts in highly charged ions: An alternative approach for arbitrary perturbation potentials. *Phys. Rev. A*, 84(3):032512, 2011.

[173] X Li and FB Rosmej. Quantum-number–dependent energy level shifts of ions in dense plasmas: A generalized analytical approach. *Europhysics Letters*, 99 (3):33001, 2012.

[174] Jean Clérouin, Augustin Blanchet, Christophe Blancard, Gérald Faussurier, François Soubiran, and Mandy Bethkenhagen. Equivalence between pressure- and structure-defined ionization in hot dense carbon. *Phys. Rev. E*, 106(4): 045204, 2022.

[175] P Hollebon, J S Wark, and S M Vinko. Excited-state potentials for modelling dense plasmas from first principles. *Plasma Physics and Controlled Fusion*, 63 (11):114006, 2021. doi: 10.1088/1361-6587/ac2615.

[176] Walter Kohn. Theory of the insulating state. *Phys. Rev.*, 133(1A):A171, 1964.

[177] Axel D Becke and Kenneth E Edgecombe. A simple measure of electron localization in atomic and molecular systems. *The Journal of chemical physics*, 92(9):5397–5403, 1990.

[178] Andreas Savin, Ove Jepsen, Jürgen Flad, Ole Krogh Andersen, Heinzwerner Preuss, and Hans Georg von Schnering. Electron localization in solid-state structures of the elements: the diamond structure. *Angewandte Chemie International Edition in English*, 31(2):187–188, 1992.

[179] Gregory H Wannier. The structure of electronic excitation levels in insulating crystals. *Phys. Rev.*, 52(3):191, 1937.

[180] Ivo Souza, Nicola Marzari, and David Vanderbilt. Maximally localized Wannier functions for entangled energy bands. *Phys. Rev. B*, 65(3):035109, 2001.

[181] Nicola Marzari, Arash A Mostofi, Jonathan R Yates, Ivo Souza, and David Vanderbilt. Maximally localized Wannier functions: Theory and applications. *Reviews of Modern Physics*, 84(4):1419, 2012.

[182] R J Bell and Paul Dean. Atomic vibrations in vitreous silica. *Discussions of the Faraday society*, 50:55–61, 1970.

[183] Franz Wegner. Inverse participation ratio in 2+ ε dimensions. *Zeitschrift für Physik B Condensed Matter*, 36(3):209–214, 1980.

[184] V I Anisimov and O Gunnarsson. Density-functional calculation of effective coulomb interactions in metals. *Physical Review B*, 43(10):7570, 1991.

[185] A I Liechtenstein, Vladimir I Anisimov, and Jan Zaanen. Density-functional theory and strong interactions: Orbital ordering in Mott-Hubbard insulators. *Physical Review B*, 52(8):R5467, 1995.

[186] Vladimir I Anisimov, Ferdi Aryasetiawan, and AI Lichtenstein. First-principles calculations of the electronic structure and spectra of strongly correlated systems: the lda+ u method. *Journal of Physics: Condensed Matter*, 9(4):767, 1997.

[187] Peter E Blöchl, Ove Jepsen, and Ole Krogh Andersen. Improved tetrahedron method for Brillouin-zone integrations. *Physical Review B*, 49(23):16223, 1994.

[188] Sam M. Vinko. X-ray free-electron laser studies of dense plasmas. *Journal of Plasma Physics*, 81(5):365810501, 2015. doi: 10.1017/S0022377815000902.

[189] James M Peek and Joseph B Mann. Continuum orbital approximations in weak-coupling theories for inelastic electron scattering. *Physical Review A*, 16 (6):2315, 1977.

[190] Robert D Cowan. *The theory of atomic structure and spectra*. Number 3. University of California Press, 1981.

[191] AAEXCITE. Available at: https://www-amdis.iaea.org/AAEXCITE/ [Last Accessed: 26.05.2023].

[192] Paul Kirkpatrick and Albert Vincio Baez. Formation of optical images by X-rays. *JOSA*, 38(9):766–774, 1948.

[193] N.A.W. Holzwarth, A.R. Tackett, and G.E. Matthews. A Projector Augmented Wave (PAW) code for electronic structure calculations, Part I: atompaw for generating atom-centered functions. *Computer Physics Communications*, 135(3):329–347, 2001. doi: https://doi.org/10.1016/S0010-4655(00)00244-7.

[194] Valentin V. Karasiev, Lázaro Calderín, and S. B. Trickey. Importance of finite-temperature exchange correlation for warm dense matter calculations. *Phys. Rev. E*, 93:063207, 2016. doi: 10.1103/PhysRevE.93.063207.

[195] T Döppner, M Bethkenhagen, D Kraus, P Neumayer, D A Chapman, B Bachmann, R A Baggott, M P Böhme, L Divol, R W Falcone, L B Fletcher, O L Landen, M J MacDonald, A M Saunders, M Schörner, P A Sterne, J Vorberger, B B L Witte, A Yi, R Redmer, S H Glenzer, and D O Gericke. Observing the onset of pressure-driven K-shell delocalization. *Nature*, 618(7964):270–275, 2023.

[196] P A Sterne, S B Hansen, B G Wilson, and W A Isaacs. Equation of state, occupation probabilities and conductivities in the average atom Purgatorio code. *High Energy Density Physics*, 3(1-2):278–282, 2007.

[197] Ryogo Kubo. Statistical-mechanical theory of irreversible processes. I. General theory and simple applications to magnetic and conduction problems. *Journal of the Physical Society of Japan*, 12(6):570–586, 1957.

[198] DA Greenwood. The Boltzmann equation in the theory of electrical conduction in metals. *Proceedings of the Physical Society*, 71(4):585, 1958.

[199] E I Blount. Formalisms of band theory. In *Solid state physics*, volume 13, pages 305–373. Elsevier, 1962.

[200] Neil W Ashcroft and N David Mermin. *Solid state physics*. Holt, Rinehart & Winston, New York ; London, 1976. ISBN 9780030839931.

[201] Willy Thomas. Über die Zahl der Dispersionselektronen, die einem stationären Zustande zugeordnet sind.(Vorläufige Mitteilung). *Naturwissenschaften*, 13 (28):627–627, 1925.

[202] Fritz Reiche and Willy Thomas. Über die Zahl der Dispersionselektronen, die einem stationären Zustand zugeordnet sind. *Zeitschrift für Physik*, 34(1): 510–525, 1925.

[203] Werner Kuhn. Über die Gesamtstärke der von einem Zustande ausgehenden Absorptionslinien. *Zeitschrift für Physik*, 33(1):408–412, 1925.

[204] Lucas Calderin, Valentin V Karasiev, and Samuel B Trickey. Kubo–Greenwood electrical conductivity formulation and implementation for projector augmented wave datasets. *Computer Physics Communications*, 221:118–142, 2017.

[205] US Whang, ET Arakawa, and TA Callcott. Optical properties of K between 4 and 10.7 eV and comparison with Na, Rb, and Cs. *Physical Review B*, 6(6): 2109, 1972.

[206] T Kobayasi and M Watabe. Remark on the conductivity sum rule for the optical absorptions of alkali metals. *Solid State Communications*, 13(1):59–62, 1973.